FACULTY
OF MATHEMATICS
AND PHYSICS
Charles University

DOCTORAL THESIS

Anastasiya Yilmaz

Evolution of Accreting Black Holes in X-ray Binaries

Astronomical Institute of Charles University

Supervisor of the doctoral thesis:	RNDr. Jiří Svoboda, Ph.D.
Advisor of the doctoral thesis:	Dr. Victoria Grinberg
Study programme:	Theoretical Physics, Astronomy and Astrophysics
Study branch:	P4F1A

Prague 2024

I declare that I carried out this doctoral thesis independently, and only with the cited sources, literature and other professional sources. It has not been used to obtain another or the same degree.

I understand that my work relates to the rights and obligations under the Act No. 121/2000 Sb., the Copyright Act, as amended, in particular the fact that the Charles University has the right to conclude a license agreement on the use of this work as a school work pursuant to Section 60 subsection 1 of the Copyright Act.

In .... date ....
Author's signature

To the loving memory of my mother, one of the most empowering women to ever walk this planet whose extraordinary resilience, courage and wisdom still light up my way while exploring the darkest corners of the universe.

Title: Evolution of Accreting Black Holes in X-ray Binaries

Author: Anastasiya Yilmaz

Institute: Astronomical Institute of Charles University

Supervisor: RNDr. Jiří Svoboda, Ph.D., Astronomický ústav AV ČR

Advisor: Dr. Victoria Grinberg, European Space Agency, ESTEC

Abstract: Accretion disks around compact objects provide an ideal environment to study the accretion phenomena in strong gravitational potentials. Accreting black holes in X-ray binaries and a sample of ultraluminous X-ray sources (ULXs) are known to undergo changes in their observed properties, which pose an important challenge to our understanding of the accretion phenomena in these systems. In this thesis, we present a systematic analysis of ∼1800 RXTE observations of GRO J1655-40 and LMC X-3 and report on a new transient ULX candidate (ULX*) in M51. Using the spectral continuum fitting method with kerrbb, we also report a new black hole spin measurement of LMC X-3 which was later confirmed by the spectropolarimetric analysis of simultaneous IXPE, NuSTAR, NICER, and Swift observations. Our analysis of GRO J1655-40 and LMC X-3 showed that the non-relativistic modeling of these disks leads to a significant oversight of the measured disk temperatures and radii as they evolve through different accretion states. We showed this overestimation of disk temperatures in non-relativistic modeling leads to unphysically low values of the inner disk radius. Its relativistic counterparts provided a more self-consistent description of the observed spectra along with more physically realistic values of the disk radius when evaluated as a free parameter in the model. Additionally, a previous global study of the known Galactic black hole X-ray binaries revealed that a significant portion of the studied sample showed an overturn in the observed relationship between observed disk luminosity and temperature. With increasing luminosities, disk temperatures transitioned to much higher values than expected, characterized by a negative slope. However, LMC X-3 has undergone multiple outbursts reaching luminosities much higher compared to the majority of the observed outbursts while not exhibiting a similar trend. It contradicts the assumption that this behavior would be a result of the need to invoke a different accretion disk solution due to the higher mass accretion rates. After a thorough investigation of the parameter space of the three models used in the analysis, this overturn was recovered by adopting the accretion disk model which uses the ray tracing method to calculate the spectrum and accounts for the relativistic effects at different radii. On the other hand, ULXs have shown a similar negative slope without presenting clear evidence of similar spectral state transitions but showing long-term variability in the observed luminosity. A better understanding of the long-term variability of both populations is crucial to develop a unified accretion scheme across the mass accretion scale. With its discovery, M51 ULX* now contributes to a growing population of transient ULXs where the “transient” nature of the accretion phenomenon cannot be explained by currently available accretion disk models.

Keywords: black holes - accretion physics - active galactic nuclei

Acknowledgements

Without intending any offense, I must give the highest credit to the thirteen-year-old girl who chose to stay alive when her life was brutally turned upside down in an instant. She never thought she would see the daylight again but she got out of that orphanage to find herself living a life she promised her mother she would. She forged a path through the jungle of her life, a path no one had walked before, without anyone cheering her on. Today, I continue on that path but I am no longer alone. I wish this work to be taken as a tribute to all the extraordinary people I met who helped me clear the branches out of my way and I dedicate this title to that girl who so bravely rejected all the other ones society tried imposing on her. On us, on all the women born into this world, on my dear mother.

I do not wish to leave it without special emphasis, I would not have been able to get thus far to see the end of this thesis without the valuable support I was gifted by my human and furry friends, colleagues, and family. I feel exceptionally fortunate and will always remind myself how rare of an occasion it is to have a lot to be grateful for.

First and foremost, I would like to acknowledge the support I received from my supervisors, Dr. Jiří Svoboda and Dr. Victoria Grinberg, along the way.

I am thankful for Jiří's guidance and support throughout my entire time at Charles University and the Astronomical Institute of the Czech Academy of Sciences. The past four years have taught me a lot more than I thought I needed while still leaving me a lot of room for independence. I will always cherish our nice memories and laughter together as long as my mind can hold on to this part of my life.

Victoria's support, mentorship, and critique have not only improved this thesis and the publications leading to the completion of this degree but also positively influenced my future career as far as I am able to continue. In a world full of people continuously showing me the kind of person and scientist I do not want to become, thank you for being your strong, honest, and kind-hearted self.

I am incredibly grateful to have met (future Dr.) Camille Landri, my dear friend and sane side. Never could I imagine this very unlikely match in an old dorm room in the middle of a pandemic would turn into a friendship I would be so thankful for. I will always cherish our countless coffee and doodling dates, badminton matches, and that one 5k race I miraculously convinced you to run with me. You have always been an inspiration to me, I only hope the world is kind enough not to push us apart.

I would like to thank Dr. Enrico Bozzo, for his mentorship and patience along the way and for believing in me in moments when I could not. By some chance I would not even think could exist, my very ordinary two-week visit to Geneva back in February of 2019 has shaped my life in ways I did not see coming. Each time I came back, it always felt like I was back home. That was never a feeling I was familiar with until very recently. Thank you for your endless support and guidance while still allowing me to explore this academic world on my own and reminding me of the courage and strength that got me through this Ph.D.

Dear Dr. Michal Bursa, Michal Dovčiak, and Dr. Jiří Horák, I will always remember the smile you both had on your faces every time I asked questions and fruitful hours-long discussions followed each one of them. I can only wish for

many more future occasions.

Dear Dr. Felix Fuerst and Dr. Carlo Ferrigno, thank you both so much for your encouragement, support, and guidance. It has been one of my greatest pleasures to get to learn from you.

Dear Dr. Abhijeet Borkar, thank you for being the friend and colleague I needed to survive this circus. I will always treasure your friendship and support and can only hope we will have many more brunches and runs to go for.

My dear friend and colleague, Dr. Debora Lančová, thank you so much for the extent of support you were kind enough to provide while it was never your responsibility to do so. It is not always you get to call one your close friend and also your collaborator without ruining one side over the other. I am so very grateful to have met you and only hope our bond will grow stronger as we age. I would also like to acknowledge the valuable contribution of your two black holes, Kočka and Kocour. I hope the many hugs and pets I am looking forward to giving in the future will be able to match their efforts in making this thesis possible.

My greatest support, Dr. Eda Oktay, I am so happy that our paths crossed. We both met at a time of great exhaustion from the world we worked so hard to walk away from but our bond proved to be stronger than the people who tried so hard to take us down. Thank you for understanding me in ways not many could.

Önder Çatmabacak, one of my oldest friends in the academic world, I will always be grateful for your trust in me. Separated by continents, you have done for me more than I could even ask for. I can only hope one day our roads will cross outside of the digital world of Skype and we get to look back at our old days with a sip of good coffee. Thank you for being you.

Dear Dr. Romana Mikušincová, my friend and colleague, thank you for being by my side at times I could not even keep my sanity. It was a great luck to meet you and I am so grateful I was granted it at the right time and place. I will always look forward to our next morning run to Colosseo, the nice cappuccino I can drink with full Italian approval, and another picture of us with our faces bright red from the sun. My coffee didn't get cold for hours and I said "Thankfully this is Rome". Miracles might be a thing.

Possibly one of the greatest coincidences, having met at a conference very last minute, I am so happy to be able to call Sabela Reyero Serantes my friend and colleague. I am really looking forward to calling you "doctor" once these days pass.

Vittoria Gianolli, my partner in food chasing and furry friends... thank you for all the laughter in places I never thought I could ever enjoy. I am so glad that I got to meet you in all this craziness academia brought upon us and I am looking forward to the days we will sit back and laugh about these days. Probably surrounded by many cats and good food.

I would like to acknowledge all of the support I received from the Astronomical Institute of Charles University, the Institute of Theoretical Physics of Charles University, and the Astronomical Institute of the Czech Academy of Sciences. I am forever grateful for all the help, every single answer to my questions, and guidance through the Czech bureaucracy.

I am also incredibly grateful to the Department of Astronomy of the University of Geneva, the Institute of Physics of the Silesian University, ESA-ESTEC and ESAC- and finally INAF-IAPS in Rome for always making me feel at home.

Last but not least, I would also like to acknowledge each and every one of the students and academics around the world and throughout history, who never got to see their graduation and celebrate their success because they were born in the wrong part of the world at the wrong time. I am no longer sure if there will be a sunrise on the horizon to put an end to the worst nightmare humanity has been left to watch on repeat for as long as our history books can go back.

This thesis was supported by GAUK project No. 102323, GAČR projects No. 21-06825X, and No. 19–05599Y. The research leading to these results has received funding from the European Union's Horizon 2020 Programme under the AHEAD2020 project (grant agreement n. 871158) based on observations with INTEGRAL, an ESA project with instruments and science data center funded by ESA member states (especially the PI countries: Denmark, France, Germany, Italy, Switzerland, Spain), and with the participation of the Russian Federation and the USA. I also acknowledge support from the ESA Archival Research Visitor Programme during my stay at ESAC, Madrid Spain, and ESTEC, Noordwijk Netherlands.

”Started making it, had a breakdown, Bon Appétit!”
James Acaster

Contents

1. Introduction

1.1 Black Holes

A star with a mass of several tens of solar masses nears the end of its life as it exhausts the fuel in its interior and as a result, the thermonuclear reactions can no longer supply the radiation pressure which is necessary to balance the gravitational contraction. Such stars eventually either undergo a catastrophic explosion as supernovae or directly collapse into a region of spacetime in which the curvature at the center becomes infinite creating a strong gravitational potential around it. Such extreme potentials result in escape velocities even higher than the speed of light, leading to the infamous name "black hole".

Despite Einstein as the commonly presumed "creator" of the idea of black holes, it was originally John Michell who first postulated that an astrophysical object with escape velocity exceeding the speed of light would appear black as it would no longer be able to emit light to an observer [Michell, 1784]. This prediction was in response to his mission to calculate the mass of a star from the speed of light it emits, which needed more than a century to show that the speed of light in vacuum is constant. Following Einstein's Theory of Relativity, Karl Schwarzschild solved Einstein's equations for a spherically symmetric region of spacetime [Schwarzschild, 1916] but it was only in 1968 that the name "black hole" was invented.

In 1915, Einstein formulated the field equations (Einstein's field equations or shortly Einstein's equations) describing the geometry of spacetime in relation to the distribution of mass across it [Einstein, 1915, 1916].

$$R_{\mu\nu} - \frac{1}{2}Rg_{\mu\nu} + \Lambda g_{\mu\nu} = \kappa T_{\mu\nu} \tag{1.1.1}$$

where $R_{\mu\nu}$ is the Ricci curvature tensor, R is the Ricci scalar, Λ is the cosmological constant, G is the gravitational constant, $g_{\mu\nu}$ is the spacetime metric, $T_{\mu\nu}$ is the energy-momentum tensor and c is the speed of light.

In vacuum,

$$G_{\mu\nu} \equiv R_{\mu\nu} - \frac{1}{2}Rg_{\mu\nu} = 0 \tag{1.1.2}$$

where $G_{\mu\nu}$ is called the Einstein tensor.

For a spherically symmetric object of mass M, the escape velocity is easily calculated by balancing the potential and kinetic energies of a test particle of m adopting the classical Newtonian theory of gravity:

$$\frac{1}{2}mv^2 = \frac{GmM}{r} \tag{1.1.3}$$

From which, the escape velocity reads

$$v_{\mathrm{esc}}^2 = \frac{2GM}{r} \tag{1.1.4}$$

The simplest assumption is that if there is a critical value for r, r_c, one would have a region where the escape velocity is larger than the speed of light. For escape velocities larger than the speed of light, this region corresponds to

$$r_c < \frac{2GM}{c^2} \tag{1.1.5}$$

While this radius is Newtonian, Schwarzschild's metric also predicts the same limit in General Relativity (GR) and hence is defined as Schwarzschild radius:

$$r_{\mathrm{s}} = \frac{2GM}{c^2} = 2r_{\mathrm{g}} \tag{1.1.6}$$

where G denotes the gravitational constant, c is the speed of light in vacuum and M is the black hole mass.

In standard units, the Schwarzschild metric reads

$$\mathrm{d}s^2 = -\left(1 - \frac{2GM}{c^2 r}\right) c^2\ \mathrm{d}t^2 + \frac{\mathrm{d}r^2}{1 - \frac{2GM}{c^2 r}} + r^2 \left(\ \mathrm{d}\theta^2 + \sin^2\theta \mathrm{d}\phi^2\right) \tag{1.1.7}$$

Where r is the radial coordinate, φ is the azimuthal angle and θ is the latitude.

In a more general sense, the Schwarzschild metric describes a non-rotating black hole [Schwarzschild, 1916]. In 1963, Kerr derived a solution for a spinning black hole [Kerr, 1963] where the metric in Boyer-Lindquist coordinates (t,r,θ,φ) reads

$$\begin{gathered} ds^2 = -\left(1 - \frac{2Mr}{\Sigma}\right) dt^2 - \frac{4aMr\sin^2\theta}{\Sigma} dtd\phi + \frac{\Sigma}{\Delta} dr^2 + \Sigma d\theta^2 + \\ \left(r^2 + a^2 + \frac{2a^2 Mr\sin^2\theta}{\Sigma}\right)\sin^2\theta d\phi^2, \end{gathered} \tag{1.1.8}$$

in which

$$a = \frac{J}{Mc}, \tag{1.1.9}$$

$$\Sigma^2 = r^2 + a^2\cos^2\theta, \tag{1.1.10}$$

$$\Delta = r^2 - r_{\mathrm{s}} r + a^2. \tag{1.1.11}$$

The above metric represents the line element for a rotating Kerr black hole of mass M with the angular momentum J. In a more general sense, a is described as the angular momentum per unit mass.

In contrast to the Schwarzschild case, the Kerr metric has two horizons represented by

$$r_{\pm} = M \pm \sqrt{M^2 - a^2} \tag{1.1.12}$$

which are referred to as outer (+) and inner (-) event horizons.

Innermost stable circular orbit

The innermost stable circular orbit or ISCO, defines the limit closest to the black hole in which matter can remain in stable circular orbits around the black hole. Beyond this limit, matter can no longer sustain stable orbits and spiral down into the black hole.

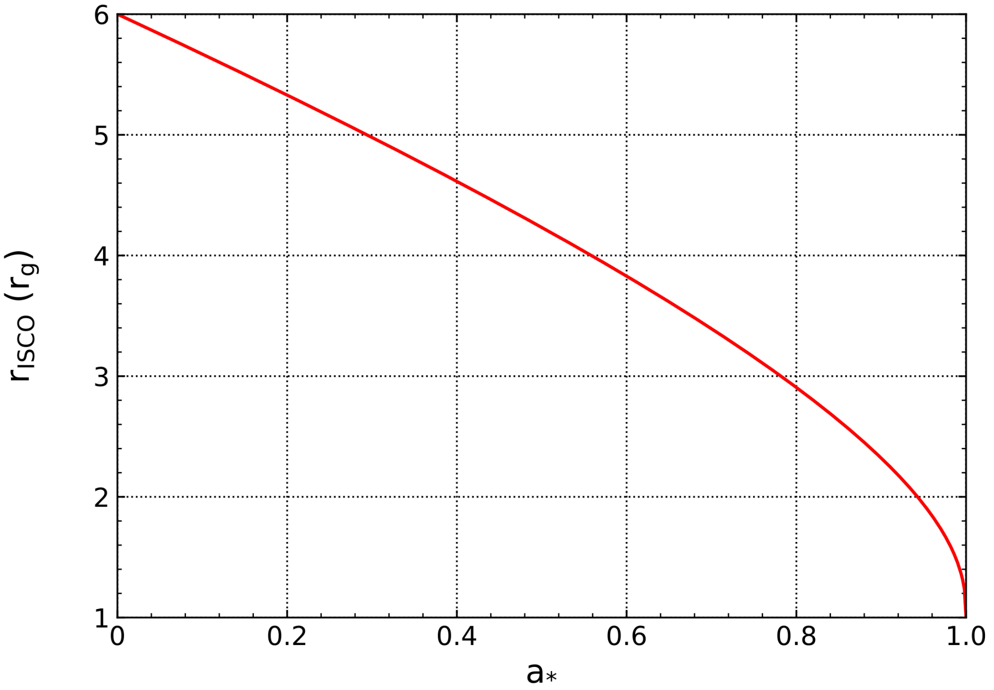

Figure 1.1: Location of the ISCO in the units of gravitational radii with respect to black hole spin values ranging between 0 and 1.

The extent of this region is described mainly by two parameters, the dimensionless black hole spin a and black hole mass M,

$$r_{\mathrm{ISCO}} = r_{\mathrm{g}} \left\{ 3 + A_2 \pm \left[\left(3 - A_1\right)\left(3 + A_1 + 2A_2\right) \right]^{1/2} \right\} \tag{1.1.13}$$

$$A_1 = 1 + \left(1 - a_*^2\right)^{1/3} \left[\left(1 + a_*\right)^{1/3} + \left(1 - a_*\right)^{1/3} \right] \tag{1.1.14}$$

$$A_2 = \left(3a_*^2 + A_1^2\right)^{1/2} \tag{1.1.15}$$

$$a_* = \frac{|\mathbf{J}|c}{GM^2} \tag{1.1.16}$$

where a_* ranges between -1 and 1 where - and + values correspond to retrograde and prograde rotations, respectively. Figure 1.1 shows the position of ISCO in the units of gravitational radii (r_{g}) with respect to the dimensionless black hole spin in the $0 < \mathrm{a}_* < 1$ range.

1.1.1 Dissecting Black Hole X-ray Binaries

As the matter approaches the black hole, the material heats up due to the viscosity, eventually illuminating the X-ray sky. These X-ray bright systems are called X-ray binaries and provide unique environments to study the behavior of matter in such extreme environments due to the strong gravitational potentials around black holes.

The majority of the broadband X-ray spectra observed from BHXRBs can be dominantly described by two main components throughout an outburst: hard and soft components. However, there are several components to the physical system

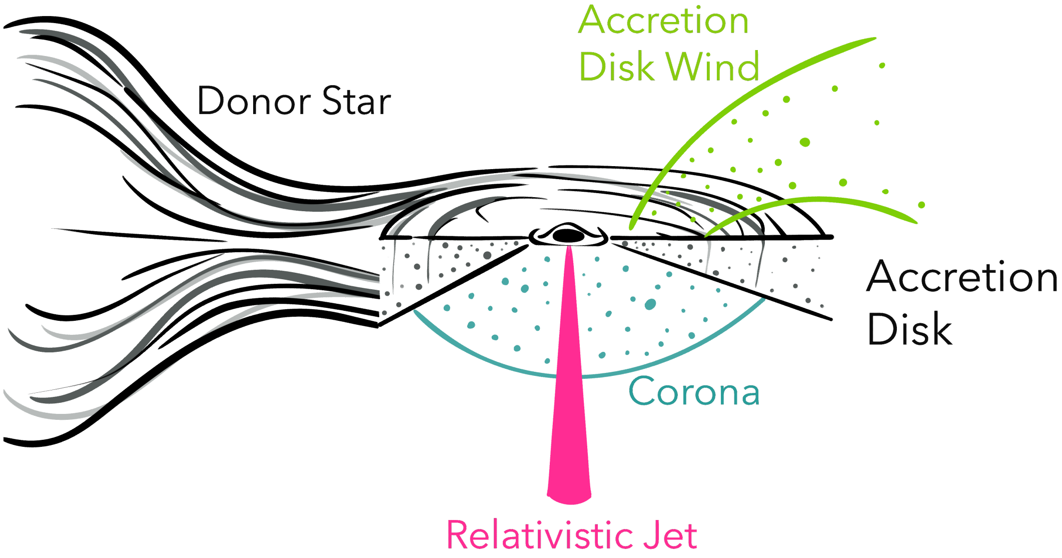

Figure 1.2: A sketch of a BHXRB showing each component: accretion disk, disk wind, corona, relativistic jet, and the donor star. For simplicity, the relativistic jet and corona are illustrated only in one direction. The jet structure is expected to be symmetrical and the geometry of the corona is not only limited to a spherical structure. See Figure 1.5 for possible geometries.

that evolve along with certain properties of the accretion state. In a more general picture, the following components are found to contribute to the X-ray spectra and present characteristics that evolve throughout an outburst: (i) accretion disk, (ii) corona, (iii) relativistic jet, (iv) accretion disk wind. Figure 1.2 provides a general overview of these components.

Accretion Disk

When a compact object such as a black hole or a neutron star is in a binary system, the companion star remains gravitationally bound to the compact object. Under certain circumstances, the companion can start transferring mass onto the black hole via an accretion disk. Accretion disks form when the infalling material from the companion/donor star has enough angular momentum to begin orbiting around the black hole. On the other hand, the further radial infall of the material is halted due to the presence of a centrifugal potential barrier which the infalling material cannot pass through unless the angular momentum is transported outwards, eventually forming a disk-like structure.

X-ray binaries (XRBs), regardless of the nature of the compact object, are categorized by the mass of the companion or the donor star into two groups, high-mass and low-mass X-ray binaries (HMXRBs and LMXRBs, respectively). This categorization also enables a direct link to the nature of the process that is assumed to induce the accretion:

(i) *Accretion via Strong Stellar Winds and High-Mass X-ray Binaries*: High-mass X-ray binaries are systems in which the compact object accretes from a rather massive star with a mass of $\geq 10 M_{\odot}$. The material flow from the massive donor star is induced by the strong stellar winds which reach the mass loss rate of $\geq 10^{-6} M_{\odot}\mathrm{yr}^{-1}$.

(ii) *Roche Lobe Overflow and Low-Mass X-ray Binaries*: A large fraction of low-mass X-ray binaries consists of a donor star that is either a main sequence star or a sub-giant or red giant that is filling its Roche Lobe where the material flows onto the compact object forming an accretion disk. Many of the observed galactic BHXRBs are in a LMXRB. First formulated by Edouard Roche, the so-called Roche problem describes the orbit of a test particle under the influence of the gravitational potential of two orbiting bodies of M_1 and M_2 which are massive enough that their orbits are not perturbed by the test particle. These two bodies are assumed to be "centrally condensed" and in circular and Keplerian orbits around each other. Figure 1.3 gives a general overview of this interacting system.

The separation between the two stars d can be easily derived from Kepler's law in terms of the period of the binary system:

$$4\pi^2 d^3 = GMP^2 \tag{1.1.17}$$

where $M = M_1 + M_2$. Then, any gas flow between these two masses can be described by Euler's equation in the reference frame rotating with the binary system with angular velocity ω:

$$\frac{\partial \mathbf{v}}{\partial t} + (\mathbf{v} \cdot \nabla)\mathbf{v} = -\frac{1}{\rho}\nabla P - \nabla \Phi_{\mathrm{R}} - 2\omega \times \mathbf{v} \tag{1.1.18}$$

where the last term on the right-hand-side describes the Coriolis force per unit mass and the angular velocity can be described in terms of a unit vector normal to the orbital plane:

$$\omega = \left[\frac{GM}{d^3}\right]^{1/2} \mathbf{n}$$

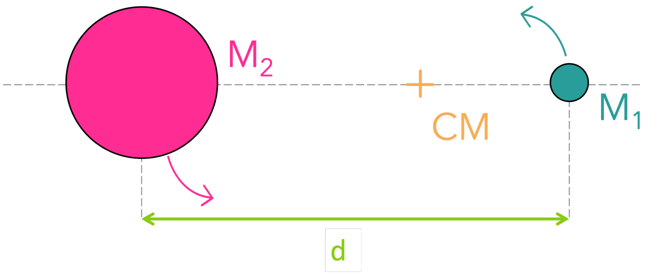

Figure 1.3: Illustration of a binary system of two massive bodies of M_1 and M_2 rotating around a center of mass CM separated by a distance d.

$\Phi_{\mathrm{R}}(\mathbf{r})$ is called the Roche Potential, and accounts for gravitational and centrifugal forces in the binary system:

$$\Phi_{\mathrm{R}}(\mathbf{r}) = -\frac{GM_1}{|\mathbf{r}-\mathbf{r}_1|} - \frac{GM_2}{|\mathbf{r}-\mathbf{r}_2|} - \frac{1}{2}(\omega \times \mathbf{r})^2 \tag{1.1.19}$$

where $\mathbf{r_1}$ and $\mathbf{r_2}$ are position vectors of center of masses of M_1 and M_2, respectively. Figure 1.4 shows the equipotential lines of the Roche potential of an LMXB.

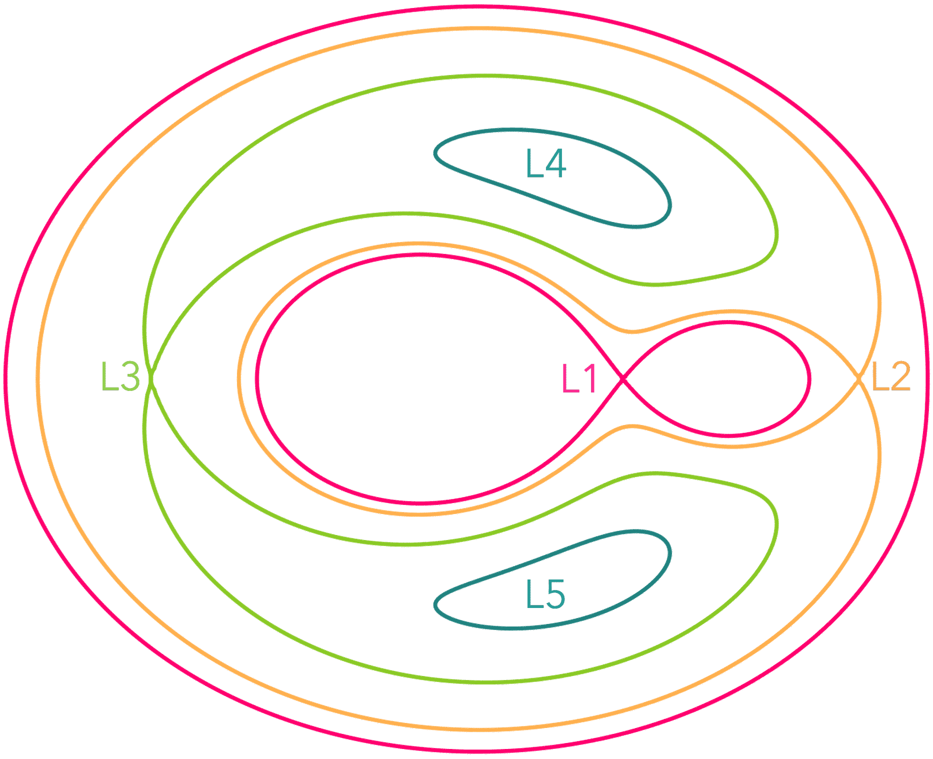

Figure 1.4: Roche potential in a LMXRB with Lagrangian points L1 through L5 indicated.

In practical terms, both accretion mechanisms may contribute to forming the disks in LMXRBs, with the dominant process varying by case. Accretion remains one of the most energetic processes in the universe, causing material in the innermost parts of the accretion disk near the black hole to reach extremely high temperatures. These temperatures, which can rise to several keV, produce electromagnetic radiation that is primarily visible in the X-ray spectrum.

X-ray Corona

The high energy emission in the broadband X-ray spectrum is produced in a cloud of hot electrons where the thermal emission originating from the accretion disk is upscattered to higher energies via inverse Compton scattering [Sunyaev and Titarchuk, 1980]. This process takes place when the electron's energy is greater than the energy of the "seed" photon emitted from the accretion disk, transferring a portion of its energy to the photon contributing to the non-thermal hard tail of the spectrum. The origin and exact geometry of the corona are not well understood yet. There are three models widely accepted: (i) lamp-post, (ii) spherical/extended, and (iii) sandwich. Figure 1.5 provides a general illustration of each model.

(i) *Lamp-post Corona*: This model assumes a small corona located at a certain distance from the black hole on the rotation axis [Matt et al., 1991, Martocchia and Matt, 1996, Miniutti and Fabian, 2004]. It's presumed that the corona is located close to the black hole and the emission carries the signatures of strong relativistic effects.

(ii) *Spherical/Extended Corona*: The spherical geometry of the corona describes a larger spherical structure [Wilkins et al., 2016, Chainakun et al., 2019]. The general assumption is that this spherical geometry usually accompanies a truncated accretion disk and extends to the ISCO. In contrast to the lamp-post geometry, only a small portion of the emission originates from the vicinity of the black hole and is not influenced by strong relativistic effects. While the spherical and lamp-post models result in comparably similar output, the distinguishing factor between the two is the relative contribution of the reflection component to the spectral continuum.

(iii) *Sandwich Corona*: Initially proposed for active galactic nuclei (AGN) [Haardt and Maraschi, 1991, 1993], describes a geometry "sandwiching" the accretion disk. Contrasting the predicted rather flat spectrum at energies above 5 keV, the spectra produced by this model are reportedly softer with $\Gamma \sim 2.1$ [Malzac et al., 2001] because half of the primary radiation from the corona illuminates the disk.

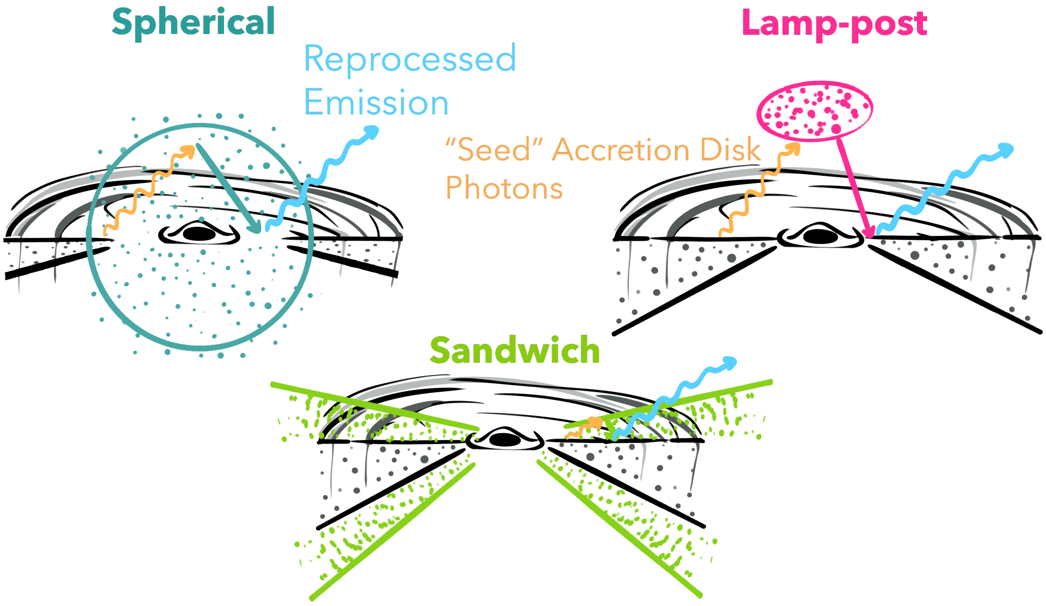

Figure 1.5: A simplistic illustration showing the three geometries for the corona: spherical(blue), sandwich(green) and lamp-post(pink). Orange rays represent the "seed" photons emitted from the accretion disk.

Accretion Disk Wind

Accretion disk winds are strong outflows of material being launched from the accretion disk, often identified through the existence of blueshifted absorption lines in the X-ray spectrum[Ebisawa, 1997, Kotani et al., 1997, Brandt and Schulz, 2000, Kotani et al., 2000b,a, Lee et al., 2002, Díaz Trigo et al., 2012, King et al., 2013, Díaz Trigo and Boirin, 2016, Ponti et al., 2016]. The driving mechanism of these outflows is not easy to identify but the ionization state of the wind and the characteristics of the absorption lines play a crucial role in determining the nature and possibly the origin of the wind, eventually providing further insight into the accretion-ejection phenomena in XRBs. Due to the small cross-sections of certain ions like Al, Mg, Na, Ne, O, and Si at energies above 10 keV, the ionization of these winds is dominantly affected by the soft emission.

In the more generally accepted picture, there are three main launching mechanisms: (I) magnetically-driven (ii) radiation-driven (iii) thermally-driven winds [Miller et al., 2011, Neilsen and Lee, 2009, Ueda et al., 2009, 2010, Neilsen et al., 2011, 2012, Ponti et al., 2012]. These three mechanisms are usually driven by different processes that require different properties of the physical system.

Relativistic Jet

Relativistic jets are powerful outflows of plasma that are assumed to form in the close vicinity of the black hole. The non-thermal emission, dominantly observed in radio, is presumed to originate from the relativistic electrons accelerated by the presence of a magnetic field. The formation of such ejecta is not well understood yet as the physical process would strongly depend on the geometry and the strength of the magnetic field and the distribution of the plasma around the black hole. The formation of these jets is usually associated with the accretion state in which the mass accretion rate is significantly lower and the X-ray spectrum is dominated by the non-thermal emission from the corona and the strength of the jet is observed to diminish over time as the mass accretion rate increases and the source enters a disk-dominated state, hence suggesting a coupled nature between the mass accretion and ejection or the so-called ”disk-jet coupling”.

A possible scenario proposed by Blandford and Znajek [1977] suggests a mechanism where the launching of the relativistic jet is facilitated by extracting the rotational energy of the black hole with the help of a magnetized plasma. In this scenario, the transfer of the rotational energy happens in the presence of magnetic fields in the close vicinity of the black hole subject to the frame-dragging effect due to the spin of the black hole. As the black hole spins, the magnetic field lines get twisted and the rotational energy of the black hole gets transported to the magnetized plasma resulting in strong ejecta along the rotational axis of the black hole.

Similar to the principles outlined in the Blandford-Znajek mechanism [Blandford and Znajek, 1977], Blandford and Payne [Blandford and Payne, 1982] propose a model where the ionization of plasma within the accretion disk strengthens magnetic fields. As matter accretes onto the black hole, relativistic effects cause the toroidal magnetic field to twist due to frame-dragging. This twisting exerts a force on the accreting matter, propelling some of it along the black hole’s rotational axis, a process known as magneto-centrifugal acceleration.

The Blandford Payne (1982) mechanism emphasizes the role of the accretion disk's magnetic field and the magneto-centrifugal acceleration in launching relativistic jets from accreting black holes. It provides an alternative to the Blandford-Znajek mechanism and has been widely studied as a potential explanation for the observed jet phenomena in AGNs, quasars, and other accreting black hole systems.

1.1.2 Eddington Limit

In order to be able to quantify certain properties of the system, it is necessary to define a few fundamental characteristics of the accretion flow. By doing so, it becomes easier to assess the evolution of the accretion disks and describe the interplay between the components contributing to the broadband spectral continuum.

Let us first assume the simplest accretion geometry, the Bondi accretion [Bondi, 1952], which describes a spherically symmetric accretion flow consisting of a homogeneous gas cloud of mainly fully ionized hydrogen. Under this assumption, we can derive a maximal value for the luminosity beyond which the spherical accretion can no longer be sustained. The spherical accretion will be sustainable only if the gravitational pull on the material is greater than or balanced by the radiation pressure which mainly acts on the free electrons via Thomson scattering.

In the above case, the gravitational force is simply

$$F_g = \frac{GMm}{R^2} \tag{1.1.20}$$

and the radiation force on the cloud of gas is derived from the radiation pressure for its opacity κ ($\kappa = \sigma_{\mathsf{T}}/m_{\mathsf{p}}$ where σ_{T} is the Thomson cross-section and m_{p} is the proton mass.)

$$F_r = \frac{L}{c}\frac{\kappa m}{4\pi R^2} = \frac{L}{c}\frac{\sigma_{\mathsf{T}} m}{4\pi m_{\mathsf{p}} R^2} \tag{1.1.21}$$

Balancing the radiation and gravitational forces yields the critical value for the luminosity which is called the Eddington Luminosity,

$$\begin{aligned} L_{\mathrm{Edd}} &= \frac{4\pi G M m_{\mathrm{p}} c}{\sigma_{\mathrm{T}}} \\ &\cong 1.3 \times 10^{38} \frac{M}{M_{\odot}} \mathrm{erg\ s}^{-1} \end{aligned} \tag{1.1.22}$$

The observed luminosity from a given accretion rate $\dot{M}$ can be described as

$$L_{\mathrm{acc}} = 2\eta G M \dot{M}/R_s \tag{1.1.23}$$

where $R_{\mathrm{s}} = \frac{2GM}{c^2}$ is the Schwarzschild radius, η is the radiative efficiency which describes the fraction of the radiation produced from mass accretion that is able to escape the system. This specific parameter is sensitive to the black hole spin and can reach as high as 0.42 for a maximally rotating black hole and decreases significantly with decreasing black hole spin [Thorne, 1974].

We can derive the accretion rate corresponding to the Eddington limit using

$$L_{\mathrm{Edd}} = \eta \dot{M}_{\mathrm{Edd}} c^2 \Rightarrow \dot{M}_{\mathrm{Edd}} = \frac{L_{\mathrm{Edd}}}{\eta c^2} \tag{1.1.24}$$

Eddington luminosity as derived above is favorably trivial but does not account for the general relativistic effects on the photon trajectories. it still can be used as an approximation to characterize the accretion state the source is found in, even for a disk geometry. On the other hand, the practicality this critical value introduces to the study of accreting compact objects diminishes as one observes systems with accretion disk geometries that are not well understood with a multitude of radiative efficiencies significantly harder to compute.

1.1.3 Evolution of Accreting Black Holes in X-ray Binaries

The majority of BHXRBs spend most of their lifetime in a quiescent state and only occasionally go through an outburst where the system appears to get brighter. This is usually associated with a significant increase in the mass accretion rate over time and eventually the formation of an accretion disk close enough to the black hole to emit enough flux to be detected. The long-term evolution of these sources as they go through an outburst is usually tracked by two properties of the system: (i) the ratio of the detected photons at high energy (hard) to ones which are less energetic (soft) and (ii) the total intensity over the energy range of the observed spectrum. The ratio is usually referred to as the hardness ratio and this evolution is tracked on a diagram called a hardness-intensity diagram (HID) where many of these systems are found to follow a well-defined ”q-shaped” path [Fender et al., 2004, Dunn et al., 2010]. This ratio provides a good indicator of which accretion state the system is in, characterized by the relative contribution of two distinct emission components: thermal and non-thermal emission. The thermal component is expected to arise from the accretion disk which can be described as the sum of blackbody radiation originating from different radii on the accretion disk [Shakura and Sunyaev, 1973]. Generally, this is referred to as a multicolor or multi-temperature disk black body. The non-thermal component, on the other hand, dominates at energies above ~ 5 keV arises from the process of Comptonization of the so-called ”seed” photons emitted from the innermost regions of the accretion disk by a hot and an optically thin cloud of electrons called a ”corona”[Sunyaev and Titarchuk, 1980, Zdziarski, 1985, Chakrabarti and Titarchuk, 1995, Narayan et al., 1996, Zdziarski and Gierliński, 2004].

Once ignited, a long-term overview of an outburst is usually divided by certain accretion states which are characterized by the relative distribution of thermal and non-thermal emission alongside the evolution of the components making up the system. These accretion states correspond to different regions of the q-shaped path in an HID and can be listed as follows: low-hard state (LHS), intermediate state (IMS) (includes soft and hard)– or occasionally referred to as the steep powerlaw state, and high-soft state (HSS). The top part of Figure 1.6 shows a general overview of a typical HID with each state marked across the q-shaped path. A global study by Dunn et al. [2010] showed that this evolution is not only specific to one source or one outburst, the majority of the known galactic BHXRBs follow a similar path throughout each of their successful outbursts. In some instances, however, some sources may not be able to complete the full q-shape and have a failed outburst where the source either shows a quick rise in the flux for a very short period of time while remaining hard, or briefly enters the hard-intermediate state and return back to quiescent without entering the HSS.

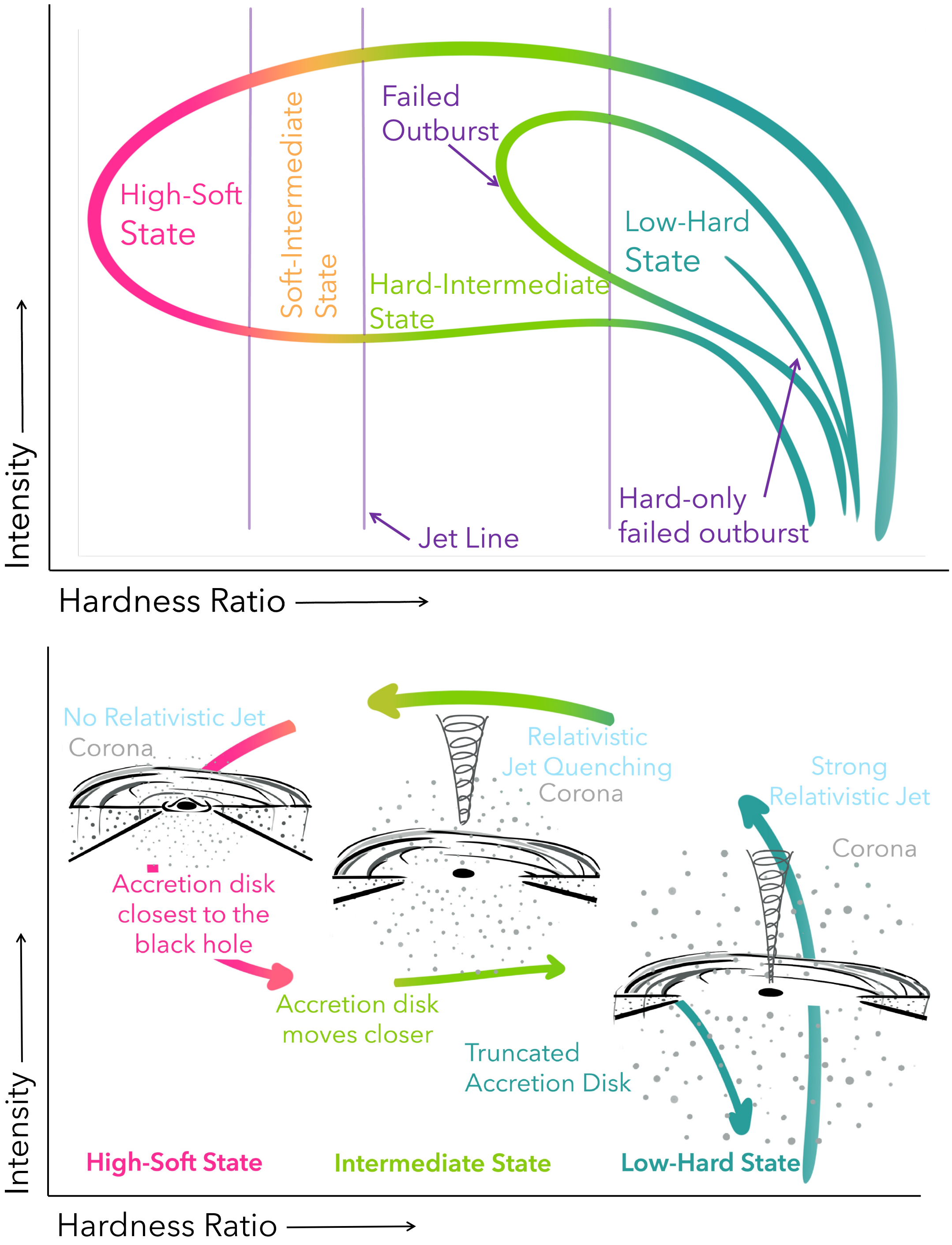

Figure 1.6: *Top*: A sketch of a general hardness-intensity diagram showing each accretion state throughout an outburst. *Bottom*: A simplistic scenario showing the evolution of the innermost edge of the accretion disk and the relativistic jet across the low-hard, intermediate, and high-soft state. The arrows indicate the direction of the evolution starting from the LHS at the beginning of an outburst, following the IMS and HSS until it eventually returns to LHS. For simplicity, the corona is illustrated in a spherical geometry.

Low-Hard State

Low-hard state or LHS is observed at the very beginning and the end of an outburst. Once the system starts to transition from the quiescent phase with the increasing mass accretion rate, it is usually followed by an increase in the observed flux while the spectrum remains hard. In this state, the source is observed to have an accretion disk forming at larger radii while accompanied by a strong relativistic jet. The broadband X-ray spectrum remains fairly flat and can be modeled by a powerlaw with $\Gamma \sim 1.7$ and a high energy cut-off as a result of the high energy Comptonizing photons in the corona. The accretion disk in this state remains further away from the black hole with low effective temperatures [Poutanen, 1998] and the spectrum is dominated by this Comptonized emission [Corbel et al., 2000, 2003].

The increase in broadband X-ray emission as the source transitions through the LHS is usually accompanied by a compact radio emission associated with synchrotron radiation originating from a steady relativistic jet. The radio spectrum of the jet is usually flat but some cases reported an inverted slope [Blandford and Königl, 1979, Fender, 2001, Fender and Gallo, 2014]. Going upwards on the right-hand side of the HID, the source remains fairly hard regardless of the increase in the observed flux.

While the X-ray spectra observed from sources in the LHS are exceptionally flat, a third component occasionally appears superimposed on the continuum. Some sources show signatures of a Fe Kα emission line accompanied by a high-energy hump dominating energies around and above 30 keV in the LHS. This component is assumed to be produced by the emission from a hot corona reflecting off the surface of the accretion disk giving rise to a set of emission lines including the Fe Kα complex.

Intermediate State

A further increase in the accretion rate results in a transition to the intermediate or steep powerlaw state where the X-ray emission remains fairly stable for a portion of the outburst and the spectrum is dominated by a steep powerlaw ($\Gamma > 2.4$ [Dexter and Blaes, 2014]) [Remillard and McClintock, 2006, Belloni and Motta, 2016]. The intermediate state can be divided into two parts, the hard intermediate state (HIMS) and soft intermediate state (SIMS) where the transition over time is from the powerlaw-dominated HIMS to more disk-dominated SIMS. During this transition, the accretion disk approaches the black hole further and the contribution of the thermal disk emission to the spectral continuum becomes stronger. This also results in much higher disk temperatures compared to the LHS. The source becomes softer over time and eventually crosses the ”jet line” before transitioning to the HSS after which the jet is assumed to be quenched and the radio emission vanishes [Fender et al., 1999, Corbel et al., 2000, Russell et al., 2011].

High-Soft State

With increasing mass accretion rates, the thermal emission from the innermost regions of the accretion disk starts to dominate the spectral continuum which can be primarily modeled with a multi-temperature accretion disk blackbody emission with a peak temperature of $kT \sim$ 1-1.5 keV and an additional powerlaw emission with a photon index of $\Gamma \sim 2.5$ or even higher.

During the transition to the HSS, the X-ray luminosity increases substantially and the radio emission starts to decrease and eventually vanishes as the radio jet is quenched in this state. The softening of the spectrum from the LHS to HSS occurs relatively faster compared to the time spent in the LHS [Dunn et al., 2010]. The third state, the steep powerlaw or the intermediate state, is entered as the powerlaw also starts to dominate over the thermal disk emission with $\Gamma \sim 2.5 - 3$ but the spectrum continues to be very soft. As the disk continues to recede and the disk emission is fading away, the system returns to the LHS completing the q-path at the end of the outburst before re-entering the quiescent state. Such sharp increases in the X-ray luminosity throughout the outburst while transitioning to the HSS are primarily explained by rapidly increasing accretion rates, $\dot{M}$, in a geometrically thin, optically thick disk originally characterized by Shakura and Sunyaev [1973].

1.1.4 Accretion Disk Solutions

The formulation of solutions to describe the physics of accretion onto black holes still stands as a cornerstone in the history of high-energy astrophysics, shedding light onto one of the most energetic phenomena in the universe. Not only did it open multiple doors to improving our understanding of the processes behind the X-ray bright events, but it also provided a framework to understand the behavior of matter under strong gravitational potentials through a set of observations of the environment which we cannot reconstruct in an Earth-based laboratory.

The foundational works of Nikolai Shakura and Rashid Sunyaev in the early 1970s, along with the consecutive contributions of Novikov and Thorne in the following few months, laid the groundwork for a theoretical framework that further outlines the complex dynamics governing accretion processes onto compact objects. With more advanced simulations and an expanding array of high energy phenomena, the theory of accretion expanded even further now filling in the gap in our understanding of accretion across the mass of the compact object and observed luminosity scale.

Spherical Accretion Bondi (1952)

The concept of spherical accretion, originally proposed by the Australian physicist Hermann Bondi in 1952 describes a stationary and spherically symmetric accretion onto a compact object [Bondi, 1952]

we start with the continuity equation in spherical coordinates,

$$\frac{\partial \rho}{\partial t} + \frac{1}{r^2}\frac{\partial(\rho r^2 v_r)}{\partial r} + \frac{1}{r\sin\theta}\frac{\partial(\rho v_\theta \sin\theta)}{\partial \theta} + \frac{1}{r\sin\theta}\frac{\partial(\rho v_\phi)}{\partial \phi} = 0 \qquad (1.1.25)$$

Bondi accretion describes a material flow that is spherically symmetric and stationary which means any terms in Eq 1.1.4, hence

$$\frac{\partial}{\partial t} = \frac{\partial}{\partial \theta} = \frac{\partial}{\partial \phi} = 0 \qquad (1.1.26)$$

And the continuity equation for a spherically symmetric stationary inflow of material, then reduces to

$$\frac{1}{r^2}\frac{\partial(\rho r^2 v_r)}{\partial r} = 0 \tag{1.1.27}$$

Simply integrating Eq. 1.1.4, one obtains the rate of material flow as

$$-\dot{M} = 4\pi\rho r^2 v_r = constant \tag{1.1.28}$$

the negative sign is used for the inflow of the material, i.e. accretion onto the compact object. As the material continues to fall onto the central compact object, it accelerates eventually reaching the speed of sound of the material. The speed of sound is a function of pressure and density, so given that both these quantities in the context of accretion will depend on the radius, it's expected that the speed of sound is also a function of a radius. So there will be a radius around the compact object that will characterize a transition from subsonic to supersonic speeds. Once the material crosses this radius, it can no longer transmit information about pressure changes upstream through sound waves, leading to different flow dynamics compared to before. This radius is referred to as the sonic radius and has the following form

$$r_s = \frac{GM}{2c_s(r_s)^2} \tag{1.1.29}$$

where G is the gravitational constant, M is the mass of the compact object and $c_s(r_s)$ is the speed of sound at the sonic radius.

Accompanying the sonic radius, the Bondi radius characterizes a boundary where the gravitational force by the compact object is balanced by the pressure forces within the surrounding gas which has the same form as Eq. 1.1.4,

$$r_B = \frac{GM}{2c_s(r_B)^2} \tag{1.1.30}$$

a solution where the escape velocity is equal to the speed of sound at Bondi radius would imply $r_s = r_B$.

There are two physical solutions to a spherically symmetric and steady flow of material (see Fig. 1.7):

(i) Bondi accretion, i.e. spherical inflow of material from infinity where it is subsonic and passing through the sonic radius and becoming supersonic between $r_* < r < r_s$ where the r_* is the radius of the central object. In the case of a black hole, this limit is the event horizon after which the material never reaches a surface and continues to accrete onto the black hole.

(ii) Stellar winds, i.e. outflow of material which are subsonic at smaller radii before the material crosses the sonic radius and supersonic at radii larger than the sonic radius.

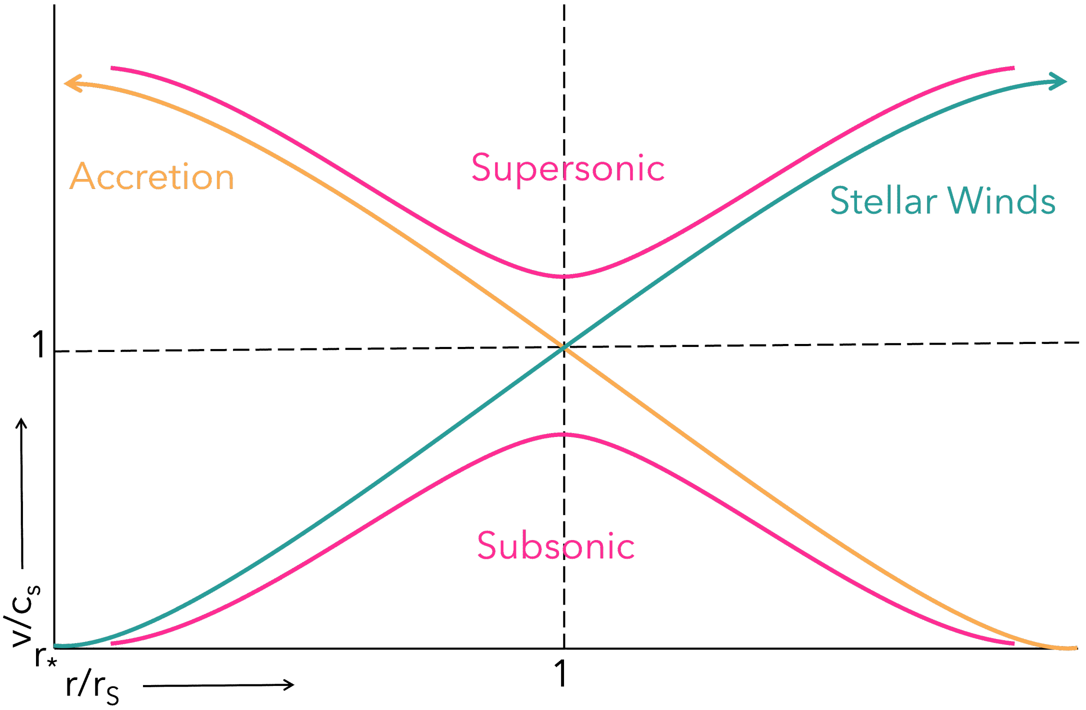

Figure 1.7: Solutions of steady state spherical flows. The orange and blue curves describe the evolution of the speed of the material in units of the speed of sound with respect to the radius in units of sonic radius for accretion and stellar winds, respectively. The upper pink curve shows the limit for supersonic flow and the bottom shows the limit for the subsonic flow of material. The lower limit for the radius is not zero but is set at the surface of the accretor, in the case of a black hole refers to the event horizon.

The Shakura&Sunyaev (1973) Disk Solution

The Shakura-Sunyaev (SS) accretion disk model, initially proposed by Nikolai Shakura and Rashid Sunyaev in 1973, still stands as one of the most widely used disk solutions to describe the properties of accretion disks around compact objects [Shakura and Sunyaev, 1973]. The SS disk model is based on 7 fundamental assumptions: (i) the disk is vertically thin with $h(r) \ll r$ where h is the vertical height and r is the radial distance to the outermost edge of the disk, (ii) the companion/donor star is assumed to not exert any gravitational force on the disk, (iii) the orbits of material within the disk are Keplerian, (iv) the self-gravitation due to the material within the disk is insignificant compared to the gravitational potential of the compact object, (v) the disk is axisymmetric, (vi) the disk is radiatively efficient where the only cooling of the disk is achieved by radiation, (vii) the disk is stationary and in hydrostatic equilibrium vertically.

The process of angular momentum transport within the accretion disk is usually attributed to the viscosity, parameterized by the effective viscosity coefficient α which describes the strength of the viscous stress within the disk. Occasionally, the SS disk is also referred to as the α disk, and the derivation of this parameter and further description of the physical processes taking place within the disk is governed by 4 fundamental equations: (i) conservation of mass, (ii) conservation of angular momentum, (iii) transport of angular momentum and (iv) conservation of energy.

(i) *Conservation of mass:*

$$\dot{M} = -2\pi r \Sigma V \tag{1.1.31}$$

Where $\dot{M}$ is the mass accretion rate, Σ is the surface density ($\Sigma = \int_{-h}^{h}$) and V is the radial velocity of the matter.

(ii) *Conservation of angular momentum:*

Since the accretion disk is assumed to be stationary and in hydrostatic equilibrium (assumption (vii)), we can write the balance of the vertical components of the gravitational force and pressure gradient as follows:

$$\frac{1}{\rho}\frac{\partial p}{\partial z} = -\frac{GM}{r^2}\frac{z}{r} \tag{1.1.32}$$

substituting the differentials with finite differences for the parameters following the standard approximation, we can derive the disk thickness h as follows

$$h \approx \sqrt{\frac{p}{\rho}\frac{r^3}{GM}} \approx \frac{c_s}{\Omega} \tag{1.1.33}$$

where c_s is the speed of sound in the mid-plane of the disk.
(iii) *Angular momentum transport:*

$$\frac{\dot{M}}{2\pi}(\mathcal{J} - \mathcal{J}_{\text{in}}) = -2hr^2 t_{r\phi} \tag{1.1.34}$$

where $\mathcal{J} = \Omega r^2$ is the angular momentum and $\mathcal{J}_{\text{in}}$ is the angular momentum of the material at the innermost edge of the disk where the net torque is assumed to be zero. Finally, $t_{r\phi}$ is the viscous stress tensor.

(iv) *Conservation of energy:*

The heat generated by viscosity can be written as [Shapiro and Teukolsky, 1983]:

$$q_{\text{vis}} \approx \frac{(t_{r\phi})^2}{\nu\rho} \tag{1.1.35}$$

Using Eq. 1.1.4, we can obtain

$$t_{r\phi} = -\frac{\dot{M}}{4h\pi r^2}(\mathcal{J} - \mathcal{J}_{\text{in}}) \tag{1.1.36}$$

For a Newtonian disk,

$$t_{r\phi} = -\frac{3}{2}\rho\nu\Omega \tag{1.1.37}$$

Combined with Eq. 1.1.4, we can derive the total heat generated by viscosity at radius r

$$Q_{\mathrm{vis}} = \frac{3\dot{M}}{4\pi r^2}\frac{GM}{r}\left(1 - \sqrt{\frac{r_{\mathrm{in}}}{r}}\right) \tag{1.1.38}$$

Given that the only cooling mechanism in the disk is radiation, we can assume that the heat generated by viscous processes will be radiated away immediately. Hence, the total flux from only one of the surfaces of the disk,

$$F = \frac{1}{2}Q_{\mathrm{vis}} = \frac{3\dot{M}}{8\pi r^2}\frac{GM}{r}\left(1 - \sqrt{\frac{r_{\mathrm{in}}}{r}}\right) \tag{1.1.39}$$

Assuming the magnetic pressure is negligible, the pressure balance in the innermost region of the accretion disk can be written as

$$p = NkT + \frac{1}{3}\alpha T^4 \tag{1.1.40}$$

where each component corresponds to gas and radiation pressure, respectively. Here, α is the dimensionless viscosity parameter that can be described in terms of the viscous stress tensor:

$$\alpha = -\frac{p}{t_{r\phi}} \tag{1.1.41}$$

Re-arranging Eq. 1.1.4,

$$t_{r\phi} = -\alpha p \tag{1.1.42}$$

Further distribution of the temperature across the accretion disk is dominantly governed by the balance between heating due to viscous dissipation and radiative cooling.

The local effective temperature in the Newtonian metric is a function of the radius and depends primarily on the mass accretion rate ($\dot{M}$), black hole mass (M), and the position of the innermost edge of the accretion disk (r_{in}):

$$T_{\mathrm{eff}}(r) = \left\{\frac{3GM\dot{M}}{8\pi r^3\sigma}\left[1 - \left(\frac{r_{\mathrm{in}}}{r}\right)^{1/2}\right]\right\}^{1/4} \tag{1.1.43}$$

where σ is the Stefan-Boltzmann constant and G is the gravitational constant. The thermal emission originating at each given radius is approximated to be a blackbody emission and the observed spectrum is then the sum of each blackbody emission which is usually referred to as a multicolor or multi-temperature disk blackbody. The multicolor disk blackbody emission is characterized by a peak temperature $T_{\mathrm{eff,max}}$ which is assumed to be the temperature of photons emitted from the region of the accretion disk closest to the black hole. The lowest value of the innermost disk radius is presumed to be limited by the location of ISCO which is a function of black hole mass and spin. Therefore, the spectral continuum of the multicolor disk blackbody is also affected strongly by these two parameters. For lower black hole spin for a given mass, the innermost edge of the disk is expected to be at larger distances resulting in $T_{\mathrm{eff,max}}$ much lower than a maximally spinning counterpart.

The flux radiated away is at a given radius r, therefore,

$$F(r) = \frac{3GM\dot{M}}{8\pi r^3}\left(1 - \sqrt{\frac{r_{\text{in}}}{r}}\right) \tag{1.1.44}$$

as obtained by Stefan-Boltzmann law.

Novikov&Thorne Solution (1973)

Shortly after the formulation of the thin disk solution by Shakura and Sunyaev [1973], Igor Novikov and Kip Thorne provided a rather upgrade to their solution and rewrote the equations in the framework of general relativity [Novikov and Thorne, 1973]. Their solution assumed a thin accretion disk in the equatorial plane of the black hole and was derived for a Kerr spacetime metric. In other words, the Novikov%Thorne (NT) solution introduces modifications to the SS disk solution in the framework of accretion in strong gravitational potentials and accounts for relativistic (general and special) effects.

(i) *Gravitational Redshift*: occurs when the wavelength of photons increases as they escape the gravitational influence of a dense compact object [Einstein, 1916].

(ii) *Doppler Boosting*: Also known as relativistic beaming, this effect involves the amplification of the observed radiation from a moving source [Rybicki and Lightman, 1979]. The observed flux increases due to the relative motion between the source and the observer, with additional enhancements if the source's velocity approaches the speed of light [Rees, 1966].

The observed "boosted" flux F_{b} can be described in terms of the Doppler factor δ and the intrinsic flux of the radiation emitted from the moving source in the rest frame F_{r}:

$$F_{\text{b}} = \delta^3 F_{\text{r}} \tag{1.1.45}$$

Where the Doppler factor is

$$\delta = \frac{1}{\gamma(1 - \beta\cos\theta)} \tag{1.1.46}$$

and γ is the Lorentz factor given by

$$\gamma = \frac{1}{\sqrt{1 - \beta^2}} \tag{1.1.47}$$

(iii) *Light Bending*: Refers to the bending of the photon trajectories due to the curvature of spacetime around compact objects. The bending is expected to be stronger in the regions close to the compact object, and in the case of a black hole, the curvature of the spacetime is further enhanced with increasing spin. In the framework of black hole accretion, this has strong implications for the trajectories of photons emitted from the innermost regions of the accretion disk.

(iv) *Frame Dragging*: Known as the Lense-Thirring effect, this phenomenon occurs when a massive rotating object, like a black hole or Earth, causes the surrounding spacetime to rotate along with it [Lense and Thirring, 1918]. General relativity predicts that such a spinning mass not only distorts the space around it due to gravitational effects but also induces a rotational motion in the nearby spacetime [Einstein, 1915].

Such an effect can be derived from the geodesics related to an infalling particle around a BH. Even if its initial rotational velocity is null during the fall (basically, a radial free fall), a particle will gain angular momentum that makes it rotate in the same direction as the BH rotation.

(v) *Self-irradiation*: Also called "returning radiation", is a phenomenon that is a direct result of the effects of light bending near the black hole. Self-irradiation of the accretion disk takes place when the trajectory of a light ray is bent and photons following that trajectory irradiate the accretion disk instead of reaching the observer.

Slim Disk Solution, Abramowicz (1988)

Following the thin disk solutions proposed in 1973 Shakura and Sunyaev [1973], Novikov and Thorne [1973], originally proposed by Abramowicz et al. [1988], the slim disk solution describes an accretion disk that is optically thick, but contrastingly to the thin disk solution not so thin. The thin disk approximation assumes that the accretion process is radiatively efficient which directly implies that all the thermal energy produced by viscosity at a specific radius is immediately radiated away.

Additionally, the heat generated by viscosity is assumed to be counterbalanced by local radiative cooling. This condition applies to sub-Eddington accretion rates where the system does not exceed $\sim 0.3L_{\mathrm{Edd}}$. Once the mass accretion reaches this critical luminosity, the radial velocity increases significantly, leading to a thickening of the disk, which in turn triggers another cooling mechanism, advective cooling. Advective cooling is a result of the viscosity-generated heat not having enough time to convert into radiation and leave the accretion disk before being carried inward by the gas motion [Kato et al., 2008],

$$Q_{\mathrm{adv}} \approx -\frac{1}{r}VP = \frac{\dot{M}}{2\pi r^2}\frac{P}{\Sigma} \tag{1.1.48}$$

assuming the radiation pressure dominates, we can express the total pressure as

$$P_{\mathrm{rad}} = 2H\frac{4\sigma}{3}T^4 \tag{1.1.49}$$

and the rate of radiative cooling is,

$$Q_{\mathrm{rad}} = \frac{64\sigma T^4}{3\kappa_{\mathrm{es}}\Sigma} \tag{1.1.50}$$

where $\kappa_{\mathrm{es}}h$ is the electron scattering opacity coefficient, using Eq. 1.1.4 and 1.1.4, we can estimate the rate of advective cooling

$$Q_{\mathrm{adv}} \approx \frac{\dot{M}}{2\pi r^2}\frac{P}{\Sigma}Q_{\mathrm{rad}} \tag{1.1.51}$$

This expression becomes dominant compared to the radiative cooling Q_{rad} for,

$$\frac{64\sigma T^4}{3\kappa_{\mathrm{es}}\Sigma} = \frac{M\kappa_{\mathrm{es}}h}{16\pi r^2}Q_{\mathrm{rad}} \tag{1.1.52}$$

The degree of contribution by the advective cooling increases with increasing mass accretion rate eventually reaching a level comparable to or even larger than radiative cooling. For mass accretion rate of $\dot{M}\frac{16\pi r^2}{\kappa_{\mathrm{es}}h}$, the standard thin disk approximation is no longer applicable due to this complex interplay between the two cooling mechanisms. This transition to the regime where the advection becomes a significant part of the equation is a direct result of the dynamic nature of accretion disk physics across the wide luminosity scale.

Due to the increasing contribution to the cooling mechanisms within the disk by advection, the radiative efficiency which is defined by how efficiently the gravitational energy released during the accretion process is converted into radiation decreases compared to the thin disk approximation where the only cooling mechanism included in the solution is radiation.

$$F_{\mathrm{Tot}} = \mathcal{N}\frac{4\pi E^3}{h^3c^2}\int_1^{\infty}\frac{r}{e^{E/kT_{\mathrm{eff}}(r)}-1}\,\mathrm{d}r \tag{1.1.53}$$

where E is the energy of the photon, h is the Planck's constant, k is the Boltzmann constant, c is the speed of light and $r = \frac{R}{R_{\mathrm{in}}}$.

Puffy Disks, Lančová 2019

Somewhere in between transitioning from low accretion rates to reaching and exceeding the Eddington limit lies the puffy disk approximation, a numerical accretion disk model around stellar-mass black holes accreting at sub-Eddington luminosities. This ”puffy” disk distinguishes itself from the thin and slim disk approximation with a vertically extended layer that is optically thick, encompassing a high-density core on the equatorial plane that is geometrically thin and resembling a thin disk geometry [Lančová et al., 2019]. The ”puffy” vertical structure is almost two orders of magnitude less dense than the thin core and can heat up to ~ 1 kEV at the photosphere due to the turbulent dissipation. In addition to the puffy disk structure, there is a funnel zone that consists of a low-density outflow of material driven by the collimated radiation [Wielgus et al., 2022].

The presence of this new element in our interpretation of the accretion flow around stellar-mass black holes contrasts the assumptions of both SS and NT disk solutions. This funnel and the orientation of the disk no longer produce the same output of luminosity as a thin disk due to the effect of beaming introduced by the funnel. At small inclinations $\Theta \leq 30°$, we observe the expanded disk structure through the region of low optical depth known as the funnel. The emitted radiation then transitions into a collimated form within the funnel, which is surrounded by the thick puffed-up accretion disk that is both geometrically and optically thick. This phenomenon resembles the traditional analytical solutions of thick disks [Abramowicz et al., 1978].

The radiation, then, is amplified through reflections off of the optically dense walls of the funnel. This geometric beaming effect, however, is different from the relativistic beaming, which involves the Doppler effect associated with an emitter moving at relativistic speeds, dominantly observed in jets. The Doppler effect is not prevalent as the velocity of the outflowing material reaches only 10% of the speed of light and remains significantly low density.

At the time of writing, the puffy disk structure is constructed only for a non-spinning black hole of mass 10 $\odot M$ accreting at 60 % of the Eddington limit due to the high cost of computations.

1.1.5 Ultraluminous X-ray Sources

Ultraluminous X-ray sources (ULXs) are identified as compact and point-like sources located within [see Earnshaw et al., 2019b, for a detailed catalog] observed at luminosities that exceed the Eddington limit for a stellar-mass compact object (Eq. 1.1.22) [see Kaaret et al., 2017, Fabrika et al., 2021, King et al., 2023, for detailed reviews]. These sources form a different subgroup of binary systems dominantly visible in X-rays and still remain one of the biggest challenges to our understanding of stellar evolution and the accretion onto compact objects. First discovered in the 1980s with the Einstein Observatory [Giacconi et al., 1979], the initial models usually centered around intermediate-mass black hole accretors ($\sim 10^3 - 10^5 M_\odot$) in sub-Eddington regime in order to explain such high observed luminosities [Colbert and Mushotzky, 1999, Kong et al., 2004, Miller et al., 2004, Liu and Di Stefano, 2008]. For decades, these sources were believed to be the perfect candidates to host intermediate-mass black holes. The field would remain rather dormant until the surprising discovery of coherent pulsations M82 X-2 [Bachetti et al., 2014a] which shed light on our understanding of the nature of the accretor in these systems. Shortly after the discovery, many other sources followed and now contribute to a growing family of pulsating ULXs or PULXs [Fürst et al., 2016, Israel et al., 2017a,c, Carpano et al., 2018, Sathyaprakash et al., 2019, Rodríguez Castillo et al., 2020]. Such high luminosities initially invoked the need for a massive compact object to not violate the Eddington limit on the emitted radiation. However, the discovery of neutron stars as powering mechanisms also introduced a new challenge since $\sim 1-2M_\odot$ mass scale indicates $\sim 100 L_{\rm Edd}$ or even more. Independent of how unlikely it was presumed to be, the high energy turnover in the 5-10 keV XMM-Newton and NuSTAR spectra of a few sources is believed to be a signature of the super-Eddington accretion flow [Stobbart et al., 2006, Gladstone et al., 2009, Walton et al., 2014, 2015, Mukherjee et al., 2015].

The presence and evolution of ULXs actually hold several keys vital to bridge our understanding of accretion onto compact objects across the mass accretion rate scale for several reasons. First, our current understanding of the processes involved within an accretion disk suggests that the radiative efficiency of the accretion disk decreases with increasing mass accretion rate due to the emergence of additional cooling mechanisms accompanying the radiative cooling. These additional terms in the solutions suggest that not each process of energy increase will result in radiation but will be cooled down by additional elementary processes taking place throughout the accretion disk. This will result in an additional decrease in the effective maximum temperature of the accretion disk as well as the observed luminosity. This specific state is not well integrated into our understanding of the evolution of accreting compact objects. Motta et al. [2021] added this ultraluminous state in their interpretation of the HID, while none of the observed ULXs have shown a clear q-shaped path eventually evolving into the ultraluminous state before returning to the quiescent phase. However, the main driving mechanism behind the observed evolution in the HID is presumed to be the changes in the mass accretion rates but the disk is assumed to be radiatively efficient throughout the outburst unless the sources are either in the LHS or reach luminosities above $\sim 30\% L_{\mathrm{Edd}}$.

If we are to speculate that the observed luminosities are due to only high mass accretion rates, then the effective mass accretion rate should be much higher since the accretion process will be less efficient in converting the potential energy into radiation emitted away from the disk. From the stellar evolution standpoint, the nature and powering mechanisms of such extreme flows are not understood yet. A majority of ULXs are usually associated with regions that have signatures of high star-formation rates [Swartz et al., 2011, Mineo et al., 2012, Lehmer et al., 2019, Qiu et al., 2019]. One possible scenario suggested to explain the persistent nature of a sizeable population of ULXs is constructed around a high-mass donor star feeding the accretion disk via the launching of strong stellar winds [see Martínez-Núñez et al., 2017, for a review]. On the other hand, this alone cannot be assumed to be the main powering engine of the super-Eddington accretion. Stellar winds observed in the hottest B-type stars are expected to result in a mass loss rate of $10^{-9} year^{-1}$ and this rate decreases by at least three orders of magnitude for cooler stars[Krtička, 2014]. This is expected to reach $\sim 10^{-6} year^{-1}$ for post-main sequence stars[Cranmer and Winebarger, 2019]. This, on the other hand, does not directly translate to the effective mass accretion rate. Considering the binary interaction and accretion disk formation, it is plausible to assume less than half of it would potentially be transferred into the disk. For a typical black hole X-ray binary (see discussion of GRO J1655-40 and LMC X-3 in Figure 3.12) the mass accretion rate in the highest luminosity state can be estimated to reach $10^{-7} year^{-1}$. This estimated value is calculated using an accretion disk model with a certain radiative efficiency. For less efficient disks exceeding the Eddington luminosity, this value will increase by a few orders of magnitude. It is not straightforward to estimate the radiative efficiency to calculate a more reliable value of the effective mass accretion rate. The case of the super-Eddington emission observed in ULXs should require mass accretion rates significantly larger than predicted mass loss rates for the more massive end of the stellar population.

A majority of the BHXRB sample studied in Dunn et al. [2010] and Dunn et al. [2011] showed a large variation in the observed luminosities but did not reach values any higher than 40% of the Eddington limit. How ULXs manage to reach such super-Eddington luminosities is still under debate. A few potential scenarios were eventually proposed: (i) For stellar-mass black hole accretors, the dense nature of the disk leads to a phenomenon known as photon trapping, where emitted photons undergo multiple scatterings within the disk and may even become absorbed, effectively becoming trapped within the disk instead of being emitted. However, with increasing mass accretion rates, the density perturbations within the accretion flow could potentially surpass the effects of photon trapping. This occurs when the diffusion timescale within the disk becomes longer in comparison to the accretion timescale, creating an opportunity for more photons to escape from the innermost regions of the disk, resulting in super-Eddington luminosities observed [Arons, 1992, Gammie, 1998, Begelman, 2002]. (ii) Discussed in Canuto et al. [1971], Mushtukov et al. [2015], the electron opacity in X-rays for neutron star accretors with magnetic fields on the orders of $\sim 10^{12-13}$G will decrease making the disk less opaque. (iii) Relativistic beaming in jets along the line of sight can be explained by a jet/disk model based on [Falcke and Biermann, 1999, Markoff et al., 2001] which was found to be consistent with the luminosity function of X-ray binaries in nearby galaxies but this still requires a black hole mass of $\sim 1000 M_\odot$ for ULXs given that an isotropic disk model is assumed [Körding et al., 2002]. All three scenarios pose a limit to the luminosity around a few 10^{40}erg s^{-1} which might not be applicable for systems reaching well above that.

While the connection between the two groups of X-ray bright binary systems is not clearly defined yet, the long-term evolution of M82 X-1 introduces a probability that the link between the two extremes of the luminosity scale can be developed by further systematic studies similar to Dunn et al. [2010] and Dunn et al. [2011]. M82 X-1, the less famous sibling of the first discovered PULX, has been considered as the perfect candidate to host an intermediate-mass black hole with a mass range of ($100 < M_{\rm BH} < 10000 M_\odot$) [Ptak and Griffiths, 1999, Rephaeli and Gruber, 2002, Kaaret et al., 2006]. Additionally, mass-scaling using QPOs detected [Strohmayer and Mushotzky, 2003, Dewangan et al., 2006, Mucciarelli et al., 2006] and twin-peaked QPOs with frequencies 3.3 and 5.1 Hz provided more support to a likely IMBH host scenario for M82 X-1 [Pasham et al., 2014]. While the detection of QPOs indicates a compact object with a mass of several hundred $M_\odot$ this growing support for the black hole nature of the source still cannot reduce the large uncertainties in the measured mass. More uncertainty was introduced with the spectral modeling of the X-ray continuum of M82 X-1 using XMM-Newton data suggesting a mass of ($19 < M_{\rm BH} < 32 M_\odot$) [Okajima et al., 2006]. However, due to the small angular separation between M82 X-1 and M82 X-2 (only 5), this analysis is subject to uncertainties introduced by possible contamination by the neighboring PULX due to the limited spatial resolution provided by the instrument. A broadband X-ray spectral analysis of M82 X-1 provided more support for a $\sim 30\mathrm{M}_\odot$ case [Brightman et al., 2016, 2020] by inferring a mass estimate from the measured inner disk radius and the observed scaling between the luminosity and inner disk temperature.

Contrary to the obvious trend in the evolution of the accretion states in BHXRBs, many ULXs do not exhibit signs of the canonical state transitions consistently across the observed sample [Berghea et al., 2008, Grisé et al., 2012, Sutton et al., 2013] . While some sources were found to have significant variations in their long-term lightcurve some sources appear to be persistent Weng et al. [2009], Bachetti et al. [2014b], Carpano et al. [2018], Israel et al. [2017b,d] some (Holmberg IX X-1, NGC 1313 X-1 and X-2, NGC 7793 S26, and NGC 5585 ULX) were later discussed to be active for $\sim 10^5$ yrs through the study of the highly ionized nebulae around the sources [Pakull and Mirioni, 2002, Pakull et al., 2010, Moon et al., 2011, Weng et al., 2014, Berghea et al., 2020, Soria et al., 2021, Gúrpide et al., 2022].

Transient ULXs, on the other hand, are usually detected serendipitously and hence less studied compared to BHXRBs and persistent ULXs and contribute to a growing gap in our understanding of the mechanism powering such extreme environments [Dage et al., 2021]. This is mainly due to the lack of long-term

X-ray monitoring campaigns sensitive enough to detect these sources at such distances. Walton et al. [2022] recently provided the most comprehensive catalog of 1843 sources, later continued by Brightman et al. [2023]. Unfortunately, the composition of the entire population is not known.

It's not yet clear if the transient/persistent nature of these sources can be attributed to the nature of the accretor but neutron stars are generally found to show more variability and the time scale of the transient nature is observed to decrease with the magnetic field of the neutron star suggesting a rather short-lived nature compared to their weakly magnetized counterparts and black holes [Thompson and Duncan, 1995]. A subgroup of ULXs showing transient nature in their long-term lightcurves is usually characterized by the bimodal distribution in the observed luminosities in which the source appears to transition through "on" and "off" states abruptly with no signs of state transitions in between [Tsygankov et al., 2016, Earnshaw et al., 2018a, Song et al., 2020, Vasilopoulos et al., 2021, Middleton et al., 2023]. This "off" state is usually referred to as the propeller stage meaning a sudden halting of the accretion. In this scenario, the accretion process in neutron star harboring systems depends on the magnetic field of the neutron star. The formation of an accretion disk in this scenario will only be possible when the corotation radius is located outside the magnetospheric radius for spherical accretion. In this case, if there's a drop in the luminosity, the magnetospheric radius can become larger and eventually enter the propeller regime and shred the accretion disk apart. Here, the magnetospheric radius is defined as

$$\begin{aligned} r_m =& 2.7 \times 10^8 \left(\frac{L_x}{10^{37} \mathrm{erg s}^{-1}}\right)^{-2/7} \left(\frac{M}{1.4 M_\odot}\right)^{1/7} \\ & \times \left(\frac{B}{10^{12} \mathrm{G}}\right)^{4/7} \left(\frac{R}{10^6 \mathrm{~cm}}\right)^{10/7} \mathrm{~cm}, \end{aligned} \tag{1.1.54}$$

where L_x is the bolometric X-ray luminosity, B is the surface polar magnetic field and R is the neutron star radius and the co-rotation radius is

$$r_\mathrm{co} = 1.7 \times 10^8 P^{2/3} \left(\frac{M}{1.4 M_\odot}\right)^{1/3} \mathrm{~cm}, \tag{1.1.55}$$

where P is the neutron star spin period [Cui, 1997].

Propeller effect, however, is usually used to explain the bimodal distribution of the observed flux in some ULXs over a longer period of time, spanning months or even years.

The transient behavior is rather hard to characterize into definitive groups as the observed luminosities and short/long-term variability show no apparent pattern. One significantly large group can easily be identified by a non-periodic and sudden transition between accreting and propeller regimes for neutron star-powered systems. These changes in the X-ray luminosity happen suddenly, leading to a nearly bimodal distribution over time [e.g., Tsygankov et al., 2016]. The long-term variability of accretion onto neutron stars can include phases where the accretion process is interrupted. This interruption can be caused by a centrifugal barrier created by the rotation of a neutron star with a strong magnetic field [Illarionov and Sunyaev, 1975]. During these phases, the neutron star can enter a dormant state, contrasting with periods of intense accretion that result in significant X-ray emissions.

The remaining portion of the transient ULXs does not show an apparent trend in the observed properties of these systems. The timescales, peak luminosities and evolution of spectral parameters vary from one source to another. Irwin et al. [2016] discovered two sources in the nearby elliptical galaxies with short flares on the time scales of minutes with luminosities reaching up to several 10^{40} erg s^{-1} while the before and after the flares the sources remained within a few 10^{38} erg s^{-1} for 0.3-10 keV energy range. Both flaring events have been associated with globular clusters in low-star-forming galaxies, and only a few more recurring flares have been reported in the 16 years of observations with XMM-Newton and Chandra. Furthermore, Earnshaw et al. [2018b] searched for transient ULXs, most of which could be explained by transitions to the propeller regime in neutron star-powered ULXs. Their sample included two sources (M106 ULX-1 and M74 ULX-2) that reached above the detection limit of Chandra, Swift and XMM-Newton only once. Identified by Winter et al. [2006], M106 ULX-1 was found to be observed only once and Earnshaw et al. [2018b] showed no significant detection in their sample. Similar to M106 ULX-1, M74 ULX-2 was detected only once by XMM-Newton [Soria and Kong, 2002] and went below the detection threshold shortly afterward [Soria et al., 2004]. These early detections of such sources later turned out to contribute to a growing population of transient ULXs with relatively shorter lifetimes. M83 was also found to be the birthplace of another transient reaching luminosities about 10^{39} erg s^{-1} [Soria et al., 2010, 2012]. The source was detected over a longer period of time with an ultraluminous outburst spanning about six months showing clear spectral evolution with a later optical detection of a possibly irradiated accretion disk.

Kaaret et al. [2004] showed that sources with similar observed luminosities in three starburst galaxies (M82, NGC 1569 and NGC 5253) are located preferably close to the star clusters but not within them. ULXs in star-forming environments are also found to be more variable than those located in older populations[Feng and Kaaret, 2006, Kaaret et al., 2017]. M86 tULX-1, however, residing in an elliptical galaxy, was found to reach luminosities as high as $\sim 5 \times 10^{39}$ erg s^{-1} with disk temperatures at around 0.66 keV. While M86 tULX-1 was observed in a more luminous state, the disk temperature measured for this transient event is higher than many other transient ULXs [van Haaften et al., 2019, Kajava and Poutanen, 2009]. Kajava and Poutanen [2009] showed that four out of 11 sources they analyzed were able to be well described with a simple absorbed multicolor disk blackbody model. Furthermore, these sources were found to follow a similar trend in the observed $L_{\rm Disk} - T_{\rm Disk}$ diagram to the known tracks of black hole XRBs. On the other hand, the rest that required the addition of a power law in the modeling of the spectral continuum followed a different trend with $L_{\rm Disk} \propto T_{\rm Disk}^{-3.5}$ in contrast to many black hole XRBs which dominantly follow $L_{\rm Disk} \propto T_{\rm Disk}^{4}$. However, with the exception of a few instances that can be explained by more consistent relativistic modeling of the accretion disk in the presence of a strong gravitational potential around a black hole [Yilmaz et al., 2023]. Miller et al. [2013] used this same sample and showed a two-component multicolor disk model produced similar slopes to the expected value for a standard accretion disk. They reported lower limits on absorption lines than those observed in black hole XRBs pointing to the absence of the suggested strong outflows contrasting the optically thick disk wind model. Additionally, while the majority of the sample in Kajava and Poutanen

[2009] followed a trend in the evolution of the disk temperatures with respect to disk luminosity, their sample showed no preferred or specific track in the evolution of the power-law index with respect to the observed X-ray luminosity.

1.1.6 Summary of Results

This thesis aims to study the evolution of accretion disks around black holes via relativistic and non-relativistic accretion disk models to provide a better understanding of the evolution of parameters describing the properties of the accretion disk. By studying the evolution of the position of the innermost edge of the accretion disk and disk temperature throughout multiple outbursts of BHXRBs and transient ULXs, we can describe the interplay between different components of the system. The thesis is structured as follows: Chapter 2 provides detailed information about the data reduction process and spectral analysis carried out throughout the analysis. We provide information on the data reduction and spectral analysis tools as well as the instruments used. In Chapter 3 we present the results of our analysis of the two BHXRBs GRO J1655-40 and LMC X-3. We attached a pre-copyedited version of the article published in the Monthly Notices of the Royal Society (published version is available online `https://doi.org/10.1093/mnras/stad2339`). In this paper, we employed a systematic approach to investigate the accretion disc evolution in GRO J1655-40 and LMC X-3 black hole X-ray binaries. We analyzed a substantial dataset comprising approximately 1800 spectra obtained from Rossi X-Ray Timing Explorer (RXTE) observations. To explore the nature of the accretion disk, both relativistic and non-relativistic disk models were utilized. To assess the thermal emission properties in the black hole X-ray binaries, we compared the non-relativistic disc model DISKBB with relativistic counterparts KYNBB and KERRBB. We showed that the non-relativistic modeling often resulted in inner disc radii that were notably lower and occasionally unrealistic, coupled with higher ($\sim 50\%$) disk temperatures.

We showed that for systems like GRO J1655-40 in which the innermost edge of the accretion disk is observed to be variable, the relativistic disk model `kerrbb` is unable to produce good fits for a fixed spin parameter across the outburst. This is due to the model's assumption that the inner disk radius extends to the innermost stable circular orbit and for a disk situated at larger radii, the spectra cannot be well fit for the known parameters of the system. This issue was easily recovered with `kynbb` by allowing the model to estimate the position of the inner edge of the accretion disk. Using the X-ray spectral continuum fitting method with the relativistic disk models, we obtained the dimensionless black hole spin parameters for GRO J1655-40 ($a_* = 0.774 \pm 0.069$ and $a_* = 0.752 \pm 0.061$ using KERRBB and KYNBB, respectively) and LMC X-3 ($a_* = 0.098 \pm 0.063$ using the updated black hole mass of 6.98 $M_\odot$).

Our analysis with `kynbb` emphasizes the importance of self-consistent modeling of thermal emission from systems harboring such compact objects as accretors. The deviations previously observed in the observed disk luminosity and disk temperature relationship were successfully recovered to the expected trend when the model included the inner edge of the disk as a free parameter.

In Chapter 4, we report the discovery of a new candidate transient ULX in M51 using publicly available archival XMM-Newton, Chandra, and Swift observations. In the two decades of available observing campaigns with multiple X-ray observatories, the source was observed going through an outburst only once in 2018, lasting about 81 days. The observed X-ray luminosity peaked at around $7.8 \times 10^{3}8$ erg/s, which is equal to or higher than the Eddington limit for a stellar-mass accretion object. Simultaneous XMM-Newton OM and Swift UVOT observations revealed no optical or UV counterparts, eliminating the possibility of being a background active galactic nucleus (AGN) or a black hole mass of intermediate-range or higher. Accretion disks around intermediate or supermassive black holes are expected to be much cooler with maximum disk temperatures at ~ 0.1 keV and lower. Such accretion disks regardless of the length of the outbursts are then very luminous in UV and optical. A comparison with the observed properties of tidal disruption events as well as the absence of multiwavelength counterparts leaves the source an outlier to that population, providing a strong indication for a stellar-mass accretor, whether a neutron star or a black hole.

M51 ULX* showed no variability in its spectral properties, both XMM-Newton observations revealed a consistently soft spectrum with a photon index of $\Gamma \sim 2.6$. We also did not detect any significant pulsations, with upper limits on the pulsed fractions around $\leq 30\%$. The emergence of such soft spectra is usually associated with a thermal emission from an accretion disk obscuring the pulsed emission from the inner accretion flow, consistent with the absence of significant pulsations while presenting upper limits on the pulsed fractions close to the observed PULX population. On the other hand, the absence of pulsations and the transient nature of the event challenge existing models of accretion disks. The timescale of the outburst and spectral properties do not easily fit into one subclass of X-ray bright sources. The short nature of the outburst might suggest potential magnetic instabilities in the inner regions of the accretion flow.

Unlike the growing population of well-studied BHXRBs and some ULXs, transient sources like M51 ULX* are identified serendipitously. The lack of long-term observing campaigns of these sources limits our understanding of accretion phenomena in super-Eddington regimes and challenges the currently available accretion disk solutions.

In Chapter 4.6, we provide a summary of our conclusions based on the results presented in this thesis alongside a brief discussion.

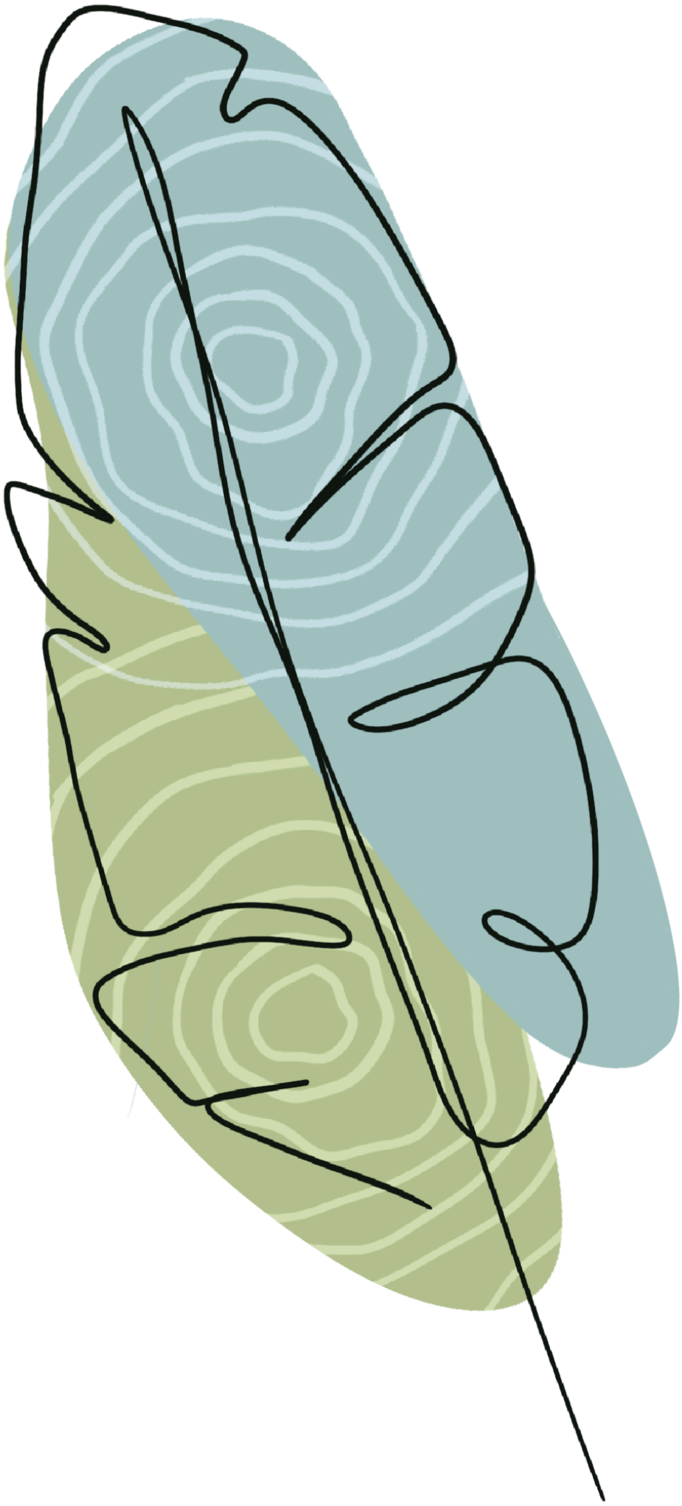

2. Data Reduction and Spectral Analysis

2.1 X-ray Instruments

2.1.1 Rossi X-ray Timing Explorer – RXTE

Launched on December 30, 1995, aboard a Delta II rocket, the Rossi X-ray Timing Explorer (RXTE) [Bradt et al., 1993] was equipped with three instruments with the mission of studying the spectral and timing properties of compact objects: the Proportional Counter Array (PCA), the High-Energy X-ray Timing Experiment (HEXTE) and the All Sky Monitor (ASM). With its precise timing capabilities and high sensitivity and capabilities covering energies ranging from 2 to 200 keV, RXTE stood as one of the most successful missions contributing greatly to our understanding of accretion phenomena around compact objects. The operations of RXTE were terminated on 12 January 2012.

The Proportional Counter Array (PCA): the primary instrument aboard the RXTE with a total collective area of 6500 cm^2 in the energy range of 2-60 keV, was composed of 5 nearly identical proportional counter units (PCUs) [Jahoda et al., 1993]. Each PCU consisted of an array of Xenon-filled proportional counter tubes, arranged in layers (1 propane veto and 3 Xenon each split into two) to optimize detection efficiency. These detectors operated based on the principle of proportional counting, where incoming X-rays ionize the gas within the tubes, producing electrical pulses proportional to the energy of the incident photons.

The High-Energy X-ray Timing Experiment (HEXTE): designed to complement the capabilities of the PCA extending to the energy range of 15-250 keV, consisted of two detector clusters which contained 4 Na/CsI phoswich scintillation detectors arranged in a co-aligned configuration, providing simultaneous observations of X-ray sources [Gruber et al., 1996]. These clusters operated on the principle when X-rays interacted with the scintillation material, they produced flashes of light that were converted into electrical signals enhancing HEXTE's sensitivity and spectral resolution in the hard X-ray band.

2.1.2 X-ray Multi-Mirror Mission – XMM-Newton

X-ray Multi-Mirror Mission or shortly XMM-Newton, launched in December 1999, XMM-Newton to this day remains one of the most powerful X-ray missions operated by the European Space Agency (ESA)[Mason et al., 1995, Schartel et al., 2022]. XMM-Newton is equipped with three instruments, each equipped with nested, grazing-incidence mirror shells. These mirrors are coated with thin layers of gold to enhance their reflectivity, making XMM-Newton sensitive to energies ranging from 0.1 to 15 keV. The design of the telescope's mirrors provides a large effective collecting area, providing high sensitivity to faint X-ray sources.

The European Photon Imaging Camera (EPIC): configured around two Metal Oxide Semiconductor CCD (Charge-Coupled Device) – (EPIC-MOS) [Turner et al., 2001] and one PN-junction array CCD (EPIC-PN) that provide imaging and spectroscopic capabilities across a wide field of view with an effective area of around 450 cm^2 at 1.5 keV.

Reflection Grating Spectrometer (RGS): accompanying EPIC, RGS employs two Focal Plane Cameras each consisting of 9 MOS CCDs situated in a curve referred to as the Rowland circle. Each camera is equipped with a Reflection Grating Array which diffracts the X-rays to an array of CCDs providing high-resolution X-ray spectra in the range of 2.5 to 0.35 keV or 5 to 35 Å.

The Optical/UV Monitor (OM): complementing the X-ray modules, OM consists of a Telescope Module and a separate Digital Electronics Module with two distinct detector chains. OM allows simultaneous observations of the targets in optical and ultraviolet bands accompanying X-rays providing a great coverage between 170-650 nm within the 17 arcminute square in the field of view of the X-ray cameras.

2.1.3 International Gamma-Ray Astrophysics Laboratory – INTEGRAL

The International Gamma-Ray Astrophysics Laboratory (INTEGRAL), launched by the European Space Agency (ESA) in October 2002, is equipped with four primary instruments [Winkler et al., 2003]. Designed to complement X-ray missions that detect energies as low as 0.1 keV, INTEGRAL focuses on observing high-energy emissions up to 8 MeV.

Imager onboard the INTEGRAL Satellite (IBIS): a high-resolution gamma-ray imager [Ubertini et al., 2003], sensitive to a wide energy range of 15 keV - 10 MeV consists of two main components, Integral Soft Gamma-Ray Imager (ISGRI) and the PIxelated CsI Telescope (PICsIT) that are sensitive up to 1 MeV and 10 MeV, respectively.

Spectrometer on INTEGRAL (SPI): Accompanying IBIS, ISP onboard INTEGRAL, consists of a coded mask of hexagonal tungsten tiles, is designed for high-resolution gamma-ray spectroscopy covering a range of 20 keV-8 MeV [Vedrenne et al., 2003].

Joint European X-ray Monitor (JEM-X): consists of two identical detectors sensitive to 3-35 keV, JEM-X complements IBIS and SPI to localize gamma-ray sources with higher precision and provides a piece of preliminary information about their emission properties [Lund et al., 2003].

Optical Monitoring Camera (OMC): an optical camera that provides accompanying observations in the optical and near-infrared bands (440-900 nm). It is used to monitor the optical counterparts of gamma-ray sources, providing further information to understand the multiwavelength counterparts of the gamma-ray bright events [Mas-Hesse et al., 2003].

2.1.4 The Chandra X-ray Observatory (CXO):

The Chandra X-ray Observatory (CXO, most commonly referred to as Chandra), launched on July 23, 1999, is still one of the most advanced space machines. Named after the famous astronomer Subrahmanyan Chandrasekhar, Chandra is still the most sensitive X-ray instrument to date, a couple of orders of magnitude compared to XMM-Newton providing exceptional spatial and spectral resolution.

Advanced CCD Imaging Spectrometer (ACIS): the primary detector on Chandra, it consists of two arrays of CCDs designed to provide an impeccable spatial resolution ($\sim$ 1 arcsec) [Garmire, 1997].

High-Resolution Camera (HRC): Another imaging detector on Chandra, provides high-resolution images of X-ray sources [Kenter et al., 1996]. Unlike ACIS, the HRC employs microchannel plates instead of CCDs to improve the spatial resolution and timing capabilities.

High-Energy Transmission Grating Spectrometer (HETGS): The HETGS is a spectrograph that utilizes diffraction gratings to disperse X-rays into their component wavelengths [Markert et al., 1994]. HETGS can provide spectral resolution to detect Doppler shifts even for significantly low velocities This instrument allows astronomers to study the detailed spectra of X-ray sources, revealing information about their composition, temperature, and velocity.

Low-Energy Transmission Grating Spectrometer (LETGS): Like the HETGS, the LETGS utilizes diffraction gratings [Brinkman et al., 1987]. However, it is optimized for lower-energy X-rays, providing high-resolution spectra in the soft X-ray band (0.07-0.15 keV, 80-175 Å).

2.1.5 The Neil Gehrels Swift Observatory – Swift

The Neil Gehrels Swift X-ray Observatory was launched by NASA on November 20, 2004 [Gehrels et al., 2004]. Swift is a multi-wavelength space observatory designed primarily to detect and observe Gamma-ray Bursts (GRBs) and their multi-wavelength afterglows. Equipped with three main instruments, Swift excels in the rapid detection and precise localization of GRBs. The mission also provided long-term observing campaigns of many other sources covering UV, optical, X-ray, and Gamma-rays.

Burst Alert Telescope (BAT): BAT is a wide-field instrument that utilizes a coded-aperture mask design to systematically scan the sky for gamma-ray bursts [Barthelmy et al., 2005]. The BAT covers a large portion of the sky, detecting bursts by identifying sudden increases in gamma-ray activity. Once a burst is detected, BAT calculates its position with an accuracy of about 1-4 arcminutes and sends this information to the spacecraft's onboard system, which quickly repositions Swift to focus on the burst's location with its other instruments.

X-Ray Telescope (XRT): After the detection with, the XRT focuses on the burst's location to capture the images and spectra in the X-ray band [Burrows et al., 2005]. It achieves a position accuracy of about 1-2 arcseconds and covers the energy range from 0.3 to 10 keV with an effective area of 110 cm^2.

Ultraviolet/Optical Telescope (UVOT): Complementing the BAT and XRT, the UVOT observes the GRB afterglow in the ultraviolet and optical wavelengths [Roming et al., 2005]. This instrument captures images and spectra, providing data on the lower-energy emissions of the burst. The UVOT's sensitivity extends from the near-ultraviolet (170 nm) to the visible light (650 nm).

2.2 Data Reduction

2.2.1 RXTE

The RXTE observations are publicly available and distributed through The High Energy Astrophysics Science Archive Research Center (HEASARC) archive[1]. The source spectra were extracted `standard2f` mode for more optimal spectral resolution and the response matrices and background spectra following the standard procedure in the RXTE cookbook[2] using `FTOOLS/HEASOFT` version 6.29[3] software package. Following the suggested prospectus, the data lying within 10 minutes of the South Atlantic Anomaly were excluded. While all PCUs are operated simultaneously throughout a significant portion of the observations, PCU-2 was operated almost always on and is calibrated the best among other PCUs. Hence, we opt out to make use of PCU-2 only in order to avoid introducing additional uncertainties to the results of further analysis. To account for instrumental uncertainties in the obtained spectra, the traditional method is to add 10% of uncertainties to the spectrum which results in large error margins. This approach might affect the efficiency of modeling the emission and absorption lines that might be present in the spectrum. To overcome this, we adopted `pcacorr`[4], a calibration tool developed to enhance the quality of spectral fits by correcting for residuals in the data [García et al., 2014]. `pcacorr` is a Python code that uses correction files based on multiple Crab spectra for each epoch gain which correspond to different calibration statuses of the instrument. It is still recommended to apply an additional 0.1% systematic errors post-processing of the spectra.

2.2.2 XMM-Newton

XMM-Newton observations are publicly available both on HEASARC's archive and on XMM-Newton's Science Archive[5]. XMM-Newtons Science Archive provides further information and some data products regarding specific observations and is preferable. We used the XMM-Newton Science Analysis System (`SAS`[6]) (v.21.0.0) for data reduction and extracting science products following the analysis threads provided online. We reprocessed the observation data files (ODFs) obtained from EPIC-PN using the task `epproc` and obtained the calibrated event files. The corresponding task used for the same purpose for EPIC-MOS (1&2) is `emproc`. We obtained the good time interval (GTI) files using respective `RATE EXPRESSION` conditions for each EPIC detector and later filtered the event files using GTI files for further analysis. This process is based on extracting an overall lightcurve from the event files and looking for count rates where the emission doesn't show any signs of an outburst which might affect the results of any further step.

In contrast to RXTE, XMM-Newton has imaging capabilities, and extracting any further science products requires defining source and background regions on

---

[1] `https://heasarc.gsfc.nasa.gov/docs/archive.html`

[2] `https://heasarc.gsfc.nasa.gov/docs/xte/recipes/cook_book.html`

[3] `https://heasarc.gsfc.nasa.gov/docs/software/lheasoft/`

[4] `https://sites.srl.caltech.edu/~javier/crabcorr/index.html`

[5] `http://nxsa.esac.esa.int/nxsa-web/#search`

[6] `https://www.cosmos.esa.int/web/xmm-newton/sas-threads`

the image of the field of view on each instrument. We extracted the images for each instrument using the `evselect` task in `SAS` using the filtered event files and selected a circular region centered around the source coordinates. Background regions, on the other hand, will depend on the source of emission around the source. The most common practice for point-like sources like XRBs is to select a source-free region around the source usually from a region either the same size as the source or bigger to collect enough counts to extract a background spectrum. We followed the recommended selection expression and restricted the patterns only to single and double events (`PATTERN<=4` for EPIC-PN and `(PATTERN<=12)` for EPIC-MOS). We then used the `SAS` tools `rmfgen` and `arfgen` to generate redistribution matrices (rmf) and ancillary files (arf), respectively. The obtained spectra were then grouped with the `specgroup` task and binned to have at least 20 counts per bin.

2.2.3 Chandra

Similar to XMM-Newton, the data files are publicly accessible through both HEASARC's archive and Chandra's science archive[7]. Unlike many other X-ray instruments, the data analysis software `CIAO` (Chandra Interactive Analysis of Observations) is distributed separately. We first used the `chandra_repro` task within `CIAO` to extract the cleaned level 2 event files. Similar to XMM-Newton, Chandra has imaging capabilities and extraction of science products such as lightcurves or spectra follows the same procedure. For known sources like many black hole XBRs, the source coordinates are usually well-defined and can be found on archives while it could be a good practice to perform a source detection task when working with new sources or sources that are not well studied. To do so, we first extracted a full detector image using the task `fluximage` and the corresponding point spread function (PSF) maps in the $0.5-7.0$ keV energy band with `mkpsfmap`. We then used the `wavdetect` routine for source detection. We also used the `srcflux` task to calculate the flux values directly from the even files. We selected the source and background regions based on the same criteria as the case of XMM-Newton and used `specextract` and `dmextract` to extract spectra and lightcurves, respectively.

2.2.4 Swift

We used the standard online tool [Evans et al., 2009] provided by the UK Swift Science Data Centre to obtain Swift-XRT images for each observation. Swift-XRT was employed only to search for the detection of M51 ULX* prior to its first detected outburst. We do not extract any further data products due to the distant nature of the source. For Swift-UVOT, we used `xselect` within HEASOFT's `ftools` to extract images and search for optical and UV counterparts.

2.2.5 INTEGRAL

We extracted IBIS-ISGRI images, spectra, and lightcurves of observations simultaneously taken with RXTE during the 2005 outburst of GRO J1655-40. We

---

[7] `https://cda.harvard.edu/chaser/`

combined all of the available science windows within the same day of RXTE observations to obtain good count statistics. We employed publicly available Jupyter notebooks developed by Carlo Ferrigno[8], based on the generic cookbook provided to extract science products of INTEGRAL[9].

2.3 Spectral Fitting

2.3.1 X-ray Spectral Fitting Package –XSPEC

The spectral analysis tool `xspec` [Arnaud, 1996] distributed within `HEASOFT` is a command-driven and interactive program designed for X-ray spectral fitting. The algorithm is purposefully tailored for any spectrum obtained by any instrument since its first distribution almost three decades ago. The software is designed to take the following files as input:

- Source and background spectral files, usually saved in a `.FITS` format and carries information about the rate at which the photon arrives at the detector and at which energy,
- Detector response matrix, usually identified with `.rmf` extension and carries the characteristics of the instrument. This corresponds to a 2-D matrix of the mapping between the properties of the incident photons on the detector and the properties as detected by the instrument.
- Ancillary response files, usually identified by the `.arf` extension and can be described as the multiplicative product of the detector's geometric area in the units of cm^2 and the quantum efficiency of the detector.

The spectral fitting procedure includes constructing an observed spectrum from the output of the instruments which doesn't necessarily record the spectrum but the information about the rate at which the photon arrives at the detector (F) and at which energy convolved through the instrumental response ($R(c, E)$) which is directly proportional to the probability of a photon with a certain energy E will be detected by the channel of interest (C).

$$F(C) = \int f(E)R(C, E)dE \tag{2.3.1}$$

The most common approach to determine the intrinsic spectrum of the observed source $f(E)$ is to find a chosen model M_S constructed by a number of parameters that fit the observed spectrum. This is accomplished by predicting a "count spectrum" for each $f(E)$ and comparing it to the observed data $F(C)$ eventually computing a "fit statistic" from this comparison to evaluate the success of the fitting procedure. The most common fit statistic used for this purpose is χ^2 statistics which is defined as

---

[8] `isgri-spectrum.ipynb`, `isgri-lightcurve.ipynb`, `isgri-full-image.ipynb` provided on the public repository `https://registry.gitlab-b.unige.ch/Carlo.Ferrigno/gallery-notebooks/-/tree/master`

[9] `https://www.isdc.unige.ch/integral/analysis`

$$\chi^2 = \sum \frac{(F(C) - F_p(C))^2}{(\sigma(C))^2} \tag{2.3.2}$$

where $F_p(C))$ is the predicted count spectrum and $\sigma(C)$ is the error for a given channel C.

`xspec` obtains the background-subtracted observed spectrum in the units of counts per second by utilizing the source and background spectral files,

$$F(C) = \frac{S(C)}{a_S t_S} - \frac{b_S}{b_{B(C)}} \frac{B}{a_b t_B} \tag{2.3.3}$$

where S_C and B_C are source and background spectral files, t_S and t_B are source and background exposure times, b_S, b_B, a_S, a_B are the background and area scaling factors for source and background spectral files, respectively.

Before one can define a spectral model and a set of parameters, `xspec` need to be able to read the instrumental response matrix file or the rmf in which the matrix for energy ranges E_J is defined as

$$R_S(C, J) = \frac{\int_{E_{J-1}}^{E_J} R(I, E) dE}{E_J - E_{J-1}} \tag{2.3.4}$$

Further, the data reduction processes of some instruments include creating the ancillary response files (arfs) which are multiplied into $R_S(C, J)$,

$$R_S(I, J) \to R_S(I, J) \times A_S(J) \tag{2.3.5}$$

Then, `xspec` calculates the model spectrum in the units photons per second per cm^2 $M(E)$ using these energy ranges defined by the instrumental response file as follows:

$$M_S(J) = \int_{E_{J-1}}^{E_J} M(E) dE \tag{2.3.6}$$

The models defined in `xspec` are characterized by the algebraic operation, i.e. convolution or additive models.

A simple syntax within `xspec` for defining a simplistic model comprised of two additive models (`diskbb` and `powerlaw`) and a convolution model (`tbabs`) will take the following form

```
model tbabs×(diskbb+powerlaw)
```

2.3.2 Bayesian X-ray Analysis – BXA

To further improve our analysis, specifically for M51 ULX*, we used the Bayesian X-ray Analysis (BXA) for parameter estimation (Chapter 4). BXA [Buchner et al., 2014] is a statistical approach that effectively employs the Bayesian approach that is based on a nested sampling algorithm UltraNest [Buchner, 2016, 2019, 2021]. BXA offers parameter estimation across any number of dimensions and facilitates the plotting of spectral models against data to determine the best fit, using either posterior samples or individual components. It also supports comprehensive model selection by calculating the evidence for each model.

BXA has a strong standpoint when handling very large datasets, distant sources with low count rates, and complex parameter spaces with strong degeneracies introduced within a model. We used this approach specifically to account for the significantly lower count rate of the M51 ULX* spectra, to obtain a better estimation of the model parameters. It also uses Quantile-Quantile (QQ) plots to visualize differences between the model and data. Unlike residuals, QQ plots do not rely on binning and provide a more thorough assessment of these deviations.

For a given model, BXA computes the likelihood function, which evaluates how accurately the selected model matches the observed data. This function measures the probability of observing the data given the model parameters and is usually based on the underlying physical model and the uncertainties associated with the observations. It then uses Nested Sampling to explore the posterior distribution which is defined as

$$P(\theta \mid D) = \frac{P(D \mid \theta)P(\theta)}{P(D)} \tag{2.3.7}$$

where $P(D \mid \theta)$ represents the likelihood function, $P(\theta)$ denotes the prior distribution, and $P(D)$ is the evidence or marginal likelihood, acting as a normalization factor that ensures the posterior distribution integrates to 1 across all possible values of θ. From the posterior samples, BXA derives estimates for the model parameters for a given model along with their respective uncertainties.

2.4 Modelling the Accreting Black Holes in X-ray Binaries

2.4.1 Non-Relativistic Accretion Disk Models

One of the earliest models to describe a multi-color blackbody disk emission from a Shakura and Sunyaev [1973] accretion disk was `diskbb` [Mitsuda et al., 1984, Makishima et al., 1986] within `xspec` environment. This model is very simplistic and has only two free parameters, the maximum disk temperature kT_{max} and the normalization. In this model, the disk temperature is the maximum disk temperature calculated from the SS solution (Eq. 1.1.43) which corresponds to the innermost edge of the accretion disk R_{in}. At that boundary, `diskbb` assumes a finite non-zero torque [Gierliński et al., 1999]. Finally, the normalization is described as

$$\mathcal{N} = \left[\frac{R_{\text{in}}}{D_{10}}\right]^2 \cos\theta \tag{2.4.1}$$

where θ is the inclination angle of the disk, R_{in} is the inner edge of the disk and D_{10} is the distance to the source in units of 10 kpc. The common practice, therefore, is to use this normalization parameter to calculate the position of the innermost edge of the disk.

`diskbb`, to this day, still provides statistically accepted fit test statistics which might lead to an oversight of certain properties of the disk. By default `diskbb` assumes $T \propto R^{-3/4}$. This assumption will hold as long as the disk geometry remains within the thin disk approximation where the main cooling of the disk is dominantly achieved by radiation. Alternative to `diskbb`, `diskpbb`, included another free parameter p which parametrizes the radial dependency of the disk temperature as $T \propto R^{-p}$. For $p = 0.75$, `diskpbb` now describes the same SS accretion disk as `diskbb`, and changes to the accretion disk structure and advective cooling is expected to correspond to values in the range of $0 < p < 0.75$ [Mineshige et al., 1994, Hirano et al., 1995, Watarai et al., 2000, Kubota and Makishima, 2004, Kubota et al., 2005].

2.4.2 Relativistic Accretion Disk Models

`diskbb` has played a significant role in our understanding of how accretion disks around black holes evolved. Historically, it was in the center of each model that placed the q-track on the HID, showed the evolution of the innermost edge of the disk and disk temperatures, it helped us identify spectral states and this list can go as long as one wants to keep it. On the other hand, it was always known that this was a very simplistic model and had its shortcomings if one needs to identify certain characteristics of an accretion state using either the disk temperature or the inner disk radius. Both parameters were derived from the SS disk solution and did not account for changes to the photon energies due to special and general relativistic effects (see Section 1.1.4 for more on these effects the following section refers to).

There have been a few attempts to account for these relativistic effects. It took almost a decade until `kerrbb` was developed for `xspec` [Li et al., 2005]. `kerrbb` describes the NT disk solution and utilizes the ray-tracing method which calculates an observed spectrum accounting for the changes in the trajectories of the photons around a black hole before they finally reach the observer. Unlike `diskbb`, the disk temperature is not a free parameter, and the innermost edge of the accretion disk is set at the location of the ISCO, $R_{\rm ISCO}$ with zero torque boundary condition. The inclination angle of the disk is a separate parameter, not embedded in the normalization which is not explicitly defined as in the case of `diskbb` and is recommended to be set at 1 if the black hole mass, distance to the source and the inclination angle are known. The exact value of the parameter can be left to the user given the fact that these parameters can have uncertainties.

`diskbb` is a lot simpler than `kerrbb` in its way of measuring the peak disk temperature. It assumes a "perfect" blackbody emission which is a sum of multiple components emitted at different radii and treats this value as the true value of the effective disk temperature. In reality, as the disk gets warmer with increasing mass accretion rate, it is expected that the complex electron scatterings taking place in the disk atmosphere start to dominate over free-free absorption. This results in an increase in color temperature compared to the effective disk temperature. In addition to the relativistic treatment of the disk emission, this change is mitigated with a parameter, the color correction factor or hardness factor which is described as

$$f_{\rm col} = T_{\rm col}/T_{\rm eff} \tag{2.4.2}$$

where $T_{\rm col}$ and $T_{\rm eff}$ are color and effective temperatures, respectively. `kerrbb` is fundamentally not a model that includes the calculations needed to model

Table 2.1: Model parameters of `kynbb` and their respective values used in the analysis. –* refers to parameter values that are source-dependent.

Parameter	Description	Value	Free/Frozen
η	"Scale" of the torque at the inner boundary	0	Frozen
a	Dimensionless spin parameter	–	Free
θ	Inclination angle of the disk	–*	Frozen
M_{bh}	Blak hole mass	–*	Frozen
M_{dd}	Accretion rate	–	Free
d	Distance to the source	–*	Frozen
f_{col}	color correction factor	1.7	Frozen
rflag	self irradiation flag	0	Frozen
lflag	limb-darkening flag	0	Frozen
Norm	Normalization of the model	1	Frozen

these scatterings appropriately, hence the most widely accepted value to adopt is $f_{\mathrm{col}} = 1.7$.

`kerrbb` also includes the dimensionless spin parameter a between -1 and 1. This parameter is measured by identifying the position of the inner edge of the disk which is assumed to be exactly at ISCO. The mass accretion rate is also included and calculated in the units of 10^{18} g/s. The remaining parameters are "switch" parameters which help users set up the model according to their needs. All parameters can be found in `xspec`'s manual and are summarized in Table 2.1.

More comprehensive than `kerrbb`, `kynbb` [Dovčiak et al., 2008] is a rather later addition to the spectral model family `KYN`[10] [Dovčiak et al., 2004]. In contrast to both `diskbb` and `kerrbb`, `kynbb` is not included in `xspec` and needs to be downloaded externally. Just like `kerrbb`, `kynbb` also describes an NT disk solution with the dimensionless black hole spin parameter between -1 and 1. Similarly, it also utilizes the ray tracing method. One big difference that sets `kynbb` apart is the ability to define the inner edge of the disk at a different value than the ISCO. The model also provides more freedom in setting it up for further analysis, one being the polarization calculations [Mikusincova et al., 2023, Taverna et al., 2022]. There are other additional parameters that allow users to calculate the spectrum for a portion of the disk and the outer edge of the disk. All parameters can be found in `KYN`'s manual and are summarized in Table 2.2. For our analysis, polarization calculations are switched off (Stokes parameter set at 0) and the model calculates the spectrum the same way as `KERRBB` with the only difference of the innermost edge of the accretion disk no longer terminating at R_{ISCO} (with ms switch set at 1). See Yilmaz et al. [2023] for a more detailed comparison of `KERRBB` and `KYNBB`. We do not apply any smoothing on the spectrum (smooth parameter set at 0) and assume no obscuring cloud by setting $\mathrm{r}_{\mathrm{cloud}}$=0. Similar to `DISKBB`, the normalisation parameter of `KYNBB` is defined as

$$\mathcal{N} = \frac{1}{D_{10}^2} \tag{2.4.3}$$

where D_{10} is the distance to the source in units of 10 kpc.

---

[10] `https://projects.asu.cas.cz/stronggravity/kyn`

Table 2.2: Model parameters of `kynbb` and their respective values used in the analysis. –* refers to parameter values that are source dependent, (a) set at zero to turn off polarization computations which directly turns off χ and τ as well (b) the value is user dependent and was changed at times to accommodate the computation speed/efficiency,

Parameter	Description	Value	Free/Frozen
a/M	Black Hole Spin	–	Free
θ_o	Inclination Angle	–*	Frozen
r_{in}	Inner Radius	–	Free
r_{out}	Outer Disk Radius	1000	Frozen
ϕ	lower azimuth	0	Frozen
$d\phi$	upper azimuth	360	Frozen
BHmass	Black Hole Mass	–*	Frozen
arate	Mass Accretion Rate	–	Free
f_{col}	Color Correction Factor	1.7	Frozen
α	Position of the Obscuring Cloud in α	0	Frozen
β	Position of the Obscuring Cloud in β	0	Frozen
r_{cloud}	Radius of the cloud	0	Frozen
zshift	Redshift	0	Frozen
ntable	Identifier for the Table of Relativistic Transfer Functions to be used in the Model	80	Frozen
n_{rad}	Number of Grid Points in Radius	150	Frozen
division	Type of Division for Integration	1	Frozen
n_{ϕ}	Number of Grid Points in Azimuth	180	Frozen
smooth	Switch for Smoothing	0	Frozen
Stokes	Stokes Parameter for Polarization	0	Frozen (a)
χ_0	Orientation of the System	0	Frozen
τ	Opacity of the Disk Atmosphere	11	Frozen
$n_{threads}$	Number of Threads for the Computation	Variable	Frozen
norm	Normalization	– (b)	Frozen

3. Accretion Disc Evolution in GRO J1655-40 and LMC X-3 with Relativistic and Non-Relativistic Disc Models[1]

Anastasiya Yilmaz, Jiří Svoboda, Victoria Grinberg, Peter G. Boorman, Michal Bursa, Michal Dovčiak

Published in Monthly Notices of the Royal Astronomical Society, Volume 525, Issue 1, October 2023, Pages 1288–1310

3.1 Abstract

Black hole X-ray binaries are ideal environments to study the accretion phenomena in strong gravitational potentials. These systems undergo dramatic accretion state transitions and analysis of the X-ray spectra is used to probe the properties of the accretion disc and its evolution. In this work, we present a systematic investigation of ∼1800 spectra obtained by RXTE PCA observations of GRO J1655-40 and LMC X-3 to explore the nature of the accretion disc via non-relativistic and relativistic disc models describing the thermal emission in black-hole X-ray binaries. We demonstrate that the non-relativistic modelling throughout an outburst with the phenomenological multi-colour disc model `DISKBB` yields significantly lower and often unphysical inner disc radii and correspondingly higher (∼50-60%) disc temperatures compared to its relativistic counterparts `KYNBB` and `KERRBB`. We obtained the dimensionless spin parameters of $a_* = 0.774 \pm 0.069$ and $a_* = 0.752 \pm 0.061$ for GRO J1655-40 with `KERRBB` and `KYNBB`, respectively. We report a spin value of $a_* = 0.098 \pm 0.063$ for LMC X-3 using the updated black hole mass of 6.98 $M_\odot$. Both measurements are consistent with the previous studies. Using our results, we highlight the importance of self-consistent modelling of the thermal emission, especially when estimating the spin with the continuum-fitting method which assumes the disc terminates at the innermost stable circular orbit at all times.

---

[1] This chapter is a pre-copyedited and author-edited version of the article published in the Monthly Notices of the Royal Society. The published version (Anastasiya Yilmaz, Jiří Svoboda, Victoria Grinberg, Peter G. Boorman, Michal Bursa, Michal Dovčiak, *Accretion disc evolution in GRO J165540 and LMC X-3 with relativistic and non-relativistic disc models*, Monthly Notices of the Royal Astronomical Society, Volume 525, Issue 1, October 2023, Pages 1288–1310) is available online at `https://doi.org/10.1093/mnras/stad2339`

3.2 Introduction

Black Hole X-ray Binaries (BHXRBs) are a sub-class of X-ray binaries with a black hole as the central compact object and most of them are observed to be transient sources. The spectral properties of these accreting systems are primarily described depending on the relative contribution of two distinct emission components: thermal and non-thermal. The thermal component of the X-ray spectrum is composed of radiation at different radii in the accretion disc [Shakura and Sunyaev, 1973] and the non-thermal contribution to the spectrum arises due to the thermal Comptonisation of the ”seed” photons from the innermost regions of the accretion disc by a hot corona (an optically thin cloud of electrons close to the black hole) usually responsible for the emission above ~ 5 keV [Sunyaev and Titarchuk, 1980, Zdziarski, 1985, Chakrabarti and Titarchuk, 1995, Narayan et al., 1996, Zdziarski and Gierliński, 2004]. Superimposed on the continuum, a third component, the relativistic reflection appears in the event of non-thermal emission being reprocessed by the optically thick disc.

While only a few systems are observed to be persistently active, a big majority of the BHXRBs spend their time in a quiescent state where the total luminosity in all bands is very low and their evolution as a system is mainly described by properties of accretion states. To date, several accretion states were identified in BHXRBs (see, e.g., Fender et al. [2004] and Remillard and McClintock [2006]) that rapidly change over time depending on the relative dominance of the thermal and non-thermal components of the spectral continuum. Once the outburst begins, the system starts to transit across three predominantly identified distinct accretion states according to the X-ray intensity and X-ray spectral hardness parameters. These accretion states are usually tracked using a hardness-intensity diagram (HID) and many BHXRBs are found to follow a clear ”q-shape” [Fender et al., 2004, Dunn et al., 2010]. For a typical outburst, these accretion states are identified as the low/hard state (LHS), high/soft state (HSS) and the steep powerlaw or intermediate state.

At the very beginning and the end of the outburst, the binary system is observed to be in the LHS state where the luminosity is significantly lower and most of the X-ray flux is dominated by the hard emission from an X-ray corona which can be described by a powerlaw with a relatively flat photon index with $\Gamma \sim 1.5-2$ and a weak disc component characterized by lower disc temperatures with $kT < 1$ keV [Poutanen, 1998]. The increase in the X-ray luminosity throughout the rise of the outburst is usually followed by a rise in the radio luminosity. This ”compact” radio emission is associated with synchrotron radiation from a steady relativistic jet with a flat or in some cases inverted radio spectrum (see Blandford and Königl [1979], Fender [2001], Fender and Gallo [2014]). Independent of the increasing luminosity by a few orders of magnitude (both in radio and X-rays), the spectrum remains hard throughout the LHS [Corbel et al., 2000, 2003]. As the accretion rate increases, the system then transitions to the steep powerlaw or the intermediate state where the luminosity is high and the spectrum is dominated by a steep powerlaw ($\Gamma \sim 1.9$) [Remillard and McClintock, 2006, Belloni and Motta, 2016]. This state can often be divided into two arms with the hard intermediate state (HIMS) and the soft intermediate state (SIMS) where the source transitions through a powerlaw-dominated state to a more thermal state before transitioning to the HSS. During this transition to the HSS, the system crosses a "jet line" which is described as a point throughout the outburst where the compact radio jet is quenched [Fender et al., 1999, Corbel et al., 2000, Russell et al., 2011]. During the HSS, where the X-ray luminosity can increase by orders of magnitude and the big majority of the flux is observed to be emitted from the accretion disc with a spectrum that is primarily characterized by a multi-temperature blackbody with a peak temperature of $kT \sim$ 1-1.5 keV with an additional powerlaw with a photon index of $\Gamma \sim 2.5$ or even softer. In contrast to the substantial increase in the X-ray luminosity during the rise to the HSS, the radio emission starts to decrease and eventually vanishes as the radio jet is quenched in this state. The softening of the spectrum from the LHS to HSS occurs relatively faster compared to the time spent in the LHS [Dunn et al., 2010]. The third state, the steep powerlaw or the intermediate state, is entered as the powerlaw also starts to dominate over the thermal disc emission with $\Gamma \sim 2.5-3$ but the spectrum continues to be very soft. As the dominance of the disc continues to fade away, the system returns to the LHS completing the q-path at the end of the outburst before re-entering the quiescent state. Such sharp increases in the X-ray luminosity throughout the outburst while transitioning to the HSS are primarily explained by rapidly increasing accretion rates, $\dot{M}$, in a geometrically thin, optically thick disc originally characterized by Shakura and Sunyaev [1973].

The most extensive global spectral study of BHXRBs was introduced by Dunn et al. [2010] where they analysed a sample of 25 known low-mass BHXRBs observed by the RXTE mission with multiple outbursts covered adopting a non-relativistic multi-colour disc model with an additional powerlaw component. They extended their work in Dunn et al. [2011] focusing on the study of the long-term evolution of accretion discs in BHXRBs throughout the outburst phases of the same sample. For the majority of BHXRBs in their sample, the results followed the expected theoretical $L_{\mathrm{Disc}} \propto T^4$ relation with some exceptions at the low and high ends of L_{Disc} with arms extending out to significantly higher temperatures compared to observations with similar L_{Disc} values. It was argued that a changing colour correction factor f_{col} could account for such deviations from the theoretically expected trend but they didn't suspect it to be such a huge influence on the measurements of inner disc radius and temperature. This colour correction factor accounts for spectral hardening of the accretion disc emission which can deviate from a "perfect" blackbody emission due to reprocessing of the disc emission in the disc atmosphere and relates the colour temperature to the effective temperature as $f_{\mathrm{col}} = T_{\mathrm{col}}/T_{\mathrm{eff}}$. For a typical [Shakura and Sunyaev, 1973] disc with sufficiently high temperature at the disc surface, electron scatterings start to dominate over any absorption leading to photons emitted from the disc to be up-scattered to higher temperatures. These up-scattering processes produce an emissivity profile modified by the colour correction factor. This colour correction factor can be considered to vary with the accretion state, though constrained measurements of f_{col} become very difficult from X-ray spectra (for a more in-depth review, see Salvesen and Miller [2021] and references therein). Similar results for individual sources were previously reported by Gierliński and Done [2004], Done et al. [2007] and Dunn et al. [2008]. They showed that a similar trend was present in R_{in} - T where they reported notably low R_{in} values at the beginnings and ends of the outbursts in response to their L_{Disc} - T findings.

In the most widely accepted picture (see the reviews by Fender et al. [2004], Homan and Belloni [2005], Remillard and McClintock [2006], Done et al. [2007], Dunn et al. [2010], Belloni et al. [2011], Dunn et al. [2011], Fender and Belloni [2012], Fender and Muñoz-Darias [2016]), the radius and the temperature of the innermost region of the accretion disc change throughout the outburst. While transitioning from the beginning of the outburst to the HSS with increasing luminosity, the innermost region of the disc starts to get closer to the black hole [Gierliński and Done, 2004, Steiner et al., 2010, Reynolds and Miller, 2013], eventually resulting in a significant increase in the disc temperature peaking at kT $\sim 1 - 1.5$ keV. During the peak of the HSS, the disc can extend all the way down to the innermost stable circular orbit (ISCO) with a contrastingly cold disc truncated at much larger radii in the LHS at the beginning and end of an outburst [Narayan and Yi, 1995, Esin et al., 1997, D'Angelo et al., 2008, Reis et al., 2010, Plant et al., 2015]. The exact accretion disc geometry throughout the LHS remains less understood compared to HSS. Both in relativistic and non-relativistic solutions, a "zero-torque" boundary condition at the ISCO is assumed [Shakura and Sunyaev, 1973, Novikov and Thorne, 1973] while, in reality, magnetic fields strong enough to exert such torques might exist but can not be strong enough to dominate over the mass accretion [Krolik, 1999, Gammie, 1999]. When magnetic torques at the inner boundary are taken into account, the radiative efficiency of the accretion disc increases significantly.

This changing inner disc radius was challenged by XMM-Newton and RXTE observations of SWIFT J1753.5-0127 where Miller et al. [2006] reported an inner disc radius $R_{\rm in} \leq 6GM/c^2$ in the LHS for all of their spectral models. A similar trend was later reported by Reis et al. [2010] for 8 black hole X-ray binary systems in the LHS while the disc temperatures remained below 0.3 keV.

The radius of the ISCO is determined primarily by the spin and mass of the black hole,

$$R_{\rm ISCO} = r_{\rm g} \left\{ 3 + A_2 \pm \left[(3 - A_1)(3 + A_1 + 2A_2) \right]^{1/2} \right\} \tag{3.2.1}$$

$$A_1 = 1 + \left(1 - a_*^2\right)^{1/3} \left[(1 + a_*)^{1/3} + (1 - a_*)^{1/3} \right] \tag{3.2.2}$$

$$A_2 = \left(3a_*^2 + A_1^2\right)^{1/2} \tag{3.2.3}$$

$$a_* = \frac{|\mathbf{J}|c}{GM^2} \tag{3.2.4}$$

where J is the black hole angular momentum, G is the gravitational constant, c is the speed of light, M is the black hole mass, $r_{\rm g} = GM/c^2$ is the gravitational radius and the upper and lower signs correspond to a prograde disc ($a_* > 0$) and a retrograde disc ($a_* < 0$), respectively. By this relation, an accretion disc around a maximally spinning black hole with $a_* = 1$ can extend all the way down to just $R_{\rm ISCO}$ $(a_* = 1) = r_{\rm g}$ while in the canonical Schwarzschild case with $a_* = 0$ it can be only as close as $R_{\rm ISCO}$ $(a_* = 0) = 6r_{\rm g}$.

In this paper, we focus on several outbursts of GRO J1655-40 and LMC X-3 and perform a detailed spectral analysis of all of the publicly available RXTE observations spanning nearly 16 years of observing time. The structure of this paper is as follows: in Section 3.3, we summarize the properties of GRO J1655-40 and LMC X-3, outline the selected observations and data reduction process, provide a review of the spectral modelling of accretion discs in black hole X-ray binaries and summarize the spectral analysis using these models. In Section 4.3, we present the results of our analysis with each model and provide a discussion in Section 4.4. Section 3.6 provides a summary of our conclusions based on our analysis.

3.3 Sources, Data Reduction and Analysis

3.3.1 GRO J1655-40

GRO J1655-40, one of the most extensively studied Galactic low mass black hole X-ray binaries (LMBXRBs)[Hjellming and Rupen, 1995, Orosz et al., 1997, Abramowicz and Kluźniak, 2001], was discovered in 1994 by the Burst and Transient Source Experiment (BATSE) onboard the Compton Gamma Ray Observatory [Zhang et al., 1994]. Orosz and Bailyn [1997] measured a black hole with a mass of $M_{\rm BH} = 6.3 \pm 0.5\ M_{\odot}$ and a companion star of $M_{*} = 2.4 \pm 0.4\ M_{\odot}$ based on optical observations with an orbital period of 2.6 d [Greene et al., 2001]. Based on optical/NIR observations, Beer and Podsiadlowski [2002] reported $M_{\rm BH} = 5.4 \pm 0.3\, M_{\odot}$ and $M_{*} = 1.45 \pm 0.35\, M_{\odot}$. The inclination angle has been reported as $i = 70.2^{\circ} \pm 1.9^{\circ}$ [Kuulkers et al., 2000] while radio observations revealed a difference of 15° between the binary orbital plane inclination angle and the jet inclination angle [Orosz and Bailyn, 1997, Maccarone, 2002]. Although a distance of $\sim 3.2 \pm 0.2$ kpc is commonly used, Foellmi et al. [2006] argued that it should be lower than 1.7 kpc. In this study, we adopt d $\sim 3.2 \pm 0.2$ kpc based on Hjellming and Rupen [1995]. Different methods to measure the spin on GRO J1655-40 revealed a controversy, with $0.65 < a_{*} < 0.75$ obtained from spectral continuum fitting with ASCA and RXTE observations [Shafee et al., 2006] while Fe emission line profile predicts much higher values, with a lower limit on the spin at $a_{*} = 0.9$ [Reis et al., 2009] based on XMM-Newton observations. On the contrary to these measurements pointing towards a high spin case for GRO J1655-40, timing analysis of the entire set of RXTE data using the relativistic precession model [Stella and Vietri, 1998, 1999] resulted in a much smaller spin parameter $a_{*} = 0.290 \pm 0.003$ [Motta et al., 2014]. During the 2005 outburst, GRO J1655-40 was observed mainly in HSS except for unusually soft or hyper-soft states [Uttley and Klein-Wolt, 2015] where detection of a strong accretion disc wind with a line-rich X-ray absorption spectrum was reported using Chandra X-ray HETG [Miller et al., 2008]. This hyper-soft state is suggested to arise from a Compton-thick accretion disc wind and might even indicate intrinsic luminosities above the Eddington limit due to the obscuration [Neilsen et al., 2016]. While the underlying mechanism is still not well understood, one of the explanations to describe the nature of this strong disc wind is based on a hybrid magnetically/thermally driven mechanism [Neilsen and Homan, 2012].

3.3.2 LMC X-3

LMC X-3, a bright and persistent low mass X-ray binary system in the Large Magellanic Cloud (LMC), was discovered by UHURU in 1971 [Leong et al., 1971] located at a distance of d ∼48.1 kpc [Orosz et al., 2009]. The system harbours a black hole with an estimated mass of $M_{\mathrm{BH}} = 6.98 \pm 0.56 M_\odot$ and a companion star categorized as a B3 V star with an estimated mass of $M_* = 3.63 \pm 0.57 M_\odot$. This highly variable binary system has an inclination angle $i = 69^\circ \pm 0.72^\circ$ [Orosz et al., 2014] and has been observed to be dominantly in the HSS [Nowak et al., 2001] except for a few occasions with observations in LHS [Boyd et al., 2000, Wilms et al., 2001] with a few anomalous low/hard state (ALS) observations with a dramatic drop in the total X-ray flux down to $\sim 1 \times 10^{35}$ erg s^{-1} in 2-10 keV range [Smale and Boyd, 2012, Torpin et al., 2017] making it an object of interest to study the accretion phenomena and various accretion disc models in BHXRBs [Davis et al., 2006, Kubota et al., 2010, Straub et al., 2011]. LMC X-3 stands out as a unique object due to the almost always-on and dominantly soft nature of its X-ray observations. Its nearly constant inner disc radius [Steiner et al., 2010] puts LMC X-3 in the spotlight for spin measurements using X-ray spectral continuum fitting. Spin measurements to date using the X-ray spectral continuum fitting method with models based on a thin disc structure revealed a relatively low spin parameter in the range of $0.22 < a_* < 0.41$ [Davis et al., 2006, Steiner et al., 2014, Bhuvana et al., 2021, 2022] while spectral modelling adopting a relativistic slim disc model with different viscosity and colour correction parameters gave much higher spin values of $a_* \sim 0.7$ [Straub et al., 2011]. We provide a summary of all of the physical parameters adopted in this paper for each source in Table 3.1.

Source	M_{BH} ($M_\odot$)	D (kpc)	i (deg)	N_{H} (10^{22} cm^{-2})
LMC X-3	6.98 ± 0.56^a	$48.1\ ^b$	69.0 ± 0.72^a	0.04^c
GRO 1655-40	6.3 ± 0.5^d	3.2 ± 0.2^e	70.2 ± 1.9^f	0.8^d

Table 3.1: Parameter Values for LMC X-3 and GRO J1655-40
[a] Orosz et al. [2014], [b] Orosz et al. [2009], [c] Page et al. [2003], [d] Orosz and Bailyn [1997], [e] Hjellming and Rupen [1995], [f] Kuulkers et al. [2000]

3.3.3 Observations

The Rossi X-Ray Timing Explorer (RXTE) observed LMC X-3 and GRO J1655-40 extensively throughout the entire mission spanning multiple outbursts between 1997-2011 and 1996-2012, respectively. For the spectral fitting, we used a total of more than 1800 observations publicly available on HEASARC (High Energy Astrophysics Science Archive Research Center) archive . The full list of proposal numbers of the observations used can be found in Table 4.1.

3.3.4 RXTE Data Reduction

We extracted the source spectra in the `standard2f` mode which provides the optimal spectral resolution and generated response matrices and background spectra following the standard procedure in the RXTE cookbook[2] using `FTOOLS/HEASOFT`

---

[2] `https://heasarc.gsfc.nasa.gov/docs/xte/recipes/cook_book.html`

Table 3.2: Proposal numbers and observation dates of RXTE observation used in spectral analysis (in ascending order).

Proposal Number	Start Date	End date	Number of Observations
	GRO J1655-40		
10255	1996-05-09	1997-01-26	31
10261	1996-05-14	1996-06-30	1
10263	1996-05-12	1996-05-12	1
10404	1996-03-14	1996-03-14	15
20187	1996-11-07	1996-11-07	1
20402	1997-02-26	1997-09-11	32
90019	2005-03-13	2005-03-13	1
90058	2005-02-20	2005-03-02	6
90428	2005-02-25	2005-03-03	11
90704	2005-03-10	2005-03-10	2
91404	2005-03-04	2005-03-07	6
91702	2005-03-07	2005-11-11	473
91704	2005-09-24	2005-09-24	3
		Total:	583
	LMC X-3		
10252	1996-02-09	1996-10-24	67
20188	1996-11-30	1997-12-12	27
20189	1997-08-29	1997-09-02	2
30087	1998-01-06	1998-09-30	17
40066	1998-12-08	1998-12-14	19
40067	1999-01-19	1999-09-19	26
50411	2000-05-05	2000-10-22	12
60097	2001-03-09	2002-02-27	57
60098	2001-06-30	2001-07-07	4
80103	2003-10-04	2004-03-10	73
80118	2004-01-07	2004-01-12	24
90099	2004-04-20	2004-05-08	12
91105	2005-03-07	2007-03-16	189
92095	2006-03-04	2007-06-27	255
93113	2007-06-29	2008-12-23	156
93114	2007-06-28	2007-07-09	11
94113	2008-12-27	2009-12-29	102
95113	2010-01-03	2010-12-29	103
96113	2011-01-02	2011-12-28	98
		Total:	1254

version 6.29[3] software package. We also removed data lying within 10 minutes of the South Atlantic Anomaly. In order to avoid any variations during the data reduction process, we only used the Proportional Counter Unit-2 (PCU-2) of RXTE's Proportional Counter Array (PCA, Jahoda et al. [2006]) with all of its layers included since it was almost always operating throughout the RXTE mission and has the best calibration among other PCUs on-board PCA. We then carried out the calibration of data using publicly available tool `pcacorr` [García et al., 2014] and applied an additional 0.1% systematic errors to account for uncertainties in the telescope's response following García et al. [2014].

`KYNBB` [Dovčiak et al., 2008] was developed as an extension to the original non-axisymmetric general relativistic spectral model package `KYN`[4] by Dovčiak et al. [2004] as an external model to `XSPEC` environment describing an accretion disc around a black hole with spin values spanning the whole parameter space from -1 to 1. Similar to the case of `KERRBB`, `KYNBB` makes use of the ray-tracing method for photon paths in vacuum in a Kerr space-time to compute the transfer functions for the tables used in the model, describing a Novikov and Thorne [1973] accretion disc. In contrast to `KERRBB`, `KYNBB` offers the option to define the inner disc radius at a different distance than ISCO. One also has the freedom of including polarization calculations [Mikusincova et al., 2023, Taverna et al., 2022], calculating the spectrum only for a certain part of the accretion disc and defining a range on the disc radius from which the spectrum will be calculated. For the purpose of our analysis, polarization calculations are switched off (Stokes parameter set at 0) and the model calculates the spectrum the same way as `KERRBB` with the only difference of the innermost edge of the accretion disc no longer terminating at R_{ISCO} (with ms switch set at 1). See Yilmaz et al. [2023] for a more detailed comparison of `KERRBB` and `KYNBB`. We do not apply any smoothing on the spectrum (smooth parameter set at 0) and assume no obscuring cloud by setting $\mathrm{r}_{\mathrm{cloud}}=0$. Similar to `DISKBB`, the normalisation parameter of `KYNBB` is defined as

$$\mathcal{N} = \frac{1}{D_{10}^2} \tag{3.3.1}$$

where D_{10} is the distance to the source in units of 10 kpc. The list of physical parameters and values used for our analysis can be found in Table 3.3.

3.3.5 Spectral Analysis

For spectral analysis, we used the `HEASOFT` (v.6.29) package `XSPEC (v.12.12)` [Arnaud, 1996] and `PyXspec`[5], a Python interface to the `XSPEC`. RXTE PCA covers the energy range of 2-60 keV while the count statistics become significantly poorer beyond the range of 3-25 keV. We, therefore, restricted the energy range to 3-25 keV for all of the PCA spectra. We used `grppha` to group the spectra to have 25 counts per bin. All of the models used for the spectral analysis consist of a thermal disc component, either relativistic or non-relativistic, and a simple powerlaw component accounting for the non-thermal component of the continuum (`POWERLAW` in `XSPEC`). We use `TBABS` to account for the ISM absorption. For conve-

---

[3] `https://heasarc.gsfc.nasa.gov/docs/software/lheasoft/`

[4] `https://projects.asu.cas.cz/stronggravity/kyn`

[5] `https://heasarc.gsfc.nasa.gov/docs/xanadu/xspec/python/html/`

nience, each model (`TBABS`×`(DISKBB+POWERLAW)`, `TBABS`×`(KERRBB+POWERLAW)`) and `TBABS`×`(KYNBB+POWERLAW)` will be referred to as the specific model used for the disc component. We adopted a selection criteria by assessing reduced χ^2 (χ^2/d.o.f.) values and applied a cut at reduced $\chi^2 = 2.0$ excluding the observations that lie outside this range. We used the normalisation parameter of `DISKBB`, $\mathcal{N}$, (see equation (2.4.1)), to calculate the inner disc radius and apply no additional corrections to any parameter value obtained from the fitting. All of the errors on model parameters presented throughout the paper are calculated at the 90% confidence level.

Throughout our analysis with `KYNBB`, we assumed an emission integrated above the measured $R_{\rm in}$ covering the entire disc with an exponential radial grid and defined the outer edge of the non-zero disc emissivity as 1000 $R_{\rm g}$. We did not apply any smoothing on the calculated spectrum. We set the number of radial grid points on the disc at the default value of 150 for sufficient resolution of the spectrum and switched off the parameters of the model regarding an obscuring cloud and polarization calculations. We summarize the values of relevant parameters as adopted in the spectral analysis in Table 3.3.

We used disc fractions to distinguish observations based on how much the disc component is dominating over powerlaw following Körding et al. [2006], Dunn et al. [2008, 2010] with the disc fraction defined as

$$F_{\rm Disc} = \frac{L_{\rm Disc}(0.001 - 100.0 \text{ keV})}{L_{\rm Disc}(0.001 - 100.0 \text{ keV}) + L_{\rm Power}(1.0 - 100.0 \text{ keV})} \tag{3.3.2}$$

where $L_{\rm Disc}$ and $L_{\rm Power}$ are the unabsorbed disc luminosity in $0.001 - 100.0$ keV and unabsorbed powerlaw luminosity in $1.0 - 100.0$ keV energy range, respectively. We used the convolution model `CFLUX` in `XSPEC` for flux calculations of each component.

3.4 RESULTS

3.4.1 GRO J1655-40

We first analysed the entire sample of observations of GRO J1655-40 listed in Table 4.1 using `DISKBB`. The majority of the excluded observations with reduced $\chi^2 > 2.0$ were distributed throughout the entire outburst with a subset concentrated in the region of the HID corresponding to the transition from SIMS to HSS when tracked on a light curve and an HID. Spectral fitting of these specific observations with `DISKBB` showed residuals at energies between 5-7 keV.

We proceeded further to obtain the flux values of the unabsorbed model components separately. Due to unconstrained parameters of the disc model, the fitting procedure with `PyXspec` during flux calculations of the disc component was interrupted for states with significantly low count rates where the source was either at the very beginning or the end of the outburst. A total of 71 observations are excluded from further analysis due to this complication. We also obtained significantly high reduced χ^2 values for the observations covering the outbursts from 1996 and 1997 due to a significant increase in the sensitivity of the PCA instrument after calibration with `pcacorr` instead of previously adopted methods. Simple spectral modelling with `DISKBB` with just a powerlaw component

Table 3.3: Values adopted for model parameters of `DISKBB`, `KERRBB` and `KYNBB`

Model Parameter	Value	Free/Frozen
	`DISKBB`	
T_{in}	–	Free
Normalisation	–	Free
	`KERRBB`	
η	0	Frozen
Black Hole Spin	–	Free (see Section 3.3.5)
Inclination Angle	(see Table 3.1)	Frozen
Black Hole Mass	(see Table 3.1)	Frozen
Mass Accretion Rate	–	Free
Distance	(see Table 3.1)	Frozen
f_{col}	1.7	Frozen (see Section 3.5.3)
Self-irradiation Flag	0	Frozen
Limb-darkening Flag	0	Frozen
Normalisation	1	Frozen
	`KYNBB`	
Black Hole Spin	–	Free (see Section 3.3.5)
Inclination Angle	(see Table 3.1)	Frozen
Inner Radius	–	Free
Switch for Inner Radius	0	Frozen
Outer Radius	1000	Frozen
ϕ	0	Frozen
$d\phi$	360	Frozen
Black Hole Mass	(see Table 3.1)	Frozen
Mass Accretion Rate	–	Free
f_{col}	1.7	Frozen
α	0	Frozen
β	0	Frozen
r_{cloud}	0	Frozen
Redshift	0	Frozen
ntable	80	Frozen
nrad	150	Frozen
Division	1	Frozen
$n\phi$	180	Frozen
Smooth	0	Frozen
Stokes	0	Frozen
χ_0	0	Frozen
τ	11	Frozen
nthreads		Frozen
Normalisation	(see Table 3.1 and Equation 3.3.1)	Frozen

produced significant residuals for some of these observations at energies between 5-7 keV which couldn't be modelled with a simple Gaussian line (`GAUSS`) with line energies between 6-7 keV. While an additional `GAUSS` component improved the fits significantly, these observations did not fall into our selection criteria due to reduced χ^2 values well above 10, suggesting a more detailed analysis of these specific observations. More sophisticated modelling of the reflection component introduces a new level of model dependency when used with `KERRBB` and `KYNBB` since both models still extend to higher energies, eventually coinciding with the 5-7 keV energy range. With RXTE's limited spectral resolution, proper modelling of such line features introduces a risk of bias we choose to avoid for the purpose of our analysis. A detailed analysis of the line properties will be presented in further studies. Hence, we exclude these 81 observations from these two outbursts for further investigation and only include the 2005 outburst which already encompasses more than 86% of the entire sample for GRO J1655-40. The number of remaining observations after the selection criteria applied for GRO J1655-40 stood at 202 for `DISKBB`.

Using the reduced set of observations, we replaced `DISKBB` with `KERRBB`. We also tested the poor fits obtained in the previous step of the analysis with `KERRBB` but did not observe any significant improvement in reduced χ^2 values to match the selection criteria. Throughout our analysis with `KERRBB`, we left the mass accretion rate $\dot{M}$ as a free parameter and use a fixed colour correction factor of $f_{\mathrm{col}} = 1.7$ throughout the outbursts [Shimura and Takahara, 1995]. We also fixed $\eta = 0$ to adopt a stress-free boundary condition at R_{ISCO}. Following the discussion in Li et al. [2005], we fix the normalisation at 1.0 since the mass, inclination angle of the disc and distance to the source are fixed while one still has the freedom of choosing a different value due to the uncertainties in measurements of these parameters.

We first attempted to fit the same set of spectra with a fixed spin at $a_* = 0.7$ following the results from the X-ray spectral continuum fitting method by Shafee et al. [2006]. Adopting a spin value fixed at a value in `KERRBB` produced poorer fits with reduced χ^2 much larger than 2.0 for $\sim$ 89% of observations due to the residuals in the lower energies where the model was not able to reproduce the spectral shape for the same physical parameters and a specific spin value. As a result, we carried out the analysis for GRO J1655-40 with a spin parameter left free to vary between 0.0-0.9982. Figure 3.5 shows the evolution of the measured spin parameter throughout the outburst. Limiting the spin parameter to a smaller range between 0.65-0.75 following the measurements by Shafee et al. [2006] did not improve the number of fits with reduced $\chi^2 < 2.0$.

In contrast to `DISKBB`, disc temperature is not a model parameter in `KERRBB` and `KYNBB`. To obtain the value for the disc temperature in a similar sense to `DISKBB`, we evaluated the position of the peak of the disc component in the model. Due to the zero-torque boundary condition at the innermost disc radius adopted by `KERRBB`, this peak corresponds to a disc radius not exactly at R_{ISCO} but slightly further out. This is still a valid approximation of the accretion disc temperature as measured by `KERRBB`.

Due to difficulties in fitting with a fixed spin for GRO J1655-40, we replaced the relativistic disc model with `KYNBB` to have more freedom with the definition of the innermost edge of the accretion disc R_{in}. Additional to the mass accretion rate,

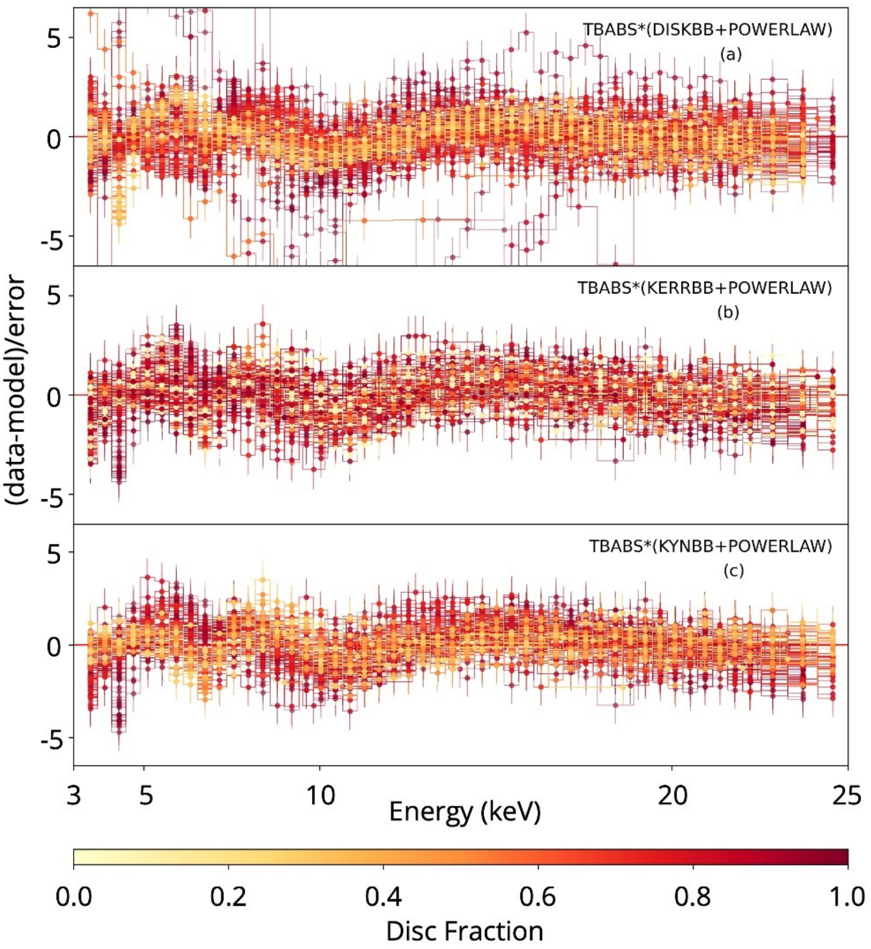

Figure 3.1: (a) Residuals in (data-model)/error for fits of GRO J1655-40 with reduced $\chi^2 < 2.0$ obtained from spectral fitting with `TBABS`×`(DISKBB+POWERLAW)` (b) Residuals in (data-model)/error for fits of GRO J1655-40 with reduced $\chi^2 < 2.0$ obtained from spectral fitting with `TBABS`×`(KERRBB+POWERLAW)` (c) Residuals in (data-model)/error for fits of GRO J1655-40 with reduced $\chi^2 < 2.0$ obtained from spectral fitting with `TBABS`×`(KYNBB+POWERLAW)`

we let $R_{\rm in}$ vary throughout our analysis with `KYNBB`. This allowed us to recover 93% of the observations `KERRBB` was able to fit only with a free spin parameter. We fixed the normalisation parameter to their respective values following equation (3.3.1) calculated using distances adopted in Table. We present the residuals in (data-model)/error obtained from our spectral fits of GRO J1655-40 for each model in Figure 3.1.

Apart from the initial sample obtained by fitting with `DISKBB`, we also analysed the 1996 and 1997 outbursts of GRO J1655-40 with `KERRBB` but we observed no significant improvement in reduced χ^2 below 2. Due to the long computation times required for `KYNBB`, we did not proceed with the same analysis with `KYNBB` for these outbursts. We present the spectral fits of these outbursts with `DISKBB` and `KERRBB` in Figure 3.11 in Appendix A.

3.4.2 LMC X-3

We adopted the same approach to LMC X-3 and first analysed the entire sample of observations with `DISKBB`. We applied the same selection criteria with a cut at reduced $\chi^2 = 2.0$ excluding the observations that lie outside this range. We also excluded the observations where the disc component was not constrained and caused the fitting procedure with `PyXspec` to be interrupted during the flux calculations with `CFLUX`. The number of such observations was significantly lower due to the almost-persistent nature of LMC X-3 in contrast to GRO J1655-40.

We continued with our analysis using `KERRBB` for LMC X-3 to investigate the behaviour of the spin parameter across different luminosities. We fixed the physical parameters to their respective values listed in Table 3.1. Unlike in the case of GRO J1655-40, we were able to fit $\sim 95\%$ of these observations with a spin fixed at $a_* = 0.25$ following Steiner et al. [2014]. The outliers in this sample did not correspond to a specific state of the system, showing no indication of the effects of a significant change in the inner disc radius affecting the fitting process as observed in GRO J1655-40.

Following our analysis of GRO J1655-40, we used the same setup for `KYNBB` and fit the spectra with a fixed spin at $a_* = 0.25$ and values for the black hole mass, inclination angle, the distance to the source (i.e. the normalisation parameter in `KYNBB`) to their respective values and did not change any of the other model parameter setups we used for GRO J1655-40. We present the residuals in (data-model)/error obtained from our spectral fits of LMC X-3 for each model in Figure 3.2.

In Figure 3.3, we present the distribution of reduced χ^2 values from all of the fits with $\chi^2/\text{d.o.f.} < 2.0$ across each model for GRO J1655-40 and LMC X-3 combined. With each fit, the number of observations producing good fits was reduced with a cut at $\chi^2/\text{d.o.f.} < 2$. For a big majority of these observations, adding a simple Gaussian line did not recover the fit. To preserve the simplicity of the model configuration described in Section 3.3.5, we did not perform a more sophisticated analysis for these specific observations and instead chose to remove them from our analysis.

3.4.3 Disc Luminosity L_{Disc} and Disc Temperature T_{Disc}

We used the physical description from Gierliński et al. [1999] to calculate the relation between the disc luminosity and the temperature,

$$\frac{L_{\text{Disc}}}{L_{\text{Edd}}} \approx 0.583 \left(\frac{1.8}{f_{\text{col}}}\right)^4 \left(\frac{M}{10\text{M}_\odot}\right) \left(\frac{kT_{\text{max}}}{1\text{keV}}\right)^4 \tag{3.4.1}$$

Following the general description for `DISKBB`, to account for strong gravitational potentials, we adopt the following relativistic correction by Zhang et al. [1997] between T_{max} and T_{obs}

$$T_{\text{max}} = T_{\text{obs}}/f_{GR}(\theta, a_*)\xi \tag{3.4.2}$$

where $\xi = 1.04$ is for the stress-free boundary layer, $f_{GR}(\theta, a_*)$ is the fractional change of the colour temperature (assumed 1.064 following Table 1 in Zhang et al. [1997], derived by Cunningham [1975]), θ is the inclination angle and a_* the

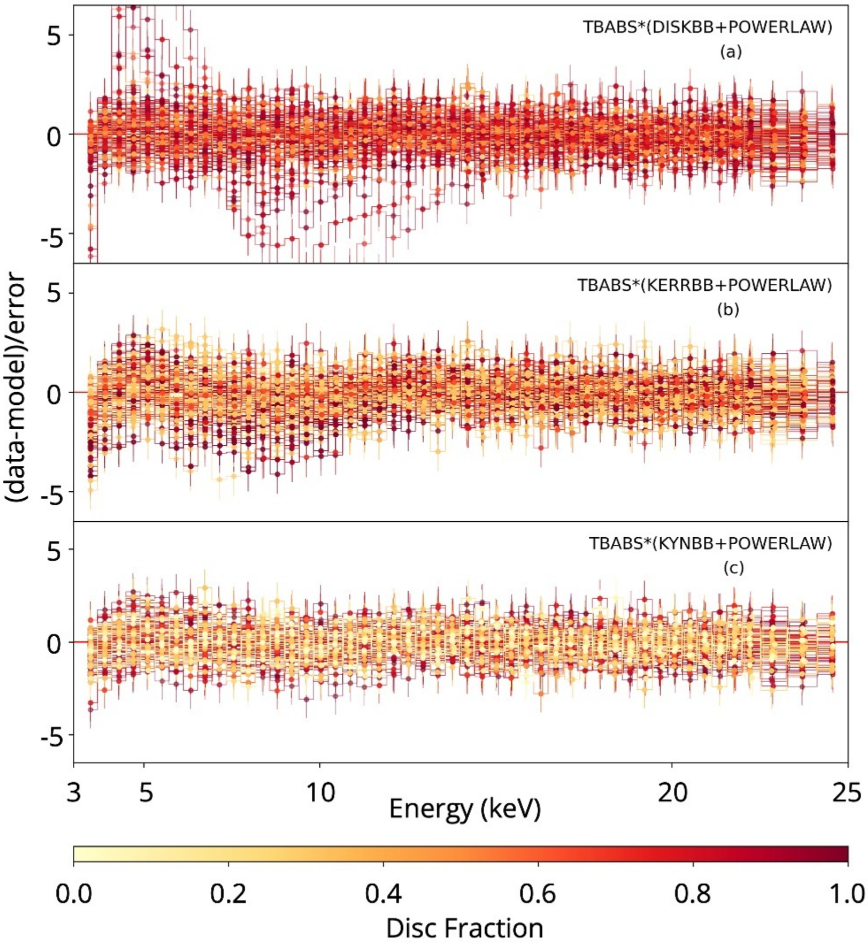

Figure 3.2: (a) (data-model)/error residuals for fits of LMC X-3 with reduced $\chi^2 < 2.0$ obtained from spectral fitting with `TBABS`×`(DISKBB+POWERLAW)` for observations with observation ID's between 80103-01-24-00 and 91105-03-03-11. (b) (data-model)/error residuals for fits of LMC X-3 with reduced $\chi^2 < 2.0$ obtained from spectral fitting with `TBABS`×`(KERRBB+POWERLAW)` for observations with observation ID's between 80103-01-24-00 and 91105-03-03-11. (c) (data-model)/error residuals for fits of LMC X-3 with reduced $\chi^2 < 2.0$ obtained from spectral fitting with `TBABS`×`(KYNBB+POWERLAW)` for observations with observation ID's between 80103-01-24-00 and 91105-03-03-11.

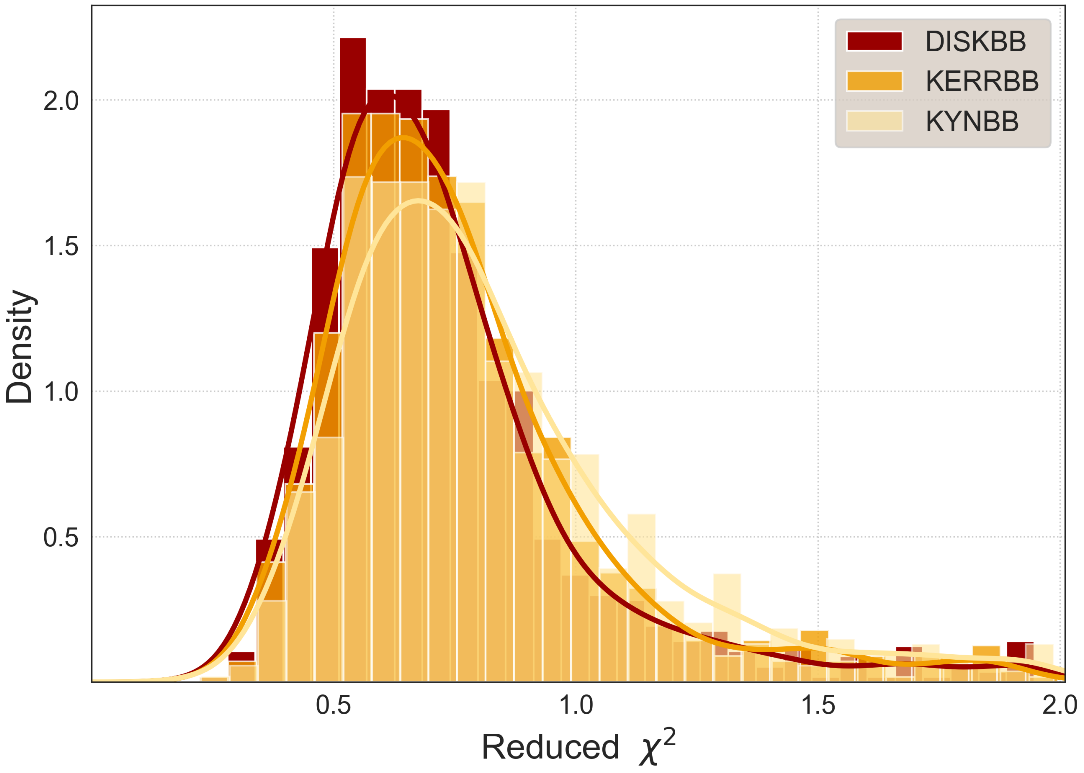

Figure 3.3: The distribution of reduced χ^2 values obtained from all of the fits with χ^2/d.o.f. < 2.0 analysed with `DISKBB` (red), `KERRBB` (orange) and `KYNBB` (yellow) for GRO J1655-40 and LMC X-3 combined.

dimensionless spin parameter. Dotted lines in Figure 3.4 show the calculated relationships for GRO J1655-40 for different f_{col} values in comparison to the observed trend which is indicated with a red solid line.

We obtained similar results as previously presented by Gierliński and Done [2004], Done et al. [2007] and Dunn et al. [2008, 2010, 2011] from the fitting with `DISKBB` for GRO J1655-40 and LMC X-3. 2005 outburst of GRO J1655-40, analysed with `DISKBB`, revealed the same deviations from expected the L_{Disc} - T_{Disc} trend or "spurs" as previously labeled by Dunn et al. [2011]. We present the changes in disc luminosities with respect to disc temperatures (L_{Disc} - T_{Disc}) obtained from `DISKBB`, `KERRBB` and `KYNBB` for $f_{\mathrm{col}} = 1.7$ in Figure 3.4. These structures correspond to observations where the luminosity remains comparatively the same while the temperature rises significantly, making these specific states shift towards the right of the general trend. Since these deviations from the trend are observed in the states corresponding to the smallest inner disc radii and highest disc temperature, we explored the possible effect of changes in f_{col} due to changes in the accretion states by letting f_{col} as a free parameter in `KERRBB` throughout the outburst. Our results did not indicate any changes to the observed trend in the upper and middle panels of Figure 3.4. As also presented by Dunn et al. [2011], we did not observe these deviations from the general trend for the entire sample of LMC X-3 observations. We, therefore, do not include the corresponding plots for LMC X-3 in further discussion.

For the entire set of observations of both GRO J1655-40 and LMC X-3, we measured ~52% (on average) higher disc temperatures with `DISKBB` than `KERRBB` while L_{Disc} is measured to be ~8% lower on average. This temperature difference, however, did not provide an improvement to the previously reported "spurs" since this temperature change was a result of f_{col} correction to the spectrum and was applied throughout the entire sample during the analysis, not for these states only. When compared to `KYNBB` with the inner disc radius as a free parameter, `DISKBB` gives disc temperature values 40% higher on average while the luminosity is measured to be 2% lower. When the two relativistic accretion disc models are compared, `KYNBB` gives disc temperatures 18% higher than `KERRBB` on average while the disc luminosities are very similar with `KYNBB` measuring only 0.3% higher on average than `KERRBB`.

Figure 3.4 shows that an initial comparison of the non-relativistic disc model `DISKBB` to its relativistic counterpart `KERRBB` was inconclusive in the context of treating the trend in L_{Disc} - T_{Disc} previously reported by Dunn et al. [2010]. Adopting a relativistic model where the inner disc radius was left free to vary with `KYNBB` provided a significant recovery to the L_{Disc} - T_{Disc} trend observed by `DISKBB` and `KERRBB` for GRO J1655-40 while the disc temperature for the rest of the sample remained dominantly unchanged with only 3% of increase on average. The observations corresponding to these observed deviations were moved to lower temperatures matching other observations with similar $L_{\mathrm{Disc}}/L_{\mathrm{Edd}}$ values. We also observed more scattering in the trend possibly due to R_{in} being an additional free parameter, causing larger deviations in the scatter compared to `DISKBB` and `KERRBB`.

3.4.4 Inner Disc Radius R_{in} and Disc Temperature T_{in}

Our first attempt at spectral analysis for GRO J1655-40 using `KERRBB` with a fixed spin produced significantly high χ^2/d.o.f. values for ~ 89% of our sample. We didn't find a certain spin value the fit favoured significantly in terms of the goodness of the fit with the model. We explored the parameter space of `KERRBB` to better understand the nature of the source that would mimic a changing spin scenario by first attempting to fix the spin parameter at 0.7 following Shafee et al. [2006], Stuchlík and Kološ [2016] and leave the normalisation free throughout the sample. This allowed us to have a global spin value for the sample but revealed a big variation in the normalisation values. The normalisation parameter of `KERRBB` is sensitive to uncertainties in the black hole mass, distance to the source and the inclination angle of the system. However, such a great variation in the normalisation cannot be explained by uncertainties in these parameters of the model and shouldn't be different on this scale for each observation. Considering the core assumption of `KERRBB` that the position of R_{in} always terminates at R_{ISCO} and dependence of R_{ISCO} on the black hole mass in equation (3.2.1), we interpret this as a strong indication for changing inner disc radius throughout the outburst. As a result, our attempt to fit the entire outburst with a fixed global spin parameter with `KERRBB` produced significantly poorer fits compared to different combinations of free parameters we applied before. We then analysed the same set of spectra with `KYNBB` replacing `KERRBB` with R_{in} as a free parameter. We found the same trend in the evolution of the inner disc radius both with `DISKBB` and `KYNBB` and the spin parameter measured by `KERRBB` showed to be in the expected reverse trend throughout the outburst. We present this change in

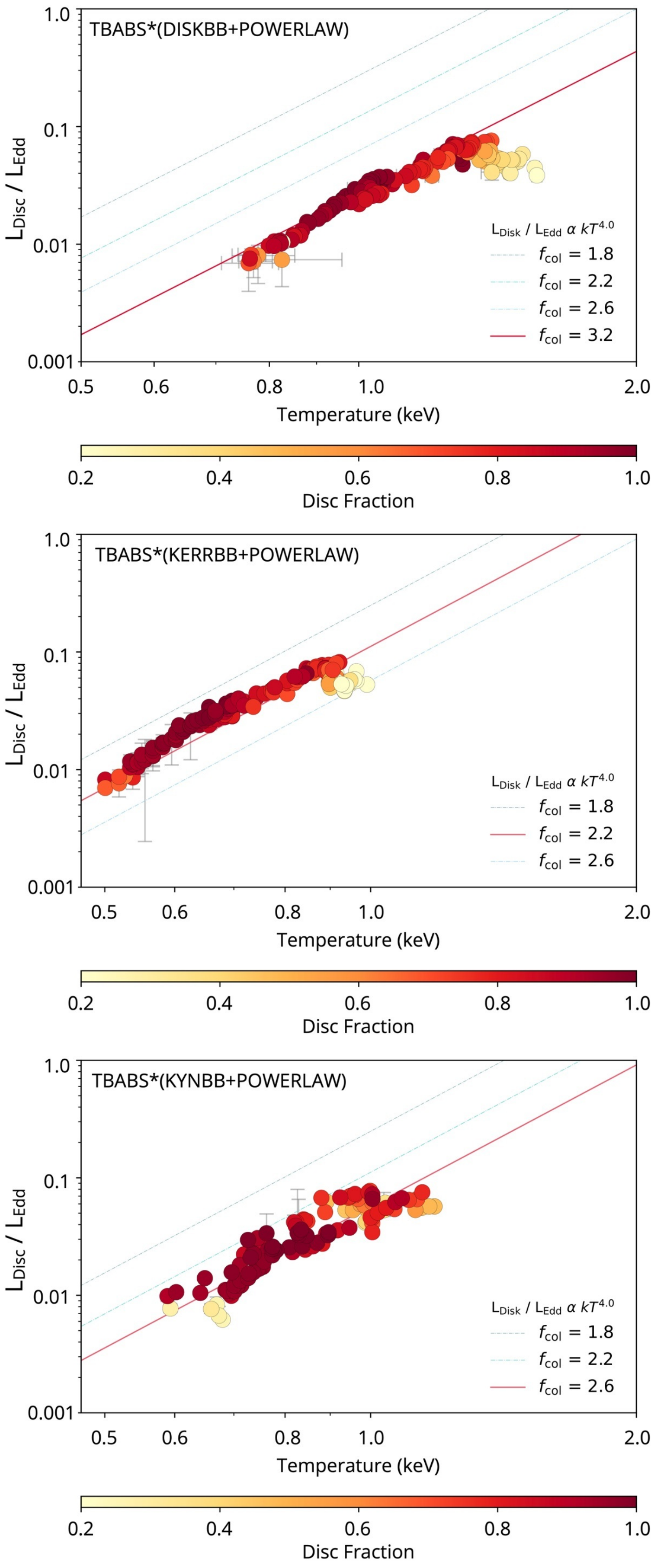

Figure 3.4: *Top*: Change in disc luminosity with respect to disc temperature for GRO J1655-40 as measured by `DISKBB`, *Middle*: Change in disc luminosity with respect to disc temperature for GRO J1655-40 as measured by `KERRBB`, *Bottom*: Change in disc luminosity with respect to disc temperature for GRO J1655-40 as measured by `KYNBB`

the measured dimensionless spin parameter with respect to time in the top panel of Figure 3.5 in comparison with the change in disc radius measured by `DISKBB` and `KYNBB` (middle and bottom panels, respectively).

We also investigated the relationship between the inner disc radius and the disc temperature using `DISKBB` and `KYNBB`, comparing these results for both non-relativistic and relativistic accretion disc models. As expected, our results showed that $R_{\rm in}$ measurements calculated from the normalisation of `DISKBB` correspond to physically unrealistic values that are way beyond the $R_{\rm ISCO}$ even for a Kerr black hole with $a_* = 0.98$ (Figure 3.6) for the big majority of the observations. It is important to note that this method of inner disc radius calculation is still affected by uncertainties in measurements of the inclination angle of the disc and distance to the source. However, subtle changes in these parameters aren't expected to produce such small values for $R_{\rm in}$ in comparison with $R_{\rm ISCO}$ values calculated for different spin parameters, occasionally reaching a scale of having an accretion disc with its inner edge extending down to the event horizon for a Schwarzschild black hole.

Our analysis with `KYNBB`, however, revealed much larger radii corresponding well above $R_{\rm ISCO}$ for $a_* = 0.7$. We observed a very similar pattern for the changes in the inner disc radius to the results from `DISKBB` but with values that are at least 5 times larger on average. Except for two observations, all measurements corresponded to regions with $R_{\rm in} > R_{\rm ISCO}$ for all spin values. In addition to significantly larger values, these results also cover a much wider parameter range (50-150 km) compared to `DISKBB` (10-25 km).

Since `KERRBB` assumes that $R_{\rm in}$ always extends down to $R_{\rm ISCO}$, we compared the $R_{\rm ISCO}$ values obtained from spin measurements and obtained values 50% higher on average than $R_{\rm in}$ values derived from `DISKBB`. We also investigated the evolution of $R_{\rm in}$ with respect to $T_{\rm in}$ throughout all of the outbursts of LMC X-3. LMC X-3 is not observed to follow a similar trend as observed by `KERRBB` and `KYNBB` for GRO J1655-40 while similar shifts in values of $R_{\rm in}$ and $T_{\rm in}$ can be observed in Figure 3.7.

3.4.5 Colour Correction Factor $f_{\rm col}$

Using `KERRBB`, we investigated the evolution of $f_{\rm col}$ throughout the 2005 outburst of GRO J1655-40, allowing it to respond to changes in the accretion disc temperature with changing accretion states, following the discussion by Salvesen et al. [2013] on using $f_{\rm col}$ as an alternative to the disc truncation scenario during the state transitions in black hole X-ray binaries. We fixed the spin at 0.7 during this analysis but did not observe the same improvement to the $L_{\rm Disc}$ - $T_{\rm Disc}$ trend to match the reduced χ^2 selection criteria as we observed in the previous analysis with spin as a free parameter, in an analogy to changing inner disc radius as discussed in Section 3.4.4. We obtained values for $f_{\rm col}$ covering a range between 1.09-2.12 throughout the outburst. In contrast to the discussion by Reynolds and Miller [2013], Salvesen and Miller [2021], we observed a trend where $f_{\rm col}$ increases with decreasing hardness ratio suggesting a positive correlation between changes in accretion state throughout the outburst and the need for a changing correction factor. We also observed an increase in $f_{\rm col}$ with an increasing accretion rate and $L_{\rm Disc}/L_{\rm Edd}$ with a turnover at $f_{\rm col} \sim 1.6$ where the accretion rate and

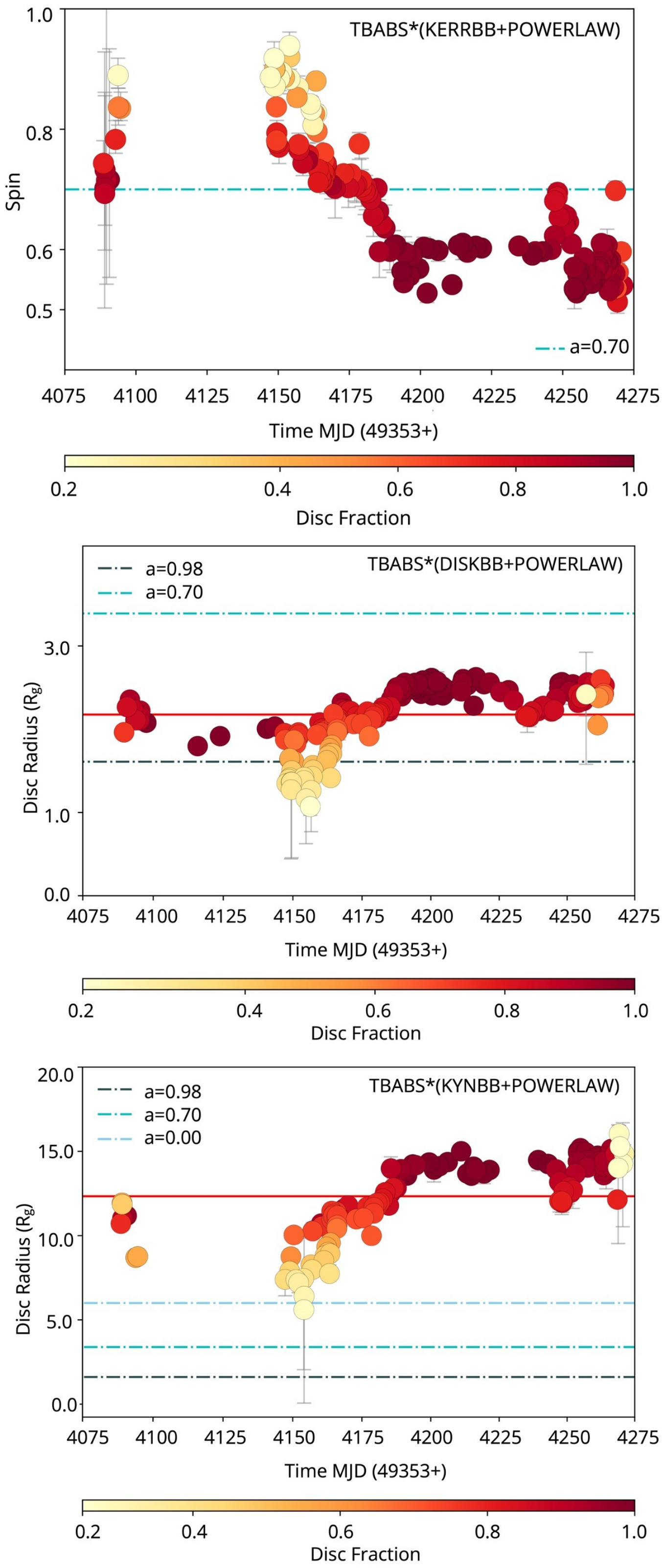

Figure 3.5: *Top*: Change in the spin measurements with respect to time for GRO J1655-40 as measured by `KERRBB`, *Middle*: change in the disc radius measurements with respect to time as measured by `DISKBB` in units of R_g, *Bottom*: Change in the disc radius measurements with respect to time for GRO J1655-40 as measured by `KYNBB` in units of R_g. Red vertical solid lines in the middle and bottom plots indicate the average of the measured inner disc radius values.

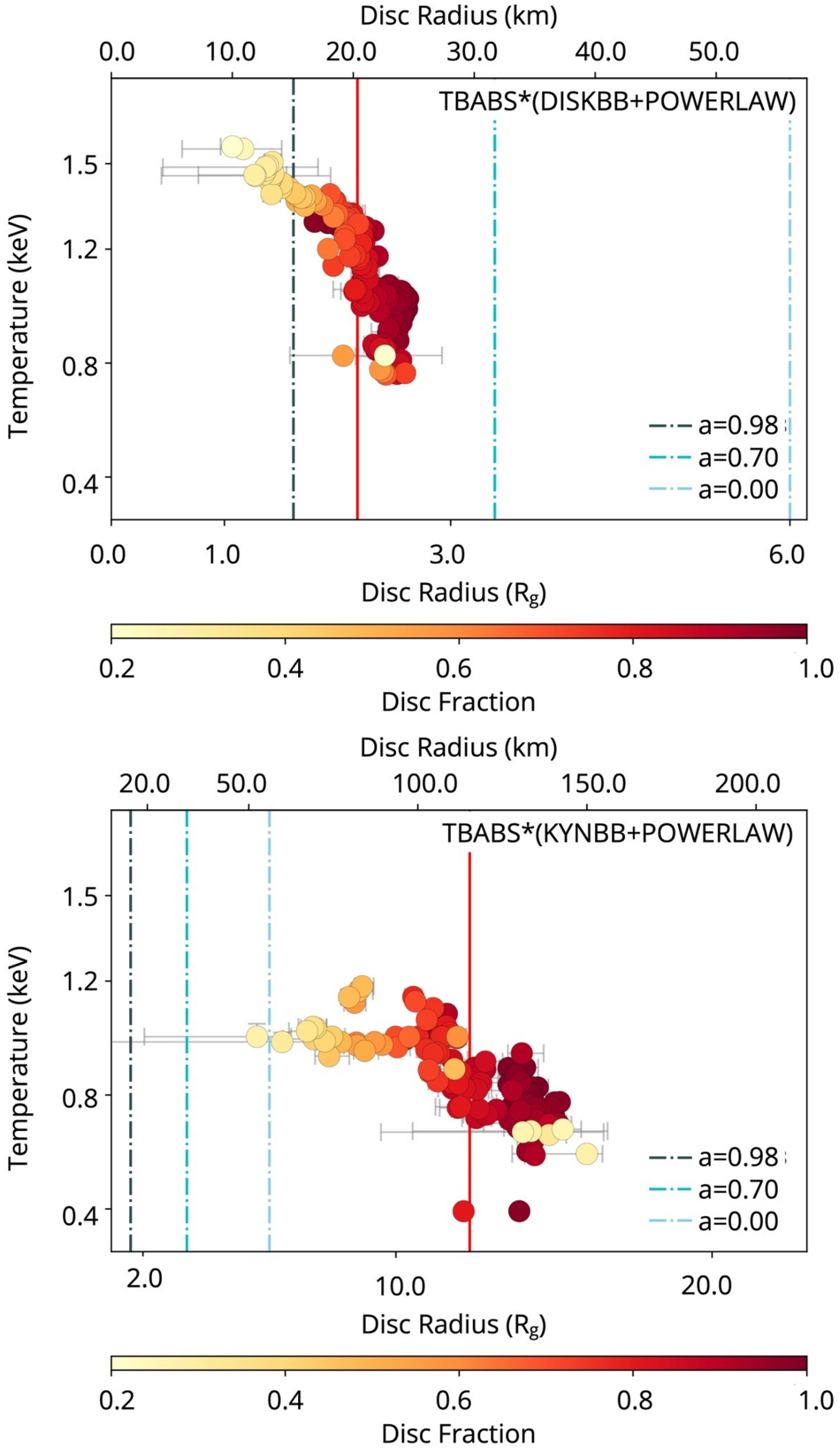

Figure 3.6: *Top*: Relationship between the inner disc radii and the disc temperature for GRO J1655-40 as measured by `DISKBB` in units of R_g *Bottom*: Relationship between the inner disc radii and the disc temperature for GRO J1655-40 as measured by `KYNBB` in units of R_g. Dashed lines correspond to R_{ISCO} values for the spin parameter at 0.0, 0.7 and 0.98, respectively. Red vertical solid lines indicate the average of the measured inner disc radius values.

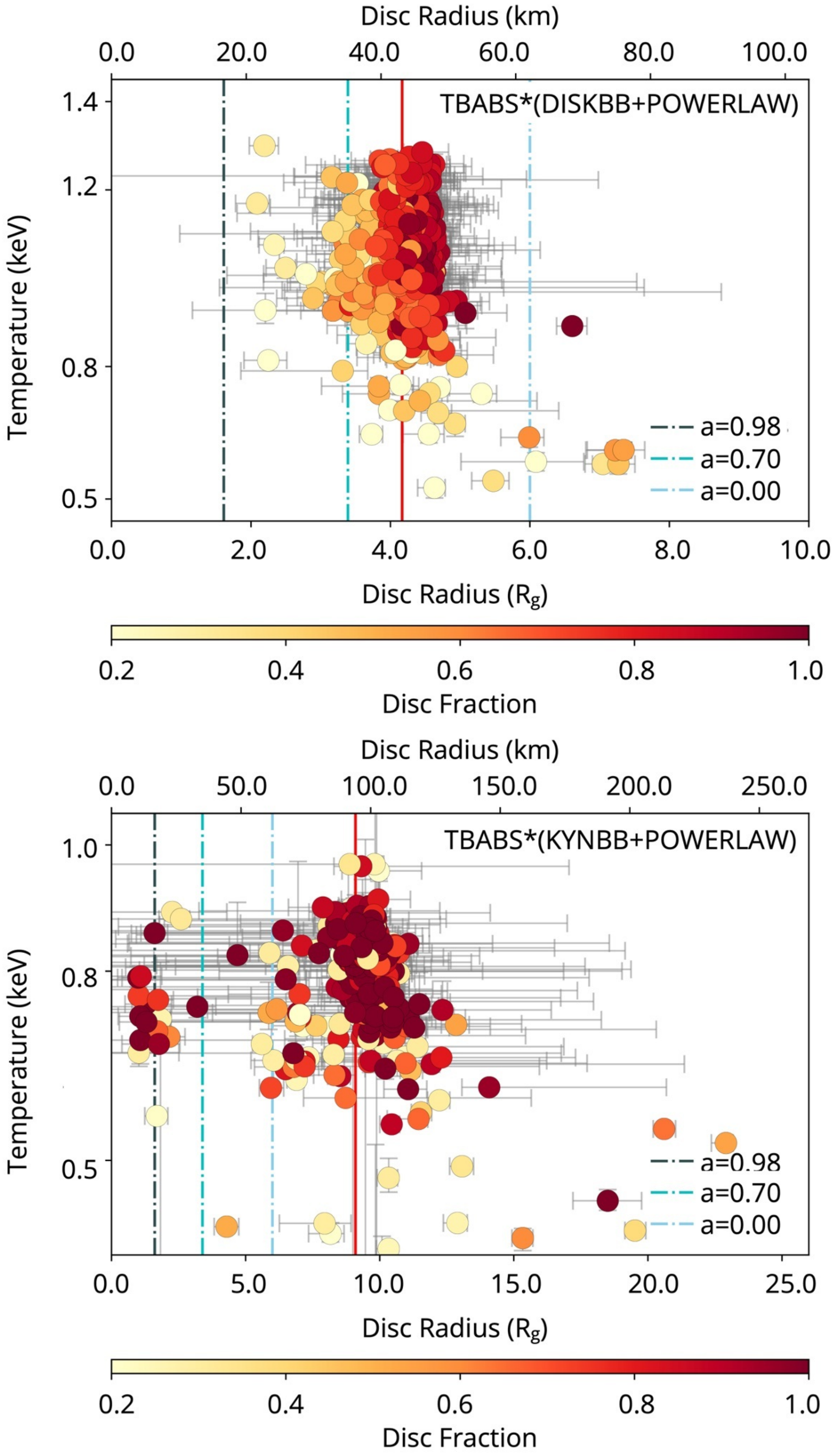

Figure 3.7: *Top*: Change in the inner disc radii with respect to disc temperature for LMC X-3 as measured by `DISKBB` in units of km *Bottom*: Change in the inner disc radii with respect to disc temperature for LMC X-3 as measured by `KYNBB` in units of R_g. Red vertical solid lines indicate the average of the measured inner disc radius values.

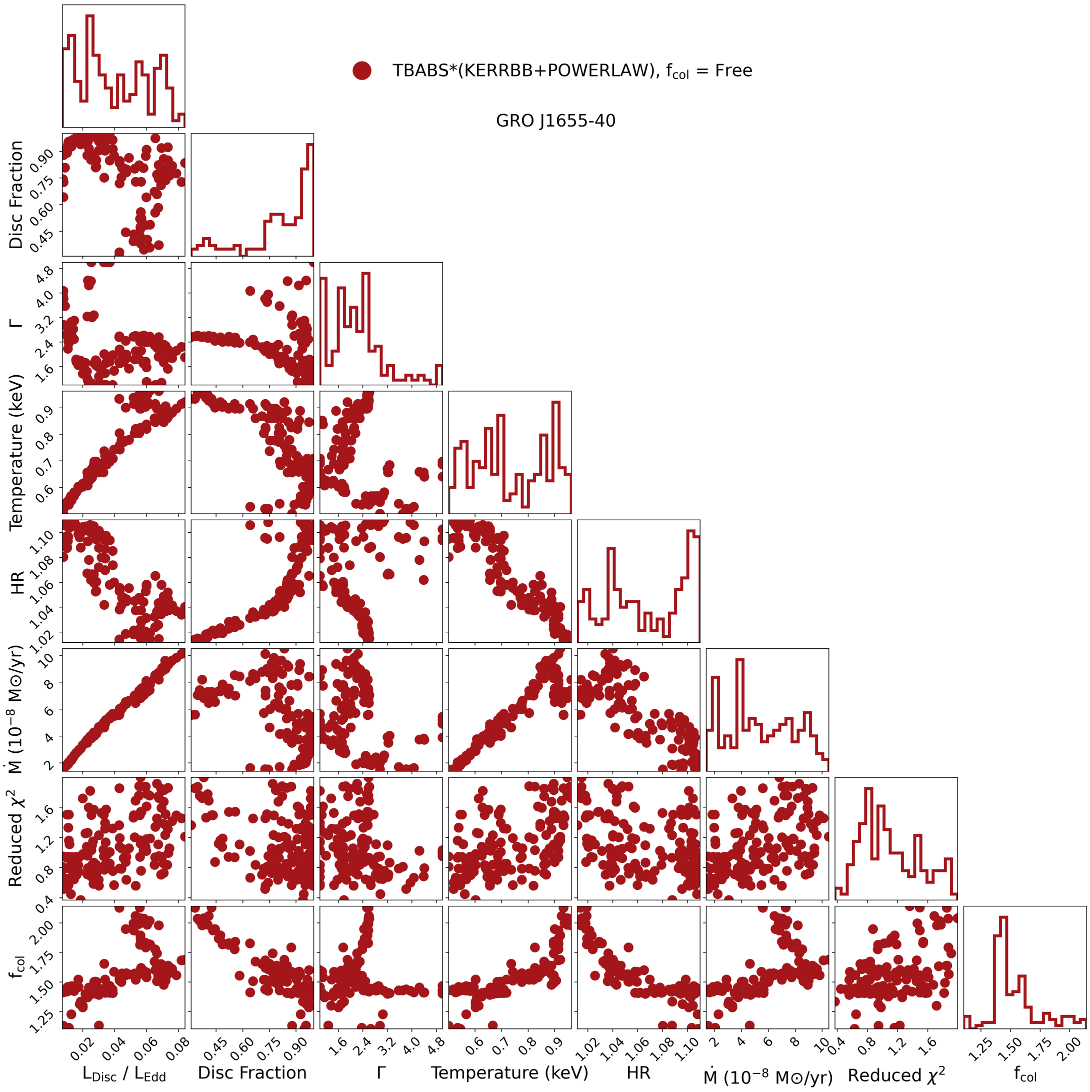

Figure 3.8: Corner plot showing the evolution of the parameters from our analysis with f_{col} as a free parameter in `KERRBB` for GRO J1655-40.

$L_{\mathrm{Disc}}/L_{\mathrm{Edd}}$ start to decrease until $L_{\mathrm{Disc}}/L_{\mathrm{Edd}} \sim 0.04$ with increasing f_{col}, finally reaching $f_{\mathrm{col}} = 2.12$. This turnover occurs with the observations corresponding to the ”spurs” in the top two panels of Figure 3.4. Figure 3.8 shows the corner plot presenting the evolution of the parameters from our analysis with f_{col} as a free parameter. In this analysis, we were able to have a global spin parameter and a steady R_{ISCO} throughout the outburst of GRO J1655-40 in a similar way observed with variable R_{in} in our previous analysis with `KYNBB` and observed comparably similar χ^2/d.o.f. values (within less than %1 of difference).

3.4.6 Spin Measurements

GRO J1655-40

Our initial analysis with `KERRBB` across the entire 2005 outburst was based on individual fits of each observation with the spin as a free parameter. We present the distribution of values of the spin parameter measured by `KERRBB` for both GRO J1655-40 and LMC X-3 in Figure 3.9. The parameter space for the spin spanned values between $0.5 < a_* < 0.9$ with a mean at $a_* = 0.676$. However, such a wide range of parameter values for the spin is not expected to be observed for a black hole even when the statistical deviations arising from the fitting procedure are taken into account. Considering the dependency of spin measurements using the X-ray continuum fitting method on the modelling of the innermost accretion disc and the accretion state, we selected the part of the spectrum where the outburst is on the rise towards and including the HSS. We calculated the hardness ratios (HR) for the entire 2005 outburst where

$$\text{Hardness Ratio(HR)} = \frac{\text{Flux}(6.0 - 25.0\,\text{keV})}{\text{Flux}(3.0 - 6.0\,\text{keV})} \tag{3.4.3}$$

Based on the evolution of HR throughout the outburst, we selected a subset of 56 observations with HR < 0.8 and $0.05 < L_{\text{Disc}}/L_{\text{Edd}} < 0.09$. To eliminate any dependencies on other components in the spectra at higher energies, we limited the energy ranges to 3.0-6.0 keV. We fit the subset with a free global spin parameter and left the accretion rate and powerlaw component free to vary throughout the sample. We obtained a spin parameter $a_* = 0.79^{+0.012}_{-0.005}$ with χ^2/d.o.f. = 543.28/446. Using the same subset of observations, we obtain a spin parameter $a_* = 0.74 \pm 0.002$ with `KYNBB`. Both values are consistent with the results reported by Shafee et al. [2006] ($0.65 < a_* < 0.75$ and $a_* \sim 0.75$ for RXTE and ASCA observations of the 1997 outburst, respectively). The small difference in the measured value by `KERRBB` most likely arises from the different set of observations used and free f_{col} used in their analysis with `KERRBB` (see Section 3.5.3 for more discussion on f_{col} and spin measurements). Additionally, we emphasise that the actual distribution of the spin parameter obtained from individual fits spans a larger range of values between $0.5 < a_* < 0.9$ than the errors estimated by the global fitting of multiple observations and a more realistic distribution of the parameter could be seen from Figure 3.9. To be able to obtain a better description of the parameter space of the measured spin from the observations used for the global fit with Xspec, we utilize the nested sampling Monte Carlo algorithm MLFriends [Buchner et al., 2014, Buchner, 2019] using the UltraNest[6] package [Buchner, 2021] to explore the intrinsic distribution with asymmetric error bars and resample the data points using these error bars. We then assume a Gaussian distribution and obtain the mean and scatter of the distribution ($a_* = 0.774 \pm 0.069$ and $a_* = 0.752 \pm 0.061$ for `KERRBB` and `KYNBB`, respectively). We, therefore, suggest caution when taking smaller-scale error margins obtained from the global fit into consideration.

LMC X-3

Initial analysis of the entire sample of observations with `KERRBB` with spin as a free parameter throughout the entire sample of observations revealed dominantly constant spin values with a mean at $a_* = 0.106$. As previously reported by Torpin et al. [2017], LMC X-3 does not follow the traditional q-shape in the HID as a consequence of its almost ”always on” behaviour. They observed different patterns

---

[6] `https://johannesbuchner.github.io/UltraNest/`

for different cycles as observed by RXTE PCA between 2004-2012. Due to its intrinsically different nature with $L_{\rm Disc}/L_{\rm Edd}$ spanning a much larger parameter space from ~ 0.01 and ~ 0.5 compared to GRO J1655-40 where the system reached $0.082 L_{\rm Disc}/L_{\rm Edd}$ in the highest state, we followed the time evolution of $L_{\rm Disc}/L_{\rm Edd}$ throughout our entire sample (Table 4.1) to define different selection criteria. For simultaneous fitting of LMC X-3, due to the long computational time required for fitting more than 800 spectra with `KERRBB`, we selected a subset of 72 spectra from one cycle where the observations were dominantly in the soft state with HR < 0.5 and $0.1 < L_{\rm Disc}/L_{\rm Edd} < 0.3$. We restricted the energy range of the fit to 3.0-6.0 keV and measured the spin at $a_* = 0.112^{+0.003}_{-0.021}$ with χ^2/d.o.f. = 296.90/215. We tested the two different spin cases as reported by Straub et al. [2011] and Steiner et al. [2014] and compared these fits with our result $a_* = 0.112^{+0.003}_{-0.021}$. We found that the fit favoured the lower spin case with $a_* = 0.1$ over $a_* \sim 0.6$ or $a_* \sim 0.25$ with much lower χ^2/d.o.f. throughout the entire sample while $a_* = 0.1$ is still consistent with the error margin provided by Steiner et al. [2014] ($a_* = 0.25^{0.20}_{0.29}$). We also analysed the same set of observations with `KYNBB` and obtained consistent results while leaving the inner disc radius as a free parameter introduced a larger uncertainty on the measured black hole spin which lead to a value of $a_* = 0.6^{+0.004}_{-0.005}$, in contrast to the low spin case observed by `KERRBB` and previously reported by Steiner et al. [2014]. Similar to spin measurements of GRO J1655-40, these errors estimated on the black hole spin are considerably small compared to the distribution of measured spin values from individual fits and a more realistic distribution of the parameter could be seen from Figure 3.9. We employed the same approach as described in Section 3.4.6 and obtained $a_* \sim 0.098 \pm 0.063$ for `KERRBB`. We again suggest caution when considering significantly smaller-scale error margins obtained from global fitting with Xspec.

Yilmaz et al. [2023] provides an extensive analysis of the 2005 outburst of GRO J1655-40 using the same observations presented in Table 4.1 to compare `KERRBB` and `KYNBB` when the innermost edge in `KYNBB` is set at ISCO and showed that both models are identical and the minor differences in the measured parameter values between `KERRBB` and `KYNBB` can be explained by small statistical fluctuations arising from the fitting procedure with Xspec. While GRO J1655-40 provided an ideal set of observations to study the differences as a result of changing boundary conditions when the inner edge of the disc is no longer at ISCO, this significant difference in the measured black hole spin by `KERRBB` and `KYNBB` with $R_{in} > R_{ISCO}$ can be explained by the larger error margins in the measured inner disc radii introduced by the reduced signal-to-noise ratio of LMC X-3 spectra due to its distance when combined with the instrumental uncertainties. It is, therefore, to be taken into consideration with caution.

This contrast in the measured spin by `KERRBB` (when compared with Straub et al. [2011]) is dominantly due to the difference in the assumed black hole mass and inclination angle in the analysis. Before a more constrained update was provided by Orosz et al. [2014], the study of the inner disc radius and spin measurements by Steiner et al. [2010] and Straub et al. [2011], respectively, was based on a mass of $M_{\rm BH} = 10 M_\odot$. In this study, we adopt the more recent value of $M_{\rm BH} = 6.98 \pm 0.56 M_\odot$. We tested the effect of this difference by setting black hole mass in the analysis described above with `KERRBB` to $M_{\rm BH} = 10 M_\odot$ and we

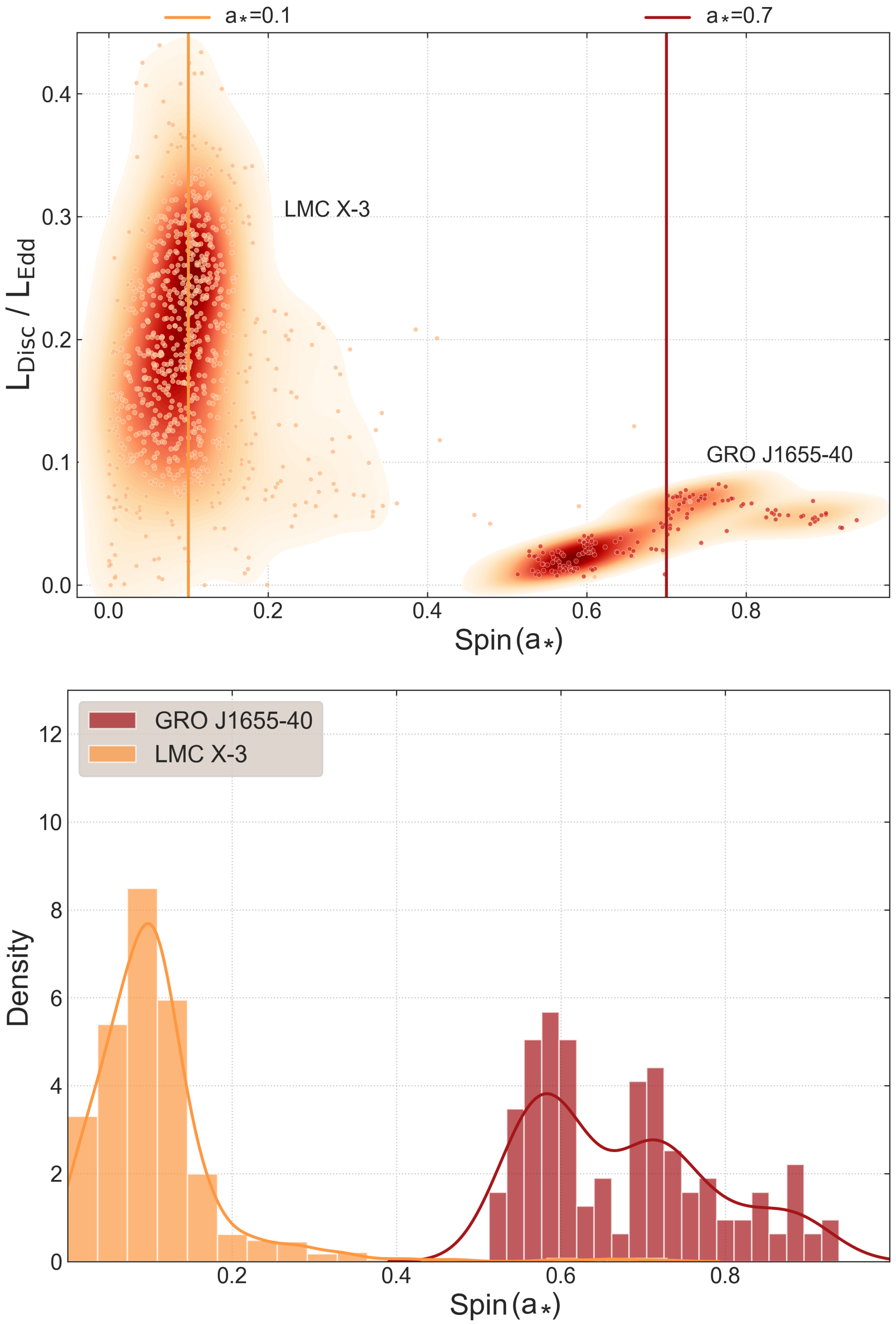

Figure 3.9: *Top*: Evolution of the measured spin values with respect to $L_{\mathrm{Disc}}/L_{\mathrm{Edd}}$ obtained by fitting with `KERRBB` for LMC X-3 (left) and GRO J1655-40 (right) throughout the entire set of observations listed in Table 4.1. *Bottom*: Distribution of the black hole spin values as measured by fitting with `KERRBB` for LMC X-3 (orange) and GRO J1655-40 (red) throughout the entire set of observations described in Section 3.3.5.

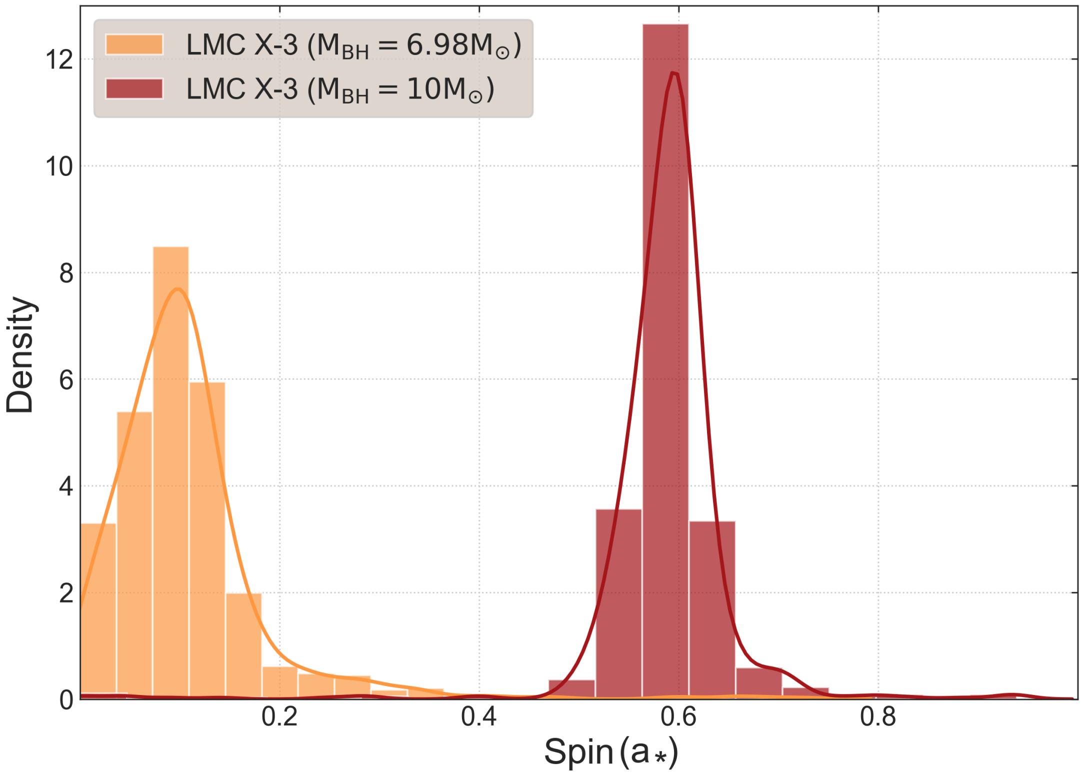

Figure 3.10: Distribution of black hole spin values as measured by `TBABS×(KERRBB+POWERLAW)` throughout the entire set of observations of LMC X-3 for $M_{\rm BH} = 6.98M_{\odot}$ (orange) and $M_{\rm BH} = 10M_{\odot}$ (red).

obtained $a_* = 0.601^{+0.011}_{-0.009}$. On the other hand, the effect of inclination angle was not as strong in the measured spin for $M_{\rm BH} = 6.98M_{\odot}$. Similar to the analysis described previously, we didn't observe the same deviations in the measured spin as previously reported by Straub et al. [2011]. Figure 3.10 shows the difference in the distribution of black hole spin parameter as measured by `KERRBB` throughout the entire set of observations of LMC X-3 for two black hole masses ($M_{\rm BH} = 6.98M_{\odot}$ (orange) and $M_{\rm BH} = 10M_{\odot}$ (red)).

3.5 DISCUSSION

We investigated the evolution of the accretion discs throughout multiple outbursts of GRO J1655-40 and LMC X-3 by analysing $\sim$ 1800 spectra obtained using RXTE with a wide range of disc luminosities of $1.0 \times 10^{-4} < L_{\rm Disc}/L_{\rm Edd} < 0.5$.

`DISKBB` has been used extensively in many spectral studies of accretion discs in BHXRBs and was found to provide a significantly reasonable approximation for the spectral shape of a geometrically thin and optically thick Newtonian Shakura and Sunyaev [1973] disc. It was criticized by Gierliński et al. [2001] for ignoring the inner torque-free boundary condition at the inner edge of the accretion disc. This non-zero torque assumption at the inner boundary of the accretion disc was put into test by Zimmerman et al. [2005] where they presented a comparison of `DISKBB` with its zero-torque counterpart `EZDISKBB`. They showed that `DISKBB` temperature

($T_{\max}$) values were $\approx 5\%$ higher on average than those obtained by fitting with `EZDISKBB`. In contrast, they observed higher values for R_{in} with `DISKBB` by more than a factor of ~ 2.17 on average. They showed that the application of a zero-torque boundary condition has little to no effect on an accretion disc temperature peaking at ~ 1.8 keV as observed in GRO J1655-40 with `DISKBB` while the biggest impact is on the inner accretion disc radius.

In comparison to the relativistic disc models, `DISKBB` was shown to produce significantly higher disc temperatures for two main reasons:

1. It assumes a perfect blackbody emission from the accretion disc independent of the accretion state the system is in, not accounting for non-blackbody emission arising from the complicated scatterings in the accretion disc atmosphere. This assumption essentially means $f_{\text{col}} = 1.0$ for the fit while in $f_{\text{col}} \sim 1.7$ is widely accepted to provide a correction to deviations of the local accretion disc spectrum from the "perfect blackbody" emission for the unaccounted scattering and Comptonisation processes in the disc atmosphere.

2. `DISKBB` provides a relatively simplistic description of a multi-colour accretion disc without any general relativistic effects accounting for strong gravitational fields around black holes. These relativistic effects include frame-dragging, returning radiation, Doppler boost, gravitational redshift, self-irradiation etc. which are needed to provide a better solution for the emitted spectrum from the innermost region of the accretion disc around a black hole of any mass. These corrections modify the calculated local specific intensity as the photons escape the gravitational potential of the black hole and eventually reach the observer. Before any relativistic corrections to `DISKBB` were made available, some attempts have been made to adopt the correction by Zhang et al. [1997] to the observed temperature while Li et al. [2005] compared the results of such applications with four disc models and found that the approach was still lacking in the treatment of relativistic processes on the calculated spectra.

Our investigation showed that a simple change from the non-relativistic model `DISKBB` to `KERRBB` did not improve the trend except for a significant decrease in the disc temperatures throughout the outburst. This trend was significantly improved by employing `KYNBB` with R_{in} allowed to vary with the state transitions. This behaviour suggests a dominating power of R_{in} in combination with general relativistic effects for the states with the smallest measured inner disc radii. For these states, `KERRBB` measured spin values as high as $0.8 < a_* < 0.98$ which correspond to a region $1.6\,R_{\text{g}} < R_{\text{ISCO}} < 2.9\,R_{\text{g}}$.

RXTE stood out as one of the most successful X-ray missions in the study of stellar-mass black holes in X-ray binaries but possesses a limiting factor due to its limited energy resolution and poor effective area at lower energies where the thermal emission from the accretion disc is expected to peak. It has an advantageous position in the field with its ability to observe a significant number of sources throughout many outbursts making it an important tool for the purpose of studying the evolution of accretion states in black hole X-ray binaries. RXTE PCA is sensitive to energy ranges above ~ 3 keV. This still corresponds to a range where the tail of the thermal emission can be modelled with `DISKBB` as the source transitions to the HSS throughout the outburst while it can be extended to around 6-7 keV with its relativistic counterparts `KERRBB` and `KYNBB`. To test the effects of these instrumental limitations, we made use of 6 out of 39 publicly available Swift observations of GRO J1655-40 which could be modelled by the same model setups adopted throughout our analysis and obtained consistent results in the parameter values presented in this work. Additional to Swift observations, we made use of INTEGRAL/ISGRI which is much better calibrated at higher energies to test the effect of the contribution of high energy emission on measured parameter values. We used 6 sets of observations obtained simultaneously to compare the measured parameter values of disc temperatures, disc radii and spin using `DISKBB` and `KERRBB` and obtained consistent values. For simplicity, we exclude these observations from further discussion.

X-ray continuum fitting method to measure the spin depends on determining the inner edge of the accretion disc $R_{\rm in}$ based on the assumption that the disc always extends down to the $R_{\rm ISCO}$ in the HSS and inferring the spin using equation (3.2.1). However, this method has its limitations even after careful treatment of $f_{\rm col}$. Even though the most commonly accepted value of $f_{\rm col}$ stands at 1.7, the precise determination of this correction factor for each observed accretion state still prevails to be beyond the bounds of what current instruments and methods allow. Both `KERRBB` and `KYNBB` depend on how precisely the mass, inclination angle and distance to the source are measured. Our analysis of GRO J1655-40 with `KYNBB` showed a wide range of inner disc radii. While these radii are observed to be much larger than $R_{\rm ISCO}$ for $0.8 < a_* < 1.0$, it's worth keeping in mind that these observations were obtained using RXTE PCA spectra limited to 3.0-25.0 keV which delivers extra uncertainties to these measurements. The much larger scatter in $R_{\rm in}$ vs Temperature can be interpreted as these uncertainties since measuring the inner disc radius with much lower temperatures than previously observed will be compromised by PCA's limited energy range.

3.5.1 Comparing GRO J1655-40 and LMC X-3

Both GRO J1655-40 and LMC X-3 are ideal candidates to study the evolution of accretion discs around black holes in XRBs. Both are known to harbour a black hole of similar mass and have similar inclination angles (Table 3.1). LMC X-3 stood out as a perfect source for black hole spin measurements due to its dominantly stable inner disc radius. Our analysis of LMC X-3's inner disc radius with `DISKBB` and `KYNBB` yielded consistent results to previous studies (Figure 3.7). Despite this large difference in $\dot{M}$, the innermost edge of the accretion disc doesn't show as much variance as observed from GRO J1655-40. LMC X-3 also doesn't show the reported "spurs" in $L_{\rm Disc}$ - $T_{\rm Disc}$ in contrast to GRO J1655-40 and other BHXRBs reported by Dunn et al. [2011]. Considering the changes to this relationship introduced by relativistic modelling of the accretion disc using `KYNBB` with free $R_{\rm in}$ (Figure 3.4), this can indicate either a strong dependency on the inner disc radius evolution or weaker relativistic effects acting on the observed spectrum due to the low spin of LMC X-3 and the accretion disc being truncated at larger radii (Figure 3.7).

Each corner plot in Figure 3.12 shows the evolution of relevant parameters in our analysis with `TBABS`×`(DISKBB+POWERLAW)`, `TBABS`×`(KERRBB+POWERLAW)` and

`TBABS×(KYNBB+POWERLAW)` for GRO J1655-40 (red) and LMC X-3 (orange), respectively. Independent of the nature of the disc model, RXTE observations of LMC X-3 have shown that the source evolves through a larger parameter range for both $L_{\rm Disc}$ and $\dot{M}$ compared to GRO J1655-40. This larger parameter range translates to a difference in $\dot{M}$ by about an order of magnitude for both `KERRBB` and `KYNBB`. Both GRO J1655-40 and LMC X-3 were observed to show changes in the inner disc temperature $T_{\rm Disc}$ throughout the entire set of observations, covering multiple accretion states. While this change in $T_{\rm Disc}$ was directly reflected in the evolution of $R_{\rm in}$ in GRO J1655-40, a similar evolution was not observed for LMC X-3 with both `DISKBB` and `KYNBB`. There's a clear trend between the disc fraction and $T_{\rm Disc}$ for GRO J1655-40 however, it's not easy to observe a clear trend in disc fraction with respect to any other parameters for all of the models described above. We also acknowledge the unexpected inverse relationship between the disc fractions and measured $R_{\rm in}$. According to the standard scenario describing the evolution of thermal and non-thermal components, smaller disc radii are expected to correspond to more disc-dominated states while a disc truncated at a larger distance is usually associated with a powerlaw-dominated state. Our analysis showed a direct relationship between the hardness ratio and disc fractions where increasing disc fractions correspond to higher hardness ratios. While we observed a similar during the entirety of our analysis, we present it only in Figure 3.8 and exclude this evolution for each model to avoid increasing the complexity of the parameter space presented in each corner plot. This trend is not naturally expected and might be explained by a powerlaw component dominating the disc emission when extrapolated to lower energies for a specific photon index while both the spectral shapes and hardness ratios point towards softer spectra and hence lower hardness ratios in comparison to higher disc fractions. Instead of using the empirical `POWERLAW`, it is usually suggested to adopt a Comptonisation model `SIMPL` [Steiner et al., 2009] to overcome this divergence of the powerlaw component at lower energies, though a simple interchange of these models produced worse fits for the majority of our sample. Therefore, a detailed investigation of the powerlaw component is out of the scope of the analysis presented here.

Regardless of the contrasting measurements of the black hole spin reported over the past decade for LMC X-3 (see discussion in Section 3.3), our results show a polarized distribution of the spin parameter across observations (Figure 3.9). The distribution of the measured spin values of LMC X-3 is more concentrated at around ~ 0.1 while GRO J1655-40 shows a bimodal distribution of the spin parameter throughout the entire outburst. This bi-modality in measured spin values of GRO J1655-40 corresponds to the two sets of observations that can be grouped by whether these observations are on the expected $L_{\rm Disc}$ - $T_{\rm Disc}$ line or the so-called "spurs". The higher spin case ($a_* \sim$0.8) dominantly corresponds to these "spurs" while the lower end of the distribution ($a_* \sim$0.6) corresponds to the rest of the observations. A more detailed evolution of the spin parameter can be seen from the top plot of Figure 3.5. These spurs are also the observations where the inner edge of the disc is observed to be the closest to the black hole, which can explain the observed high spin by `KERRBB` while disc fractions are significantly lower when compared to the rest of the observations. The absence of such clear evolution in $R_{\rm in}$ in LMC X-3 is observed in a more or less steady black hole spin throughout the entire set of observations covering multiple outbursts. This also could explain the absence of spurs in LMC X-3. From our analysis, it's clear that these spurs are not luminosity dependent and a simple increase in the mass accretion rate or disc luminosity cannot explain their presence in the majority of 25 BHXRBs as presented in Dunn et al. [2011]. The distribution of measured inner disc radii for GRO J1655-40 showed a significant variation in the parameter for similar disc fractions, suggesting the possibility of evolving inner disc even within an accretion state. Our analysis also revealed that the disc might not be extending all the way down the ISCO even in the highest luminosity states. As can be observed from Figure 3.6, the lowest inner disc radius in GRO J1655-40 measured by `KYNBB` is a few gravitational radii away from ISCO for both $a_* \sim 0.7$ and $a_* \sim 0.8$. While constraining $R_{\rm in}$ in LMC X-3 with `KYNBB` was rather difficult, a similar trend was observed in which a significant portion of the values correspond to $R_{\rm in} > R_{\rm ISCO}$ for $a_* \sim 0.1$. This peculiar behaviour of $R_{\rm in}$ introduces strong implications for the reliability of the X-ray spectral continuum method for black hole spin measurements.

A more careful investigation of reduced χ^2 distribution revealed no clear evidence for a bias arising from the selection criteria adopted with a cut at reduced $\chi^2 = 2$ (Figure 3.12). While such investigation could prove to be useful when assessing the presence of emission lines and the appropriate modelling of such features, specific observations with strong Fe emission lines (especially during the 1996-1997 outburst of GRO J1655-40) were excluded to avoid introducing the risk of any selection bias and model dependency.

3.5.2 Relativistic vs. Non-Relativistic $R_{\rm in}$ Measurements

Expectedly, the inner disc radius measurements of GRO J1655-40 from spectral fitting with the non-relativistic disc model `DISKBB` produced results ranging between $\sim$10 and $\sim$30 km throughout the 2005 outburst, much smaller than $R_{\rm ISCO}$ values for $0.0 < a_* < 0.85$ which is the range where all reported spin values obtained from X-ray continuum method lie. With significantly higher disc temperatures, $\sim$10% of the observations yields inner disc radii corresponding to a region as close as $\sim$1-2 $R_{\rm g}$. This region corresponds to a region within $R_{\rm ISCO}$ for a moderately spinning black hole where the matter around the black hole can no longer sustain orbital motion and starts spiralling down to the black hole. While the outer radius of the disc can extend out to hundreds and even thousands of $R_{\rm g}$, inner disc radii residing within this region for the entirety of the outburst covering disc fractions from 0.1 to 1.0 does not produce a physically reasonable picture for the accretion disc geometry even for significantly higher spin parameters. Such small radii from the normalisation of `DISKBB` result from the non-relativistic treatment of the disc and not accounting for the non-blackbody emission due to scattering and Comptonisation processes in the accretion disc atmosphere. Changes in disc fractions throughout all of the outbursts demonstrated that even a temperature difference of $\sim$ 0.2 keV becomes significant to increase the disc fraction from $\sim$0.3 to $\sim$0.6 switching from a powerlaw dominated spectrum to a moderately disc-dominated spectrum. Calculated throughout the same outbursts, this difference corresponds to a 50% higher temperatures obtained from `DISKBB` and this results in $\sim$5 times larger inner disc radii.

There have been attempts to include the necessary relativistic corrections following Zhang et al. [1997], Kubota et al. [1998], Gierliński and Done [2004] while the main approach has been focused on a correction applied post-analysis using a constant calculated for a set of certain parameters (See Li et al. [2005] and references therein). While such corrections provide improvements to a certain degree, the post-analysis approach is lacking in the proper application of relativistic corrections as it is based on adopting a factor calculated for a set of parameter values and does not take into account the fact that any relativistic correction should have a strong dependency on the distance to the black hole and hence should correspond to different values for each observation throughout an outburst for sources that are known to exhibit a great evolution of the inner disc radius like GRO J1655-40. On the other hand, taking the example of Kubota et al. [1998], the calculated correction factor values for a set of f_{col} still remain not enough to shift the low values of radii measured by `DISKBB` or similar non-relativistic disc models.

As can be seen from the bottom plot of Figure 3.6, the needed correction is much larger than what was calculated by Zhang et al. [1997], Kubota et al. [1998], Gierliński and Done [2004]. These results suggest that the need for relativistic corrections are much greater than what a simple factor can provide and needs to be handled by self-consistent disc models such as `KERRBB` and `KYNBB` which adopts the ray tracing method with radius-dependent corrections taken into account while calculating the spectrum.

3.5.3 Effects of f_{col} on the Disc Temperature

Apart from the relativistic treatment provided by `KERRBB` and `KYNBB` to the observed spectra from the accretion discs around black holes, f_{col} is the second important parameter that sets relativistic and `DISKBB` apart. This key factor provides the correction to the spectrum to account for electron scatterings in the accretion disc atmosphere causing the spectrum to deviate from the perfect blackbody emission. The need for such a parameter arises where the gas temperature at the surface of the disc is high enough such that the electron scatterings start to dominate over absorptive processes taking place in the disc atmosphere. This corresponds to photon energies ¿ 1.0 keV [Shakura and Sunyaev, 1973]. Both `KERRBB` and `KYNBB` calculate the observed spectrum with f_{col} applied and has this correction factor as a model parameter. Determining a constrained value of the f_{col} through spectral modelling using accretion disc models like `KERRBB` and `KYNBB` is greatly affected by the strong degeneracy between the f_{col} and the black hole spin [Nowak et al., 2008, 2012]. Salvesen and Miller [2021] presented the level of sensitivity of black hole spin measurements using the X-ray spectral continuum method, suggesting a direct relationship between f_{col} and the measured black hole spin. As a result of this degeneracy, it requires extra caution during any attempt to determine the true value of f_{col} for a specific observation in a specific accretion state.

Figure 3.8 shows the relationship between f_{col} and other parameters. We found values of f_{col} spanning the range 1.09-2.12, slightly broader than previously reported 1995 and 1997 ASCA and 1997 RXTE observations of GRO J1655-40 by Shafee et al. [2006] and calculated best-fit values from `BHSPEC` [Davis et al., 2005](1.3-1.9). Our findings in terms of hardness ratio vs. f_{col} contradict the suggested scenario where $f_{\rm col}$ is expected to decrease as the source transitions to softer states to account for a non-truncated disc radius in the LHS [Reynolds and Miller, 2013]. In contrast, we observed a decrease in $f_{\rm col}$ with hardening spectra.

Our analysis showed that adopting the canonical value for $f_{\rm col}(T_{\rm col}/T_{\rm eff})$ at 1.7 following Shimura and Takahara [1995] cannot explain a difference of only 50% in disc temperatures between `DISKBB` and `KERRBB` and/or `KYNBB` on its own. The top panel of Figure 3.4 shows the observed $L_{\rm Disc}$ - $T_{\rm Disc}$ relationship for GRO J1655-40 and dashed lines represent $L_{\rm Disc}/L_{\rm Edd}$ for different $f_{\rm col}$ calculated using equation (3.4.1). $L_{\rm Disc}/L_{\rm Edd}$ - $T_{\rm Disc}$ relationships obtained from both relativistic and non-relativistic disc models corresponded to larger values of $f_{\rm col}$ independent of its set values in `KERRBB` and `KYNBB`. While our analysis with variable $R_{\rm in}$ in `KYNBB` and variable $f_{\rm col}$ in `KERRBB` produced indistinguishable results in reduced χ^2/d.o.f. values, the latter model setup did not provide an improvement to the previously discussed deviations in Figure 3.4.

3.6 SUMMARY

In this paper, we performed a comprehensive spectral analysis of the publicly available RXTE observations of GRO J1655-40 and LMC X-3 between 1996 and 2011, investigating the behaviour of the accretion disc temperature and radius by comparing relativistic and non-relativistic disc models `DISKBB`, `KERRBB` and `KYNBB` with the following conclusions:

1. To test the possible contribution to the emitted spectrum by the general relativistic effects resulting from the strong gravitational potentials in the close vicinity of black holes, we investigated the same RXTE observations of GRO J1655-40 using `KERRBB` and `KYNBB`. Simply adopting `KERRBB` instead of `DISKBB` did not provide any improvements to the deviations in $L_{\rm Disc}$ - $T_{\rm Disc}$ relationship (Section 3.4.3). These deviations, however, were not detected when $R_{\rm in}$ was defined as a free parameter in `KYNBB`.

2. The inner disc radii calculated from the normalisation parameter of the `DISKBB` (see equation (2.4.1)) are systematically lower than the values obtained from the relativistic disc models. `KYNBB` measured much larger inner disc radii throughout the entire outburst of GRO J1655-40 by at least a factor of 6 on average. This difference was even larger for LMC X-3, a factor of ~8 while the uncertainties in these measurements were much larger compared to GRO J1655-40 (Section 3.4.4). These larger uncertainties observed for LMC X-3 can be due to degeneracies between model parameters and poorer quality of spectra with much lower flux values by a factor of 100-1000 (compared to the spectra from the 2005 outburst of GRO J1655-40), on average throughout different accretion states.

3. The colour correction factor $f_{\rm col}$ (with the spin parameter fixed) is found to evolve throughout an outburst spanning a range between 1.0 and 2.2. This evolution follows a pattern where $f_{\rm col}$ increases with increasing accretion rate/Eddington ratio before reaching a turning point at $f_{\rm col} \sim 1.6$ and accretion rate/Eddington ratio starts to decrease with $f_{\rm col}$ still increasing

(Section 3.5.3). Our analysis showed that both $f_{\rm col}$ and $R_{\rm in}$ as free parameters performed equally acceptable when the reduced χ^2/d.o.f. values from each analysis are compared while adopting a variable $f_{\rm col}$ throughout the outburst did not provide the same improvement to the deviations in $L_{\rm Disc}$ - $T_{\rm Disc}$ observed in `DISKBB` and `KERRBB`. This suggests strong support for a scenario where the changing inner disc radius coupled with general relativistic effects to explain these deviations observed in GRO J1655-40.

ACKNOWLEDGMENTS

The authors thank Enrico Bozzo and Carlo Ferrigno for technical support with the analysis of INTEGRAL data and fruitful suggestions and discussions. The research leading to these results has received funding from the European Union's Horizon 2020 Programme under the AHEAD2020 project (grant agreement n. 871158) based on observations with INTEGRAL, an ESA project with instruments and science data centre funded by ESA member states (especially the PI countries: Denmark, France, Germany, Italy, Switzerland, Spain), and with the participation of the Russian Federation and the USA. A.Y. acknowledges the support from GAUK project No. 102323. A.Y. and P.G.B. acknowledge financial support from the Czech Science Foundation under Project No. 19-05599Y. M.B., M.D. and J.S. acknowledge the support from the GACR project 21-06825X. A.Y., P.G.B., M.B., M.D., and J.S. also acknowledge the institutional support from RVO:6798581. The authors also would like to thank the anonymous referee for the valuable and detailed comments and suggestions.

DATA AVAILABILITY

All of the RXTE data used in this paper (see Table 4.1) are publicly available in HEASARC's archive (`https://heasarc.gsfc.nasa.gov/docs/archive.html`).

Appendix

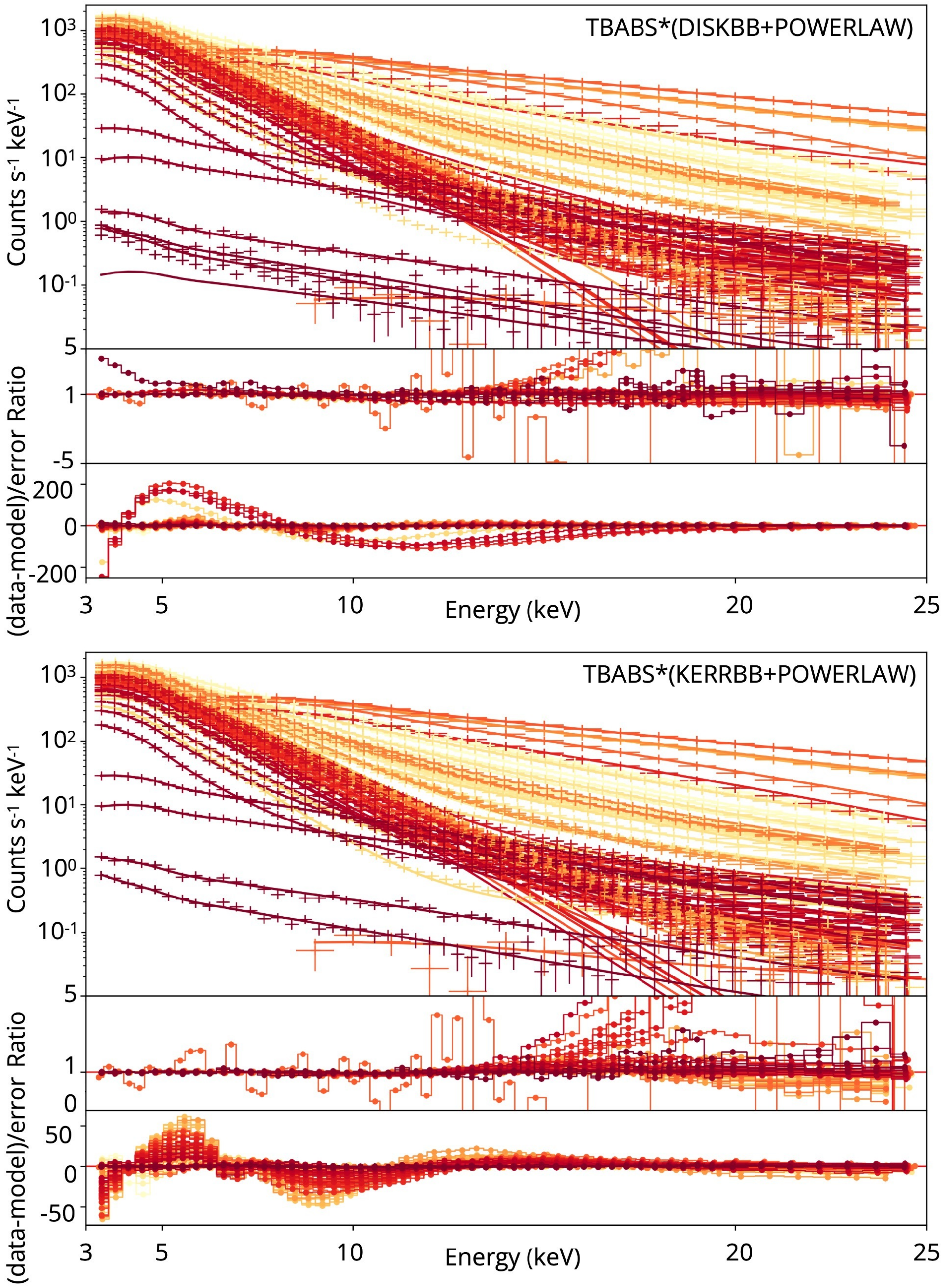

Figure 3.11: *Top*: Data and total model obtained from spectral fitting of GRO J1655-40 during 1996 and 1997 outbursts that produced significantly worse fits with reduced $\chi^2 \gg 2.0$ obtained from spectral fitting with `TBABS`×`(DISKBB+POWERLAW)`, showing the residuals in ratios (data/model) and (data-model)/error below. *Bottom*: Data and total model obtained from spectral fitting of GRO J1655-40 during 1996 and 1997 outbursts that produced significantly worse fits with reduced $\chi^2 \gg 2.0$ obtained from spectral fitting with `TBABS`×`(KERRBB+POWERLAW)`, showing the residuals in ratios (data/model) and (data-model)/error below.

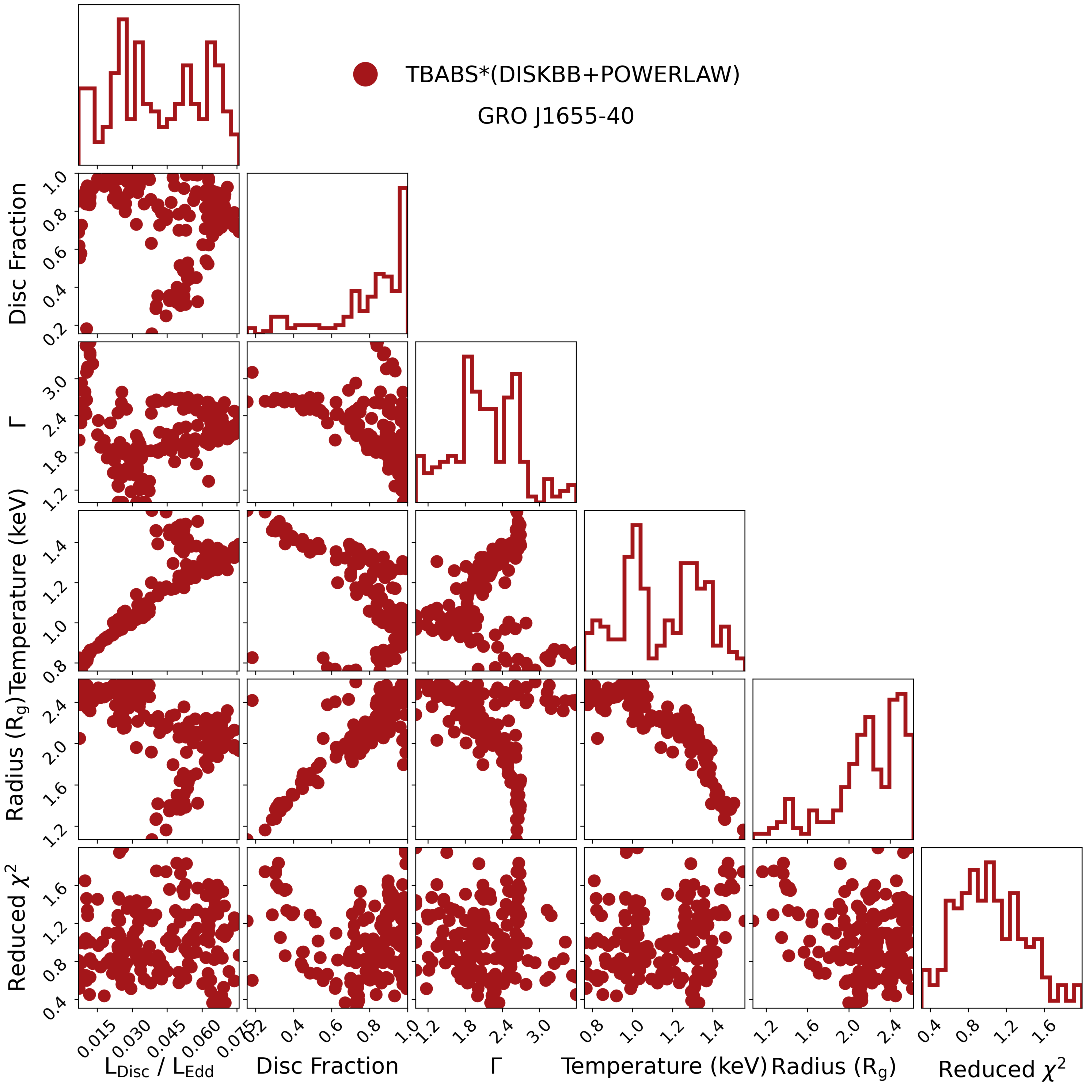

(a) Corner plot showing the evolution of the parameters from our analysis of GRO J1655-40 with `TBABS`×`(DISKBB+POWERLAW)`.

Figure 3.12

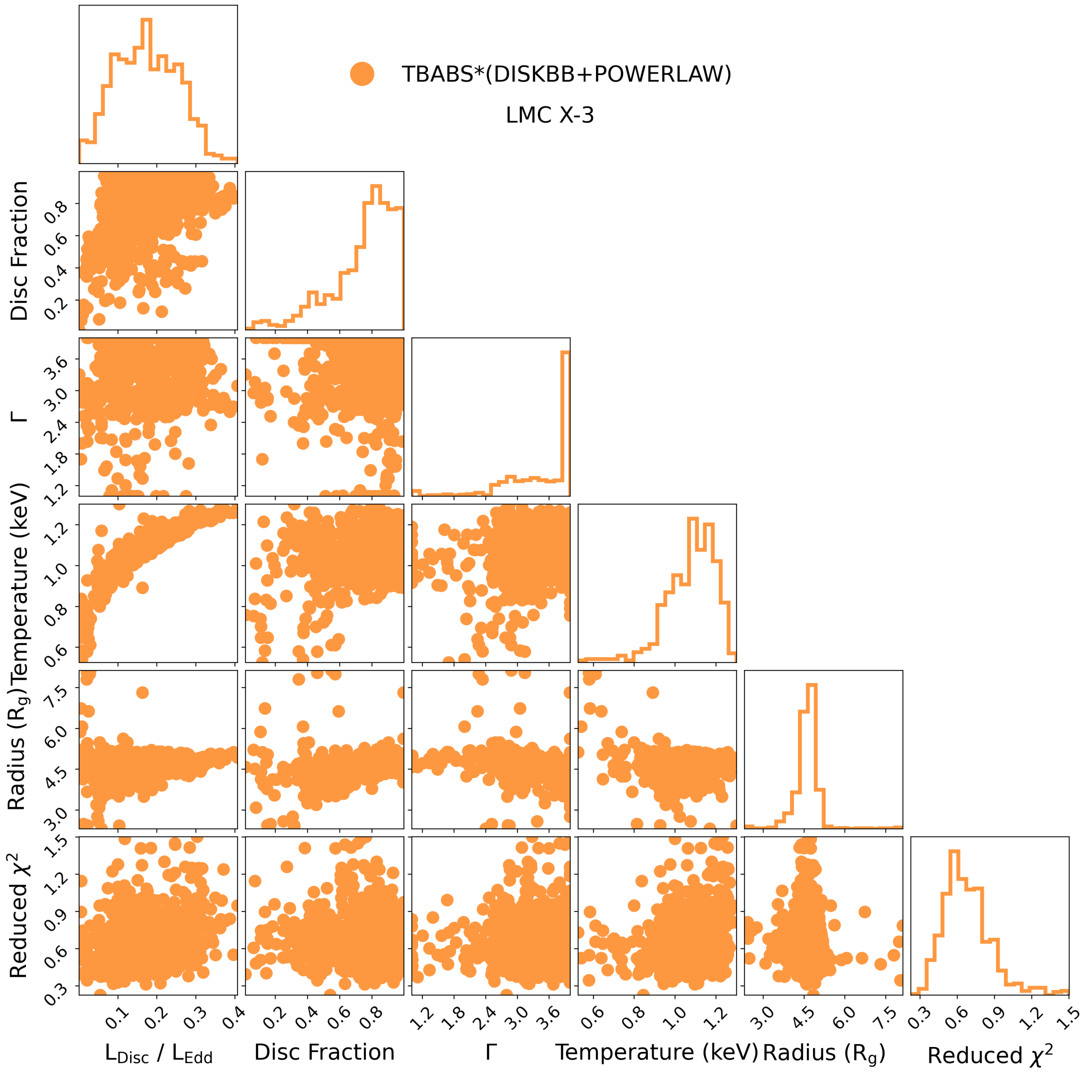

(b) Corner plot showing the evolution of the parameters from our analysis of LMC X-3 with `TBABS`×`(DISKBB+POWERLAW)`.

Figure 3.12: (Continued)

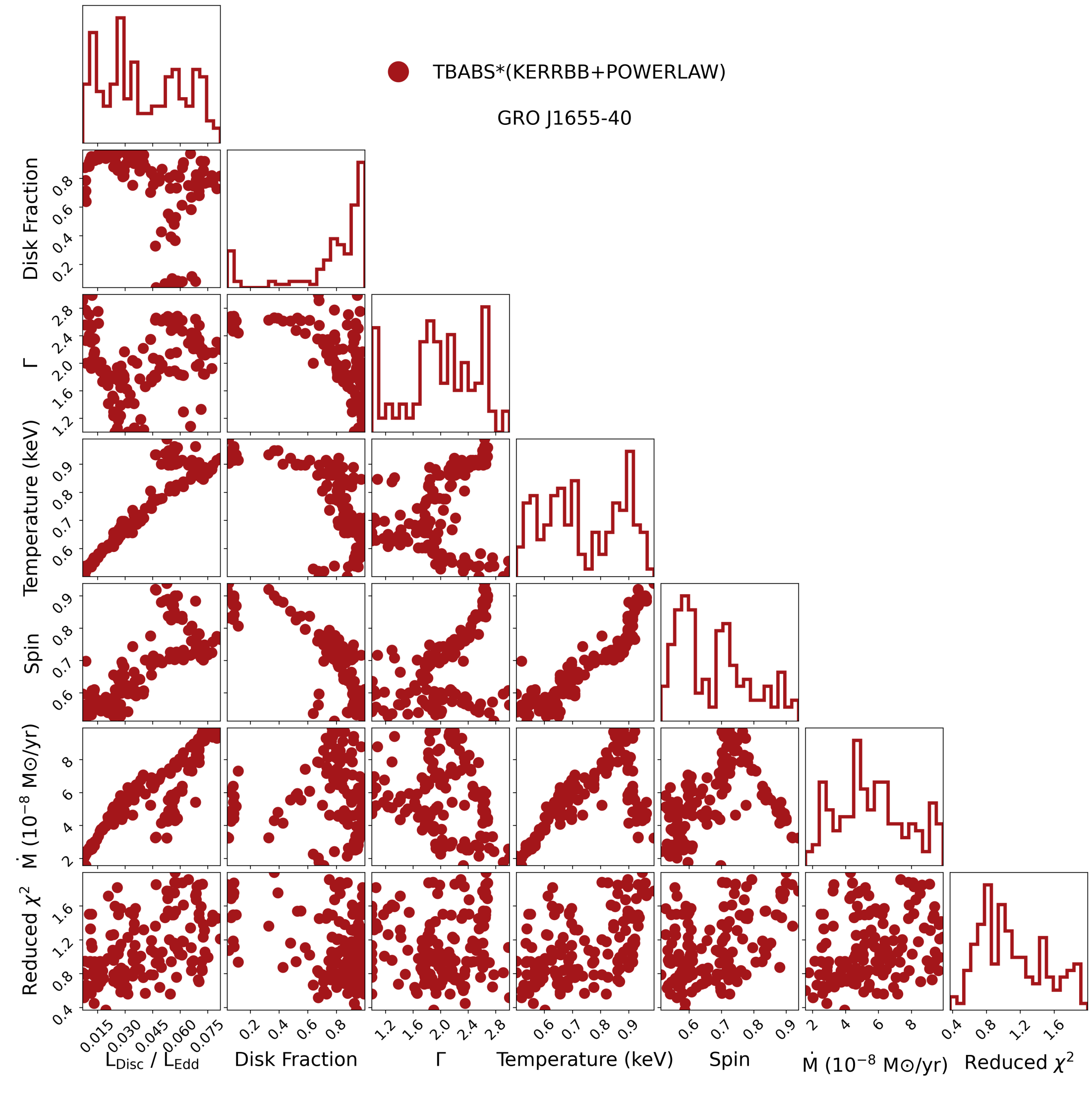

(c) Corner plot showing the evolution of the parameters from our analysis of GRO J1655-40 with `TBABS×(KERRBB+POWERLAW)`.

Figure 3.12: (Continued)

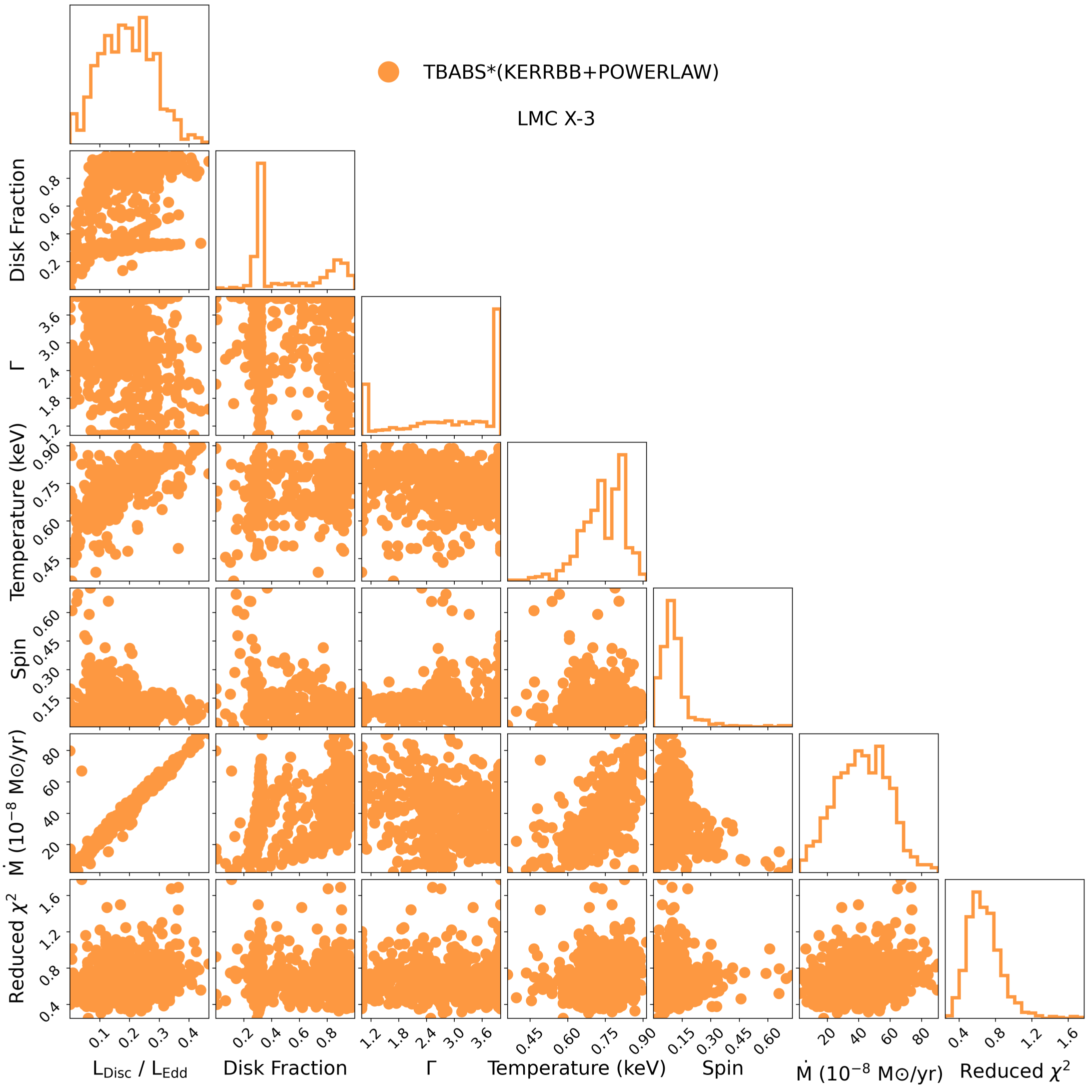

(d) Corner plot showing the evolution of the parameters from our analysis of LMC X-3 with `TBABS`×`(KERRBB+POWERLAW)`.

Figure 3.12: (Continued)

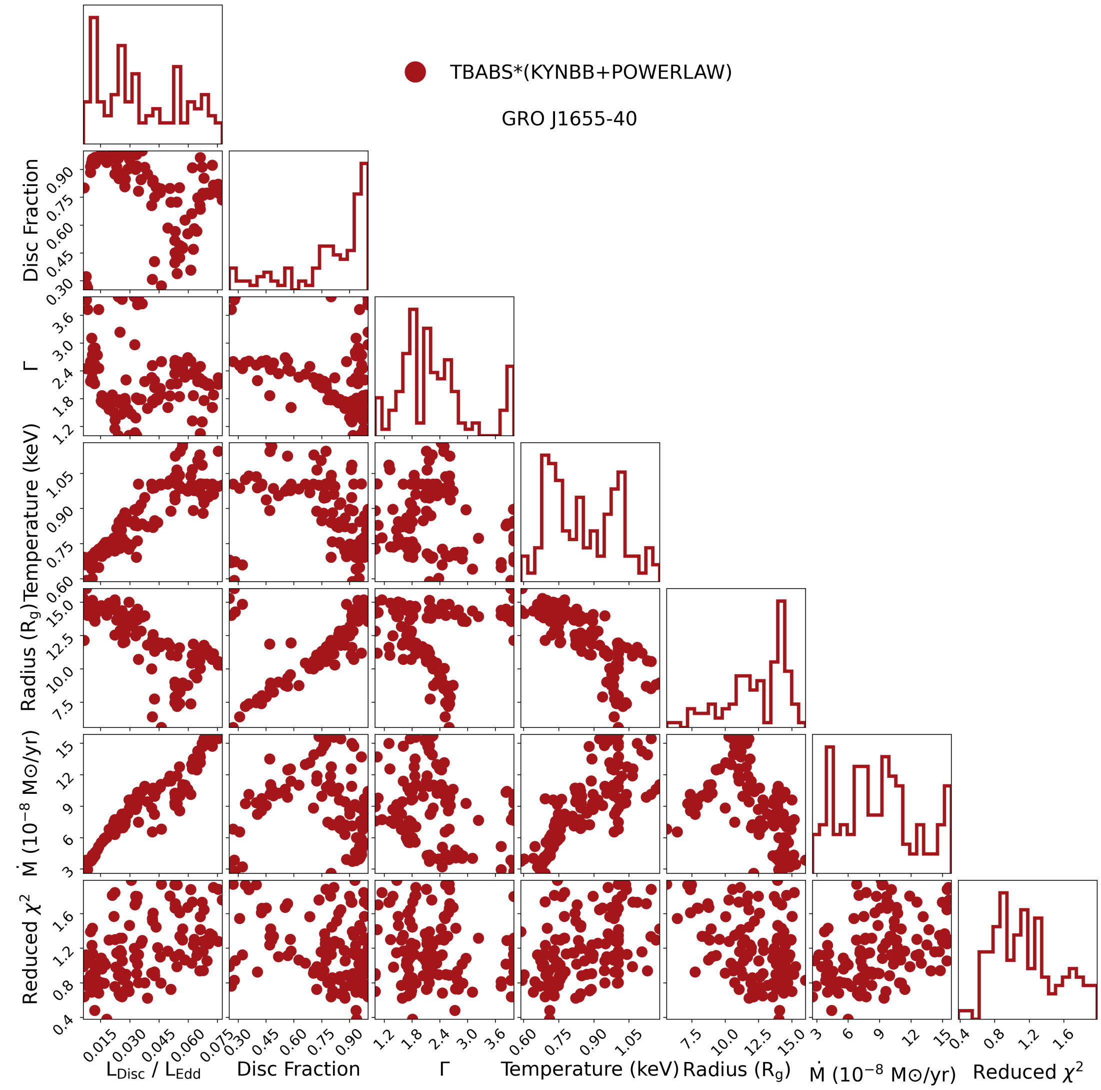

(e) Corner plot showing the evolution of the parameters from our analysis of GRO J1655-40 with `TBABS`×`(KYNBB+POWERLAW)`.

Figure 3.12: (Continued)

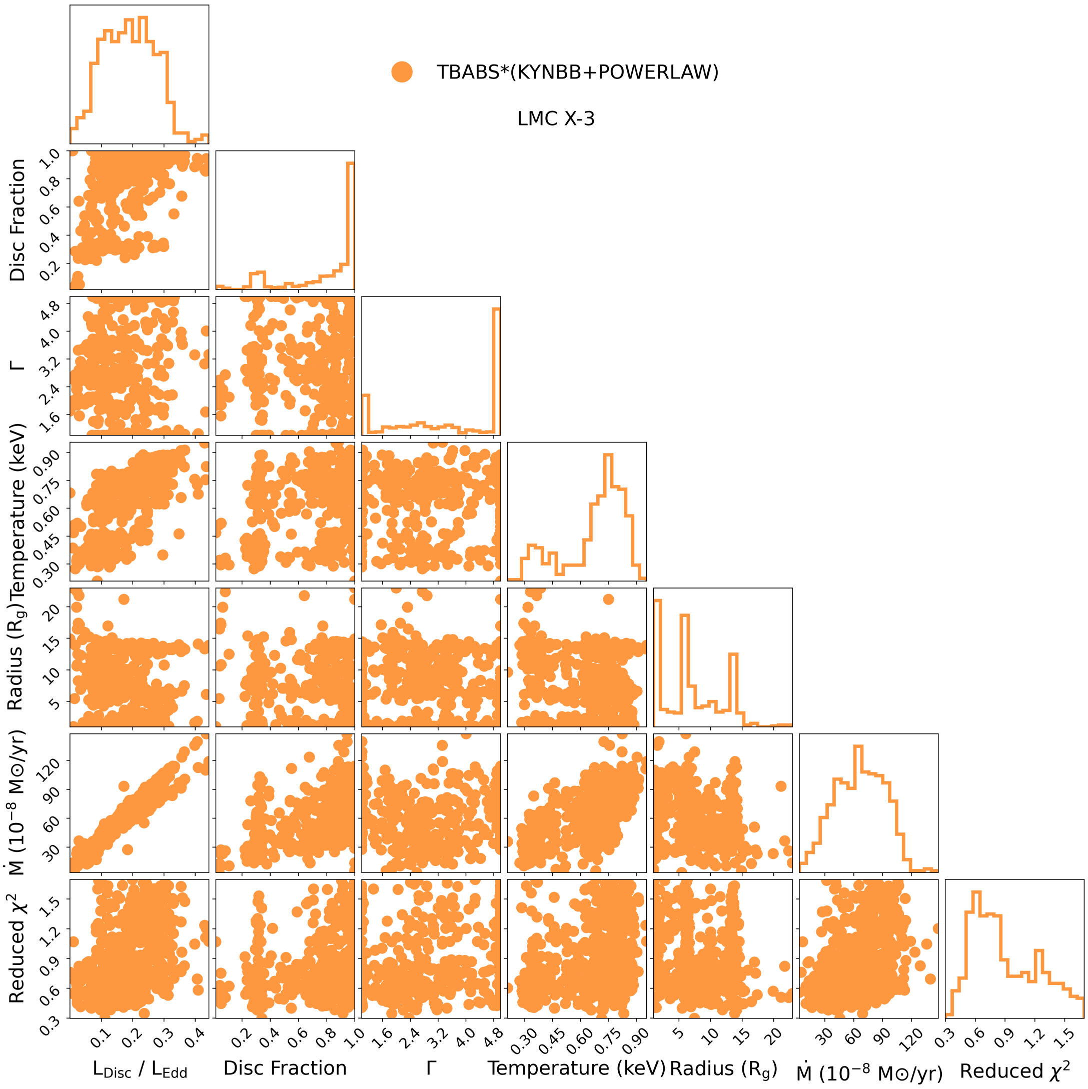

(f) Corner plot showing the evolution of the parameters from our analysis of LMC X-3 with `TBABS`×`(KYNBB+POWERLAW)`.

Figure 3.12: (Continued)

4. Discovery of a New Transient Candidate Ultraluminous X-ray Source in M51

Anastasiya Yilmaz, Debora Lančová, Felix Fürst, Diego Calderón,
Sabela Reyero Serantes, Enrico Bozzo, Jiří Svoboda

To be submitted

Abstract

Context. Ultra-luminous X-ray sources (ULXs) are now considered to be powered by super-Eddington accretion onto a stellar-mass compact object, either a black hole or a neutron star. There is now a substantially large population of ULXs showing a transient nature, which contributes to a growing gap in our understanding of accretion onto stellar-mass compact objects. The variation in the observed timescales of these transient events cannot be easily explained by currently available accretion disk models.
Aims. We aim to utilize long-term observing campaigns of M51 by using XMM-Newton, Chandra, Swift, and HST observations to explore the nature of the observed outburst in an attempt to understand the transient event and the nature of the compact object possibly powering the system.
Methods. We analyzed all of the publicly available XMM-Newton, Chandra, and Swift observations spanning a period of nearly 20 years to track the long-term evolution of the source. We used prior observations of the location using HST, XMM-Newton OM, and Swift-UVOT simultaneous to the detection to identify possible multiwavelength counterparts to further investigate both the nature of the event and the companion star.
Results. The source brightened with the second XMM-Newton observation while the spectral continuum between 0.3-10 keV remained soft with $\Gamma \sim 2.6$ throughout the outburst. The observed luminosity of the source reached as high as $\sim 7.6 \times 10^{38}$ erg s^{-1} before the XMM-Newton observing campaign ended. The entire outburst lasted 81 days from the first detection with *Swift-XRT* until the last detection with Chandra, and the source varied in the observed flux by a factor of about 200.
Conclusions. We report the discovery of a new transient ultraluminous X-ray source (ULX) candidate in M51 (hereafter M51 ULX*) located on the galactic arm southeast of the galactic center of M51a observed by Chandra, Swift, and XMM-Newton between May and August 2018. Given the spectral properties and observed luminosities, our results suggest that M51 ULX* is a strong candidate for hosting a stellar-mass compact object accretor, either a black hole or a neutron star reaching super-Eddington mass accretion rates. However, the lack of frequent long-term monitoring of M51 restricts our current understanding of the actual mechanism driving this extreme variability and sudden disappearance of the accretion disk.

keywords:Accretion, accretion disks– X-rays:binaries– stars:black holes– stars:neutron

4.1 Introduction

Ultraluminous X-ray sources (ULXs) are compact and point-like sources in nearby galaxies [see Earnshaw et al., 2019a, for a catalog] with characteristic luminosities exceeding the Eddington limit at $L_{\rm Edd} = 4\pi GMm_{\rm p}c/\sigma_{\rm T} = 1.3 \times 10^{38}(M/{\rm M}_\odot)$ erg s^{-1} [see Kaaret et al., 2017, Fabrika et al., 2021, King et al., 2023, for a review and references therein] where M is the mass of the object. Since their discoveries in the 1980s with the Einstein Observatory [Giacconi et al., 1979], ULXs have been considered ideal hosts of intermediate-mass black holes ($\sim 10^3 - 10^5$ M$_\odot$) accreting at sub-Eddington rates in an attempt to explain such extreme luminosities [Colbert and Mushotzky, 1999, Kong et al., 2004, Miller et al., 2004, Liu and Di Stefano, 2008]. The revolutionary discovery of coherent pulsations M82 X-2, shortly followed by many others eventually contributed to the now growing group of Pulsating ULXs or PULXs [Bachetti et al., 2014a, Fürst et al., 2016, Israel et al., 2017a,c, Carpano et al., 2018, Sathyaprakash et al., 2019, Rodríguez Castillo et al., 2020]. The mass range $\sim 1 - 2$ M$_\odot$ of a neutron star accretor suggests that these systems can achieve accretion rates ~ 100 $L_{\rm Edd}$. This fact is puzzling in the context of accretion disk formation in X-ray Binaries (XRBs) with stellar mass accretors. Additionally, these surprising discoveries of neutron star accretors in such extreme environments still do not rule out the intermediate-mass black hole nature. The super-Eddington accretion, however, presumed to be implausible, was later supported by the XMM-Newton and NuSTAR detections of high energy turnover in the 5-10 keV spectra of a few ULXs [Stobbart et al., 2006, Gladstone et al., 2009, Walton et al., 2014, 2015, Mukherjee et al., 2015].

While it is now widely presumed that compact objects are the accretors in these systems, the dominant engine driving such high mass accretion rates onto a possibly stellar-mass object is still challenged by the disk models available for such extreme accretion regimes. Many of these sources are associated with highly star-forming regions [Swartz et al., 2011, Mineo et al., 2012, Lehmer et al., 2019, Qiu et al., 2019], and the persistent nature of a substantial portion of the known population suggests a high-mass companion feeding the accretion disk via strong stellar winds [see Martínez-Núñez et al., 2017, for a review]. Although the wind-fed accretion in high-mass XRBs (HMXRBs) was thought to provide the best explanation for the persistent behavior over timescales on the orders of multiple years or even decades, this alone cannot be the main engine driving super-Eddington regimes even when accompanied by the Roche-Lobe overflow. The latter mechanism is dominant in low-mass XRBs (LMXRBs) and is associated with long-term variability in the accretion rates. A few alternative scenarios have been suggested to explain the super-Eddington luminosities: (a) For stellar-mass black hole accretors, density perturbations within the disk might overcome the photon-trapping due to the increased time scale of diffusion in comparison to the timescale of accretion which allow the escape of more photons from the inner regions of the disk leading to super-Eddington luminosities [Arons, 1992, Gammie, 1998, Begelman, 2002]. (b) Relativistic beaming in jets along the line of sight can be explained by a jet/disk model [Falcke and Biermann, 1999, Markoff et al.,

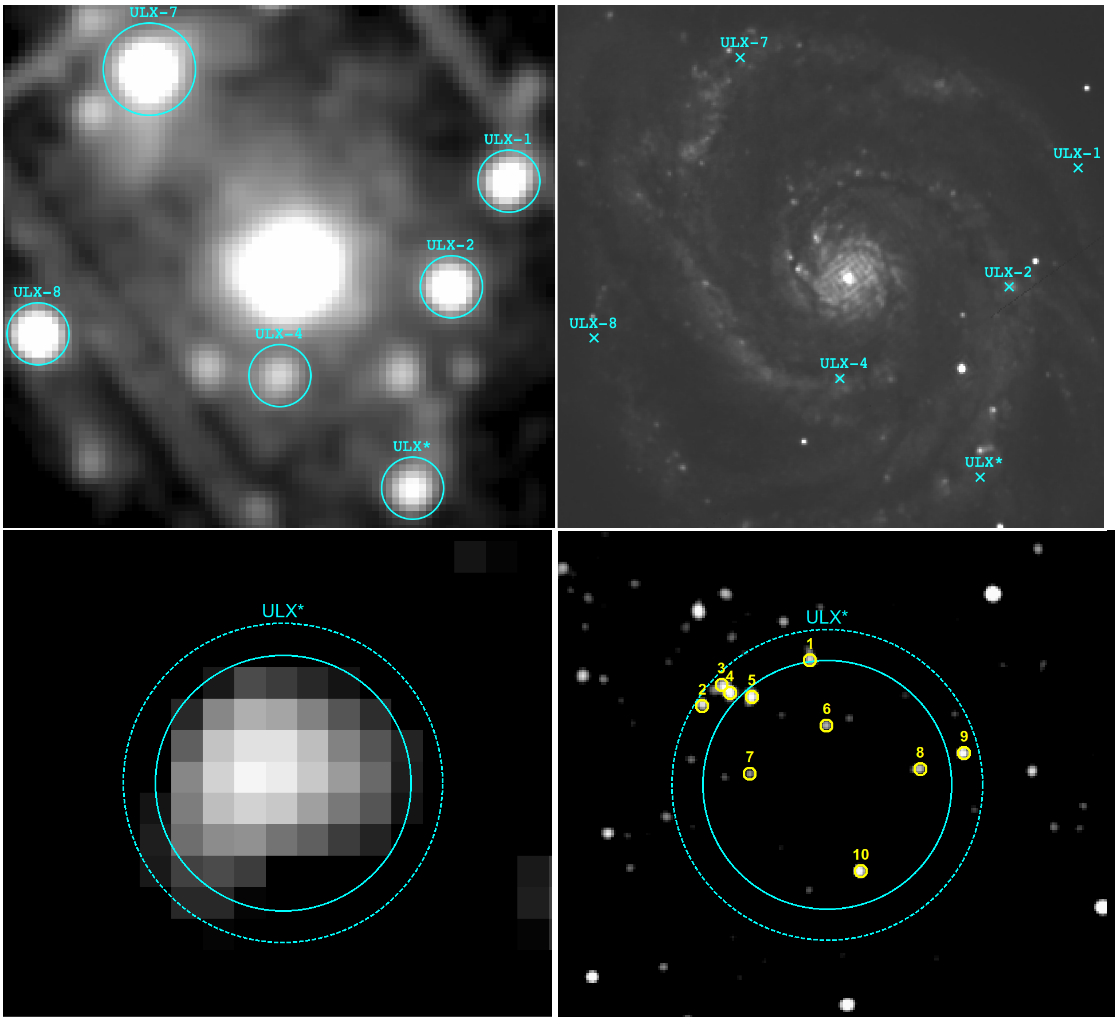

Figure 4.1: *Upper-left*: XMM-Newton EPIC-PN image of M51, *Upper-right*: XMM-Newton OM image of M51 in the B-band obtained from X2. *Buttom-left*:Chandra image of ULX*. The blue circle delimits Chandra's aperture of 2 arcsec, while the blue dashed circle corresponds to the same aperture when considering its error. *Bottom-right*: the same portion of the sky observed with *HST* WFC3 image in the F275W filter. The yellow circles show all the possible counterparts of the X-ray source in the UV (see text for details). The new candidate ULX is marked as ULX*, located at 13:29:45.46 +47:09:32.48 (J2000).

2001], which was found to be consistent with the luminosity function of XRBs in nearby galaxies but this still requires a black hole mass of $\sim$ 1000 $M_{\odot}$ for ULXs, assuming an isotropic disk model [Körding et al., 2002]. (c) A decrease in the electron opacity for X-rays for neutron star accretors with magnetic fields of $\sim 10^{12} - 10^{13}$ G [Canuto et al., 1971, Mushtukov et al., 2015]. All three scenarios pose a limit to the luminosity around a few 10^{40} erg s^{-1} which might not be applicable for systems reaching higher luminosities.

Unlike the well-studied persistent ULXs, transient systems are less understood and pose significant challenges to our knowledge of super-Eddington accretion [Dage et al., 2021]. Characterizing the transient behavior of these systems is difficult, as their observed luminosities and variability over short and long terms do not exhibit clear patterns. However, one notable group among transient systems includes neutron star-powered systems that transition non-periodically between accreting and propeller regimes. These transitions are marked by abrupt changes in X-ray luminosity, occurring suddenly without gradual increase or decrease, resulting in a nearly bimodal distribution over time [e.g., Tsygankov et al., 2016]. The long-term variability of this transition encompasses states where accretion onto the neutron star is halted due to a substantial centrifugal barrier around a rapidly rotating neutron star with a strong magnetic field [Illarionov and Sunyaev, 1975]. During these states, the source becomes dormant, with typical accretion leading to extreme X-ray luminosities.

Furthermore, the majority of known black hole XRBs are in the quiescent state and go through outbursts that can be tracked on a hardness-intensity diagram (HID) marking different accretion states dominated by different components of the system [Fender et al., 2004, Dunn et al., 2010]. These states are usually identified as the low/hard state (LHS), high/soft state (HSS), and the steep power law or intermediate state (branching into hard and soft intermediate states). The end of a quiescent state is usually characterized by a transition from the LHS to the intermediate state with an increase in the X-ray flux [Corbel et al., 2000, 2003] accompanied by a radio emission due to the synchrotron radiation from a steady relativistic jet [Blandford and Königl, 1979, Fender, 2001, Fender and Gallo, 2014]. With increasing accretion rates going through the intermediate state, an increase in the photon index is expected following the q-shaped path to the HSS. The soft characteristics of the HSS are usually due to the dominant thermal component in the X-ray continuum over the contribution from the comptonized emission. While the entirety of a complete outburst can span multiple months, a failed outburst can also occur for a few days where only an increase in the X-ray flux is observed and the spectrum remains hard with no signs of additional spectral variability. On the contrary to this clear evolution of sub-Eddington accretion disks in black hole XRBs, the majority of the known ULXs are known not to transition through these canonical soft and hard states [Berghea et al., 2008, Grisé et al., 2012, Sutton et al., 2013], while some were found to show great variations in luminosity and spectral shape. Additional to the typical LHS, HSS, and intermediate state, Gladstone et al. [2009] argued that ULXs could correspond to the so-called ”ultraluminous state” in which the source enters a super-critical accretion state.

Harboring a large population of XRBs and numerous ULXs, the nearby interacting system of two galaxies, M51, located at a distance of 8.58±0.10 Mpc [McQuinn et al., 2016] is one of the well-studied systems due to its face-on con-

Table 4.1: XMM-Newton, Chandra and Swift observations of M51 used in this paper (in chronological order).

DataID [a]	ObsID	Exposure [b]	Start Date	F_x [c]	L_x [d]
			Detection		
S1	00032017092	1.63	2018-06-12	N/A	N/A
X2	0830191501	63.00	2018-06-13	$79.9\ ^{+3.5}_{-3.3}$	$703.9\ ^{+30.8}_{-29.1}$
X3	0830191601	63.00	2018-06-15	$88.1^{+5.0}_{-5.2}$	$776.2\ ^{+44}_{-45}$
C2	20998	19.82	2018-08-31	$9.5^{+3.77}_{-5.09}$	$83.8\ ^{+33.21}_{-44.84}$
			Upper Limits		
X1	0303420101	54.11	2006-05-20	17.9	157.7
C1	13815	67.18	2012-09-23	$0.0469^{+0.5341}_{-0.0469}$	$0.413\ ^{+4.713}_{-0.413}$
X4	0852030101	77.00	2019-07-11	15.3	134.8

[a] C, S, and X denote Chandra, Swift, and XMM-Newton observations, respectively.

[b] Exposure time in ks.

[c] Flux values (10^{-15}erg s^{-1}cm^{-2}) in the 0.5-7.0 keV energy range.

[d] Luminosity values (10^{36}erg s^{-1}) in the 0.5-7.0 keV energy range.

figuration in the sky. It consists of a spiral galaxy M51a (namely the Whirlpool galaxy) and a dwarf galaxy M51b or NGC 5194 and NGC 5195, respectively. It is also known to host two neutron star powered ULXs: a PULX ULX7 [Rodríguez Castillo et al., 2020] and ULX8 that were found to exhibit a cyclotron resonant scattering feature which is a result of strong magnetic fields pointing towards the existence of a strongly magnetized neutron star [Brightman et al., 2018] while no pulsations have been detected so far. Additionally, a bimodal luminosity distribution was observed from ULX4 [Earnshaw et al., 2018b], which could be explained as a result of the propeller effect observed in neutron star powered XRBs while 4 sources (CXOM51 J132940.0+471237 and CXOM51 J132939.5+471244 [Urquhart and Soria, 2016] – previously known as a single source ULX1 [Terashima and Wilson, 2004], CXOM51 J132943.3+471135 and CXOM51 J132946.1+471042 [Wang et al., 2018]) were observed to have eclipsing behaviors. The Swift monitoring campaign in 2018 revealed a new nearby X-ray luminous transient XT in M51 [Brightman et al., 2020].

In this paper, we report the discovery and characterization of a new transient ULX in M51 using Swift [Gehrels and Swift, 2004]), XMM-Newton [Jansen et al., 2001] and Chandra [Weisskopf et al., 2002] observations. The source follows an outburst behavior with an apparent luminosity of similar orders of magnitude as its neighboring ULXs (Fig. 4.1). Previous studies of the bright star cluster population in M51 revealed a star cluster located about 5.27 arcsec away from the C2 position [Hwang and Lee, 2008], which is similar to the distribution of the sample of bright X-ray sources in starburst galaxies [Kaaret et al., 2004]. The structure of this paper is as follows: in Sect. 4.2, we describe the selected observations, the data reduction process, and spectral and timing analysis of the source. In Sect. 4.3 we present the results of our analysis and provide a discussion regarding the nature of the source and transient behavior in Sect. 4.4. Eventually, we provide a summary of our conclusions in Sect. 4.5.

4.2 Observations and Data Reduction

M51 has been extensively observed by Chandra and XMM-Newton between 2000 and 2021 enabling a long-term study of the growing ULX population in the galaxy. We utilized all of the available archival observations obtained by Chandra, Swift, and XMM-Newton to track the history of the source and calculate the upper limits of the observed flux. The source was dormant in the majority of these archival observations spanning 18 years of almost yearly observing time at sensitivities $F_{\mathrm{x}} \sim 10^{-17}$erg s^{-1}cm^{-2} in 0.5 - 7.0 keV energy band achieved with Chandra. Shortly after the first detection with Swift, the flux then increased significantly during two XMM-Newton observations which unfortunately coincided with the end of the observing campaign that lasted for a month with five evenly distributed observations. The following Chandra observation then revealed a significant drop in the flux by almost an order of magnitude only 76 days after its observed peak. The remainder of the Chandra observations either did not provide enough count rates for detection or the source was outside the field of view. We only list the archival Chandra, Swift, and XMM-Newton observations used for detection and further analysis in Table 4.1, separating the observations where ULX* was detected and observations used to obtain upper limits before and after the detection.

Including archival *Swift-XRT* observations, the "ultraluminous" phase of the outburst lasted about seven days between June 12-18 2018 and no indications of shorter bursts or any other irregularities were observed in EPIC-PN lightcurves between 0.2-10 keV. The source was barely detected at a later ∼20 ksec Chandra observation (C2). We identify this detection as a "potential detection" because while the source increased in flux by a factor of at least 200 in comparison with the observed flux obtained from C1, the extraction of any science products with statistically sufficient count rates. Using the detection in C2, we obtain the source coordinates at 13:29:45.46 +47:09:32.48 (J2000). Individual and stacked *Swift-XRT* observations before and after the outburst (until the end of 2023) did not show any significant detection, suggesting the source probably did not go through a similar outburst either as luminous or as long as this one. Simultaneous XMM-Newton OM and Swift-UVOT observations revealed no optical and ultraviolet (UV) counterpart for ULX* within 5arcsec radius around the position obtained from C2 detection.

4.2.1 Chandra

The raw data were reduced to obtain cleaned level 2 event files by using the `chandra_repro` command available within the Interactive Analysis of Observations software (`CIAO`) software (v.4.15) and the most recent calibration files at the time of writing (v.4.10.4). The source was detected only in C2, although it was still not bright enough for extracting a spectrum and a light curve with high enough signal-to-noise (S/N) ratio. We use this observation to obtain a more precise source position. To do so, we extracted a full detector image together with the corresponding exposure and point spread function (PSF) maps in the $0.5-7.0$ keV energy band. We then used the exposure and PSF maps within the `wavdetect` routine to perform source detection. For the rest of the Chandra observations in which the source was in the field of view, we performed the same routine to check for any significant detection. Even for the observations with no detection, we used the `srcflux` task to calculate the flux values to obtain upper limits. The lowest value obtained was from the 67.18 ks observation C1 with $F_{\rm x} = 4.69 \times 10^{-17}$ erg s^{-1}cm^{-2} in 0.5-7.0 keV energy range with a corresponding luminosity $L_{\rm x} = 4.13 \times 10^{35}$ erg s^{-1} assuming a distance of 8.58 Mpc. We list calculated flux values of both C1 and C2 in Table 4.1. While C2 provided a clear detection of the source, the total number of counts did not allow a proper extraction of the spectrum, hence this observation is used only for flux calculations and source coordinates.

4.2.2 X-ray Multi-Mirror Mission (XMM-Newton)

We examined all publicly available XMM-Newton observations to search for any significant source detection. Among these, only the observations listed in Table 4.1 resulted in net counts significant enough for detection with XMM-Newton and were consequently used for further analysis. The source was clearly detected in both X2 and X3 (observation IDs: 0830191501 and 0830191601, respectively). During these two observations, both EPIC-MOS1 and MOS2 were operated in small window mode around the galactic center leaving the source out of the field of view of the pointing. Only the EPIC-PN was operated in the full frame mode. In the observation prior to both X2 and X3 (observation ID: 0830191401), the source location falls on the chip gap making it impossible to get any detection. We used the XMM-Newton Science Analysis System (`SAS`) software (v.21.0.0) for data reduction following the online analysis threads. We used `epproc` to reprocess the observation data files from EPIC-PN and extract calibrated event files. Neither of the observations showed signs of a flaring particle background. The default `RATE EXPRESSION` was used to extract the good time interval (GTI) files and obtain filtered event files for further analysis. The background corrected light curves and spectra were extracted from ∼12arcsec centered around the source coordinate obtained from C2 with a background region of ∼30arcsec selected from a nearby source-free region. We followed the recommended selection expression and restricted the patterns only to single and double events (`PATTERN<=4`). We then used the `SAS` tools `rmfgen` and `arfgen` to generate redistribution matrices (rmf) and ancillary files (arf), respectively. The obtained spectra were then grouped with the `specgroup` task and binned to have at least 20 counts per bin.

Additionally, we used other observations where the source was dormant to obtain the upper limits of the source flux before and after the first detection in X2. We first produced the sensitivity maps of each observation with the `SAS` tool `esensmap` and then used HEASARC's online `webpimms` tool adopting the power-law model with $\Gamma = 2.1$ and $N_{\rm H} = 0.2 \times 10^{-22}$ cm^{-2} to convert the corresponding values into flux in the 0.5-7 keV energy band. Before X2, the lowest flux value calculated from the source location was obtained from the 54.11 ksec observation (X1), where we estimated a 90 percent c.l. upper limit of its X-ray flux to be $F_{\rm x} = 1.79 \times 10^{-14}$ erg s^{-1}cm^{-2} with a corresponding luminosity

$L_{\mathrm{x}} = 1.57 \times 10^{38}$ erg s^{-1}. Following the last XMM-Newton detection (X3), the source decreased in the luminosity below the detection limit of the instrument and the upper limit on the flux and luminosity was even lower than before the detection with $F_{\mathrm{x}} = 1.53 \times 10^{-14}$ erg s^{-1}cm^{-2} with a corresponding luminosity $L_{\mathrm{x}} = 1.34 \times 10^{38}$ erg s^{-1}.

In Fig. 4.2, the long-term evolution of M51 ULX* using Chandra and XMM-Newton observations shows the evolution of the observed X-ray luminosity in the 0.5-7.0 keV energy band with upper limits obtained before and after the brightening.

4.2.3 Neil Gehrels Swift Observatory (Swift)

Swift has observed M51 extensively since 2005. We make use of this long-term monitoring to study the long-term variability of M51 ULX* and better identify the length of the outburst. For that, we used *Swift-XRT* images of each observation spanning nearly three years before and after the first XMM-Newton detection. We extracted *Swift-XRT* images using the standard online tools provided by the UK Swift Science Data Centre [Evans et al., 2009] for each observation. Before the outburst, the source showed no significant variability above the instrumental sensitivities while following the XMM-Newton detection, only one Swift observation provided a detection. Unfortunately, the net count rate for that observation was not enough to extract a background-subtracted spectrum with a sufficient number of bins for proper spectral modeling.

4.2.4 Hubble Space Telescope (HST)

HST, unfortunately, did not observe M51 during or shortly after the outburst. To investigate the region further, we used HST observations taken in September 2014 with the WFC3/UVIS F275W filter (PropID: 13364, PI Calzetti). We selected a region of 2 arcsec centered around the source coordinates obtained by the Chandra detection and assumed an error margin of 0.5 arcsec. We then performed a PSF photometry with the DAOPHOT package on `IRAF` with a 2 pixel aperture. The bottom left image in Fig. 4.1 shows the population of possible point sources we were able to identify within this region highlighted with yellow smaller circles.

4.3 Data Analysis and Results

4.3.1 Spectral Analysis

We performed the spectral analysis with `xspec` (v.12.13.0c) [Arnaud, 1996] within `HEASOFT` (v.6.31.1). We utilized Cash statistic namely C-stat [Cash, 1979] to account for the Poisson distribution of the observed photons in such low count rate spectra. We performed the initial analysis using `xspec` to explore the possible contributions to the model and make a preliminary model comparison. We initially used a simplistic model consisting of an absorbed power law. Both spectral fits resulted in reduced χ^2 values well below two while the second spectrum had a statistically significant increase. To improve the parameter estimation and perform a more comprehensive model comparison, we made use of the Bayesian

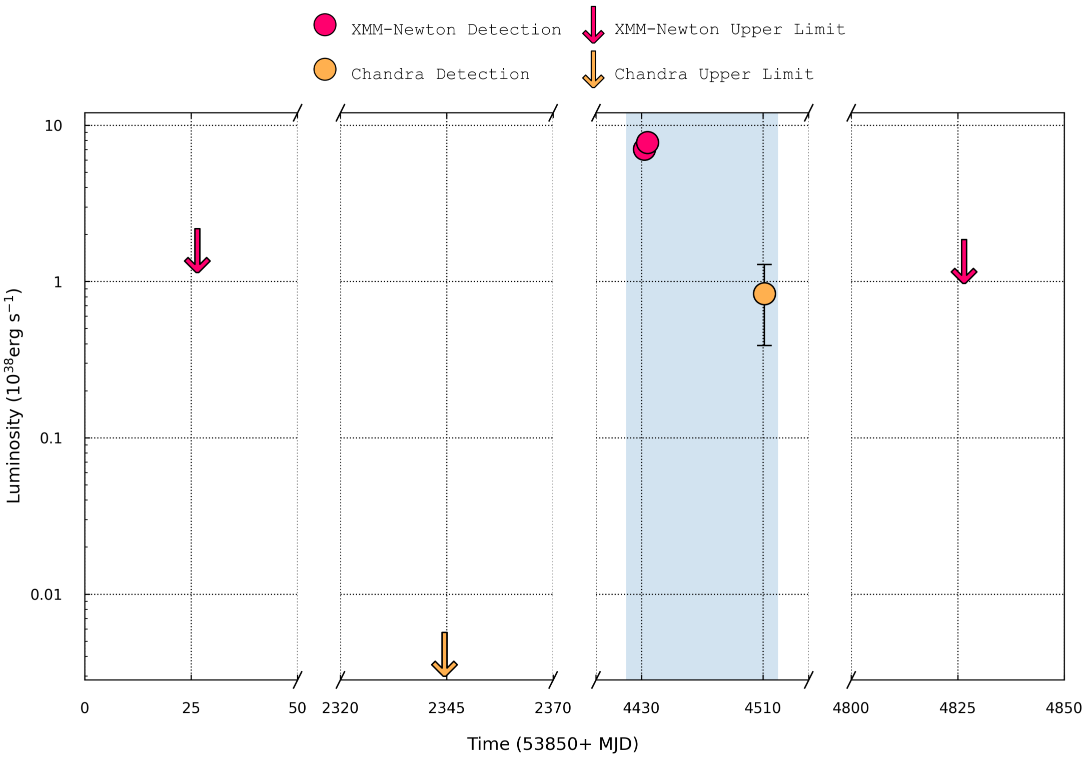

Figure 4.2: Long-term evolution of the observed X-ray luminosity in the 0.5-7.0 keV energy range. Arrows correspond to the calculated upper limits for XMM-Newton (pink) and Chandra (orange) and circles denote the observations in which M51 ULX* was detected. The observed outburst is marked with a blue-shaded region.

Analysis Package (BXA, Buchner et al. [2014]), which is a Bayesian framework utilizing the nested sampling algorithm UltraNest [Buchner, 2016, 2019, 2021] to explore the parameter space of any given model and provided priors. For n_H and normalization parameters of both models, we used wide log-uniform and uniform priors for T_{in} and Γ, respectively.

We first applied a simple absorbed power-law model (`TBabs`×`powerlaw`) to both spectra using default element abundances and cross-sections [Anders and Grevesse, 1989, Verner et al., 1996] with all parameters left free to vary. While spectral shapes of both observations remained similar with only a small increase in the flux (see both panels of Fig. 4.3b), the second observation (X3) produced significantly worse fit test statistics with χ^2/dof=57.83/36. Given the increase in the χ^2/d.o.f. with increasing flux, we attempted an additional fit with a multicolor accretion disk model in `TBabs`×`(powerlaw+diskbb)`. While the fit test statistics improved, the residuals in lower energies do not exhibit significant differences between the two observations. We conclude that this is unlikely a statistically significant contribution, if present due to the reduced count rates at such distances and instrumental limitations.

In addition to the phenomenological model `powerlaw`, we tried different models of the Comptonisation component to better describe the high energy contribution to the continuum but given the soft nature of both spectra, we found no significant improvement to the fit. Following the discussion in [Stobbart et al., 2006,

Table 4.2: Results of the spectral fits with `TBabs`×`powerlaw` to all XMM-Newton data used in this paper. Here N_H is the absorption column density, Γ the power-law photon index.

DataID	χ^2/d.o.f.[a]	N_H (10^{22})	Γ	L_x[b] (10^{38} erg s^{-1})
X2	34.66/31	$0.13^{+0.03}_{-0.02}$	$2.68^{+0.14}_{-0.15}$	$7.04^{+0.31}_{-0.29}$
X3	57.83/36	0.14 ±0.02	$2.67^{+0.13}_{-0.12}$	$7.59^{+0.45}_{-0.46}$

[a] Both fits with Xspec and BXA were performed with C-stat fit statistics and Chi-squared fit test statistics are presented here to evaluate the goodness of fit between the two observations.

[b] Luminosity in the 0.3-10.0 keV energy range calculated using the flux values obtained from spectral fitting assumed distance of 8.58 Mpc.

Gladstone et al., 2009, Koliopanos et al., 2017b, Walton et al., 2021], we included two disk components to test the presence of a two-temperature thermal component, which is usually characterized by two nodes of temperatures of around 0.3 keV and 3 keV where the latter is used to describe an inner accretion flow; and the low-temperature component is assumed to arise from either the outer regions of the accretion disk or the photosphere of a strong wind [King and Pounds, 2003]. While this approach is preferred for super-Eddington accretion disks, the addition of another disk component provided only a statistically insignificant decrease in the fit test statistics which could be interpreted as a result of the addition of two more free parameters to the fit. Both disk temperatures remained relatively low, with the higher temperature component reaching only $kT_{\rm in} \sim 0.62$ keV.

Fig. 4.3a presents the corner plot showing the distributions of parameters in `TBabs`×`powerlaw`. The increase in the flux resulted only in a change in the normalization parameter of `powerlaw` for X2(blue) and X3(green).

4.3.2 Timing Analysis

We carried out a detailed timing analysis to look for coherent pulsations in the *XMM-Newton* EPIC-pn data. We did not use data from other instruments or satellites, as they do not provide sufficient time resolution for pulsation search with periods around 1 s, which is the period typically found for this kind of source. First, we performed a Fast Fourier Transform (FFT) analysis on the light curves with a time resolution of 74.3 ms (the frame time of the EPIC-pn detector) between 10^{-4}–7 Hz. We did not find any significant peaks in either the X2 or the X3 data.

We then performed an accelerated pulse period search by performing epoch-folding over a grid in P and $\dot{P}$ space, between periods $P = 0.25$–1.25 s and period derivatives $\dot{P} = -1.5 \times 10^{-9}$–$1.5 \times 10^{-9}\,\mathrm{s}^{-1}$. This range covers the typical values found in other ULX pulsars [e.g., Israel et al., 2017a, Fürst et al., 2016]. Again, no significant pulsations could be identified in either the X2 or X3 data.

To put upper limits on the pulsed fraction in these observations, we simulate butevent files based on an input event list with the same average count rate as the real data, but with added sinusoidal pulsations, resulting in a pulsed fraction $\mathrm{PF}_{\rm sim}$. The simulations follow the method described in Fürst et al. [2021] and

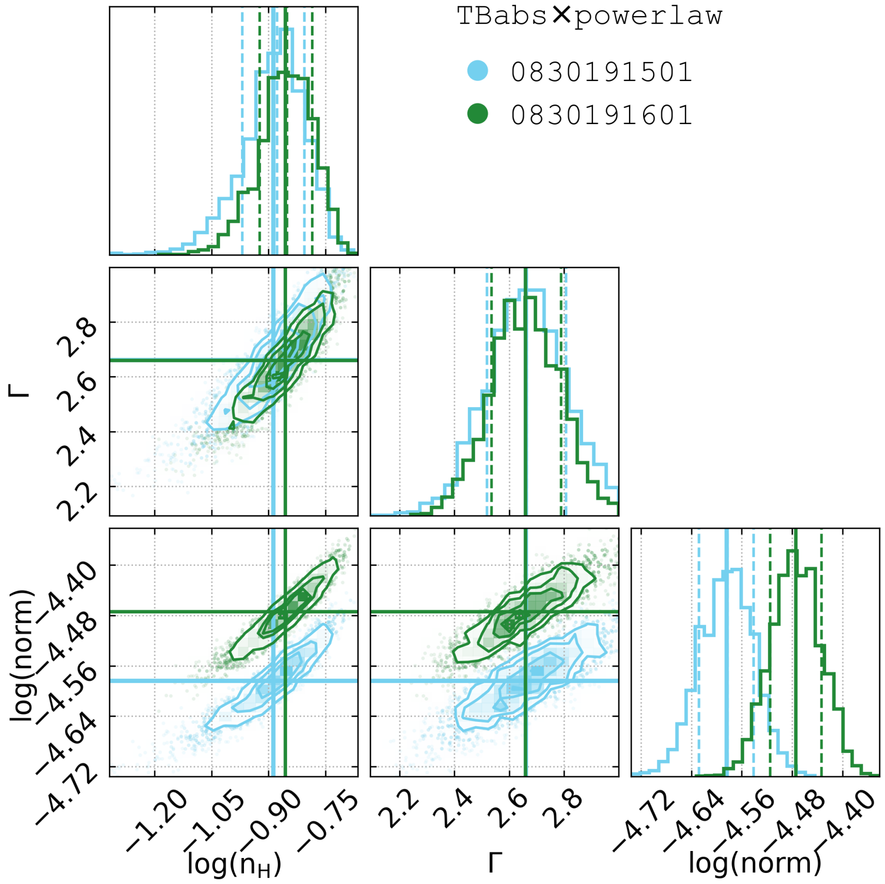

(a)

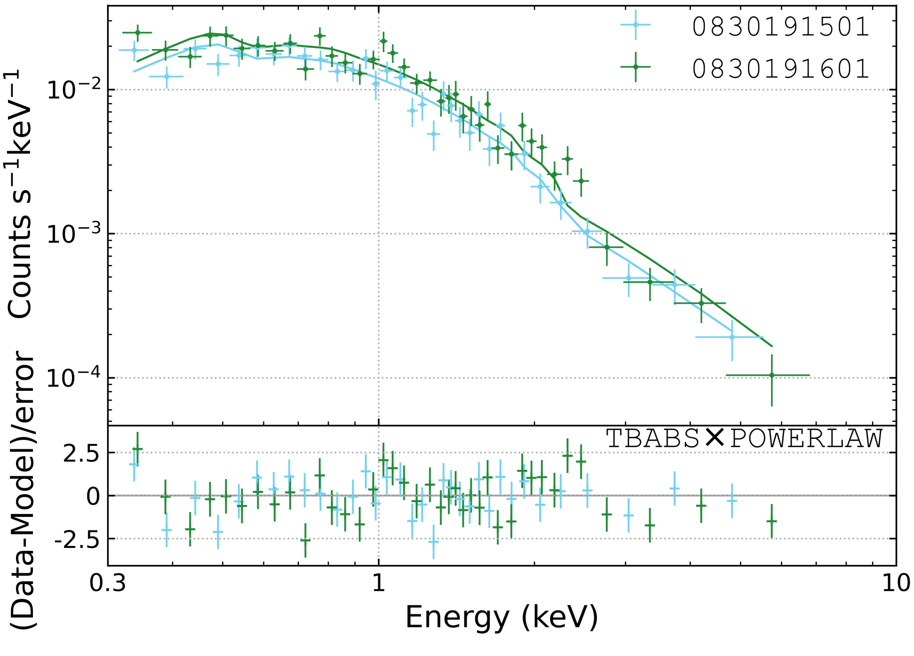

(b)

Figure 4.3: (a): Corner plot showing the fit results of BXA with `TBabs`×`powerlaw` for X2(blue) and X3(green). (b): *Top*: Total model (`TBabs`×`powerlaw`, solid lines) and data for X2(blue) and X3(green), *Bottom*: Residuals in (data-model)/error for each fit.

are based on the method used in the `Stingray` software package [Huppenkothen et al., 2019]. Specifically, we simulate event lists with pulsed fractions for each observation, $\mathrm{PF}_{\mathrm{sim}}$, $0.1 \leq \mathrm{PF}_{\mathrm{sim}} \leq 0.9$ in steps of 0.01. For each value of $\mathrm{PF}_{\mathrm{sim}}$ we generate 100 statistically independent event lists and search within each list for pulsations using the epoch folding technique. We do not include $\dot{P}$ in these simulations as it does not influence the obtained upper limit. We define the upper limit on the pulsed fraction as the value where at least 90 per cent of all simulated event lists provide detection of the pulse with at least 99.5 per cent significance. We find an upper limit of PF $<$ 32 per cent for X2 and PF $<$ 29 per cent for X3.

4.4 Discussion

M51 has been subject to extensive observing campaigns by XMM-Newton, Chandra, and Swift spanning over almost two decades. However, prior to the 2018 long-term Swift monitoring [Brightman et al., 2018], no continuous observation campaign had been conducted. Starting in May 2018, the monitoring period extended almost 1.5 years without yielding any significant detection of M51 ULX* reported. This could be attributed to the distance to M51 and relatively shorter snapshots obtained by Swift compared to XMM-Newton and Chandra observations. Due to the sparse long-term coverage of M51, it remains challenging to identify the course of the outburst between May and August 2018 and the overall duration of the decay subsequent to the initial detection in X2. During the XMM-Newton observation before X2, the exact source location obtained by the Chandra detection coincided with a chip gap, precluding the observation from being used for any further analysis. M51 ULX* was out of the field of view in the consecutive Chandra observations until it was detected in C2 before the observed flux fell below the detection limit again, thus setting a maximum decay period of 78 days. It is possibly reasonable to expect that the two-day rise continued a little further reaching and even exceeding 10^{39} erg s^{-1}, instead of abruptly stopping after X3. It is, however, not possible to infer the exact value of the peak luminosity. We, therefore, favor identifying ULX* as a candidate ULX since the source is observed to be accreting at super-Eddington rates for a stellar-mass compact object, critically close to the appointed limit of 10^{39} erg s^{-1} adopted in the literature for the identification of a ULX [Kaaret et al., 2017, Fabrika et al., 2021].

4.4.1 Spectral Properties and Variability

Except for the slight increase in the X-ray flux, no significant variability was observed in either X2 or X3 spectra. This slight change resulted only in a small difference in the normalization parameter of `powerlaw` when fitted with a simple absorbed power law (`TBabs`×`powerlaw`) (Fig. 4.3a). Both spectra remained soft throughout the increase in the flux with $\Gamma \sim 2.6$.

4.4.2 Timing Variability and Geometry of the System

The light curves for X2 and X3 showed no significant variability on the short-time scales within the observation exposures and no signs of significant outbursts or eclipsing behavior. The lack of eclipsing behavior might be interpreted as a sign of a lower inclination angle of the system, however, this argument might not be valid for orbital periods on the scales longer than a few days or weeks. Unfortunately, due to the lack of more observations with the source in an outburst, it is not possible to infer the timescale of the orbit of the system.

A detailed timing analysis using both X2 and X3 revealed no significant pulsations. This is not surprising, since only a very small fraction of the observed ULXs is accompanied by pulse detection [Misra et al., 2024] while the majority of these sources are expected to harbor neutron stars [King and Lasota, 2016]. In many of the cases, significant pulse detection requires a large PF [Mushtukov et al., 2021], and Earnshaw et al. [2019a] showed that only a small fraction of almost 400 ULXs with XMM-Newton observations can actually provide the statistics needed for significant detection. A significant portion of pulsation ULXs are expected to have large PFs. Typically, ULXs with detected pulsations are accompanied by PF>10-20 per cent and Mushtukov et al. [2021] argued that only an insignificant portion of PULXs with PF>10 per cent will be strongly beamed along the line of sight with high amplification factors. This means the apparent luminosity will not be a result of amplification of the intrinsic accretion luminosity. Misra et al. [2020], on the other hand, invokes the geometrical beaming as the only condition to explain super-Eddington luminosities.

The upper limit on PFs from X2 and X3 falls close to the observed pulsating ULXs, ruling out the detection of strong pulsations. In a more recent study, P13 was found to show an anti-correlation between the observed PF and flux but no clear trend with the spectral shape [Fürst et al., 2021]. The high PFs at lower fluxes could be a result of pulsed emission from the accretion column dominating the observed emission where this component would be expected to dominate at higher energies of the X-ray spectrum [Walton et al., 2018]. Transitioning to higher fluxes where the contribution from the disk emission could surpass the pulsed emission, the spectrum is expected to be dominantly softer. However, King and Lasota [2020] argues that the system needs to be observed in a very specific geometric configuration to reveal pulsed emission to the observer. When the system is observed when the spin axis of the neutron star is along the line of sight, the pulsed emission is expected to successfully escape the system before it gets scattered, going through an obscuring column. Additionally, the alignment of the spin and accretion axes will result in the obscuration of the pulsed emission.

At accretion rates close to the critical value, the disk is expected to be geometrically thick, enclosing the central neutron star at the base of a radiation-pressure-dominated funnel. The radiation escapes from both the thick accretion disk surface and the neutron star at the base of the funnel, which leads to strong beaming and magnification of the observed luminosity [King and Lasota, 2020, Abarca et al., 2021]. A face-on configuration of the system would then result in a beamed emission, where this amplification in the apparent luminosity was suggested to be present in all ULXs to explain their bright nature. If this were to be the case for M51 ULX*, the spectrum would be expected to be harder since the hot inner accretion flow would dominate the broadband spectrum. On the other hand, if the inclination angle is assumed at $i \sim 50^\circ$, we can then explain observed properties of ULX* as beamed emission of a disk accreting at around the Eddington limit and observed at an angle close to the expected surface of the thick disk. Then, we could observe the disk up to its center, and the apparent luminosity would be only slightly beamed. Nevertheless, it is not easy to identify by what factor it will contribute to the apparent luminosity. From a different point of view, while only a small fraction of PULXs is expected to show signs of geometrical beaming (see Mushtukov et al. [2021] and references therein), it is considered to be a key component of the theories explaining the ionization of intergalactic medium (e.g. Rickards Vaught et al. [2021], Kovlakas et al. [2022]). However, the geometrical beaming fails to explain the transient behavior of the population.

While the absence of eclipsing behavior can be used to assume a rather low-inclination angle of the system only under the assumption that the orbital period of the system is short enough to be observed within the 3-day period between X2 and X3, it does not give any information about the configuration of the spin and disk axes. On the other hand, Super-Eddington accretion also invokes the launching of strong disk winds and the presence of such powerful outflows observed at higher inclination systems was used to explain the soft nature of some ULX spectra [Pinto and Walton, 2023]. The observed properties of these outflows are affected by a combination of the inclination angle of the system and the mass accretion rate which defines the opening angle of the funnel. The hardness ratio, however, shows a pattern with respect to the line of sight velocity of the wind where harder ULX spectra were associated with fast and hot outflows and vice versa [Pinto and Kosec, 2023]. The soft nature of M51 ULX* fits well with a higher inclination angle, possibly not nearing the extreme edge-on geometry, and will support the non-detection of pulsations. However, if the non-detection of the pulsations is only expected to be explained by a strong obscuration along the line of sight, it would indicate larger absorbing columns than our spectral analysis revealed.

4.4.3 Nature and Mass of the Accretor

High luminosities of observed ULXs raised the assumption that these objects should be intermediate-mass black holes accreting at sub-Eddington rates, however now there is growing support for the idea that these sources are dominantly powered by accretion onto neutron stars instead [Koliopanos et al., 2017b]. This support, however, simply does not provide enough grounds to make it easy to completely rule out the black hole nature of these compact objects. It might not be appropriate to rely solely on the lack of pulsation observations or propeller regime-like variability to infer the existence of a black hole accretor. In this section, we consider potential scenarios to investigate the nature of the compact object and the structure of the accretion disk based on available observed properties.

Stellar-mass Compact Object: Black Hole vs. Neutron Star

A stellar-mass black hole with $M_{\rm BH} < 10{\rm M}_\odot$ would suggest that the accretion can surpass the Eddington limit entering the ultraluminous state (e.g. see Gladstone et al. [2009] and Motta et al. [2021] for a review). For a typical black hole XRB, each state is characterized by a certain timescale [Dunn et al., 2010], and a typical outburst observed in many XRBs can last for several months while outbursts on much shorter timescales are referred to as failed outbursts where the source fails to transition from the low/hard state (LHS) to the high/soft state (HSS). However, these failed outbursts are characterized by a short-lived increase in flux accompanied by much harder spectra ($\Gamma \sim 1.7$). In the case of a typical black hole XRB, the transition from a quiescent state to ultraluminous following an increase in the observed flux by several orders of magnitude is not expected to take place on timescales similar to the outburst observed in ULX*. Additionally, the transition from an LHS to HSS observed in many black hole XRBs is expected to have signatures of accretion state changes characterized by the hardness of the spectrum while M51 ULX* showed no signs of spectral variability throughout the outburst, with a somewhat soft spectrum ($\Gamma \sim 2.6$) accompanied by a slight increase in the observed flux. If these two observations are to be taken as the ”awakening” of a black hole accretor, then the rise in the X-ray flux should have been accompanied by a hard spectrum with $\Gamma \sim 1.7$ which stays constant before entering the intermediate state (see Dunn et al. [2010] and Dunn et al. [2011] for a more detailed discussion). On the other hand, sudden softening of the spectrum throughout the rise from the LHS is not that unexpected in the case of a Compton-thick disk wind as observed in GRO J1655-40 [Uttley and Klein-Wolt, 2015] while this scenario is hard to either prove or rule out due to significantly reduced signal-to-noise ratio at higher energies where the signatures of absorption due to a disk wind are expected to be observed. The anomalous case of GRO J1655-40 is so far observed to be isolated and the accretion rate through that shift remained well below the Eddington limit for a stellar-mass black hole accretor [Dunn et al., 2010, 2011, Uttley and Klein-Wolt, 2015, Yilmaz et al., 2023].

The sudden increase of the flux, resulting in the soft nature of the spectra could indicate the presence of an accretion disk. However, currently available accretion disk models are not able to explain the short-lived outbursts observed in several ULXs. For a stellar-mass black hole accretor powering ULX*, then, the accretion disk is expected to be geometrically very thick due to the high mass accretion rate, and emit a soft spectrum. As accretion continues, the material in the accretion disk drags the magnetic field along toward the innermost regions of the disk. This ”piling up” of these weak magnetic fields results in a rise in the strength of the total magnetic field within the inner regions of the disk. Once the magnetic field strength reaches a critical limit, the accreted material is then ”arrested” by the magnetic field and can no longer accrete onto the black hole. This structure is therefore called the magnetically arrested disk or MAD [Narayan et al., 2003].

Currently, the MAD transition remains an accretion regime to be discovered in more sources and a detailed description of the phenomenon can only be obtained by complex numerical simulations. Unfortunately, due to the lack of frequent radio observations, the outburst was not accompanied by a spatially resolved detection. Although the MAD state can possibly describe the sudden break in accretion, a possible transition to this state might not explain the state leading to the sudden brightening of ULX*.

Another possible scenario for transient ULXs with a superorbital period is the presence of a precessing warped disk that is inclined with respect to the rotational axis of the central object. The Lense-Thirring precession would lead to a periodical obscuration of the central regions, as was observed in similar transient

NGC 925 ULX-3 [Earnshaw et al., 2020]. However, in the case of ULX*, we do not observe any periodicity, which could be the result of the lack of long-term observing campaigns of M51. The sharp decay and a single occurrence of the source are strongly in contradiction with this scenario, and we can almost certainly rule it out.

Neutron stars, on the other hand, are found to be more variable and neutron stars with stronger magnetic fields are observed to be short-lived [Thompson and Duncan, 1995]. Considering M51 is a star-forming galaxy and the association of neutron stars with recent star-formation history (e.g. Heger et al. [2003] and Cerda-Duran and Elias-Rosa [2018] for a more recent review), it is not straightforward to rule out the neutron star nature of the accretor. Invoking a neutron star as an accretor could ideally provide a plausible scenario in which the accretion stops abruptly. A neutron star will only be able to accrete matter when the corotation radius is located outside the magnetospheric radius for spherical accretion. In this case, if there is a drop in the luminosity, the magnetospheric radius can become larger and eventually enter the propeller regime and shred the accretion disk apart.

Propeller effect, however, is usually used to explain the bimodal distribution of the observed flux in some ULXs over a longer period of time, spanning months or even years. Although the M51 ULX* does not show similar properties, we cannot definitively consider this as an isolated event and rule out the absence of a possible bimodal distribution in the future due to the lack of more frequent long-exposure observations. For a known PULX M82 X-2, Brightman et al. [2016] argued that a luminosity on the orders of $\sim 2\times10^{39}$ erg s^{-1} is required for a magnetic field of 10^{13} G and a pulse period of 1.37 s. In the presence of a neutron star, Koliopanos et al. [2017a] showed that there is a clear trend of increasing magnetic field strength and observed luminosity in neutron star-powered ULXs. While stronger magnetic field neutron stars can maintain efficient super-Eddington accretion, weakly magnetized neutron stars are argued to be able to reach super-Eddington regimes, launching powerful outflows instead [King and Lasota, 2016].

Another set of transient X-ray binary systems is known to harbor a Be star as a companion in which the compact object is usually a neutron star (see Reig [2011] for a more detailed review and the references therein). Be/XRBs or BeXRBs are found to undergo two types of outbursts: (i) Type-I, periodic or quasi-periodic short outbursts spanning a small fraction of the orbital period where the peak X-ray luminosity is usually below $\sim 10^{37}$ erg s^{-1}; (ii) Type-II, relatively longer and less frequent outbursts that show a significantly larger increase by three to four orders of magnitude in the X-ray luminosity reaching the Eddington limit for a neutron star accretor. The Type-II outbursts are not usually characterized by the orbital phase of the binary and are thought to persist for a significant portion of an orbital period, sometimes even stretched across multiple orbital periods. It is possible to introduce the long-lasting quiescent phase of ULX* as a result of a large orbital period of the system but it is clear that the long-term evolution of the source spanning almost two decades rules out the Type-I outburst. On the other hand, the increase in the flux by a factor of ~ 200 remains significantly lower by the increase characterizing the Type-II outburst and the outburst ULX* was observed to transition through could be considered relatively short if it were to encompass multiple orbital periods which can be reasonably assumed to be large enough to explain the long-term quiescence of the system. The distant nature of many ULX-harbouring galaxies, including M51, limits the investigation of whether an infrared excess or the presence of emission lines in the spectrum and, hence, the identification of the donor star in the majority of cases.

Background Tidal Disruption Event or Active Galactic Nucleus

The absence of bright optical or UV counterparts with comparable flux densities to the observed X-ray emissions eliminates the possibility of the source being a background quasar or blazar [Shang et al., 2011]. This lack of counterparts is not uncommon among a wider sample of ULXs. Ptak et al. [2006] found that only 28 out of 44 ULXs in their sample had optical counterparts, and only 10 showed activity in other wavelengths. On the other hand, the transient nature of the emission from ULXs is common but the observed trends are not as easily characterized by similar parameters as XRBs accreting at sub-Eddington limit, regardless of being a black hole or a neutron star. Isolated bursts on the timescales of 2-3 months across almost two decades of observing time of their host galaxies can infer the rise and decline of a tidal disruption event (TDE).

A TDE occurs when a star approaches close enough to a massive object, whose tidal field overcomes the self-gravity of the star. As a result, the star is elongated into a stream. Immediately after the first pericentre passage, half of the star is ejected while the other half remains bound. As a result, a fraction of the bound material is accreted, which generates a bright signal with a characteristic power-law decay that can last from days to years [Hills, 1975, Rees, 1988, Alexander, 2005]. TDEs have been detected across the whole electromagnetic spectrum but mostly in optical, UV, and X-ray bands [see Gezari, 2021, for a review]. Although the power mechanism of TDEs is not completely understood yet, it is possible to compare our sources with the confirmed TDE sample, especially with the ones detected in X-ray [see Saxton et al., 2020, for a review]. By doing so, we can get an idea if the TDE hypothesis is consistent with these sources or not. We use the sample collected by Gezari [2021], who compared the peak luminosity with the black-body temperature of the events [see Fig. 2 in Gezari, 2021]. In this analysis, they showed that the events can be separated between the ones detected in the optical and X-ray bands, shown as grey and black dots, respectively. To include our sources in the analysis it is necessary to assume a distance so that we can compare intrinsic properties of the events.

Assuming a distance to the source at 8.58 Mpc, the X-ray luminosities ULX* is about 5×10^{39} erg s^{-1}, which is significantly smaller than the X-ray observed sample ($10^{41} - 10^{45}$ erg s^{-1}). Given that the majority of the observed population of TDEs is observed in post-starburst galaxies at the relatively lower end of the redshift ($z < 0.5$) scale [Arcavi et al., 2014, French et al., 2016], we can assume a maximum distance at around 42.9 Mpc where this assumed limit to the distance in the TDE scenario corresponds to redshift $z \sim 0.5$. By doing so, we can position both temperature values from X2 and X3 in the region of low peak luminosities ($10^{39} - 10^{40}$ erg s^{-1}). Following our results, these observations are relatively far from the typical luminosity of the X-ray detected TDEs (about two orders of magnitude).

On the other hand, short-lived X-ray outbursts lasting only a couple of months are not expected to be observed in active galactic nuclei (AGN). AGN variability could be observed on timescales of hours to years in a subclass of this population "changing-look AGN" where the subtle changes in the obscuring column are thought to be caused by a clumpy medium located at distances much smaller than the canonical torus structure[Matt et al., 2003, LaMassa et al., 2015, Graham et al., 2020]. The rapid long-term variability on the orders of days observed in ULX* accompanied by no strong variations in the line-of-sight column density further eliminates the possibility of a background AGN nature [see Ricci and Trakhtenbrot, 2022, for a review].

4.4.4 Multiwavelength Counterparts

We extended our analysis to search for possible multiwavelength counterparts within the region corresponding to the Chandra detection. *XMM-Newton-OM* provided no detection during the outburst although it is most probably a result of the instrument's limited sensitivity to detect a companion at such large distances similar to the case of M51. Even in the case of a possible detection, it is highly unlikely that the contribution will be observed only from the companion but could correspond to a populated region which can be better resolved with *HST*. Unfortunately, *HST* did not observe the region where ULX* was detected on the same temporal frame of Chandra and XMM-Newton detections, neither during nor shortly after the outburst. We could not identify any strong candidates for counterparts in the optical range although, in different temporal frames, several sources were located within the Chandra aperture of 2 arcsec in the *UV* (see Fig. 4.1). When the metallicity of the galaxy is considered [Wei et al., 2020] in combination with the distance, we were able to identify a total of 10 possible counterparts compatible with OB-type stars and magnitudes between 23 and 26 mag. However, we cannot make any certain conclusions about these possible counterparts due to the lack of several other filters which makes it impossible to create a color-magnitude diagram.

4.5 Conclusions

We report the discovery of a new candidate ULX in M51, ULX* located at 13:29:45.46 +47:09:32.48 (J2000), which is only 5.27 arcsec away from a star cluster, consistent with ULXs found in starburst galaxies. We observed no variability in the spectral shape, the spectra remained fairly soft with $\Gamma \sim 2.6$. During the observed portion of its outburst, ULX* reaches a maximum luminosity of $\mathrm{L_x} \sim 7.6 \times 10^{38} \mathrm{ergs}^{-1}$. Given that this luminosity will be equal to or higher than the Eddington limit for a stellar-mass object, we categorize this source as a "candidate" ULX. The lack of subsequent XMM-Newton observations following X3 limits our attempt to further investigate the peak of the outburst while it is fairly reasonable to expect the maximum observed luminosity reaching $10^{39} ergs{-}1$ or even more. A detailed timing analysis revealed no detection of pulsation in X2 and X3 with an upper limit to pulsed fractions at <32 per cent and <29 per cent, respectively. We also detected no short-term variability in both of the light curves during the bright epoch. Simultaneous XMM-Newton OM and Swift-UVOT observations did not detect any counterparts in optical or UV wavelengths. The absence of emission in these longer wavelengths rules out the presence of a background quasar or a foreground star. Therefore, we conclude that the compact object is likely to be either a stellar-mass black hole or a neutron star.

The absence of pulsations with upper limits on the PFs close to the PULX regime could only help to constrain a possible geometrical configuration of the system. However, this is not enough to explain the powering mechanism of the transient nature of the event. We conclude that the source contributes to a now growing gap in our understanding of the accretion phenomenon at high mass accretion rates. It is unlikely to sustain an accretion disk that is geometrically thin at super-Eddington accretion rates assuming geometrical beaming does not result in significant amplification to the apparent luminosity. Such high and variable accretion rates are expected to result in instabilities in the innermost regions of the accretion flow due to the configuration of magnetic fields, resulting in the shredding of the disk structure halting the accretion altogether. We conclude that the lack of long-term observing campaigns of M51 limits our understanding of the properties of the system as well as the true mechanism behind the sudden disruption to the outburst.

4.6 Acknowledgments

The authors thank Luigi Stella, Jiří Horák, and K. Yavuz Eksi for the insightful discussions. A.Y. and D.L. acknowledge GAČR project No. 21-06825X for the support. A.Y. acknowledges the support from GAUK project No. 102323. D.L. acknowledges the internal grant of the Silesian University SGS/25/2024. J.S. acknowledges the support from the GAČR project 22-22643S and institutional support from RVO:67985815. The research of D.C. has been supported by the Deutsche Forschungsgemeinschaft (DFG, German Research Foundation) under Germany's Excellence Strategy - EXC 2121 - "Quantum Universe" - 390833306. S.R.S. acknowledges financial support from the Deutsches Zentrum für Luft und Raumfahrt (DLR) grant FKZ 50OR2108.

Conclusions and Discussion

Accretion disks around compact objects especially black holes in X-ray binaries are perfect environments we cannot recreate on Earth to study the behavior of matter under the influence of strong gravitational potentials around these objects. Due to the X-ray bright nature of these binary systems, continuous observing campaigns of these sources provide an exceptional set of spectra to study the formation, geometry and evolution of accretion disks. In this thesis, we used publicly available RXTE observations of GRO J1655-40 and LMC X-3 to study the evolution of accretion disks as these two sources transitioned through multiple outbursts between 1996-2012. In contrast to the previous studies, we focused on spectral analysis of the accretion disk emission using disk models that can account for the relativistic effects on the material orbiting in the closest region to the black hole. We also report the discovery of a new transient ULX candidate in M51, exhibiting an unusual long-term variability. It now contributes to a growing population of serendipitously discovered transient ULXs and challenges our current understanding of the evolution of accretion disks across a large range of observed X-ray luminosities.

We utilize this section to emphasize the main results of the research that has led to the completion of this thesis and provide a short discussion on the importance of the findings in the context of the accretion phenomenon.

Evolution of Accretion Disks Around Black Holes Across the Luminosity Scale

Accretion disks around stellar-mass black holes evolve as the system adapts to the changes in the rate at which the material is being accreted. With increasing X-ray flux, the innermost edge of the accretion disk is expected to approach the black hole which results in the further heating of the material. Meanwhile, the radiative efficiency of the accretion flow increases as the disk assumes a geometrically thin but optically thick geometry (Shakura&Sunyaev/Novikov&Thorne accretion disk solution). At this stage, the dominant cooling mechanism is presumed to be radiation. The radiative efficiency depends strongly on the black hole mass and is expected to increase up to 42% for a maximally spinning Kerr black hole. Further increase in the mass accretion rate, on the other hand, results in an additional radial cooling mechanism via advection. Consequently, the radiative efficiency of the disk starts to decrease as advective cooling gains dominance. The accretion disk geometry at this stage is expected to experience an increase in the geometrical thickness while the exact structure and components of this specific geometry are still under heated debate.

It is now a common practice to study the interplay between the different components contributing to the broadband X-ray spectrum by tracing the path a source follows in a diagram highlighting the changes in the intensity and hardness, the hardness-intensity diagram. This diagram is nearly perfectly constructed for many X-ray binaries that are known to harbor stellar-mass black holes but the further introduction of higher luminosities to the diagram is still a missing link between sub-Eddington accretion in black hole X-ray binaries and super-Eddington luminosities observed in ultraluminous X-ray sources in the context of the accretion phenomenon.

Not every outburst is identical to one another even though the properties of the binary system are not subject to dramatic changes. The 2012 outburst of GRO J1655-40 showed that the premature launching of an accretion disk wind shifted the rising arm of the q-shaped path in HID to much softer states while LMC X-3 was actually found to not have a well-constructed q-shape at all. Both black holes residing in these two systems are found to have very similar black hole masses and the inclination of the accretion disk is almost identical within a well-constrained range. This disparity in the observed HID clearly shows that even fundamentally similar black holes can in fact transition through the same accretion rates but not exhibit similar spectral properties throughout each outburst. It is also worth noting that both systems are low-mass X-ray binaries with fairly similar orbital periods.

Ultraluminous X-ray sources, however, remain on the less understood part of the X-ray bright universe. Perhaps it requires even more time to develop a better understanding of the accretion flows powering these extremely luminous events. Motta et al. [2021] recently included the ultraluminous state as an additional part of the HID, while there has been not a single source observed to remain in the ultraluminous state long enough to be identified as a ULX and yet transition through the traditional q-shaped path in the HID. They also do not follow the same trends as neutron star powered X-ray binaries. Many of the sources that exhibit a transient nature are also shown to not have significant spectral variability similar to black hole X-ray binaries even though the changes in the observed luminosities can reach as high as few orders of magnitude. This introduces a new challenge to our understanding of the interplay between the ”hard” and ”soft” emission and their origins.

The currently available accretion disk solutions unfortunately lack the connection between the sub and super-Eddington accretion regimes. Our assumptions can indeed hold for a fairly small range of observed luminosities but the current state of the technology we could/can adopt in current and future X-ray observatories limits our capabilities to study the lower end of the luminosity scale. This limitation also holds for ULXs due to their distant hosts. However, we do know that accretion flows at both ends of the luminosity scale become less radiatively efficient. For super-Eddington luminosities observed from ULXs which usually reach a couple of orders of magnitude of the Eddington limit for a stellar-mass accretor suggests that the intrinsic mass accretion rate is even higher than we can observe through radiation. This further complicates the mechanisms that can result in such extreme accretion rates through stellar evolution models. Once observed, the long-term variability of ULXs can be used to infer the nature of the accretor only in a very specific distribution of the observed luminosity. The presence of a clearly defined bimodal distribution of the observed X-ray luminosity can be attributed to the presence of a neutron star accretor. In this case, the accretion is believed to be halted due to the relative position of the magnetospheric radius and the corotation radius. This, however, requires abrupt drops in the X-ray luminosity in contrast to the clear evolution observed in black hole-powered X-ray binaries. On the other hand, continuous decreases/increases in the observed flux unfortunately cannot be interpreted as a signature of a black hole accretor similar to the presence/absence of repeated outbursts.

ULX* recently discovered in M51, with its abnormally short outburst followed by two very soft spectra, now contributes to a growing population of transient ULXs that do not show the bimodal distribution in X-ray flux but rather exhibit patterns of variability that currently cannot be categorized into any well-defined groups. However, it is now also widely assumed that this is dominantly a result of the lack of long-term observing campaigns of ULXs and the fact that these transient sources were actually identified serendipitously. We conclude that a future systematic study of spectral and timing properties of a larger sample of transient ULX will provide a larger dataset that could allow us to identify the launching and evolution of the transient event. We can then start constructing a more unified scheme of accretion onto stellar-mass accretors across the luminosity scale.

Accretion Disk Luminosity and Temperature

The most widely accepted picture describing the relationship between the observed X-ray luminosity and the accretion disk temperature is expected to result in a fairly linear distribution with a positive slope. This expectation, on the other hand, was challenged when Dunn et al. [2011] presented a global study of the accretion disks in 25 known black hole X-ray binaries and showed that a significant portion of their sample revealed a turnover in the disk temperatures once the observed luminosity reaches a seemingly critical value. These results introduced a new layer of uncertainty in our understanding of how this accretion disk temperature evolves with increasing luminosity. The picture now included many observations that seemed to have similar fluxes as some others but somehow presented themselves as if the disk temperature was observed to be higher. This behavior suggested that a continuous increase in the accretion disk temperature is not directly correlated with only the increasing mass accretion rate. The fact that many sources had this pattern across multiple outbursts was taken as a sign of either an additional change in one of the components we did not account for or a specific state the rest of the sample could not enter. Each scenario eventually reduces down to the mass accretion rate as the main indicator.

The comparison of GRO J1655-40 and LMC X-3 showed this turnover does not have a dependency on the observed luminosity. GRO J1655-40 seems to enter its most luminous state barely reaching 10% of the Eddington limit while LMC X-3 was observed to reach as high as $> 40\%$ for their respective black hole masses. One of the arguments Dunn et al. [2011] provided was that these deviations could have been at specific stages of the evolution where the photons emitted from the disk surface are up-scattered to higher energies within a more prominent accretion disk atmosphere. This is also fairly easy to trace in Figure 3.4 where the diagonal lines represent different values of the color correction factor f_{col}. This appears reasonable, the color temperature is higher than the effective disk temperature with increasing mass accretion rates and hence observed luminosities.

As described in Yilmaz et al. [2023] in Chapter 3, the results showed that the patterns of evolution in both sources presented cannot be explained by the variable color-correction factor when left as a free parameter in the spectral analysis. The assumed value for the parameter is dominantly taken at 1.7 and this correction was not included in the primordial set of accretion disk models. When allowed to vary within reasonable limits, the parameter seemed to follow a similar pattern that was observed in the disk temperature (Figure 3.8) while having almost no contribution to the slope turnover in the relationship between disk luminosity and temperature of GRO J1655-40. It is not straightforward to study the true value of the color correction factor using a model that did not include a self-consistent description of the disk atmosphere. The results only suggested that this parameter was not the dominant driving mechanism behind the observed overall pattern.

It was only after introducing a new accretion disk model, `kynbb`, that we were able to see a significant change in the observed slope when we allowed the inner edge of the accretion disk to vary throughout the outburst. The recovery of these observations of GRO J1655-40 suggests the proper modeling of the accretion disk emission in states where the accretion disk resides at distances closest to the black hole is much more important than previously anticipated.

Similar to the case of both GRO J1655-40 and LMC X-3, Dunn et al. [2011] showed that there is a dichotomy in the patterns exhibited in the observed disk luminosity-temperature relationship. Sources that had long-term observing campaigns allowed a better look at the evolution of the accretion disks for each individual source as well as each outburst. Similar to GRO J1655-40, GX339-4, H1743-322, XTE J1550-564 and 4U 1630-47 showed observed deviations while XTE J1817-330 and XTE J1720-318 exhibited a similar trend as LMC X-3. On the other hand, LMC X-1 and XTE J1650-500 were only observed in the states with negative slopes.

The apparent inconsistency in the observed disk luminosity-temperature trend challenges our understanding of the accretion phenomenon and the evolution of accretion disks around black holes in X-ray binaries throughout their lifetime. The long-term observing campaigns of LMC X-1 and XTE J1650-500 provided an important set of observations that might provide the missing link between the known black hole X-ray binaries observed to be accreting at sub-Eddington regimes and a sample of ultraluminous X-ray sources that were found to exhibit patterns that the currently available models cannot explain. M82 X-1, for example, was argued to be one of the strongest candidates to host an intermediate-mass black hole. Unlike many of the other sources showing long-term variability, M82 X-1 presented a similar trend to LMC X-1 and XTE J17650-500. The similarities between these states that the known black hole X-ray binaries transition through and a further study of the spectral and timing evolution of M82 X-1 definitely is a link that needs to be investigated more to develop a better understanding of the accretion physics across such a large range of the observed X-ray luminosities. Our results provided a new insight into the long-term evolution of GRO J1655-40, a more detailed study connecting the two ends of the luminosity scale will be made possible with longer observing campaigns of many more ULXs and with the newly developing observatories to be launched in the next couple of decades. The NewAthena (Advanced Telescope for High Energy Astrophysics, expected to be operational in the late 2030s) alongside the Einstein Probe (launched early 2024) and XRISM (launched Autumn of 2023) will further improve our understanding of the interplay between different components contributing to the formation and evolution of both XRBs and ULXs.

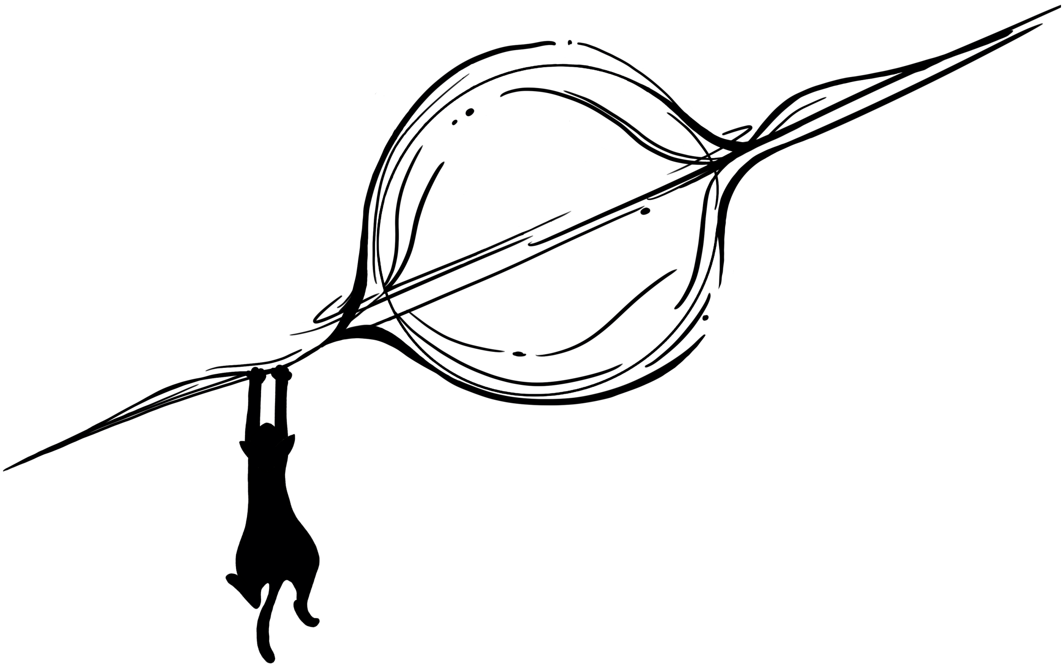

”Ignorance more frequently begets confidence than does knowledge: it is those who know little, and not those who know much, who so positively assert that this or that problem will never be solved by science.”

Charles Darwin

Bibliography

David Abarca, Kyle Parfrey, and Włodek Kluźniak. Beamed Emission from a Neutron-star ULX in a GRRMHD Simulation. , 917(2):L31, August 2021. doi: 10.3847/2041-8213/ac1859.

M. Abramowicz, M. Jaroszynski, and M. Sikora. Relativistic, accreting disks. , 63:221–224, February 1978.

M. A. Abramowicz and W. Kluźniak. A precise determination of black hole spin in GRO J1655-40. , 374:L19–L20, August 2001. doi: 10.1051/0004-6361:20010791.

M. A. Abramowicz, B. Czerny, J. P. Lasota, and E. Szuszkiewicz. Slim Accretion Disks. , 332:646, September 1988. doi: 10.1086/166683.

Tal Alexander. Stellar processes near the massive black hole in the Galactic center [review article]. , 419(2-3):65–142, November 2005. doi: 10.1016/j.physrep.2005.08.002.

E. Anders and N. Grevesse. Abundances of the elements - Meteoritic and solar. , 53:197–214, January 1989. doi: 10.1016/0016-7037(89)90286-X.

Iair Arcavi, Avishay Gal-Yam, Mark Sullivan, Yen-Chen Pan, S. Bradley Cenko, Assaf Horesh, Eran O. Ofek, Annalisa De Cia, Lin Yan, Chen-Wei Yang, D. A. Howell, David Tal, Shrinivas R. Kulkarni, Shriharsh P. Tendulkar, Sumin Tang, Dong Xu, Assaf Sternberg, Judith G. Cohen, Joshua S. Bloom, Peter E. Nugent, Mansi M. Kasliwal, Daniel A. Perley, Robert M. Quimby, Adam A. Miller, Christopher A. Theissen, and Russ R. Laher. A Continuum of H- to He-rich Tidal Disruption Candidates With a Preference for E+A Galaxies. , 793(1):38, September 2014. doi: 10.1088/0004-637X/793/1/38.

K. A. Arnaud. XSPEC: The First Ten Years. In George H. Jacoby and Jeannette Barnes, editors, *Astronomical Data Analysis Software and Systems V*, volume 101 of *Astronomical Society of the Pacific Conference Series*, page 17, January 1996.

Jonathan Arons. Photon Bubbles: Overstability in a Magnetized Atmosphere. , 388:561, April 1992. doi: 10.1086/171174.

M. Bachetti, F. A. Harrison, D. J. Walton, B. W. Grefenstette, D. Chakrabarty, F. Fürst, D. Barret, A. Beloborodov, S. E. Boggs, and F. E. Christensen. An ultraluminous X-ray source powered by an accreting neutron star. , 514:202–204, October 2014a. doi: 10.1038/nature13791.

M. Bachetti, F. A. Harrison, D. J. Walton, B. W. Grefenstette, D. Chakrabarty, F. Fürst, D. Barret, A. Beloborodov, S. E. Boggs, and F. E. Christensen. An ultraluminous X-ray source powered by an accreting neutron star. , 514:202–204, October 2014b. doi: 10.1038/nature13791.

Scott D. Barthelmy, Louis M. Barbier, Jay R. Cummings, Ed E. Fenimore, Neil Gehrels, Derek Hullinger, Hans A. Krimm, Craig B. Markwardt, David M.

Palmer, Ann Parsons, Goro Sato, Masaya Suzuki, Tadayuki Takahashi, Makota Tashiro, and Jack Tueller. The Burst Alert Telescope (BAT) on the SWIFT Midex Mission. , 120(3-4):143–164, October 2005. doi: 10.1007/s11214-005-5096-3.

Martin E. Beer and Philipp Podsiadlowski. The quiescent light curve and the evolutionary state of GRO J1655-40. , 331(2):351–360, March 2002. doi: 10.1046/j.1365-8711.2002.05189.x.

Mitchell C. Begelman. Super-Eddington Fluxes from Thin Accretion Disks? , 568(2):L97–L100, April 2002. doi: 10.1086/340457.

T. M. Belloni, S. E. Motta, and T. Muñoz-Darias. Black hole transients. *Bulletin of the Astronomical Society of India*, 39(3):409–428, September 2011.

Tomaso M. Belloni and Sara E. Motta. Transient Black Hole Binaries. In Cosimo Bambi, editor, *Astrophysics of Black Holes: From Fundamental Aspects to Latest Developments*, volume 440 of *Astrophysics and Space Science Library*, page 61, January 2016. doi: 10.1007/978-3-662-52859-4_2.

C. T. Berghea, K. A. Weaver, E. J. M. Colbert, and T. P. Roberts. Testing the Paradigm that Ultraluminous X-Ray Sources as a Class Represent Accreting Intermediate-Mass Black Holes. , 687(1):471–487, November 2008. doi: 10.1086/591722.

Ciprian T. Berghea, Megan C. Johnson, Nathan J. Secrest, Rachel P. Dudik, Gregory S. Hennessy, and Aisha El-khatib. Detection of a Radio Bubble around the Ultraluminous X-Ray Source Holmberg IX X-1. , 896(2):117, June 2020. doi: 10.3847/1538-4357/ab9108.

G. R. Bhuvana, D. Radhika, V. K. Agrawal, S. Mandal, and A. Nandi. Broadband 'spectro-temporal' features of extragalactic black hole binaries LMC X-1 and LMC X-3: an AstroSat perspective. , 501(4):5457–5467, March 2021. doi: 10.1093/mnras/staa4012.

G. R. Bhuvana, D. Radhika, and Anuj Nandi. Multi-mission view of extragalactic black hole X-ray binaries LMC X-1 and LMC X-3: Evolution of broadband spectral features. *Advances in Space Research*, 69(1):483–498, January 2022. doi: 10.1016/j.asr.2021.09.036.

R. D. Blandford and A. Königl. Relativistic jets as compact radio sources. , 232: 34–48, August 1979. doi: 10.1086/157262.

R. D. Blandford and D. G. Payne. Hydromagnetic flows from accretion disks and the production of radio jets. , 199:883–903, June 1982. doi: 10.1093/mnras/199.4.883.

R. D. Blandford and R. L. Znajek. Electromagnetic extraction of energy from Kerr black holes. , 179:433–456, May 1977. doi: 10.1093/mnras/179.3.433.

H. Bondi. On spherically symmetrical accretion. , 112:195, January 1952. doi: 10.1093/mnras/112.2.195.

Patricia T. Boyd, Alan P. Smale, Jeroen Homan, Peter G. Jonker, Michiel van der Klis, and Erik Kuulkers. Canonical Timing and Spectral Behavior of LMC X-3 in the Low/Hard State. , 542(2):L127–L130, October 2000. doi: 10.1086/312931.

H. V. Bradt, R. E. Rothschild, and J. H. Swank. X-ray timing explorer mission. , 97(1):355–360, January 1993.

W. N. Brandt and N. S. Schulz. The Discovery of Broad P Cygni X-Ray Lines from Circinus X-1 with the Chandra High-Energy Transmission Grating Spectrometer. , 544(2):L123–L127, December 2000. doi: 10.1086/317313.

M. Brightman, F. A. Harrison, F. Fürst, M. J. Middleton, D. J. Walton, D. Stern, A. C. Fabian, M. Heida, D. Barret, and M. Bachetti. Magnetic field strength of a neutron-star-powered ultraluminous X-ray source. *Nature Astronomy*, 2: 312–316, February 2018. doi: 10.1038/s41550-018-0391-6.

Murray Brightman, Fiona Harrison, Dominic J. Walton, Felix Fuerst, Ann Hornschemeier, Andreas Zezas, Matteo Bachetti, Brian Grefenstette, Andrew Ptak, Shriharsh Tendulkar, and Mihoko Yukita. Spectral and Temporal Properties of the Ultraluminous X-Ray Pulsar in M82 from 15 years of Chandra Observations and Analysis of the Pulsed Emission Using NuSTAR. , 816(2):60, January 2016. doi: 10.3847/0004-637X/816/2/60.

Murray Brightman, Hannah Earnshaw, Felix Fürst, Fiona A. Harrison, Marianne Heida, Gianluca Israel, Sean Pike, Daniel Stern, and Dominic J. Walton. Swift Monitoring of M51: A 38 day Superorbital Period for the Pulsar ULX7 and a New Transient Ultraluminous X-Ray Source. , 895(2):127, June 2020. doi: 10.3847/1538-4357/ab7e2a.

Murray Brightman, Jean-Marie Hameury, Jean-Pierre Lasota, Ranieri D. Baldi, Gabriele Bruni, Jenna M. Cann, Hannah Earnshaw, Felix Fürst, Marianne Heida, Amruta Jaodand, Margaret Lazzarini, Matthew J. Middleton, Dominic J. Walton, and Kimberly A. Weaver. A New Sample of Transient Ultraluminous X-Ray Sources Serendipitously Discovered by Swift/XRT. , 951 (1):51, July 2023. doi: 10.3847/1538-4357/acd18a.

A. C. Brinkman, J. J. van Rooijen, J. A. M. Bleeker, J. H. Dijkstra, J. Heise, P. A. J. de Korte, R. Mewe, and F. Paerels. Low Energy X-Ray Transmission Grating Spectrometer for AXAF. *Astrophysical Letters and Communications*, 26:73, January 1987.

J. Buchner, A. Georgakakis, K. Nandra, L. Hsu, C. Rangel, M. Brightman, A. Merloni, M. Salvato, J. Donley, and D. Kocevski. X-ray spectral modelling of the AGN obscuring region in the CDFS: Bayesian model selection and catalogue. , 564:A125, April 2014. doi: 10.1051/0004-6361/201322971.

Johannes Buchner. A statistical test for Nested Sampling algorithms. *Statistics and Computing*, 26(1-2):383–392, January 2016. doi: 10.1007/s11222-014-9512-y.

Johannes Buchner. Collaborative Nested Sampling: Big Data versus Complex Physical Models. , 131(1004):108005, October 2019. doi: 10.1088/1538-3873/aae7fc.

Johannes Buchner. UltraNest - a robust, general purpose Bayesian inference engine. *The Journal of Open Source Software*, 6(60):3001, April 2021. doi: 10.21105/joss.03001.

David N. Burrows, J. E. Hill, J. A. Nousek, J. A. Kennea, A. Wells, J. P. Osborne, A. F. Abbey, A. Beardmore, K. Mukerjee, A. D. T. Short, G. Chincarini, S. Campana, O. Citterio, A. Moretti, C. Pagani, G. Tagliaferri, P. Giommi, M. Capalbi, F. Tamburelli, L. Angelini, G. Cusumano, H. W. Bräuninger, W. Burkert, and G. D. Hartner. The Swift X-Ray Telescope. , 120(3-4):165–195, October 2005. doi: 10.1007/s11214-005-5097-2.

V. Canuto, J. Lodenquai, and M. Ruderman. Thomson Scattering in a Strong Magnetic Field. , 3(10):2303–2308, May 1971. doi: 10.1103/PhysRevD.3.2303.

S. Carpano, F. Haberl, C. Maitra, and G. Vasilopoulos. Discovery of pulsations from NGC 300 ULX1 and its fast period evolution. , 476(1):L45–L49, May 2018. doi: 10.1093/mnrasl/sly030.

W. Cash. Parameter estimation in astronomy through application of the likelihood ratio. , 228:939–947, March 1979. doi: 10.1086/156922.

Pablo Cerda-Duran and Nancy Elias-Rosa. Neutron Stars Formation and Core Collapse Supernovae. In Luciano Rezzolla, Pierre Pizzochero, David Ian Jones, Nanda Rea, and Isaac Vidaña, editors, *Astrophysics and Space Science Library*, volume 457 of *Astrophysics and Space Science Library*, page 1, January 2018. doi: 10.1007/978-3-319-97616-7_1.

P. Chainakun, A. Watcharangkool, A. J. Young, and S. Hancock. X-ray time lags in AGN: inverse-Compton scattering and spherical corona model. , 487(1): 667–680, July 2019. doi: 10.1093/mnras/stz1319.

Sandip Chakrabarti and Lev G. Titarchuk. Spectral Properties of Accretion Disks around Galactic and Extragalactic Black Holes. , 455:623, December 1995. doi: 10.1086/176610.

E. J. M. Colbert and R. F. Mushotzky. The Nature of Accreting Black Holes in Nearby Galaxy Nuclei. , 519:89–107, July 1999. doi: 10.1086/307356.

S. Corbel, R. P. Fender, A. K. Tzioumis, M. Nowak, V. McIntyre, P. Durouchoux, and R. Sood. Coupling of the X-ray and radio emission in the black hole candidate and compact jet source GX 339-4. , 359:251–268, July 2000.

S. Corbel, M. A. Nowak, R. P. Fender, A. K. Tzioumis, and S. Markoff. Radio/X-ray correlation in the low/hard state of GX 339-4. , 400:1007–1012, March 2003. doi: 10.1051/0004-6361:20030090.

Steven R. Cranmer and Amy R. Winebarger. The Properties of the Solar Corona and Its Connection to the Solar Wind. , 57:157–187, August 2019. doi: 10.1146/annurev-astro-091918-104416.

Wei Cui. Evidence for “Propeller” Effects in X-Ray Pulsars GX 1+4 and GRO J1744-28. , 482(2):L163–L166, June 1997. doi: 10.1086/310712.

C. T. Cunningham. The effects of redshifts and focusing on the spectrum of an accretion disk around a Kerr black hole. , 202:788–802, December 1975. doi: 10.1086/154033.

Kristen C. Dage, Noah Vowell, Erica Thygesen, Arash Bahramian, Daryl Haggard, Konstantinos Kovlakas, Arunav Kundu, Thomas J. Maccarone, Jay Strader, Ryan Urquhart, and Stephen E. Zepf. Ultraluminous X-ray sources in seven edge-on spiral galaxies. , 508(3):4008–4016, December 2021. doi: 10.1093/mnras/stab2850.

C. D’Angelo, D. Giannios, C. Dullemond, and H. Spruit. Soft X-ray components in the hard state of accreting black holes. , 488(2):441–450, September 2008. doi: 10.1051/0004-6361:200809781.

Shane W. Davis, Omer M. Blaes, Ivan Hubeny, and Neal J. Turner. Relativistic Accretion Disk Models of High-State Black Hole X-Ray Binary Spectra. , 621 (1):372–387, March 2005. doi: 10.1086/427278.

Shane W. Davis, Chris Done, and Omer M. Blaes. Testing Accretion Disk Theory in Black Hole X-Ray Binaries. , 647(1):525–538, August 2006. doi: 10.1086/505386.

G. C. Dewangan, L. Titarchuk, and R. E. Griffiths. Black Hole Mass of the Ultraluminous X-Ray Source M82 X-1. , 637:L21–L24, January 2006. doi: 10.1086/499235.

Jason Dexter and Omer Blaes. A model of the steep power-law spectra and high-frequency quasi-periodic oscillations in luminous black hole X-ray binaries. , 438(4):3352–3357, March 2014. doi: 10.1093/mnras/stu121.

M. Díaz Trigo and L. Boirin. Accretion disc atmospheres and winds in low-mass X-ray binaries. *Astronomische Nachrichten*, 337(4-5):368, May 2016. doi: 10.1002/asna.201612315.

M. Díaz Trigo, L. Sidoli, L. Boirin, and A. N. Parmar. XMM-Newton observations of GX 13 + 1: correlation between photoionised absorption and broad line emission. , 543:A50, July 2012. doi: 10.1051/0004-6361/201219049.

Chris Done, Marek Gierliński, and Aya Kubota. Modelling the behaviour of accretion flows in X-ray binaries. Everything you always wanted to know about accretion but were afraid to ask. , 15(1):1–66, December 2007. doi: 10.1007/s00159-007-0006-1.

M. Dovčiak, V. Karas, and T. Yaqoob. An Extended Scheme for Fitting X-Ray Data with Accretion Disk Spectra in the Strong Gravity Regime. , 153(1): 205–221, July 2004. doi: 10.1086/421115.

M. Dovčiak, F. Muleri, R. W. Goosmann, V. Karas, and G. Matt. Thermal disc emission from a rotating black hole: X-ray polarization signatures. , 391(1):

32–38, November 2008. doi: 10.1111/j.1365-2966.2008.13872.x10.48550/arXiv.0809.0418.

R. J. H. Dunn, R. P. Fender, E. G. Körding, C. Cabanac, and T. Belloni. Studying the X-ray hysteresis in GX 339-4: the disc and iron line over one decade. , 387 (2):545–563, June 2008. doi: 10.1111/j.1365-2966.2008.13258.x.

R. J. H. Dunn, R. P. Fender, E. G. Körding, T. Belloni, and C. Cabanac. A global spectral study of black hole X-ray binaries. , 403(1):61–82, March 2010. doi: 10.1111/j.1365-2966.2010.16114.x.

R. J. H. Dunn, R. P. Fender, E. G. Körding, T. Belloni, and A. Merloni. A global study of the behaviour of black hole X-ray binary discs. , 411(1):337–348, February 2011. doi: 10.1111/j.1365-2966.2010.17687.x.

H. P. Earnshaw, T. P. Roberts, and R. Sathyaprakash. Searching for propeller-phase ULXs in the XMM-Newton Serendipitous Source Catalogue. , 476(3): 4272–4277, May 2018a. doi: 10.1093/mnras/sty501.

H. P. Earnshaw, T. P. Roberts, and R. Sathyaprakash. Searching for propeller-phase ULXs in the XMM-Newton Serendipitous Source Catalogue. , 476:4272–4277, May 2018b. doi: 10.1093/mnras/sty501.

H. P. Earnshaw, T. P. Roberts, M. J. Middleton, D. J. Walton, and S. Mateos. A new, clean catalogue of extragalactic non-nuclear X-ray sources in nearby galaxies. , 483:5554–5573, March 2019a. doi: 10.1093/mnras/sty3403.

H. P. Earnshaw, T. P. Roberts, M. J. Middleton, D. J. Walton, and S. Mateos. A new, clean catalogue of extragalactic non-nuclear X-ray sources in nearby galaxies. , 483:5554–5573, March 2019b. doi: 10.1093/mnras/sty3403.

Hannah P. Earnshaw, Marianne Heida, Murray Brightman, Felix Fürst, Fiona A. Harrison, Amruta Jaodand, Matthew J. Middleton, Timothy P. Roberts, Rajath Sathyaprakash, Daniel Stern, and Dominic J. Walton. The (Re)appearance of NGC 925 ULX-3, a New Transient ULX. , 891(2):153, March 2020. doi: 10.3847/1538-4357/ab77b8.

K. Ebisawa. X-Ray Spectroscopy of Binary Sources with ASCA - Black Hole Candidates and Super-Soft Sources. In F. Makino and K. Mitsuda, editors, *X-Ray Imaging and Spectroscopy of Cosmic Hot Plasmas*, page 427, January 1997.

A. Einstein. Die Grundlage der allgemeinen Relativitätstheorie. *Annalen der Physik*, 354(7):769–822, January 1916. doi: 10.1002/andp.19163540702.

Albert Einstein. Die Feldgleichungen der Gravitation. *Sitzungsberichte der Königlich Preussischen Akademie der Wissenschaften*, pages 844–847, January 1915.

Ann A. Esin, Jeffrey E. McClintock, and Ramesh Narayan. Advection-Dominated Accretion and the Spectral States of Black Hole X-Ray Binaries: Application to Nova Muscae 1991. , 489(2):865–889, November 1997. doi: 10.1086/304829.

P. A. Evans, A. P. Beardmore, K. L. Page, J. P. Osborne, P. T. O'Brien, R. Willingale, R. L. C. Starling, D. N. Burrows, O. Godet, L. Vetere, J. Racusin, M. R. Goad, K. Wiersema, L. Angelini, M. Capalbi, G. Chincarini, N. Gehrels, J. A. Kennea, R. Margutti, D. C. Morris, C. J. Mountford, C. Pagani, M. Perri, P. Romano, and N. Tanvir. Methods and results of an automatic analysis of a complete sample of Swift-XRT observations of GRBs. , 397(3):1177–1201, August 2009. doi: 10.1111/j.1365-2966.2009.14913.x.

S. N. Fabrika, K. E. Atapin, A. S. Vinokurov, and O. N. Sholukhova. Ultraluminous X-Ray Sources. *Astrophysical Bulletin*, 76(1):6–38, January 2021. doi: 10.1134/S1990341321010077.

Heino Falcke and Peter L. Biermann. The jet/disk symbiosis. III. What the radio cores in GRS 1915+105, NGC 4258, M 81 and SGR A* tell us about accreting black holes. , 342:49–56, February 1999. doi: 10.48550/arXiv.astro-ph/9810226.

R. P. Fender. Powerful jets from black hole X-ray binaries in low/hard X-ray states. , 322(1):31–42, March 2001. doi: 10.1046/j.1365-8711.2001.04080.x.

R. P. Fender, S. T. Garrington, D. J. McKay, T. W. B. Muxlow, G. G. Pooley, R. E. Spencer, A. M. Stirling, and E. B. Waltman. MERLIN observations of relativistic ejections from GRS 1915+105. , 304(4):865–876, April 1999. doi: 10.1046/j.1365-8711.1999.02364.x.

R. P. Fender, T. M. Belloni, and E. Gallo. Towards a unified model for black hole X-ray binary jets. , 355(4):1105–1118, December 2004. doi: 10.1111/j.1365-2966.2004.08384.x.

Rob Fender and Tomaso Belloni. Stellar-Mass Black Holes and Ultraluminous X-ray Sources. *Science*, 337(6094):540, August 2012. doi: 10.1126/science.1221790.

Rob Fender and Elena Gallo. An Overview of Jets and Outflows in Stellar Mass Black Holes. , 183(1-4):323–337, September 2014. doi: 10.1007/s11214-014-0069-z.

Rob Fender and Teo Muñoz-Darias. The Balance of Power: Accretion and Feedback in Stellar Mass Black Holes. In Francesco Haardt, Vittorio Gorini, Ugo Moschella, Aldo Treves, and Monica Colpi, editors, *Lecture Notes in Physics, Berlin Springer Verlag*, volume 905, page 65. 2016. doi: 10.1007/978-3-319-19416-5_3.

Hua Feng and Philip Kaaret. A Comparison of Ultraluminous X-Ray Sources in NGC 1399 and the Antennae Galaxies (NGC 4038/4039). , 653(1):536–544, December 2006. doi: 10.1086/508141.

C. Foellmi, E. Depagne, T. H. Dall, and I. F. Mirabel. On the distance of GRO J1655-40. , 457(1):249–255, October 2006. doi: 10.1051/0004-6361:20054686.

K. Decker French, Iair Arcavi, and Ann Zabludoff. Tidal Disruption Events Prefer Unusual Host Galaxies. , 818(1):L21, February 2016. doi: 10.3847/2041-8205/818/1/L21.

F. Fürst, D. J. Walton, F. A. Harrison, D. Stern, D. Barret, M. Brightman, A. C. Fabian, B. Grefenstette, K. K. Madsen, M. J. Middleton, J. M. Miller, K. Pottschmidt, A. Ptak, V. Rana, and N. Webb. Discovery of Coherent Pulsations from the Ultraluminous X-Ray Source NGC 7793 P13. , 831:L14, November 2016. doi: 10.3847/2041-8205/831/2/L14.

F. Fürst, D. J. Walton, M. Heida, M. Bachetti, C. Pinto, M. J. Middleton, M. Brightman, H. P. Earnshaw, D. Barret, A. C. Fabian, P. Kretschmar, K. Pottschmidt, A. Ptak, T. Roberts, D. Stern, N. Webb, and J. Wilms. Long-term pulse period evolution of the ultra-luminous X-ray pulsar NGC 7793 P13. , 651:A75, July 2021. doi: 10.1051/0004-6361/202140625.

Charles F. Gammie. Photon bubbles in accretion discs. , 297(3):929–935, July 1998. doi: 10.1046/j.1365-8711.1998.01571.x.

Charles F. Gammie. Efficiency of Magnetized Thin Accretion Disks in the Kerr Metric. , 522(1):L57–L60, September 1999. doi: 10.1086/312207.

Javier A. García, Jeffrey E. McClintock, James F. Steiner, Ronald A. Remillard, and Victoria Grinberg. An Empirical Method for Improving the Quality of RXTE PCA Spectra. , 794(1):73, October 2014. doi: 10.1088/0004-637X/794/1/73.

G. P. Garmire. AXAF CCD Imaging Spectrometer (ACIS). In *American Astronomical Society Meeting Abstracts #190*, volume 190 of *American Astronomical Society Meeting Abstracts*, page 34.04, May 1997.

N. Gehrels and Swift. The Swift Gamma-Ray Burst Mission. In *American Astronomical Society Meeting Abstracts*, volume 205 of *American Astronomical Society Meeting Abstracts*, page 116.01, December 2004.

N. Gehrels, G. Chincarini, P. Giommi, K. O. Mason, J. A. Nousek, A. A. Wells, N. E. White, S. D. Barthelmy, D. N. Burrows, L. R. Cominsky, K. C. Hurley, F. E. Marshall, P. Mészáros, P. W. A. Roming, L. Angelini, L. M. Barbier, T. Belloni, S. Campana, P. A. Caraveo, M. M. Chester, O. Citterio, T. L. Cline, M. S. Cropper, J. R. Cummings, A. J. Dean, E. D. Feigelson, E. E. Fenimore, D. A. Frail, A. S. Fruchter, G. P. Garmire, K. Gendreau, G. Ghisellini, J. Greiner, J. E. Hill, S. D. Hunsberger, H. A. Krimm, S. R. Kulkarni, P. Kumar, F. Lebrun, N. M. Lloyd-Ronning, C. B. Markwardt, B. J. Mattson, R. F. Mushotzky, J. P. Norris, J. Osborne, B. Paczynski, D. M. Palmer, H. S. Park, A. M. Parsons, J. Paul, M. J. Rees, C. S. Reynolds, J. E. Rhoads, T. P. Sasseen, B. E. Schaefer, A. T. Short, A. P. Smale, I. A. Smith, L. Stella, G. Tagliaferri, T. Takahashi, M. Tashiro, L. K. Townsley, J. Tueller, M. J. L. Turner, M. Vietri, W. Voges, M. J. Ward, R. Willingale, F. M. Zerbi, and W. W. Zhang. The Swift Gamma-Ray Burst Mission. , 611(2):1005–1020, August 2004. doi: 10.1086/422091.

Suvi Gezari. Tidal Disruption Events. , 59:21–58, September 2021. doi: 10.1146/annurev-astro-111720-030029.

R. Giacconi, G. Branduardi, U. Briel, A. Epstein, D. Fabricant, E. Feigelson, W. Forman, P. Gorenstein, J. Grindlay, H. Gursky, F. R. Harnden, J. P. Henry, C. Jones, E. Kellogg, D. Koch, S. Murray, E. Schreier, F. Seward, H. Tananbaum, K. Topka, L. Van Speybroeck, S. S. Holt, R. H. Becker, E. A. Boldt, P. J. Serlemitsos, G. Clark, C. Canizares, T. Markert, R. Novick, D. Helfand, and K. Long. The Einstein (HEAO 2) X-ray Observatory. , 230:540–550, June 1979. doi: 10.1086/157110.

Marek Gierliński and Chris Done. Black hole accretion discs: reality confronts theory. , 347(3):885–894, January 2004. doi: 10.1111/j.1365-2966.2004.07266.x.

Marek Gierliński, Andrzej A. Zdziarski, Juri Poutanen, Paolo S. Coppi, Ken Ebisawa, and W. Neil Johnson. Radiation mechanisms and geometry of Cygnus X-1 in the soft state. , 309(2):496–512, October 1999. doi: 10.1046/j.1365-8711.1999.02875.x.

Marek Gierliński, Andrzej Maciołek-Niedźwiecki, and Ken Ebisawa. Application of a relativistic accretion disc model to X-ray spectra of LMC X-1 and GRO J1655-40. , 325(3):1253–1265, August 2001. doi: 10.1046/j.1365-8711.2001.04540.x.

Jeanette C. Gladstone, Timothy P. Roberts, and Chris Done. The ultraluminous state. , 397(4):1836–1851, August 2009. doi: 10.1111/j.1365-2966.2009.15123.x.

Matthew J. Graham, Nicholas P. Ross, Daniel Stern, Andrew J. Drake, Barry McKernan, K. E. Saavik Ford, S. G. Djorgovski, Ashish A. Mahabal, Eilat Glikman, Steve Larson, and Eric Christensen. Understanding extreme quasar optical variability with CRTS - II. Changing-state quasars. , 491(4):4925–4948, February 2020. doi: 10.1093/mnras/stz3244.

Jenny Greene, Charles D. Bailyn, and Jerome A. Orosz. Optical and Infrared Photometry of the Microquasar GRO J1655-40 in Quiescence. , 554(2):1290–1297, June 2001. doi: 10.1086/321411.

F. Grisé, P. Kaaret, S. Corbel, H. Feng, D. Cseh, and L. Tao. Optical Emission of the Ultraluminous X-Ray Source NGC 5408 X-1: Donor Star or Irradiated Accretion Disk? , 745(2):123, February 2012. doi: 10.1088/0004-637X/745/2/123.

D. E. Gruber, P. R. Blanco, W. A. Heindl, M. R. Pelling, R. E. Rothschild, and P. L. Hink. The high energy X-ray timing experiment on XTE. , 120:641–644, December 1996.

A. Gúrpide, M. Parra, O. Godet, T. Contini, and J. F. Olive. MUSE spectroscopy of the ULX NGC 1313 X-1: A shock-ionised bubble, an X-ray photoionised nebula, and two supernova remnants. , 666:A100, October 2022. doi: 10.1051/0004-6361/202142229.

F. Haardt and L. Maraschi. A Two-Phase Model for the X-Ray Emission from Seyfert Galaxies. , 380:L51, October 1991. doi: 10.1086/186171.

Francesco Haardt and Laura Maraschi. X-Ray Spectra from Two-Phase Accretion Disks. , 413:507, August 1993. doi: 10.1086/173020.

A. Heger, C. L. Fryer, S. E. Woosley, N. Langer, and D. H. Hartmann. How Massive Single Stars End Their Life. , 591(1):288–300, July 2003. doi: 10.1086/375341.

J. G. Hills. Possible power source of Seyfert galaxies and QSOs. , 254(5498): 295–298, March 1975. doi: 10.1038/254295a0.

Akira Hirano, Shunji Kitamoto, Tatsuya T. Yamada, Shin Mineshige, and Jun Fukue. Accretion Disk Structure and Branch Behavior of Cygnus X-2. , 446: 350, June 1995. doi: 10.1086/175793.

R. M. Hjellming and M. P. Rupen. Episodic ejection of relativistic jets by the X-ray transient GRO J1655 - 40. , 375(6531):464–468, June 1995. doi: 10.1038/375464a0.

Jeroen Homan and Tomaso Belloni. The Evolution of Black Hole States. , 300 (1-3):107–117, November 2005. doi: 10.1007/s10509-005-1197-4.

Daniela Huppenkothen, Matteo Bachetti, Abigail L. Stevens, Simone Migliari, Paul Balm, Omar Hammad, Usman Mahmood Khan, Himanshu Mishra, Haroon Rashid, Swapnil Sharma, Evandro Martinez Ribeiro, and Ricardo Valles Blanco. Stingray: A Modern Python Library for Spectral Timing. , 881(1):39, August 2019. doi: 10.3847/1538-4357/ab258d.

Narae Hwang and Myung Gyoon Lee. A Catalog of Bright Star Clusters in the Interacting Galaxy M51. , 135(4):1567–1579, April 2008. doi: 10.1088/0004-6256/135/4/1567.

A. F. Illarionov and R. A. Sunyaev. Why the Number of Galactic X-ray Stars Is so Small? , 39:185, February 1975.

Jimmy A. Irwin, W. Peter Maksym, Gregory R. Sivakoff, Aaron J. Romanowsky, Dacheng Lin, Tyler Speegle, Ian Prado, David Mildebrath, Jay Strader, Jifeng Liu, and Jon M. Miller. Ultraluminous X-ray bursts in two ultracompact companions to nearby elliptical galaxies. , 538(7625):356–358, October 2016. doi: 10.1038/nature19822.

G. L. Israel, A. Belfiore, L. Stella, P. Esposito, P. Casella, A. De Luca, M. Marelli, A. Papitto, M. Perri, S. Puccetti, G. A. R. Castillo, D. Salvetti, A. Tiengo, L. Zampieri, and D. D'Agostino. An accreting pulsar with extreme properties drives an ultraluminous x-ray source in NGC 5907. *Science*, 355:817–819, February 2017a. doi: 10.1126/science.aai8635.

G. L. Israel, A. Belfiore, L. Stella, P. Esposito, P. Casella, A. De Luca, M. Marelli, A. Papitto, M. Perri, S. Puccetti, G. A. R. Castillo, D. Salvetti, A. Tiengo, L. Zampieri, and D. D'Agostino. An accreting pulsar with extreme properties drives an ultraluminous x-ray source in NGC 5907. *Science*, 355:817–819, February 2017b. doi: 10.1126/science.aai8635.

G. L. Israel, A. Papitto, P. Esposito, L. Stella, L. Zampieri, A. Belfiore, G. A. Rodríguez Castillo, A. De Luca, A. Tiengo, F. Haberl, J. Greiner, R. Salvaterra, S. Sandrelli, and G. Lisini. Discovery of a 0.42-s pulsar in the ultraluminous X-ray source NGC 7793 P13. , 466:L48–L52, March 2017c. doi: 10.1093/mnrasl/slw218.

G. L. Israel, A. Papitto, P. Esposito, L. Stella, L. Zampieri, A. Belfiore, G. A. Rodríguez Castillo, A. De Luca, A. Tiengo, F. Haberl, J. Greiner, R. Salvaterra, S. Sandrelli, and G. Lisini. Discovery of a 0.42-s pulsar in the ultraluminous X-ray source NGC 7793 P13. , 466:L48–L52, March 2017d. doi: 10.1093/mnrasl/slw218.

K. Jahoda, J. H. Swank, A. B. Giles, W. Zhang, and E. H. Morgan. Initial Performance Results of the Proportional Counter Array for the X-ray Timing Explorer. In *American Astronomical Society Meeting Abstracts #182*, volume 182 of *American Astronomical Society Meeting Abstracts*, page 51.19, May 1993.

Keith Jahoda, Craig B. Markwardt, Yana Radeva, Arnold H. Rots, Michael J. Stark, Jean H. Swank, Tod E. Strohmayer, and William Zhang. Calibration of the Rossi X-Ray Timing Explorer Proportional Counter Array. , 163(2): 401–423, April 2006. doi: 10.1086/500659.

F. Jansen, D. Lumb, B. Altieri, J. Clavel, M. Ehle, C. Erd, C. Gabriel, M. Guainazzi, P. Gondoin, R. Much, R. Munoz, M. Santos, N. Schartel, D. Texier, and G. Vacanti. XMM-Newton observatory. I. The spacecraft and operations. , 365:L1–L6, January 2001. doi: 10.1051/0004-6361:20000036.

P. Kaaret, A. Alonso-Herrero, J. S. Gallagher, G. Fabbiano, A. Zezas, and M. J. Rieke. Displacement of X-ray sources from star clusters in starburst galaxies. , 348(2):L28–L32, February 2004. doi: 10.1111/j.1365-2966.2004.07516.x.

P. Kaaret, H. Feng, and T. P. Roberts. Ultraluminous X-Ray Sources. , 55: 303–341, August 2017. doi: 10.1146/annurev-astro-091916-055259.

Philip Kaaret, Melanie G. Simet, and Cornelia C. Lang. A 62 Day X-Ray Periodicity and an X-Ray Flare from the Ultraluminous X-Ray Source in M82. *Astrophys.J.*, 646:174–183, 2006. doi: 10.1086/504830.

Jari J. E. Kajava and Juri Poutanen. Spectral variability of ultraluminous X-ray sources. , 398(3):1450–1460, September 2009. doi: 10.1111/j.1365-2966.2009.15215.x.

S. Kato, J. Fukue, and S. Mineshige. *Black-Hole Accretion Disks — Towards a New Paradigm —*. 2008.

Almus T. Kenter, J. H. Chappell, Ralph P. Kraft, G. R. Meehan, Stephen S. Murray, Martin V. Zombeck, and George W. Fraser. High-Resolution Camera on AXAF. In Oswald H. Siegmund and Mark A. Gummin, editors, *EUV, X-Ray, and Gamma-Ray Instrumentation for Astronomy VII*, volume 2808 of *Society of Photo-Optical Instrumentation Engineers (SPIE) Conference Series*, pages 626–649, October 1996. doi: 10.1117/12.256037.

Roy P. Kerr. Gravitational Field of a Spinning Mass as an Example of Algebraically Special Metrics. , 11(5):237–238, September 1963. doi: 10.1103/PhysRevLett.11.237.

A. L. King, J. M. Miller, J. Raymond, A. C. Fabian, C. S. Reynolds, K. Gültekin, E. M. Cackett, S. W. Allen, D. Proga, and T. R. Kallman. Regulation of Black Hole Winds and Jets across the Mass Scale. , 762(2):103, January 2013. doi: 10.1088/0004-637X/762/2/103.

A. R. King and K. A. Pounds. Black hole winds. , 345(2):657–659, October 2003. doi: 10.1046/j.1365-8711.2003.06980.x.

Andrew King and Jean-Pierre Lasota. ULXs: Neutron stars versus black holes. , 458(1):L10–L13, May 2016. doi: 10.1093/mnrasl/slw011.

Andrew King and Jean-Pierre Lasota. Pulsing and non-pulsing ULXs: the iceberg emerges. , 494(3):3611–3615, May 2020. doi: 10.1093/mnras/staa930.

Andrew King, Jean-Pierre Lasota, and Matthew Middleton. Ultraluminous X-ray sources. , 96:101672, June 2023. doi: 10.1016/j.newar.2022.101672.

F. Koliopanos, G. Vasilopoulos, O. Godet, M. Bachetti, N. A. Webb, and D. Barret. ULX spectra revisited: Accreting, highly magnetized neutron stars as the engines of ultraluminous X-ray sources. , 608:A47, December 2017a. doi: 10.1051/0004-6361/201730922.

Filippos Koliopanos, Georgios Vasilopoulos, Olivier Godet, Matteo Bachetti, Natalie A. Webb, and Didier Barret. ULX spectra revisited: Accreting, highly magnetized neutron stars as the engines of ultraluminous X-ray sources. , 608: A47, December 2017b. doi: 10.1051/0004-6361/201730922.

A. K. H. Kong, R. Di Stefano, and F. Yuan. Evidence of an Intermediate-Mass Black Hole: Chandra and XMM-Newton Observations of the Ultraluminous Supersoft X-Ray Source in M101 during Its 2004 Outburst. , 617:L49–L52, December 2004. doi: 10.1086/427025.

E. Körding, H. Falcke, and S. Markoff. Population X: Are the super-Eddington X-ray sources beamed jets in microblazars or intermediate mass black holes? , 382:L13–L16, January 2002. doi: 10.1051/0004-6361:20011776.

Elmar G. Körding, Sebastian Jester, and Rob Fender. Accretion states and radio loudness in active galactic nuclei: analogies with X-ray binaries. , 372(3):1366–1378, November 2006. doi: 10.1111/j.1365-2966.2006.10954.x.

T. Kotani, N. Kawai, M. Matsuoka, T. Dotani, H. Inoue, F. Nagase, Y. Tanaka, Y. Ueda, K. Yamaoka, W. Brinkmann, K. Ebisawa, T. Takeshima, N. E. White, A. Harmon, C. R. Robinson, S. N. Zhang, M. Tavani, and R. Foster. ASCA observations of galactic jet systems. In Charles D. Dermer, Mark S. Strickman, and James D. Kurfess, editors, *Proceedings of the Fourth Compton Symposium*, volume 410 of *American Institute of Physics Conference Series*, pages 922–926, May 1997. doi: 10.1063/1.53963.

T. Kotani, K. Ebisawa, H. Inoue, N. Kawai, M. Matsuoka, F. Nagase, C. R. Robinson, T. Takeshima, Y. Ueda, K. Yamaoka, and A. Yoshida. Discovery of Iron-K Absorption Lines from the Transient Jets GRS 1915+105 and GRO J1655-40. *Advances in Space Research*, 25(3-4):445–448, January 2000a. doi: 10.1016/S0273-1177(99)00777-2.

Taro Kotani, Ken Ebisawa, Tadayasu Dotani, Hajime Inoue, Fumiaki Nagase, Yasuo Tanaka, and Yoshihiro Ueda. ASCA Observations of the Absorption Line Features from the Superluminal Jet Source GRS 1915+105. , 539(1): 413–423, August 2000b. doi: 10.1086/309200.

K. Kovlakas, T. Fragos, D. Schaerer, and A. Mesinger. The ionizing and heating power of ultraluminous X-ray sources under the geometrical beaming model. , 665:A28, September 2022. doi: 10.1051/0004-6361/202244252.

J. H. Krolik. Magnetized Accretion inside the Marginally Stable Orbit around a Black Hole. , 515(2):L73–L76, April 1999. doi: 10.1086/311979.

Jiří Krtička. Mass loss in main-sequence B stars. , 564:A70, April 2014. doi: 10.1051/0004-6361/201321980.

Aya Kubota and Kazuo Makishima. The Three Spectral Regimes Found in the Stellar Black Hole XTE J1550-564 in Its High/Soft State. , 601(1):428–438, January 2004. doi: 10.1086/380433.

Aya Kubota, Yasuo Tanaka, Kazuo Makishima, Yoshihiro Ueda, Tadayasu Dotani, Hajime Inoue, and Kazutaka Yamaoka. Evidence for a Black Hole in the X-Ray Transient GRS 1009-45. , 50:667–673, December 1998. doi: 10.1093/pasj/50.6.667.

Aya Kubota, Ken Ebisawa, Kazuo Makishima, and Kazuhiro Nakazawa. On the Temperature Profile of Radiatively Efficient Geometrically Thin Disks in Black Hole Binaries with the ASCA GIS. , 631(2):1062–1071, October 2005. doi: 10.1086/432900.

Aya Kubota, Chris Done, Shane W. Davis, Tadayasu Dotani, Tsunefumi Mizuno, and Yoshihiro Ueda. Testing Accretion Disk Structure with Suzaku Data of LMC X-3. , 714(1):860–867, May 2010. doi: 10.1088/0004-637X/714/1/860.

E. Kuulkers, J. J. M. in't Zand, R. Cornelisse, J. Heise, A. K. H. Kong, P. A. Charles, A. Bazzano, M. Cocchi, L. Natalucci, and P. Ubertini. Turmoil on the accretion disk of GRO J1655-40. , 358:993–1000, June 2000.

Stephanie M. LaMassa, Sabrina Cales, Edward C. Moran, Adam D. Myers, Gordon T. Richards, Michael Eracleous, Timothy M. Heckman, Luigi Gallo, and C. Megan Urry. The Discovery of the First “Changing Look” Quasar: New Insights Into the Physics and Phenomenology of Active Galactic Nucleus. , 800 (2):144, February 2015. doi: 10.1088/0004-637X/800/2/144.

Debora Lančová, David Abarca, Włodek Kluźniak, Maciek Wielgus, Aleksander Sadowski, Ramesh Narayan, Jan Schee, Gabriel Török, and Marek Abramowicz. Puffy Accretion Disks: Sub-Eddington, Optically Thick, and Stable. , 884(2): L37, October 2019. doi: 10.3847/2041-8213/ab48f5.

Julia C. Lee, Christopher S. Reynolds, Ronald Remillard, Norbert S. Schulz, Eric G. Blackman, and Andrew C. Fabian. High-Resolution Chandra HETGS and Rossi X-Ray Timing Explorer Observations of GRS 1915+105: A Hot Disk Atmosphere and Cold Gas Enriched in Iron and Silicon. , 567(2):1102–1111, March 2002. doi: 10.1086/338588.

Bret D. Lehmer, Rafael T. Eufrasio, Panayiotis Tzanavaris, Antara Basu-Zych, Tassos Fragos, Andrea Prestwich, Mihoko Yukita, Andreas Zezas, Ann E. Hornschemeier, and Andrew Ptak. X-Ray Binary Luminosity Function Scaling Relations for Local Galaxies Based on Subgalactic Modeling. , 243(1):3, July 2019. doi: 10.3847/1538-4365/ab22a8.

Josef Lense and Hans Thirring. Über den Einfluß der Eigenrotation der Zentralkörper auf die Bewegung der Planeten und Monde nach der Einsteinschen Gravitationstheorie. *Physikalische Zeitschrift*, 19:156, January 1918.

C. Leong, E. Kellogg, H. Gursky, H. Tananbaum, and R. Giacconi. X-Ray Emission from the Magellanic Clouds Observed by UHURU. , 170:L67, December 1971. doi: 10.1086/180842.

Li-Xin Li, Erik R. Zimmerman, Ramesh Narayan, and Jeffrey E. McClintock. Multitemperature Blackbody Spectrum of a Thin Accretion Disk around a Kerr Black Hole: Model Computations and Comparison with Observations. , 157 (2):335–370, April 2005. doi: 10.1086/428089.

J. Liu and R. Di Stefano. An Ultraluminous Supersoft X-Ray Source in M81: An Intermediate-Mass Black Hole? , 674:L73–L76, February 2008. doi: 10.1086/529071.

N. Lund, C. Budtz-Jørgensen, N. J. Westergaard, S. Brandt, I. L. Rasmussen, A. Hornstrup, C. A. Oxborrow, J. Chenevez, P. A. Jensen, S. Laursen, K. H. Andersen, P. B. Mogensen, I. Rasmussen, K. Omø, S. M. Pedersen, J. Polny, H. Andersson, T. Andersson, V. Kämäräinen, O. Vilhu, J. Huovelin, S. Maisala, M. Morawski, G. Juchnikowski, E. Costa, M. Feroci, A. Rubini, M. Rapisarda, E. Morelli, V. Carassiti, F. Frontera, C. Pelliciari, G. Loffredo, S. Martínez Núñez, V. Reglero, T. Velasco, S. Larsson, R. Svensson, A. A. Zdziarski, A. Castro-Tirado, P. Attina, M. Goria, G. Giulianelli, F. Cordero, M. Rezazad, M. Schmidt, R. Carli, C. Gomez, P. L. Jensen, G. Sarri, A. Tiemon, A. Orr, R. Much, P. Kretschmar, and H. W. Schnopper. JEM-X: The X-ray monitor aboard INTEGRAL. , 411:L231–L238, November 2003. doi: 10.1051/0004-6361:20031358.

Thomas J. Maccarone. On the misalignment of jets in microquasars. , 336(4): 1371–1376, November 2002. doi: 10.1046/j.1365-8711.2002.05876.x.

K. Makishima, Y. Maejima, K. Mitsuda, H. V. Bradt, R. A. Remillard, I. R. Tuohy, R. Hoshi, and M. Nakagawa. Simultaneous X-Ray and Optical Observations of GX 339-4 in an X-Ray High State. , 308:635, September 1986. doi: 10.1086/164534.

Julien Malzac, Andrei M. Beloborodov, and Juri Poutanen. X-ray spectra of accretion discs with dynamic coronae. , 326(2):417–427, September 2001. doi: 10.1046/j.1365-8711.2001.04450.x.

Thomas H. Markert, Claude R. Canizares, Daniel Dewey, Michael McGuirk, Chris S. Pak, and Mark L. Schattenburg. High-Energy Transmission Grating Spectrometer for the Advanced X-ray Astrophysics Facility (AXAF). In Oswald H. Siegmund and John V. Vallerga, editors, *EUV, X-Ray, and Gamma-Ray Instrumentation for Astronomy V*, volume 2280 of *Society of Photo-Optical Instrumentation Engineers (SPIE) Conference Series*, pages 168–180, September 1994. doi: 10.1117/12.186812.

S. Markoff, H. Falcke, and R. Fender. A jet model for the broadband spectrum of XTE J1118+480. Synchrotron emission from radio to X-rays in the Low/Hard spectral state. , 372:L25–L28, June 2001. doi: 10.1051/0004-6361:20010420.

Silvia Martínez-Núñez, Peter Kretschmar, Enrico Bozzo, Lidia M. Oskinova, Joachim Puls, Lara Sidoli, Jon Olof Sundqvist, Pere Blay, Maurizio Falanga, Felix Fürst, Angel Gímenez-García, Ingo Kreykenbohm, Matthias Kühnel, Andreas Sander, José Miguel Torrejón, and Jörn Wilms. Towards a Unified View of Inhomogeneous Stellar Winds in Isolated Supergiant Stars and Supergiant High Mass X-Ray Binaries. , 212(1-2):59–150, October 2017. doi: 10.1007/s11214-017-0340-1.

Andrea Martocchia and Giorgio Matt. Iron Kalpha line intensity from accretion discs around rotating black holes. , 282(4):L53–L57, October 1996. doi: 10.1093/mnras/282.4.L53.

J. M. Mas-Hesse, A. Giménez, J. L. Culhane, C. Jamar, B. McBreen, J. Torra, R. Hudec, J. Fabregat, E. Meurs, J. P. Swings, M. A. Alcacera, A. Balado, R. Beiztegui, T. Belenguer, L. Bradley, M. D. Caballero, P. Cabo, J. M. Defise, E. Díaz, A. Domingo, F. Figueras, I. Figueroa, L. Hanlon, F. Hroch, V. Hudcova, T. García, B. Jordan, C. Jordi, P. Kretschmar, C. Laviada, M. March, E. Martín, E. Mazy, M. Menéndez, J. M. Mi, E. de Miguel, T. Muñoz, K. Nolan, R. Olmedo, J. Y. Plesseria, J. Polcar, M. Reina, E. Renotte, P. Rochus, A. Sánchez, J. C. San Martín, A. Smith, J. Soldan, P. Thomas, V. Timón, and D. Walton. OMC: An Optical Monitoring Camera for INTEGRAL. Instrument description and performance. , 411:L261–L268, November 2003. doi: 10.1051/0004-6361:20031418.

K. O. Mason, G. Bignami, A. C. Brinkman, and A. Peacock. The XMM observatory. *Advances in Space Research*, 16(3):41–50, July 1995. doi: 10.1016/0273-1177(95)00207-U.

G. Matt, G. C. Perola, and L. Piro. The iron line and high energy bump as X-ray signatures of cold matter in Seyfert 1 galaxies. , 247:25, July 1991.

Giorgio Matt, Matteo Guainazzi, and Roberto Maiolino. Changing look: from Compton-thick to Compton-thin, or the rebirth of fossil active galactic nuclei. , 342(2):422–426, June 2003. doi: 10.1046/j.1365-8711.2003.06539.x.

Kristen. B. W. McQuinn, Evan D. Skillman, Andrew E. Dolphin, Danielle Berg, and Robert Kennicutt. THE DISTANCE TO m51. *The Astrophysical Journal*, 826(1):21, jul 2016.

John Michell. On the Means of Discovering the Distance, Magnitude, &c. of the Fixed Stars, in Consequence of the Diminution of the Velocity of Their Light, in Case Such a Diminution Should be Found to Take Place in any of Them, and Such Other Data Should be Procured from Observations, as Would be Farther Necessary for That Purpose. By the Rev. John Michell, B. D. F. R. S. In a Letter to Henry Cavendish, Esq. F. R. S. and A. S. *Philosophical Transactions of the Royal Society of London Series I*, 74:35–57, January 1784.

M. Middleton, A. Gúrpide, and D. J. Walton. Propeller states in locally supercritical ULXs. , 519(2):2224–2234, February 2023. doi: 10.1093/mnras/stac3380.

Romana Mikusincova, Michal Dovciak, Michal Bursa, Niccolo Di Lalla, Giorgio Matt, Jiri Svoboda, Roberto Taverna, and Wenda Zhang. X-ray Polarimetry as a Tool to Measure the Black Hole Spin in Microquasars: Simulations of IXPE Capabilities. , January 2023. doi: 10.1093/mnras/stad077.

J. M. Miller, A. C. Fabian, and M. C. Miller. A Comparison of Intermediate-Mass Black Hole Candidate Ultraluminous X-Ray Sources and Stellar-Mass Black Holes. , 614:L117–L120, October 2004. doi: 10.1086/425316.

J. M. Miller, J. Homan, and G. Miniutti. A Prominent Accretion Disk in the Low-Hard State of the Black Hole Candidate SWIFT J1753.5-0127. , 652(2): L113–L116, December 2006. doi: 10.1086/510015.

J. M. Miller, J. Raymond, C. S. Reynolds, A. C. Fabian, T. R. Kallman, and J. Homan. The Accretion Disk Wind in the Black Hole GRO J1655-40. , 680 (2):1359–1377, June 2008. doi: 10.1086/588521.

J. M. Miller, D. J. Walton, A. L. King, M. T. Reynolds, A. C. Fabian, M. C. Miller, and R. C. Reis. Revisiting Putative Cool Accretion Disks in Ultraluminous X-Ray Sources. , 776(2):L36, October 2013. doi: 10.1088/2041-8205/776/2/L36.

Jon M. Miller, Dipankar Maitra, Edward M. Cackett, Sudip Bhattacharyya, and Tod E. Strohmayer. A Fast X-ray Disk Wind in the Transient Pulsar IGR J17480-2446 in Terzan 5. , 731(1):L7, April 2011. doi: 10.1088/2041-8205/731/1/L7.

S. Mineo, M. Gilfanov, and R. Sunyaev. X-ray emission from star-forming galaxies - I. High-mass X-ray binaries. , 419(3):2095–2115, January 2012. doi: 10.1111/j.1365-2966.2011.19862.x.

Shin Mineshige, Akira Hirano, Shunji Kitamoto, Tatsuya T. Yamada, and Jun Fukue. Time-dependent Disk Accretion in X-Ray Nova MUSCAE 1991. , 426: 308, May 1994. doi: 10.1086/174065.

G. Miniutti and A. C. Fabian. A light bending model for the X-ray temporal and spectral properties of accreting black holes. , 349(4):1435–1448, April 2004. doi: 10.1111/j.1365-2966.2004.07611.x.

D. Misra, T. Fragos, T. M. Tauris, E. Zapartas, and D. R. Aguilera-Dena. The origin of pulsating ultra-luminous X-ray sources: Low- and intermediate-mass X-ray binaries containing neutron star accretors. , 642:A174, October 2020. doi: 10.1051/0004-6361/202038070.

Devina Misra, Konstantinos Kovlakas, Tassos Fragos, Jeff J. Andrews, Simone S. Bavera, Emmanouil Zapartas, Zepei Xing, Aaron Dotter, Kyle Akira Rocha, Philipp M. Srivastava, and Meng Sun. Exploring the nature of ultra-luminous X-ray sources across stellar population ages using detailed binary evolution calculations. , 682:A69, February 2024. doi: 10.1051/0004-6361/202347880.

K. Mitsuda, H. Inoue, K. Koyama, K. Makishima, M. Matsuoka, Y. Ogawara, N. Shibazaki, K. Suzuki, Y. Tanaka, and T. Hirano. Energy spectra of low-mass binary X-ray sources observed from Tenma. , 36:741–759, January 1984.

Dae-Sik Moon, Fiona A. Harrison, S. Bradley Cenko, and Jamil A. Shariff. Large Highly Ionized Nebulae Around Ultra-luminous X-ray Sources. , 731(2):L32, April 2011. doi: 10.1088/2041-8205/731/2/L32.

S. E. Motta, T. M. Belloni, L. Stella, T. Muñoz-Darias, and R. Fender. Precise mass and spin measurements for a stellar-mass black hole through X-ray timing: the case of GRO J1655-40. , 437(3):2554–2565, January 2014. doi: 10.1093/mnras/stt2068.

S. E. Motta, J. Rodriguez, E. Jourdain, M. Del Santo, G. Belanger, F. Cangemi, V. Grinberg, J. J. E. Kajava, E. Kuulkers, J. Malzac, K. Pottschmidt, J. P. Roques, C. Sánchez-Fernández, and J. Wilms. The INTEGRAL view on black hole X-ray binaries. *New Astronomy Review*, 93:101618, December 2021. doi: 10.1016/j.newar.2021.101618.

P. Mucciarelli, P. Casella, T. Belloni, L. Zampieri, and P. Ranalli. A variable Quasi-Periodic Oscillation in M82 X-1. Timing and spectral analysis of XMM-Newton and RossiXTE observations. , 365:1123–1130, February 2006. doi: 10.1111/j.1365-2966.2005.09754.x.

E. S. Mukherjee, D. J. Walton, M. Bachetti, F. A. Harrison, D. Barret, E. Bellm, S. E. Boggs, F. E. Christensen, W. W. Craig, A. C. Fabian, F. Fuerst, B. W. Grefenstette, C. J. Hailey, K. K. Madsen, M. J. Middleton, J. M. Miller, V. Rana, D. Stern, and W. Zhang. A Hard X-Ray Study of the Ultraluminous X-Ray Source NGC 5204 X-1 with NuSTAR and XMM-Newton. , 808(1):64, July 2015. doi: 10.1088/0004-637X/808/1/64.

Alexander A. Mushtukov, Valery F. Suleimanov, Sergey S. Tsygankov, and Juri Poutanen. The critical accretion luminosity for magnetized neutron stars. , 447(2):1847–1856, February 2015. doi: 10.1093/mnras/stu2484.

Alexander A. Mushtukov, Simon Portegies Zwart, Sergey S. Tsygankov, Dmitrij I. Nagirner, and Juri Poutanen. Pulsating ULXs: large pulsed fraction excludes strong beaming. , 501(2):2424–2429, February 2021. doi: 10.1093/mnras/staa3809.

Ramesh Narayan and Insu Yi. Advection-dominated Accretion: Underfed Black Holes and Neutron Stars. , 452:710, October 1995. doi: 10.1086/176343.

Ramesh Narayan, Jeffrey E. McClintock, and Insu Yi. A New Model for Black Hole Soft X-Ray Transients in Quiescence. , 457:821, February 1996. doi: 10.1086/176777.

Ramesh Narayan, Igor V. Igumenshchev, and Marek A. Abramowicz. Magnetically Arrested Disk: an Energetically Efficient Accretion Flow. , 55:L69–L72, December 2003. doi: 10.1093/pasj/55.6.L69.

J. Neilsen, F. Rahoui, J. Homan, and M. Buxton. A Super-Eddington, Compton-thick Wind in GRO J1655-40? , 822(1):20, May 2016. doi: 10.3847/0004-637X/822/1/20.

Joseph Neilsen and Jeroen Homan. A Hybrid Magnetically/Thermally Driven Wind in the Black Hole GRO J1655-40? , 750(1):27, May 2012. doi: 10.1088/0004-637X/750/1/27.

Joseph Neilsen and Julia C. Lee. Accretion disk winds as the jet suppression mechanism in the microquasar GRS 1915+105. , 458(7237):481–484, March 2009. doi: 10.1038/nature07680.

Joseph Neilsen, Ronald A. Remillard, and Julia C. Lee. The Physics of the “Heartbeat” State of GRS 1915+105. , 737(2):69, August 2011. doi: 10.1088/0004-637X/737/2/69.

Joseph Neilsen, Andrew J. Petschek, and Julia C. Lee. Accretion disc wind variability in the states of the microquasar GRS 1915+105. , 421(1):502–511, March 2012. doi: 10.1111/j.1365-2966.2011.20329.x.

I. D. Novikov and K. S. Thorne. Astrophysics of black holes. In *Black Holes (Les Astres Occlus)*, pages 343–450, January 1973.

M. A. Nowak, J. Wilms, W. A. Heindl, K. Pottschmidt, J. B. Dove, and M. C. Begelman. A good long look at the black hole candidates LMC X-1 and LMC X-3. , 320(3):316–326, January 2001. doi: 10.1046/j.1365-8711.2001.03984.x.

Michael A. Nowak, Adrienne Juett, Jeroen Homan, Yangsen Yao, Jörn Wilms, Norbert S. Schulz, and Claude R. Canizares. Disk-dominated States of 4U 1957+11: Chandra, XMM-Newton, and RXTE Observations of Ostensibly the Most Rapidly Spinning Galactic Black Hole. , 689(2):1199–1214, December 2008. doi: 10.1086/592227.

Michael A. Nowak, Jörn Wilms, Katja Pottschmidt, Norbert Schulz, Dipankar Maitra, and Jon Miller. Suzaku Observations of 4U 1957+11: Potentially the Most Rapidly Spinning Black Hole in (the Halo of) the Galaxy. , 744(2):107, January 2012. doi: 10.1088/0004-637X/744/2/107.

T. Okajima, K. Ebisawa, and T. Kawaguchi. A Stellar-Mass Black Hole in the Ultraluminous X-Ray Source M82 X-1? , 652:L105–L108, December 2006. doi: 10.1086/510153.

Jerome A. Orosz and Charles D. Bailyn. Optical Observations of GRO J1655-40 in Quiescence. I. A Precise Mass for the Black Hole Primary. , 477(2):876–896, March 1997. doi: 10.1086/303741.

Jerome A. Orosz, Ronald A. Remillard, Charles D. Bailyn, and Jeffrey E. McClintock. An Optical Precursor to the Recent X-Ray Outburst of the Black Hole Binary GRO J1655-40. , 478(2):L83–L86, April 1997. doi: 10.1086/310553.

Jerome A. Orosz, Danny Steeghs, Jeffrey E. McClintock, Manuel A. P. Torres, Ivan Bochkov, Lijun Gou, Ramesh Narayan, Michael Blaschak, Alan M. Levine, Ronald A. Remillard, Charles D. Bailyn, Morgan M. Dwyer, and Michelle Buxton. A New Dynamical Model for the Black Hole Binary LMC X-1. , 697(1): 573–591, May 2009. doi: 10.1088/0004-637X/697/1/573.

Jerome A. Orosz, James F. Steiner, Jeffrey E. McClintock, Michelle M. Buxton, Charles D. Bailyn, Danny Steeghs, Alec Guberman, and Manuel A. P. Torres. The Mass of the Black Hole in LMC X-3. , 794(2):154, October 2014. doi: 10.1088/0004-637X/794/2/154.

M. J. Page, R. Soria, K. Wu, K. O. Mason, F. A. Cordova, and W. C. Priedhorsky. XMM-Newton RGS spectroscopy of LMC X-3. , 345(2):639–649, October 2003. doi: 10.1046/j.1365-8711.2003.06967.x.

Manfred W. Pakull and Laurent Mirioni. Optical Counterparts of Ultraluminous X-Ray Sources. *arXiv e-prints*, art. astro-ph/0202488, February 2002. doi: 10.48550/arXiv.astro-ph/0202488.

Manfred W. Pakull, Roberto Soria, and Christian Motch. A 300-parsec-long jet-inflated bubble around a powerful microquasar in the galaxy NGC 7793. , 466 (7303):209–212, July 2010. doi: 10.1038/nature09168.

D. R. Pasham, T. E. Strohmayer, and R. F. Mushotzky. A 400-solar-mass black hole in the galaxy M82. , 513:74–76, September 2014. doi: 10.1038/nature13710.

C. Pinto and P. Kosec. Winds in ultraluminous X-ray sources: New challenges. *Astronomische Nachrichten*, 344(4):e20220134, May 2023. doi: 10.1002/asna.20220134.

Ciro Pinto and Dominic J. Walton. *Ultra-Luminous X-Ray Sources: Extreme Accretion and Feedback*, pages 345–391. Springer Nature Singapore, Singapore, 2023. ISBN 978-981-99-4409-5. doi: 10.1007/978-981-99-4409-5_12. URL `https://doi.org/10.1007/978-981-99-4409-5_12`.

D. S. Plant, R. P. Fender, G. Ponti, T. Muñoz-Darias, and M. Coriat. The truncated and evolving inner accretion disc of the black hole GX 339-4. , 573: A120, January 2015. doi: 10.1051/0004-6361/201423925.

G. Ponti, R. P. Fender, M. C. Begelman, R. J. H. Dunn, J. Neilsen, and M. Coriat. Ubiquitous equatorial accretion disc winds in black hole soft states. , 422(1): L11–L15, May 2012. doi: 10.1111/j.1745-3933.2012.01224.x.

G. Ponti, S. Bianchi, T. Muñoz-Darias, K. De, R. Fender, and A. Merloni. High ionisation absorption in low mass X-ray binaries. *Astronomische Nachrichten*, 337(4-5):512–517, May 2016. doi: 10.1002/asna.201612339.

J. Poutanen. Accretion disc-corona models and X/γ-ray spectra of accreting black holes. In M. A. Abramowicz, G. Björnsson, and J. E. Pringle, editors, *Theory of Black Hole Accretion Disks*, pages 100–122, January 1998.

A. Ptak and R. Griffiths. Hard X-Ray Variability in M82: Evidence for a Nascent Active Galactic Nucleus? , 517(2):L85–L89, June 1999. doi: 10.1086/312032.

Andrew Ptak, Ed Colbert, Roeland P. van der Marel, Erin Roye, Tim Heckman, and Brian Towne. Optical Counterparts of Ultraluminous X-Ray Sources Identified from Archival HST WFPC2 Images. , 166(1):154–187, September 2006. doi: 10.1086/505218.

Yanli Qiu, Roberto Soria, Song Wang, Grzegorz Wiktorowicz, Jifeng Liu, Yu Bai, Alexey Bogomazov, Rosanne Di Stefano, Dominic J. Walton, and Xiaojie Xu. CG X-1: An Eclipsing Wolf-Rayet ULX in the Circinus Galaxy. , 877(1):57, May 2019. doi: 10.3847/1538-4357/ab16e7.

M. J. Rees. Appearance of Relativistically Expanding Radio Sources. , 211(5048): 468–470, July 1966. doi: 10.1038/211468a0.

Martin J. Rees. Tidal disruption of stars by black holes of 10^6-10^8 solar masses in nearby galaxies. , 333(6173):523–528, June 1988. doi: 10.1038/333523a0.

Pablo Reig. Be/X-ray binaries. , 332(1):1–29, March 2011. doi: 10.1007/s10509-010-0575-8.

R. C. Reis, A. C. Fabian, R. R. Ross, and J. M. Miller. Determining the spin of two stellar-mass black holes from disc reflection signatures. , 395(3):1257–1264, May 2009. doi: 10.1111/j.1365-2966.2009.14622.x.

R. C. Reis, A. C. Fabian, and J. M. Miller. Black hole accretion discs in the canonical low-hard state. , 402(2):836–854, February 2010. doi: 10.1111/j.1365-2966.2009.15976.x.

Ronald A. Remillard and Jeffrey E. McClintock. X-Ray Properties of Black-Hole Binaries. , 44(1):49–92, September 2006. doi: 10.1146/annurev.astro.44.051905.092532.

Y. Rephaeli and D. Gruber. RXTE view of the starburst galaxies M 82 and NGC 253. , 389:752–760, July 2002. doi: 10.1051/0004-6361:20020635.

Mark T. Reynolds and Jon M. Miller. A Swift Survey of Accretion onto Stellar-mass Black Holes. , 769(1):16, May 2013. doi: 10.1088/0004-637X/769/1/16.

Claudio Ricci and Benny Trakhtenbrot. Changing-look Active Galactic Nuclei. *arXiv e-prints*, art. arXiv:2211.05132, November 2022. doi: 10.48550/arXiv.2211.05132.

Ryan J. Rickards Vaught, Karin M. Sandstrom, and Leslie K. Hunt. Keck Cosmic Web Imager Observations of He II Emission in I Zw 18. , 911(2):L17, April 2021. doi: 10.3847/2041-8213/abf09b.

G. A. Rodríguez Castillo, G. L. Israel, A. Belfiore, F. Bernardini, P. Esposito, F. Pintore, A. De Luca, A. Papitto, L. Stella, A. Tiengo, L. Zampieri, M. Bachetti, M. Brightman, P. Casella, D. D'Agostino, S. Dall'Osso, H. P. Earnshaw, F. Fürst, F. Haberl, F. A. Harrison, M. Mapelli, M. Marelli, M. Middleton, C. Pinto, T. P. Roberts, R. Salvaterra, R. Turolla, D. J. Walton, and A. Wolter. Discovery of a 2.8 s Pulsar in a 2 Day Orbit High-mass X-Ray Binary Powering the Ultraluminous X-Ray Source ULX-7 in M51. , 895(1):60, May 2020. doi: 10.3847/1538-4357/ab8a44.

Peter W. A. Roming, Thomas E. Kennedy, Keith O. Mason, John A. Nousek, Lindy Ahr, Richard E. Bingham, Patrick S. Broos, Mary J. Carter, Barry K. Hancock, Howard E. Huckle, S. D. Hunsberger, Hajime Kawakami, Ronnie Killough, T. Scott Koch, Michael K. McLelland, Kelly Smith, Philip J. Smith, Juan Carlos Soto, Patricia T. Boyd, Alice A. Breeveld, Stephen T. Holland, Mariya Ivanushkina, Michael S. Pryzby, Martin D. Still, and Joseph Stock. The Swift Ultra-Violet/Optical Telescope. , 120(3-4):95–142, October 2005. doi: 10.1007/s11214-005-5095-4.

D. M. Russell, J. C. A. Miller-Jones, T. J. Maccarone, Y. J. Yang, R. P. Fender, and F. Lewis. Testing the Jet Quenching Paradigm with an Ultradeep Observation of a Steadily Soft State Black Hole. , 739(1):L19, September 2011. doi: 10.1088/2041-8205/739/1/L19.

George B. Rybicki and Alan P. Lightman. *Radiative processes in astrophysics*. 1979.

Greg Salvesen and Jonah M. Miller. Black hole spin in X-ray binaries: giving uncertainties an f. , 500(3):3640–3666, January 2021. doi: 10.1093/mnras/staa3325.

Greg Salvesen, Jon M. Miller, Rubens C. Reis, and Mitchell C. Begelman. Spectral hardening as a viable alternative to disc truncation in black hole state transitions. , 431(4):3510–3532, June 2013. doi: 10.1093/mnras/stt436.

R. Sathyaprakash, T. P. Roberts, D. J. Walton, F. Fuerst, M. Bachetti, C. Pinto, W. N. Alston, H. P. Earnshaw, A. C. Fabian, M. J. Middleton, and R. Soria. The discovery of weak coherent pulsations in the ultraluminous X-ray source NGC 1313 X-2. *arXiv e-prints*, art. arXiv:1906.00640, Jun 2019.

R. Saxton, S. Komossa, K. Auchettl, and P. G. Jonker. X-Ray Properties of TDEs. , 216(5):85, July 2020. doi: 10.1007/s11214-020-00708-4.

Norbert Schartel, Rosario González-Riestra, Peter Kretschmar, Marcus Kirsch, Pedro Rodríguez-Pascual, Simon Rosen, Maria Santos-Lleó, Michael Smith, Martin Stuhlinger, and Eva Verdugo-Rodrigo. XMM-Newton. In *Handbook of X-ray and Gamma-ray Astrophysics*, page 114. 2022. doi: 10.1007/978-981-16-4544-0_41-1.

Karl Schwarzschild. Über das Gravitationsfeld eines Massenpunktes nach der Einsteinschen Theorie. *Sitzungsberichte der Königlich Preussischen Akademie der Wissenschaften*, pages 189–196, January 1916.

Rebecca Shafee, Jeffrey E. McClintock, Ramesh Narayan, Shane W. Davis, Li-Xin Li, and Ronald A. Remillard. Estimating the Spin of Stellar-Mass Black Holes by Spectral Fitting of the X-Ray Continuum. , 636(2):L113–L116, January 2006. doi: 10.1086/498938.

N. I. Shakura and R. A. Sunyaev. Black holes in binary systems. Observational appearance. , 24:337–355, 1973.

Zhaohui Shang, Michael S. Brotherton, Beverley J. Wills, D. Wills, Sabrina L. Cales, Daniel A. Dale, Richard F. Green, Jessie C. Runnoe, Rodrigo S. Nemmen, Sarah C. Gallagher, Rajib Ganguly, Dean C. Hines, Benjamin J. Kelly, Gerard A. Kriss, Jun Li, Baitian Tang, and Yanxia Xie. The Next Generation Atlas of Quasar Spectral Energy Distributions from Radio to X-Rays. , 196(1): 2, September 2011. doi: 10.1088/0067-0049/196/1/2.

Stuart L. Shapiro and Saul A. Teukolsky. *Black holes, white dwarfs and neutron stars. The physics of compact objects*. 1983. doi: 10.1002/9783527617661.

Toshiya Shimura and Fumio Takahara. On the Spectral Hardening Factor of the X-Ray Emission from Accretion Disks in Black Hole Candidates. , 445:780, June 1995. doi: 10.1086/175740.

Alan P. Smale and Patricia T. Boyd. Anomalous Low States and Long-term Variability in the Black Hole Binary LMC X-3. , 756(2):146, September 2012. doi: 10.1088/0004-637X/756/2/146.

X. Song, D. J. Walton, G. B. Lansbury, P. A. Evans, A. C. Fabian, H. Earnshaw, and T. P. Roberts. The hunt for pulsating ultraluminous X-ray sources. , 491 (1):1260–1277, January 2020. doi: 10.1093/mnras/stz3036.

R. Soria, E. Pian, and P. A. Mazzali. A second glance at SN 2002ap and the M 74 field with XMM-Newton. , 413:107–119, January 2004. doi: 10.1051/0004-6361: 20031506.

R. Soria, K. S. Long, L. Bianchi, W. P. Blair, P. Ghavamian, K. D. Kuntz, P. P. Plucinsky, and P. F. Winkler. Discovery of a Transient ULX in M83. *The Astronomer's Telegram*, 3092:1, December 2010.

R. Soria, M. W. Pakull, C. Motch, J. C. A. Miller-Jones, A. D. Schwope, R. T. Urquhart, and M. S. Ryan. The ultraluminous X-ray source bubble in NGC 5585. , 501(2):1644–1662, February 2021. doi: 10.1093/mnras/staa3784.

Roberto Soria and Albert K. H. Kong. XMM-Newton Observations of the Spiral Galaxy M74 (NGC 628). , 572(1):L33–L37, June 2002. doi: 10.1086/341445.

Roberto Soria, K. D. Kuntz, P. Frank Winkler, William P. Blair, Knox S. Long, Paul P. Plucinsky, and Bradley C. Whitmore. The Birth of an Ultraluminous X-Ray Source in M83. , 750(2):152, May 2012. doi: 10.1088/0004-637X/750/2/152.

James F. Steiner, Ramesh Narayan, Jeffrey E. McClintock, and Ken Ebisawa. A Simple Comptonization Model. , 121(885):1279, November 2009. doi: 10.1086/64853510.48550/arXiv.0810.1758.

James F. Steiner, Jeffrey E. McClintock, Ronald A. Remillard, Lijun Gou, Shin'ya Yamada, and Ramesh Narayan. The Constant Inner-disk Radius of LMC X-3: A Basis for Measuring Black Hole Spin. , 718(2):L117–L121, August 2010. doi: 10.1088/2041-8205/718/2/L117.

James F. Steiner, Jeffrey E. McClintock, Jerome A. Orosz, Ronald A. Remillard, Charles D. Bailyn, Mari Kolehmainen, and Odele Straub. The Low-spin Black Hole in LMC X-3. , 793(2):L29, October 2014. doi: 10.1088/2041-8205/793/2/L29.

Luigi Stella and Mario Vietri. Lense-Thirring Precession and Quasi-periodic Oscillations in Low-Mass X-Ray Binaries. , 492(1):L59–L62, January 1998. doi: 10.1086/311075.

Luigi Stella and Mario Vietri. kHz Quasiperiodic Oscillations in Low-Mass X-Ray Binaries as Probes of General Relativity in the Strong-Field Regime. , 82(1): 17–20, January 1999. doi: 10.1103/PhysRevLett.82.17.

A. M. Stobbart, T. P. Roberts, and J. Wilms. XMM-Newton observations of the brightest ultraluminous X-ray sources. , 368(1):397–413, May 2006. doi: 10.1111/j.1365-2966.2006.10112.x.

O. Straub, M. Bursa, A. Sadowski, J. F. Steiner, M. A. Abramowicz, W. Kluźniak, J. E. McClintock, R. Narayan, and R. A. Remillard. Testing slim-disk models on the thermal spectra of LMC X-3. , 533:A67, September 2011. doi: 10.1051/0004-6361/201117385.

T. E. Strohmayer and R. F. Mushotzky. Discovery of X-Ray Quasi-periodic Oscillations from an Ultraluminous X-Ray Source in M82: Evidence against Beaming. , 586:L61–L64, March 2003. doi: 10.1086/374732.

Z. Stuchlík and M. Kološ. CONTROVERSY OF THE GRO j1655-40 BLACK HOLE MASS AND SPIN ESTIMATES AND ITS POSSIBLE SOLUTIONS. *The Astrophysical Journal*, 825(1):13, jun 2016. doi: 10.3847/0004-637x/825/1/13. URL `https://doi.org/10.3847/0004-637x/825/1/13`.

R. A. Sunyaev and L. G. Titarchuk. Comptonization of X-rays in plasma clouds. Typical radiation spectra. , 500:167–184, June 1980.

Andrew D. Sutton, Timothy P. Roberts, and Matthew J. Middleton. The ultraluminous state revisited: fractional variability and spectral shape as diagnostics of super-Eddington accretion. , 435(2):1758–1775, October 2013. doi: 10.1093/mnras/stt1419.

Douglas A. Swartz, Roberto Soria, Allyn F. Tennant, and Mihoko Yukita. A Complete Sample of Ultraluminous X-ray Source Host Galaxies. , 741(1):49, November 2011. doi: 10.1088/0004-637X/741/1/49.

Roberto Taverna, Michal Bursa, Michal Dovčiak, Vladimir Karas, Frédéric Marin, Giorgio Matt, Romana Mikušincová, and Wenda Zhang. Polarization of emission from black hole accretion disks: including returning radiation. In E. S. Battistelli, R. T. Jantzen, and R. Ruffini, editors, *Fifteenth Marcel Grossmann Meeting on General Relativity*, pages 250–257, January 2022. doi: 10.1142/9789811258251_0021.

Y. Terashima and A. S. Wilson. The Luminous X-Ray Source Population in M51 Observed with Chandra. , 601:735–758, February 2004. doi: 10.1086/380505.

Christopher Thompson and Robert C. Duncan. The soft gamma repeaters as very strongly magnetized neutron stars - I. Radiative mechanism for outbursts. , 275(2):255–300, July 1995. doi: 10.1093/mnras/275.2.255.

Kip S. Thorne. Disk-Accretion onto a Black Hole. II. Evolution of the Hole. , 191:507–520, July 1974. doi: 10.1086/152991.

Trevor J. Torpin, Patricia T. Boyd, Alan P. Smale, and Lynne A. Valencic. Unusual Black Hole Binary LMC X-3: A Transient High-mass X-Ray Binary That Is Almost Always On? , 849(1):32, November 2017. doi: 10.3847/1538-4357/aa8f96.

S. S. Tsygankov, A. A. Mushtukov, V. F. Suleimanov, and J. Poutanen. Propeller effect in action in the ultraluminous accreting magnetar M82 X-2. , 457:1101–1106, March 2016. doi: 10.1093/mnras/stw046.

M. J. L. Turner, A. Abbey, M. Arnaud, M. Balasini, M. Barbera, E. Belsole, P. J. Bennie, J. P. Bernard, G. F. Bignami, M. Boer, U. Briel, I. Butler, C. Cara, C. Chabaud, R. Cole, A. Collura, M. Conte, A. Cros, M. Denby, P. Dhez, G. Di Coco, J. Dowson, P. Ferrando, S. Ghizzardi, F. Gianotti, C. V. Goodall, L. Gretton, R. G. Griffiths, O. Hainaut, J. F. Hochedez, A. D. Holland, E. Jourdain, E. Kendziorra, A. Lagostina, R. Laine, N. La Palombara, M. Lortholary, D. Lumb, P. Marty, S. Molendi, C. Pigot, E. Poindron, K. A. Pounds, J. N. Reeves, C. Reppin, R. Rothenflug, P. Salvetat, J. L. Sauvageot, D. Schmitt, S. Sembay, A. D. T. Short, J. Spragg, J. Stephen, L. Strüder, A. Tiengo, M. Trifoglio, J. Trümper, S. Vercellone, L. Vigroux, G. Villa, M. J. Ward, S. Whitehead, and E. Zonca. The European Photon Imaging Camera on XMM-Newton: The MOS cameras. , 365:L27–L35, January 2001. doi: 10.1051/0004-6361:20000087.

P. Ubertini, F. Lebrun, G. Di Cocco, A. Bazzano, A. J. Bird, K. Broenstad, A. Goldwurm, G. La Rosa, C. Labanti, P. Laurent, I. F. Mirabel, E. M. Quadrini, B. Ramsey, V. Reglero, L. Sabau, B. Sacco, R. Staubert, L. Vigroux, M. C. Weisskopf, and A. A. Zdziarski. IBIS: The Imager on-board INTEGRAL. , 411:L131–L139, November 2003. doi: 10.1051/0004-6361:20031224.

Y. Ueda, K. Honda, H. Takahashi, C. Done, H. Shirai, Y. Fukazawa, K. Yamaoka, S. Naik, H. Awaki, K. Ebisawa, J. Rodriguez, and S. Chaty. Suzaku Observation of GRS 1915+105: Evolution of Accretion Disk Structure during Limit-cycle Oscillation. , 713(1):257–268, April 2010. doi: 10.1088/0004-637X/713/1/257.

Yoshihiro Ueda, Kazutaka Yamaoka, and Ronald Remillard. GRS 1915+105 in "Soft State": Nature of Accretion Disk Wind and Origin of X-ray Emission. , 695(2):888–899, April 2009. doi: 10.1088/0004-637X/695/2/888.

R. Urquhart and R. Soria. Two Eclipsing Ultraluminous X-Ray Sources in M51. , 831:56, November 2016. doi: 10.3847/0004-637X/831/1/56.

Philip Uttley and Marc Klein-Wolt. The remarkable timing properties of a 'hypersoft' state in GRO J1655-40. , 451(1):475–485, July 2015. doi: 10.1093/mnras/stv978.

Lennart M. van Haaften, Thomas J. Maccarone, Katherine L. Rhode, Arunav Kundu, and Stephen E. Zepf. Discovery of a transient ultraluminous X-ray source in the elliptical galaxy M86. , 483(3):3566–3573, March 2019. doi: 10.1093/mnras/sty3221.

Georgios Vasilopoulos, Filippos Koliopanos, Frank Haberl, Helena Treiber, Murray Brightman, Hannah P. Earnshaw, and Andrés Gúrpide. Chandra Probes the X-Ray Variability of M51 ULX-7: Evidence of Propeller Transition and X-Ray Dips on Orbital Periods. , 909(1):50, March 2021. doi: 10.3847/1538-4357/abda49.

G. Vedrenne, J. P. Roques, V. Schönfelder, P. Mandrou, G. G. Lichti, A. von Kienlin, B. Cordier, S. Schanne, J. Knödlseder, G. Skinner, P. Jean, F. Sanchez, P. Caraveo, B. Teegarden, P. von Ballmoos, L. Bouchet, P. Paul, J. Matteson, S. Boggs, C. Wunderer, P. Leleux, G. Weidenspointner, Ph. Durouchoux, R. Diehl, A. Strong, M. Cassé, M. A. Clair, and Y. André. SPI: The spectrometer aboard INTEGRAL. , 411:L63–L70, November 2003. doi: 10.1051/0004-6361:20031482.

D. A. Verner, G. J. Ferland, K. T. Korista, and D. G. Yakovlev. Atomic Data for Astrophysics. II. New Analytic FITS for Photoionization Cross Sections of Atoms and Ions. , 465:487, July 1996. doi: 10.1086/177435.

D. J. Walton, F. A. Harrison, B. W. Grefenstette, J. M. Miller, M. Bachetti, D. Barret, S. E. Boggs, F. E. Christensen, W. W. Craig, A. C. Fabian, F. Fuerst, C. J. Hailey, K. K. Madsen, M. L. Parker, A. Ptak, V. Rana, D. Stern, N. Webb, and W. W. Zhang. Broadband X-Ray Spectra of the Ultraluminous X-Ray Source Holmberg IX X-1 Observed with NuSTAR, XMM-Newton, and Suzaku. , 793(1):21, September 2014. doi: 10.1088/0004-637X/793/1/21.

D. J. Walton, M. J. Middleton, V. Rana, J. M. Miller, F. A. Harrison, A. C. Fabian, M. Bachetti, D. Barret, S. E. Boggs, F. E. Christensen, W. W. Craig, F. Fuerst, B. W. Grefenstette, C. J. Hailey, K. K. Madsen, D. Stern, and W. Zhang. NuSTAR, XMM-Newton, and Suzaku Observations of the Ultraluminous X-Ray Source Holmberg II X-1. , 806(1):65, June 2015. doi: 10.1088/0004-637X/806/1/65.

D. J. Walton, F. Fürst, F. A. Harrison, D. Stern, M. Bachetti, D. Barret, M. Brightman, A. C. Fabian, M. J. Middleton, A. Ptak, and L. Tao. Super-Eddington accretion on to the neutron star NGC 7793 P13: Broad-band X-ray spectroscopy and ultraluminous X-ray sources. , 473(4):4360–4376, February 2018. doi: 10.1093/mnras/stx2650.

D. J. Walton, M. Heida, M. Bachetti, F. Fürst, M. Brightman, H. Earnshaw, P. A. Evans, A. C. Fabian, B. W. Grefenstette, F. A. Harrison, G. L. Israel, G. B. Lansbury, M. J. Middleton, S. Pike, V. Rana, T. P. Roberts, G. A. Rodriguez Castillo, R. Salvaterra, X. Song, and D. Stern. A new transient ultraluminous X-ray source in NGC 7090. , 501(1):1002–1012, February 2021. doi: 10.1093/mnras/staa3666.

D. J. Walton, A. D. A. Mackenzie, H. Gully, N. R. Patel, T. P. Roberts, H. P. Earnshaw, and S. Mateos. A multimission catalogue of ultraluminous X-ray source candidates. , 509(2):1587–1604, January 2022. doi: 10.1093/mnras/stab3001.

S. Wang, R. Soria, R. Urquhart, and J. Liu. Discovery of two eclipsing X-ray binaries in M 51. , 477:3623–3645, July 2018. doi: 10.1093/mnras/sty872.

Ken-ya Watarai, Jun Fukue, Mitsuru Takeuchi, and Shin Mineshige. Galactic Black-Hole Candidates Shining at the Eddington Luminosity. , 52:133, February 2000. doi: 10.1093/pasj/52.1.133.

Peng Wei, Hu Zou, Xu Kong, Xu Zhou, Ning Hu, Zesen Lin, Yewei Mao, Lin Lin, Zhimin Zhou, Xiang Liu, Shuguo Ma, Lu Ma, Tuhong Zhong, Fei Dang, Jiantao Sun, and Xinkui Lin. Physical Properties of H II Regions in M51 from Spectroscopic Observations. , 132(1015):094101, September 2020. doi: 10.1088/1538-3873/ab9d92.

M. C. Weisskopf, B. Brinkman, C. Canizares, G. Garmire, S. Murray, and L. P. Van Speybroeck. An Overview of the Performance and Scientific Results from the Chandra X-Ray Observatory. , 114(791):1–24, January 2002. doi: 10.1086/338108.

Shan-Shan Weng, Jun-Xian Wang, Wei-Min Gu, and Ju-Fu Lu. Spectral Analyses of the Nearest Persistent Ultraluminous X-Ray Source M 33 X-8. , 61:1287, December 2009. doi: 10.1093/pasj/61.6.1287.

Shan-Shan Weng, Shuang-Nan Zhang, and Hai-Hui Zhao. Super-Eddington Accretion in the Ultraluminous X-Ray Source NGC 1313 X-2: An Ephemeral Feast. , 780(2):147, January 2014. doi: 10.1088/0004-637X/780/2/147.

Maciek Wielgus, Debora Lančová, Odele Straub, Włodek Kluźniak, Ramesh Narayan, David Abarca, Agata Różańska, Frederic Vincent, Gabriel Török, and Marek Abramowicz. Observational properties of puffy discs: radiative GRMHD spectra of mildly sub-Eddington accretion. , 514(1):780–789, July 2022. doi: 10.1093/mnras/stac1317.

D. R. Wilkins, E. M. Cackett, A. C. Fabian, and C. S. Reynolds. Towards modelling X-ray reverberation in AGN: piecing together the extended corona. , 458(1):200–225, May 2016. doi: 10.1093/mnras/stw276.

J. Wilms, M. A. Nowak, K. Pottschmidt, W. A. Heindl, J. B. Dove, and M. C. Begelman. Discovery of recurring soft-to-hard state transitions in LMC X-3. , 320(3):327–340, January 2001. doi: 10.1046/j.1365-8711.2001.03983.x.

C. Winkler, T. J. L. Courvoisier, G. Di Cocco, N. Gehrels, A. Giménez, S. Grebenev, W. Hermsen, J. M. Mas-Hesse, F. Lebrun, N. Lund, G. G. C. Palumbo, J. Paul, J. P. Roques, H. Schnopper, V. Schönfelder, R. Sunyaev, B. Teegarden, P. Ubertini, G. Vedrenne, and A. J. Dean. The INTEGRAL mission. , 411:L1–L6, November 2003. doi: 10.1051/0004-6361:20031288.

Lisa M. Winter, Richard F. Mushotzky, and Christopher S. Reynolds. XMM-Newton Archival Study of the Ultraluminous X-Ray Population in Nearby Galaxies. , 649(2):730–752, October 2006. doi: 10.1086/506579.

Anastasiya Yilmaz, Jiří Svoboda, Victoria Grinberg, Peter G. Boorman, Michal Bursa, and Michal Dovčiak. Accretion disc evolution in GRO J1655-40 and LMC X-3 with relativistic and non-relativistic disc models. , 525(1):1288–1310, October 2023. doi: 10.1093/mnras/stad2339.

A. A. Zdziarski. Power-law X-ray and gamma-ray emission from relativistic thermal plasmas. , 289:514–525, February 1985. doi: 10.1086/162912.

A. A. Zdziarski and M. Gierliński. Radiative Processes, Spectral States and Variability of Black-Hole Binaries. *Progress of Theoretical Physics Supplement*, 155: 99–119, January 2004. doi: 10.1143/PTPS.155.99.

S. N. Zhang, C. A. Wilson, B. A. Harmon, G. J. Fishman, R. B. Wilson, W. S. Paciesas, M. Scott, and B. C. Rubin. X-Ray Nova in Scorpius. , 6046:1, August 1994.

S. N. Zhang, Wei Cui, and Wan Chen. Black Hole Spin in X-Ray Binaries: Observational Consequences. , 482(2):L155–L158, June 1997. doi: 10.1086/310705.

E. R. Zimmerman, R. Narayan, J. E. McClintock, and J. M. Miller. Multi-temperature Blackbody Spectra of Thin Accretion Disks with and without a Zero-Torque Inner Boundary Condition. , 618(2):832–844, January 2005. doi: 10.1086/426071.

List of Abbreviations and Notations

$a*$	Dimensionless Black Hole Spin Parameter
α	Dimensionless Viscosity Parameter
c_s	Speed of Sound
c	Speed of Light
f_{col}	Color Correction Factor or Spectral Hardening Factor
G	Gravitational Constant
Γ	Photon Index
L_{Edd}	Eddington Luminosity
L_{Disk}	Unabsorbed Disk Luminosity
$\dot{M}$	Mass Accretion Rate
M_{BH}	Black Hole Mass
$M_{\odot}$	Solar Mass
r_g	Gravitational Radius
r_{in}	Innermost Edge of the Accretion Disk
T_{Disk}	Disk Temperature
T_{col}	Color Temperature
T_{Eff}	Effective Temperature
ACIS	Advanced CC Imaging Spectrometer
AGN	Active Galactic Nucleus
arf	Ancillary Response File
ASM	All Sky Monitor
BH	Black Hole
BHXRB	Black Hole X-ray Binary
BXA	Bayesian X-ray Analysis
CCD	Charge-Coupled Device
CXO	The Chandra X-ray Observatory
EPIC	The European Photon Imaging Camera
FFT	Fast Fourier Transform
GR	General Relativity
GTI	Good Time Interval
HEASARC	High Energy Astrophysics Science Archive Research Center
HEGTS	High Energy Transmission Grating Spectrometer
HEXTE	High Energy X-ray Timing Experiment
HID	Hardness-Intensity Diagram
HIMS	Hard Intermediate State
HMXRB	High-Mass X-ray Binary
HRC	High Resolution Camera
HSS	High-Soft State
HST	Hubble Space Telescope
IBIS	Imager onboard the INTEGRAL Satellite
IMBH	Intermediate-Mass Black Hole
IMS	Intermediate State
INTEGRAL	International Gamma-Ray Astrophysics Laboratory

ISCO	Innermost Stable Circular Orbit
JEM-X	Joint European X-ray Monitor
LETGS	Low Energy Transmission Grating Spectrometer
LHS	Low-Hard State
LMXRB	Low-Mass X-ray Binary
MOS	Metal Oxide Semiconductor
NT	Novikov&Thorne
NuSTAR	Nuclear Spectroscopic Telescope Array
OMC	Optical Monitoring Camera
PCA	Proportional Counter Array
PCU	Proportional Counter Unit
PULX	Pulsating Ultraluminous X-ray Source
QPO	Quasi - Periodic Oscillation
RGS	x Reflection Grating Spectrometer
rmf	Redistribution Matrix File
RXTE	Rossi X-ray Timing Explorer
SAS	Science Analysis System
SIMS	Soft Intermediate State
SPI	Spectrometer on INTEGRAL
SS	Shakura&Sunyaev
Swift-XRT	Swift X-ray Telescope
Swift-UVOT	Swift Ultraviolet/Optical Telescope
TDE	Tidal Disruption Event
ULX	Ultraluminous X-ray Sources
UV	Ultraviolet
XMM-Newton	X-ray Multi-Mirror Mission
XRB	X-ray Binary

List of publications

Journals

First X-ray polarization measurement confirms the low black-hole spin in LMC X-3

Jiří Svoboda, Michal Dovčiak, James F. Steiner, Fabio Muleri, Adam Ingram, **Anastasiya Yilmaz**, et al.
The Astrophysical Journal, (Dec. 2023), Volume 960, Number 1. pp 3. 2023

Accretion disc evolution in GRO J1655-40 and LMC X-3 with relativistic and non-relativistic disc models

Anastasiya Yilmaz, Jiří Svoboda, Victoria Grinberg, Peter G. Boorman, Michal Bursa, Michal Dovčiak
Monthly Notices of the Royal Astronomical Society 525.1 (Oct. 2023) pp. 1288–1310. 2023

Refereed Proceedings

Testing relativistic accretion disk models with GRO J1655 -40

Anastasiya Yilmaz, Jiří Svoboda, Victoria Grinberg, Peter G. Boorman, Michal Bursa, Michal Dovčiak
Astronomische Nachrichten 344.4, e20230019 (May 2023) e20230019. 2023

Spectra of puffy accretion discs: the kynbb fit

Debora Lančová, **Anastasiya Yilmaz**, Maciek Wielgus,Michal Dovčiak, Odele Straub, Gabriel Török
Astronomische Nachrichten 344.4, e20230023 (May 2023) e20230023. 2023